Down the nanoparticle hole
^{103}Pd:Pd/Fe-oxide theranostic agents for image-assisted thermo-brachytherapy as alternative cancer treatment

Maier, A.

DOI
10.4233/uuid:97f000f7-1176-410f-8213-2bd67ce7406f

Publication date
2023

Document Version
Final published version

Citation (APA)
Maier, A. (2023). *Down the nanoparticle hole: ^{103}Pd:Pd/Fe-oxide theranostic agents for image-assisted thermo-brachytherapy as alternative cancer treatment*. [Dissertation (TU Delft), Delft University of Technology]. https://doi.org/10.4233/uuid:97f000f7-1176-410f-8213-2bd67ce7406f

Down the nanoparticle hole

^{103}Pd:Pd/Fe-oxide theranostic agents for image-assisted thermo-brachytherapy as alternative cancer treatment

Alexandra Maier

Down the nanoparticle hole:

^{103}Pd:Pd/Fe-oxide theranostic agents for image-assisted thermo-brachytherapy as alternative cancer treatment

Down the nanoparticle hole:

^{103}Pd:Pd/Fe-oxide theranostic agents for image-assisted thermo-brachytherapy as alternative cancer treatment

Dissertation

for the purpose of obtaining the degree of doctor
at Delft University of Technology,
by the authority of the Rector Magnificus prof. dr. ir. T.H.J.J. van der Hagen,
chair of the Board of Doctorates,
to be defended publicly on Thursday 19 October 2023 at 10:00 o'clock

by

Alexandra MAIER

Master of Science in Chemical Engineering, Delft University of Technology, The Netherlands
born in Bucharest, Romania

The dissertation has been approved by the promotors

Dr. K. Djanashvili
Dr. ir. A.G. Denkova

Composition of the doctoral committee:

Rector Magnificus,	chairperson
Dr. K. Djanashvili	Delft University of Technology, promotor
Dr. ir. A.G. Denkova	Delft University of Technology, promotor

Independent members:

Prof. dr. C. Platas-Iglesias	Universidade da Coruña, Spain
Prof. dr. H.T. Wolterbeek	Delft University of Technology
Prof. dr. G.C. van Rhoon	Erasmus MC, Rotterdam, The Netherlands
Dr. A. Manzin	Istituto Nazionale di Ricerca Metrologica, Torino, Italy
Dr. A.I. Dugulan	Delft University of Technology
Prof. dr. U. Hanefeld	Delft University of Technology, reserve member

The research presented in this thesis was performed in the framework of HTSM (High Tech Systemen en Materialen), a research program within the Dutch Research Council (NWO), Domain Applied and Engineering Sciences (AES), and supported by Elekta B.V., grant number 16238.

Cover design by: Alexandra Maier

Printed by: Proefschrift specialist

ISBN: 978-94-6384-489-5

"I'm not strange, weird, off, nor crazy, my reality is just different from yours"

Lewis Carroll

Contents

Summary

Cancer is one of the leading causes of death worldwide and the number of cases is expected to keep increasing in the next years. Even though nowadays most employed cancer treatments in clinical practice (surgery, chemo-, and radiotherapy) are effective, they are still associated with multiple limitations and side effects. The main pitfall stays in their non-specificity to tumour cells, which leads to affecting healthy tissues. Therefore, alternative treatments able to overcome the oncologic challenges of the current treatment regimens by specifically treating only the cancer cells, be minimally invasive, and limit short and long-term side effects are highly needed. As the number of patients diagnosed with cancer in incipient stages is constantly increasing, such alternative treatments are currently even more attractive. Due to the advances in nanotechnology, cancer nanomedicine is a fast-advancing field, employing nanoparticles to both diagnose and deliver therapy of cancer, namely, nanotheranostics. Nanobrachytherapy is the brachytherapy treatment delivered via injection of radioactive nanoparticles into the tumour. The great advantage is that nanobrachytherapy retains the characteristics of brachytherapy, such as precise and targeted dose delivery, while allowing a less invasive administration and a more uniform dose distribution in the tumour. However, the radio-resistance exhibited by the tumour cells can hinder the success of nanobrachytherapy, but the synergetic combination of cell damaging agents, as well as radioactivity and heating, is well-known. Thermal treatments, such as hyperthermia, offer a hyperthermic radiosensitization making the tumour more susceptible to irradiation, while thermal ablation can serve as surgery replacement. Furthermore, thermal treatments can be delivered by injection of colloidal suspensions of magnetic nanoparticles (MNPs) in tumours and heating them via exposure to an externally applied alternating magnetic field. An additional advantage of such magnetic nanoparticles is their ability to ensure visualization via magnetic resonance imaging (MRI), a non-invasive technique, helpful in monitoring the treatment effects. This thesis aims to develop a nanotheranostic agent, able to deliver therapeutic effects via radiation and heating, with additional imaging via magnetic resonance imaging. We envision the nanotheranostic as a core-shell hybrid nanoparticle in the form of ^{103}Pd:Pd/Fe-oxide.

The palladium core is radiolabelled with ^{103}Pd radioisotope, responsible for the required radiation dose, whereas the iron oxide coating ensures hyperthermia/thermal ablation and imaging.

The design and preparation of such magnetic hybrid nanoparticle is a challenging task, therefore, **Chapter 2** focused on the synthesis of the desired nanoparticles in their non-radioactive form (Pd/Fe-oxide NPs). A seed-mediated thermal decomposition synthesis method was identified best in producing core-shell hybrid nanoparticles with great uniformity. As the properties of the nanoparticles are strongly related to their morphologies, gaining full control of the synthesis method is essential. For this, we systematically investigated the effect of different reaction parameters on the synthesis method and unravelled important insights on the synthetic mechanism. Via this systematic investigation, variously sized and shaped batches of hybrid Pd/Fe-oxide NPs were produced.

Chapter 3 studied the magnetic properties, such as saturation magnetization (M_S), coercivity (H_C) and blocking temperature (T_B) via SQUID measurements of the aforementioned Pd/Fe-oxide NPs batches. Their dependency on characteristic parameters of the hybrid NPs was highlighted, with attention to the influence of the non-magnetic palladium component that disrupts the iron oxide crystal lattice. It was determined that the majority of hybrid nanoparticles batches exhibit a superparamagnetic behaviour, as it is desired for biomedical applications, and confirmed that the magnetic parameters (M_S, H_C, T_B) increase with the size of the nanocrystals, with few exceptions. This could be explained by shape and composition variations or by the presence of the non-magnetic palladium component that leads to substitution of Fe^{2+} with Pd^{2+} within the iron oxide crystal lattice. As the thermal decomposition synthesis method rendered the nanoparticles hydrophobic, different surfactant modification techniques to make them water dispersible, with satisfying colloidal stability, were investigated. The best results were obtained by surface modification via an additional layer with DSPE-PEG_{2000}-COOH surfactant. Lastly, the batches of Pd/Fe-oxide NPs with the best magnetic properties were tested as hyperthermia/thermal ablation and MRI agents. Pd/Fe-oxide NPs with sizes around 20 nm exhibited the best performance, being deemed best candidates.

In **Chapter 4**, the effects of manganese doping on the properties and performance of Pd/Fe-oxide NPs as thermal and MR-imaging agents were assessed. First, a seed-

mediated thermal decomposition synthesis method for producing Pd/Fe|Mn-oxide NPs with different Mn-content was established. Next, the presence and placement of Pd, Fe and Mn in the composition of the MNPs were shown. Subsequently, the magnetic properties of the Mn-doped MNPs were determined, confirming their superparamagnetism and increase of saturation magnetization with Mn-content present in the composition of the doped MNPs. Their performance as thermal and imaging agents was assessed in comparison to Pd/Fe-oxide NPs with similar sizes and shapes. Higher specific loss power (SLP) values were recorded for the two batches of doped MNPs in comparison to their non-doped analogous, with highest SLP obtained for the MNPs with highest Mn-content. Lastly, their performance as T_1 and T_2 contrast agents was assessed via MRI measurements, both batches of Pd/Fe|Mn-oxide MNPs showing r_2-relaxivities comparable to their Pd/Fe-oxide analogues, and additional increased r_1-relaxivities, with higher T_1 contrast enhancement measured for the MNPs with higher Mn-content.

Lastly, **Chapter 5** explored routes for radiolabelling of the previously introduced Pd/Fe-oxide NPs with ^{103}Pd radioisotope, to obtain ^{103}Pd:Pd/Fe-oxide theranostic nanoparticles. Solubilisation of the ^{103}Pd radioisotope powder in aqua regia, and its addition together with commercially available Pd(II)-acetate precursor during the synthesis, proved to be successful. After it was confirmed that introduction of aqua regia in the reaction mixture does not affect the size, shape and magnetic properties of the prepared hybrid nanoparticles, the radiolabelling efficiency of the method was assessed, showing consistent high radiolabelling efficiency, and additional flexibility in tuning the amount of activity with which the NPs are radiolabelled. Next, the biocompatibility of the designed nanoparticles in their non-radioactive form was investigated by monitoring the *in vitro* toxicity effects on 3D spheroid models of a breast cancer cell line MDA-MB-231. Additionally, the uptake by the spheroids was determined. It was demonstrated that the MNPs exhibited a very low uptake and showed no significant toxicity with concentrations as high as 1 mg/mL. The next step was to evaluate *in vitro* the combined therapeutic effects of hyperthermia/thermal ablation together with ^{103}Pd radiation on the spheroids. It was confirmed that the combinations of low ^{103}Pd dose with thermal ablation and high ^{103}Pd dose with hyperthermia or thermal ablation are successful in spheroids destruction, plus that

heating rate and time exposure to heat during the treatment are important factors to be considered.

Overall, this thesis lays the groundwork for the design of an alternative cancer therapy by using ^{103}Pd:Pd/Fe-oxide NPs, which, following the next steps towards injectable formulations development and *in vivo* evaluations, will unlock the full potential of these materials.

Samenvatting

Kanker is een van de meest voorkomende doodsoorzaken wereldwijd en de verwachting is dat het aantal gevallen de komende jaren zal blijven stijgen. Hoewel de meest toegepaste behandelmethodes tegen kanker al behoorlijk effectief zijn (o.a. operatief verwijderen, chemotherapie en bestralen), komen ze ook met beperkingen en bijwerkingen. Het grootste nadeel van deze behandelmethodes is dat ze niet-specifiek zijn voor tumorcellen, waardoor ook gezond weefsel aangetast wordt. Daarom is er een grote vraag naar alternatieve behandelingen, die specifiek op de kankercellen gericht zijn, minimaal invasief zijn en de bijwerkingen op de korte en lange termijn beperken. Omdat het aantal patiënten dat in een vroeg stadium gediagnostiseerd wordt met kanker toeneemt, worden deze alternatieve behandelmethodes nog aantrekkelijker. Door de ontwikkelingen in nanotechnologie worden er ook steeds meer nanomedicijnen tegen kanker ontwikkeld. Een voorbeeld is nanotheranostiek, waarbij nanodeeltjes worden gebruikt voor zowel de diagnose als de behandeling van kanker. Daarnaast is er ook nanobrachytherapie, een vorm van brachytherapie waarbij radioactieve nanodeeltjes via injectie in de tumor worden gebracht. Het grote voordeel van nanobrachytherapie is dat het de eigenschappen van brachytherapie behoudt, zoals een precieze en doelgerichte stralingsdosis, terwijl het minder invasief is en zorgt voor een gelijkmatigere dosisdistributie in de tumor. De radioresistentie van de tumorcellen kan het succes van nanobrachytherapie tegenwerken, maar de synergetische combinatie van celbeschadigende midelen, evenals radioactiviteit en verwarming, is algemeen bekend. Warmtebehandelingen, zoals hyperthermie, zorgen voor radiosensibilisering waardoor de tumor gevoeliger wordt voor bestraling, terwijl thermische ablatie een alternatief kan vormen voor chirurgische verwijdering van de tumor. Bovendien kunnen thermische handelingen worden uitgevoerd door injectie van colloïdale suspensies van magnetische nanodeeltjes in tumoren en deze te verwarmen via blootstelling aan een extern wisselend magneetveld. Een bijkomend voordeel van de magnetische nanodeeltjes is hun zichtbaarheid in MRI, een non-invasieve techniek dat helpt in het monitoren van de behandeling. Dit proefschrift heeft tot doel een nanotheranostisch middel te ontwikkelen waarmee de behandeling kan worden uitgevoerd door zowel straling

als warmte, en daarnaast kan ook zichtbaar gemaakt worden met MRI. In onze optiek bestaat dit nanotheranostische middel uit een tweelaags hybride nanodeeltje gemaakt van ^{103}Pd:Pd/Fe-oxide. De kern van het nanodeeltje is gemaakt van palladium gemengd met radioactief ^{103}Pd dat de stralingsdosis levert aan de tumor. Daaromheen zit een laag van ijzeroxide die zowel de hyperthermie als de MRI mogelijk maakt.

Het ontwerpen en maken van magnetische hybride nanodeeltjes is een uitdaging, die in **hoofdstuk 2** wordt besproken, inclusief de synthese van de nanodeeltjes in hun niet-radioactieve vorm (Pd/Fe-oxide nanodeeltjes). We hebben de meest succesvolle synthesemethode gevonden om uniforme *core-shell* hybride nanodeeltjes te maken door thermische decompositie met kleine start-kernen te combineren. Omdat de eigenschappen van de nanodeeltjes sterk afhangen van hun morfologie is het essentieel om volledige controle te krijgen over de synthese. Hiervoor hebben we het effect van diverse reactieparameters op de synthese systematisch bestudeerd en belangrijke inzichten opgedaan. Als onderdeel van deze systematische analyse zijn nanodeeltjes gemaakt in diverse groottes en vormen.

Hoofdstuk 3 onderzoekt de magnetische eigenschappen van de hierboven genoemde Pd/Fe-oxide nanodeeltjes, zoals de saturatiemagnetisatie (M_s), coërciviteit (H_c) en de blokkeertemperatuur (T_b), met gebruik van SQUID-metingen. De afhankelijkheid van karakteristieke parameters van de hybride nanodeeltjes was benadrukt, met aandacht voor de invloed van het niet-magnetische palladium dat de kristalstructuur van ijzeroxide ontwricht. Het meerderdeel van de hybride nanodeeltjes blijkt superparamagnetisch gedrag te vertonen, zoals gewenst voor biomedische toepassingen, en er is bevestigd dat de magnetische eigenschappen (M_s, H_c en T_b) toenemen met toenemende nanodeeltjesgrotte, op enkele uitzonderingen na. Dit kan verklaard worden door de variaties in vorm en samenstelling van de nanodeeltjes, of door de aanwezigheid van een niet-magnetisch palladiumcomponent dat een substitutie van Fe^{2+} door Pd^{2+} in de kristalstructuur van ijzeroxide veroorzaakt. Omdat de thermische decompositie synthesemethode de nanodeeltjes hydrofoob maakt, zijn verschillende technieken onderzocht waarmee de oppervlakte-actieve coating van de nanodeeltjes kan worden aangepast, zodat deze een voldoende stabiele suspensie in water vormen. De beste resultaten werden behaald met een techniek die gebruik maakt van een extra laag met DSPE-PEG$_{2000}$-COOH. Tot slot

werden de batches van Pd/Fe-oxide nanodeeltjes met de beste magnetische eigenschappen getest op hun geschiktheid voor hyperthermie/thermische ablatie en MRI. Pd/Fe-oxide nanodeeltjes met een grootte rond de 20 nm gaven de beste resultaten en zijn de beste kandidaten voor de nieuwe behandeling.

In **hoofdstuk 4** zijn de effecten onderzocht van een doping met mangaan op de eigenschappen van de Pd/Fe-oxide nanodeeltjes op de MRI- en verwarmingsprestaties. Na de methode met thermische decompositie en start-kernen voor de synthese van Pd/Fe | Mn-oxide nanodeeltjes met verschillende hoeveelheden mangaan werd ontwikkeld, de aanwezigheid en locatie van Pd, Fe en Mn in de structuur van de magnetische nanodeeltjes werd aangetoond. Vervolgens werden de magnetische eigenschappen van de Mn-gedoteerde nanodeeltjes bepaald, wat de superparamagnetische eigenschappen bevestigde en een verhoogte saturatiemagnetisatie vertoonde wanneer Mn in de nanodeeltjes aanwezig was. De MRI- en thermische prestaties werden getest en vergeleken met die van Pd/Fe-oxide nanodeeltjes van vergelijkbare grootte en vorm. Hogere verwarmingswaarden werden gemeten voor de twee batches van nanodeeltjes met sporen van Mn in vergelijking met de tegenhangers zonder Mn, waarbij de hoogste verwarming gemeten werd bij de nanodeeltjes met de grootste hoeveelheid Mn. Ten slotte was de geschiktheid van de nanodeeltjes als T_1 en T_2 MRI contrastmiddelen getest, waarbij de r_2-relaxatiewaarden voor beide batches van Pd/Fe|Mn-oxide nanodeeltjes vergelijkbaar waren met die van Pd/Fe-oxide, terwijl hogere r_1-relaxatie en T_1 contrast werden gemeten voor de nanodeeltjes met een hogere hoeveelheid Mn.

Als laatste, verkend **hoofdstuk 5** de routes voor het radioactief labelen van de eerder geïntroduceerde Pd/Fe-oxide nanodeeltjes met het radioactieve ^{103}Pd om ^{103}Pd:Pd/Fe-oxide theranostische nanodeeltjes te verkrijgen. De oplosbaarheid van het ^{103}Pd-radioisotoop als poeder in koningswater was succesvol, net als het combineren van deze oplossing met de commercieel verkrijgbare Pd(II)-acetaat precursor tijdens de synthese. Nadat was bevestigd dat het introduceren van koningswater in het reactiemengsel geen invloed had op grootte, vorm en magnetische eigenschappen van de hybride nanodeeltjes, werd de radiolabelingsefficiëntie bepaald. Hieruit bleek een consistent hoge efficiëntie en flexibiliteit in het aanpassen van de hoeveelheid radioactiviteit waarmee de nanodeeltjes gelabeld worden. In de volgende stap de biocompatibiliteit van de nanodeeltjes in een niet-radioactieve vorm was onderzocht

door het volgen van de *in vitro* toxiciteit in een 3D sferoïdemodel van een borstkankercellijn MDA-MB-231. Daarnaast was de opname van nanodeeltjes door de sferoïden bepaald. Een zeer lage opname en geen significante toxiciteit van de nanodeeltjes bij concentratie tot 1 mg/mL werd aangetoond. Vervolgens werden de gecombineerde effecten van hyperthermie/thermische ablatie samen met de ^{103}Pd bestraling op de sferoïden bestudeerd. Hieruit werd bevestigd dat de combinaties van een lage ^{103}Pd stralingsdosis met thermische ablatie en een hoge ^{103}Pd stralingsdosis met hyperthermie of thermische ablatie succesvol zijn bij de vernietigen van sferoïden. Daarnaast bleek dat de verwarmingssnelheid en de tijd van blootstelling aan hitte tijdens de behandeling belangrijke factoren zijn waarmee rekening moet worden gehouden.

Concluderend, dit proefschrift legt de basis voor het ontwerp van alternatieve kankertherapie met behulp van ^{103}Pd:Pd/Fe-oxide nanodeeltjes die, na de volgende stappen in de richting van de ontwikkeling van injecteerbare formuleringen en *in vitro* evaluaties, het volledige potentieel van deze nieuwe materialen zal ontgrendelen.

Rezumat

Cancerul este una dintre principalele cauze de deces la nivel mondial și se preconizează că numărul de cazuri va continua să crească în următorii ani. Chiar dacă, în prezent, tratamentele oncologice cele mai utilizate în practica (chirurgie, chimio- și radioterapie) sunt eficiente, acestea sunt în continuare asociate cu multiple limitări și reacții adverse. Principalul dezavantaj constă în lipsa de specificitate a acestor tratamente catre celulele tumorale, ceea ce conduce la afectarea țesuturile sănătoase. Prin urmare, sunt extrem de necesare tratamente alternative capabile să depășească dezavantajele tratamentelor actuale, cu abilitatea de a trata în mod specific numai celulele canceroase, a fi minim invazive și a limita efectele secundare pe termen scurt și lung. Întrucât numărul pacienților diagnosticați cu cancer în stadii incipiente este în continuă creștere, astfel de tratamente alternative sunt în prezent și mai atractive. Datorită progreselor din nanotehnologie, nanomedicina este un domeniu care se dezvoltă rapid, utilizând nanoparticule atât pentru diagnosticarea, cât și pentru terapia cancerului Nano-brahiterapia este tratamentul cu brahiterapie administrat prin injectarea de nanoparticule radioactive în tumoră. Avantajul esențial al acestui tratament constă în faptul că nanobrahiterapia păstrează caracteristicile brahiterapiei, cum ar fi administrarea precisă și direcționată a dozei de radiație, permițând în același timp o administrare mai puțin invazivă și o distribuție mai uniformă a dozei în tumori. Cu toate acestea, rezistența celulelor tumorale în urma expunerii la radioactivitate poate împiedica succesul nanobrahiterapiei, însă combinația sinergetică de agenți care dăunează celulelor, precum radioactivitatea și încălzirea, sunt factori bine cunoscuți. Tratamentele termice, cum ar fi hipertermia, oferă o radiosensibilizare hipertermică care face tumora mai sensibilă la iradiere, în timp ce ablația termică poate servi drept înlocuitor chirurgical. În plus, tratamentele termice pot fi administrate prin injectarea suspensiilor coloidale de nanoparticule magnetice în tumori și prin încălzirea acestora prin expunere la un câmp magnetic alternativ aplicat extern. Un avantaj suplimentar al unor astfel de nanoparticule magnetice este capacitatea lor de a asigura vizualizarea prin rezonanță magnetică, o tehnică non-invazivă, utilă pentru monitorizarea efectelor tratamentului. Această teză vizează dezvoltarea unui nano-agent capabil să producă efecte terapeutice prin

radiație și căldură, cu abilitatea suplimentară de a oferi imagistică de rezonanță magnetică. Considerăm nanoparticula hibridă sub formă de nucleu-caracasă ^{103}Paladiu:paladiu/oxid de fier. Nucleul de paladiu este marcat radioactiv cu radioizotopul ^{103}Pd, responsabil pentru doza de radiație necesară, în timp ce carcasa de oxid de fier asigură hipertermie/ablație termică și imagistică.

Proiectarea și prepararea unei astfel de nanoparticule hibride magnetice reprezintă o sarcină dificilă; prin urmare, **Capitolul 2** s-a axat pe sinteza nanoparticulelor dorite în forma lor neradioactivă (Pd/oxid de fier NP). O metodă de sinteză termică de descompunere mediată a fost identificată ca cea mai bună pentru producerea de nanoparticule hibride nucleu-caracasă cu o mare uniformitate. Deoarece proprietățile nanoparticulelor sunt strâns legate de morfologia lor, este esențial să se obțină un control deplin asupra metodei de sinteză. Din acest motiv, am investigat în mod sistematic efectul diferiților parametri de reacție asupra metodei de sinteză și am dezvăluit informații importante cu privire la mecanismul sintezei. Prin intermediul acestei investigații sistematice, au fost produse multiple grupuri de nanoparticule hibride Pd/oxid de fier cu diferite dimensiuni si forme.

Capitolul 3 a studiat proprietățile magnetice, cum ar fi inducția magnetică de saturație, câmpul magnetic coercitiv (Hc) și temperatura de blocare (TB) ale grupurilor de nanoparticule menționate anterior. A fost evidențiată dependența lor de parametrii caracteristici ai nanoparticulelor, acordându-se atenție influenței componentei nemagnetice a paladiului care perturbă rețeaua cristalină a oxidului de fier. S-a stabilit că majoritatea grupurilor de nanoparticule hibride prezintă un comportament superparamagnetic, așa cum este de preferat pentru aplicațiile biomedicale, și s-a confirmat că parametrii magnetici cresc odată cu dimensiunea nanocristalelor, cu câteva excepții. Acest lucru se poate explica prin variațiile de formă și compoziție sau prin prezența componentei nemagnetice a paladiului care conduce la înlocuirea ionilor de Fe^{2+} cu Pd^{2+} în interiorul rețelei cristaline a oxidului de fier. Deoarece metoda de sinteză prin descompunere termică produce nanoparticule hidrofobe, a fost necesară investigarea diferitelor tehnici de modificare a surfactanților pentru a face nanoparticulele dispersabile în apă, cu stabilitate coloidală satisfăcătoare. Cele mai bune rezultate au fost obținute prin modificarea suprafeței printr-un strat suplimentar cu surfactantul DSPE-PEG_{2000}-COOH. În cele din urmă, nanoparticulele Pd/oxid de fier cu cele mai bune proprietăți magnetice au

fost testate ca agenți pentru hipertermie/ablație termică și imagistică prin rezonanță magnetică. Nanoparticule cu dimensiuni de aproximativ 20 nm au prezentat cea mai bună performanță, fiind cei mai buni candidați pentru aplicațiile dorite.

În **Capitolul 4**, au fost evaluate efectele dopajului cu mangan asupra proprietăților magnetice și performanței nanoparticulelor palladium-oxid de fier ca agenți termici și imagistici. În primul rând, s-a stabilit o metodă de sinteză satisfăcatoare pentru producerea de nanoparticule nucleu-carcasa paladiu-oxid de fier dopat cu mangan (Pd/oxid de fier|mangan). Apoi, s-a confirmat prezența și plasarea paladiului, fierului și manganului în compoziția nanoparticulei hibride. Ulterior, au fost determinate proprietățile magnetice ale nanoparticulelor dopate cu Mn, confirmând superparamagnetismul acestora și creșterea inducției magnetice de saturație cu conținutul de Mn prezent în compoziția nanoparticulelor dopate. Performanța acestora ca agenți termici și imagistici a fost evaluată în comparație cu nanoparticulele de Pd/oxid de fier cu dimensiuni și forme similare. O abilitate mai mare de a produce căldură a fost înregistrată pentru nanoparticulele dopate, în comparație cu cele similare nedopate, cu cea mai mare abilitate de încălzire fiind obținută pentru nanoparticulele cu cel mai mare conținut de Mn.

În cele din urmă, performanța acestora ca agenți de contrast T_1 (contrast pozitiv) și T_2 (contrast negativ)a fost evaluată, prezentând relaxivități - r_2 comparabile cu analogii lor Pd/oxid de fier, si abilitate adițională de contrast T_1, cu o creștere a relaxivității – r_1 cu conținutul de mangan prezent în compoziția nanoparticulelor.

În final, **Capitolul 5** a explorat diferite căi de introducere a radioizotopului ^{103}Pd în compoziția nanoparticulelor Pd/oxid de fier prezentate anterior, pentru a obține nanoparticulele teranostice ^{103}Pd:Pd/oxide de fier dorite. Solubilizarea pulberii metalice radioactive de ^{103}Pd în apa regală (solutie de acid clorhidric si acid nitric) și adăugarea sa împreună cu precursorul de acetat de Pd disponibil pe piață în timpul sintezei s-a dovedit a fi un succes. După ce s-a confirmat faptul că introducerea apei regale în amestecul de reacție nu afectează dimensiunea, forma și proprietățile magnetice ale nanoparticulelor hibride, a fost evaluată eficiența metodei de marcare radioactivă, demonstrând o eficiență ridicată constantă, precum și o flexibilitate suplimentară în reglarea volumului de activitate cu care nanoparticulele sunt marcate radioactiv. În continuare, biocompatibilitatea nanoparticulelor proiectate în forma lor neradioactivă a fost investigată prin monitorizarea efectelor toxicității *in vitro* asupra

modelelor tumorale 3D de sferoizi ale liniei celulare canceroase de sân MDA-MB-231. În plus, a fost determinată internalizarea nanoparticulelor de către sferoizii tumorali. S-a demonstrat o internalizare foarte scăzută a nanoparticulelor de către modelele tumorale și nanoparticulele nu au prezentat nicio toxicitate semnificativă în concentrații de până la 1mg/ml. Următorul pas a constat în evaluarea *in vitro* a efectelor terapeutice combinate ale hipertermiei/ablației termice împreună cu radiația de la radioizotopul ^{103}Pd asupra sferoizilor tumorali. Combinațiile de doza scăzută de radiație și ablația termică și doza mare de radiație împreuna cu hipertermie sau ablație termică s-au dovedit de succes în distrugerea sferoizilor tumorali, la care se adaugă faptul că rata de încălzire și timpul de expunere la căldură în timpul tratamentului sunt factori importanți care trebuie luați în considerare.

În concluzie, această teză pune bazele pentru conceperea terapiei alternative împotriva cancerului prin utilizarea nanoparticulelor ^{103}Pd:Pd/oxid de fier, care, împreuna cu următoare etape de dezvoltare a formulelor injectabile și evaluări in vivo, vor debloca întregul potențial al acestor nano-materiale.

Introduction

1

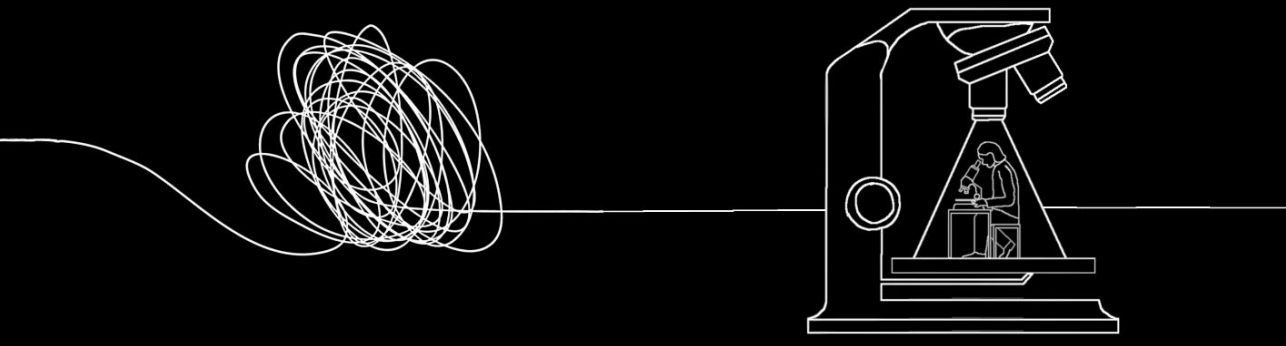

1.1 Cancer and limitations of currently available therapies

Cancer is one of the leading causes of death worldwide, being responsible for nearly 10 million deaths in 2020 only, i.e. one in six deaths being due to one of the existent types of cancer (Figure 1.1).[1] Globally, the total number of cancer cases are expected to increase from 19.3 million in 2020 to 30.2 million by 2040.[2]

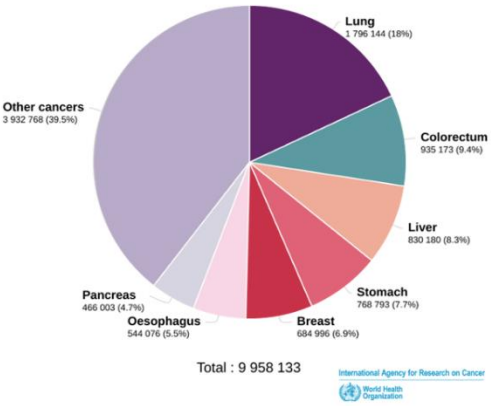

Figure 1.1 Estimated number of deaths due to cancer in 2020, worldwide, both sexes, all ages. Adapted from [2].

Curing cancer is one of the biggest challenges the medical research of our time has to face. Being such an aggressive disease, it is extremely difficult not only to diagnose, but also to treat, as the common cancer treatments are limited and cause multiple side effects.[3]

Nowadays, removal of tumour through surgery, chemotherapy and radiotherapy are still the most common types of cancer treatments available in clinical practice. But these treatments suffer from several drawbacks. Surgery is a viable option, but works only for compact tumours with well-known locations, plus it adds a high risk of infection, and in the case of breast cancer, leads to undesired and psychologically demanding cosmetic damages. Chemotherapy, although quite effective in destroying the cancerous cells, impairs the immune system and puts the patient at increased risk of infection. Moreover, it is not specifically directed to tumour cells and may also affect healthy tissues. In case of radiotherapy, it is difficult to homogeneously deliver the dose to the entire tumour, and therefore, this treatment is usually unable to eliminate the tumour completely. Furthermore, the neighbouring organs and healthy tissues are at high risk of losing their functionality due to increased exposure to radiation. Even though these treatments do overall improve the survival of the patients, the main pitfall stays in the non-specificity to tumour cells, which leads to affecting healthy tissues. Therefore, there is a high need in finding alternative therapies, which can specifically treat the cancerous cells while reducing the damage to the healthy cells, be minimally invasive, and limit short and long-term side

effects.[4-6] Such alternative treatments are even more attractive nowadays, as population screening programs are becoming more common and the number of patients diagnosed with cancer in an early stage is significant.[7,8]

1.2 In search of alternative cancer therapies

Brachytherapy

Brachytherapy, an internal form of radiation therapy, is the short distance treatment of cancer with radiation provided by small, encapsulated radionuclide sources (Figure 1.2). This type of treatment is conducted by placing the radiation source directly into or near the area of interest. Brachytherapy can be performed at a high-dose rate (HDR, > 12 GY/h) with the dose being delivered continuously over a short period of time through temporary implants, or at a low-dose rate (LDR, 0.4 – 2 Gy/h) where the implant gives off lower doses of radiation over a longer period of time, usually until complete decay of the radioactive source. The latter is employed mostly through permanent implants.[9,10]

In comparison with the external beam radiation therapy (EBRT), brachytherapy enables an improved localized dose delivery to the target area, avoiding therefore possible radiation to the healthy tissue. The main drawback of brachytherapy is that it can be used only in cases where the tumour is relatively small, accessible and well localized.[9,11,12] However, as already mentioned, the number of patients diagnosed with cancer in incipient stages is significant and continuously increasing, making brachytherapy an attractive alternative for cancer therapy.

Another limiting factor for brachytherapy is the radioresistance exhibited by tumours. The tumour environment is characterized by hypoxia and an increased acidic pH because of anaerobic metabolism and accumulation of lactic acid and other waste products. These factors are detrimental to cell killing by ionizing radiation, as a consequence of the complex interaction of various factors such as the levels of oxygen consumption, the ability of cells to repair the radiation-induced DNA damage, the number of dividing cells etc.[11-13] Considering this major biological disadvantage of brachytherapy, there is a high requirement in increasing the sensitivity of the tumour cells to the lethal effects of irradiation in order to enable a complete tumour eradication and improved rate of recovery.

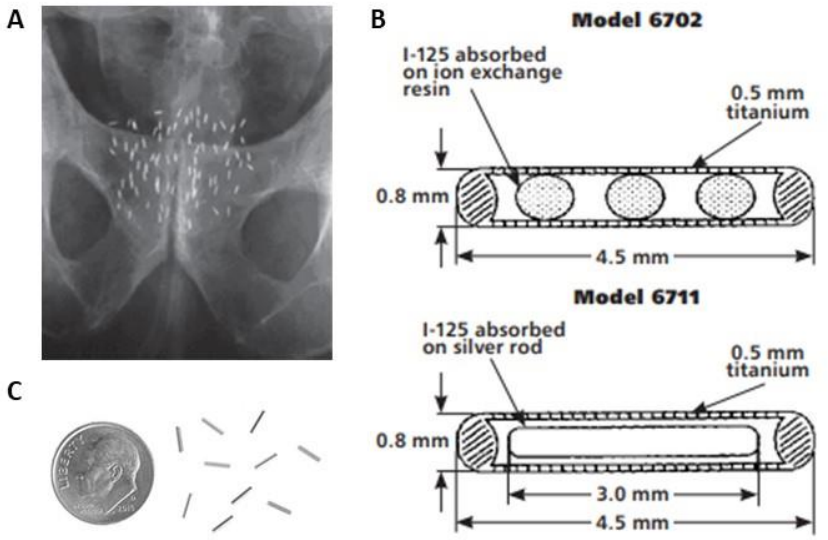

Figure 1.2 Iodine-125 (I-125) containing brachytherapy seed: **(A)** X-ray image of I-125 implants, **(B)** examples of I-125 implants, their composition and dimensions, reproduced with permission from [14], 2023 Copyright Elsevier, and **(C)** impression of the seed size.

There are over a dozen radionuclides proposed to be used as sealed sources in brachytherapy, however, only six are commonly used today in the clinic. One of them is palladium-103 (^{103}Pd), a radioisotope that decays by electron capture, which results in X-rays of 21 keV, with a half-lifetime ($T_{1/2}$) of 16.9 days. ^{103}Pd is a great candidate for brachytherapy since its low energy photons are attenuated by a few micrometres of biological tissue, thus, constraining the radiation inside the tumour. Moreover, the half-life of this radionuclide is suitable for permanent implants, without the need for invasive post-treatment removal interventions. The intensive use of ^{103}Pd in prostate cancer treatment in the form of micro-seeds has already shown promising results.[9,15-17] However, brachytherapy is still an invasive procedure. The millimetric seeds are relatively large compared to the tumour dimensions, and their insertion causes a great deal of discomfort. Therefore, there is a need to develop smaller radioactive sources with adjustable activities and injection speed, that enable less discomfort to the patients. In this context, radioactive nanoparticles (NPs) containing the ^{103}Pd radioisotope that are able to penetrate the biological tissues in a less invasive way, and that can diffuse more uniformly in the tumour represent a promising alternative to current brachytherapy implants.[15,18]

Hyperthermia/Thermal ablation

When it comes to medical treatments based on heating, there are two different regimes that can be distinguished: thermal ablation and hyperthermia. Each of them is conducted at different temperatures, and varying the time exposure produces different results and effects on the body. [19-21]

Thermal ablation refers to the application of elevated temperatures above 48-50 °C, translated into hyperthermic cytotoxicity. This mechanism results in direct killing of cancerous cells, a permanent and irreversible damage as a result of the destruction of molecular constituents of the living cells (mainly protein denaturation) and deprived micro-environment of the tumour. Cell death occurs just after a few minutes of heat exposure at such elevated temperatures. Thermal ablation is aimed as a replacement for surgery as it has an increased preservation of surrounding healthy tissues, lower morbidity, reduced cost, and shorter hospitalization times.[6,7,13,22]

Hyperthermia is the procedure of increasing the temperature of a part or the body up to 44-46 °C for a defined period of time. Nowadays, hyperthermia is an approved cancer treatment, and it can be applied either alone, or as an adjunct to various established cancer therapies, such as radio- or chemotherapy. However, even though hyperthermia can be used by itself inducing shrinkage and sometimes complete eradication of tumours, these results may not last, and the tumours can regrow.[7,13,20,22] The cells existent in the hypoxic core of tumours tend to be more acidotic, and even though this feature makes them less sensitive to radiation, it enhances their sensitivity to thermal damage.[23] Therefore, in this lower temperature range, an increased thermal sensitivity of tumour cells in comparison to healthy cells is expected, due to their different metabolism and physiological cell parameters, such as above-mentioned acidity and hypoxia. Additionally, combining cell damaging agents such as radioactive or chemotherapeutic drugs with hyperthermia is highly complementary, as hyperthermia enhances the cell killing efficiency of the administered therapeutic. Therefore, when hyperthermia and radiation treatments are applied simultaneously, there is a hyperthermic radiosensitization, which means that the tumour is more susceptible to irradiation, and this in turn leads to better therapeutic outcome.[5,13,20,22]

Collectively, the previously described factors set the biological basis for combining hyperthermia and radiation and enabling the synergy between these two cancer treatments. Just as in all other cancer therapies, in thermal therapy the main requirement for being successful remains in localizing the heat inside the cancerous tumour without causing thermal damage to the surrounding healthy tissues. From the three types of conventional hyperthermia employed nowadays in clinical practice (whole body, regional and local hyperthermia), local hyperthermia is the most tumour specific. Still, the currently available modalities of hyperthermia are often limited by their inability to selectively target the tumour tissue, carrying a risk of collateral organ damage. Another disadvantage is the incapability to homogeneously heat the targeted area, often resulting in undertreatment of tumour. Additionally, placement of external heating sources or metal antennas within and around tumours is generally invasive and extremely challenging for deep-seated tumours.[23] Therefore, while hyperthermia is a treatment modality with a lot of potential for cancer therapy, it does suffer from many inadequacies.

Luckily, the advances in engineering and fabrication of nanomaterials allow an unprecedented level of precision when it comes to the design of magnetic NPs with finely tuned properties that can interact with biological systems by generating heat.[23] Magnetic fluid hyperthermia (MFH) is a special form of interstitial thermotherapy, based on injecting colloidal suspensions of magnetic NPs and heating them through exposure to an externally applied magnetic field. Currently, iron oxide nanoparticles are the most frequently used in MFH due to their biocompatibility and good magnetic properties, that ensure effective heat generation.[3,6,13]

Magnetic resonance imaging

As previously mentioned, high tumour specificity is a primordial requirement for cancer treatments to be successful. Therefore, high resolution imaging is essential when such treatments are employed.

Magnetic resonance imaging (MRI) is a non-invasive diagnostic technique, based on the principle of nuclear magnetic resonance (NMR) spectroscopy, where images are generated by spatially encoding the NMR signal coming from protons present in the object to be imaged by applying time-varying, linear magnetic field gradients. The

main advantages of MRI are the very high spatial resolution and the ability to visualize and distinguish soft tissues.[24] The resolution of this imaging technique is comparable to X-Ray Computed Tomography (CT) and higher than Positron and Single Photon Emission Tomography (PET and SPECT, respectively). Additionally, as no ionizing radiation is involved, the whole imaging process can be conducted repeatedly, without harming the patients. However, sometimes insufficient contrast is observed, therefore, contrast agents with high relaxivities (relaxation rate enhancement per mmol of paramagnetic substance) are employed in MRI scans.[24,25] MRI contrast agents function by reducing either the longitudinal (T_1) or the transversal (T_2) relaxation times of protons in the target tissue. Two types of MR imaging representations can be generated: T_1-weighted images that give positive (bright) image contrast and T_2-weighted images that result in negative (dark) contrast. Metal-ion complexes containing paramagnetic metal ions like gadolinium (Gd^{3+}), such as Gd(III)-DOTA or Gd(III)-DTPA are usually applied for T_1-weighted imaging,[24,26,27] while superparamagnetic iron oxide nanoparticles (SPIONs) are the typical contrast agents in the case of T_2-weighted imaging, such as clinically approved Endorem™, also called Feridex™.[24] As the magnetic moment associated with SPIONs is much higher than that associated with paramagnetic ions,[28] magnetic iron oxide nanoparticles have become extremely promising candidates for MR imaging.

Magnetic nanoparticles in biomedicine

Magnetic nanoparticles (MNPs) refer to nanomaterials that show some response once they are exposed to a magnetic field.[28] There has been a tremendous interest in MNPs over the last half century, which is reflected by the vast body of published research about novel synthesis methods of unique shapes and composite structures, characterization techniques, and their possible applications in a plethora of fields such as catalysis[29,30], biomedicine[31-34], magnetic nanofluids[35], magnetic energy storage[36] etc.

MNPs exhibit unique magnetic properties than the ones found in their corresponding bulk materials due to their finite size effects, such as high surface-to-volume ratio and various crystal structures.[28,37] The behaviour and inherent magnetism of MNPs under the influence of external magnetic fields make such nanostructures particularly

attractive for biomedical applications.[38] Therefore, through the extensive research efforts that have been put in developing novel nanotechnologies aimed at biomedical advancements, MNPs have been intensively studied for hyperthermia, target drug delivery systems, imaging and extraction of biomolecules, becoming an extremely important tool and providing new perspectives for challenging problems, such as cancer treatment.[33,39]

Generally, MNPs are classified as diamagnetic, paramagnetic, ferromagnetic, ferrimagnetic and antiferromagnetic, based on the response of the net magnetization and the intrinsic MNP magnetic dipole in the presence and absence of magnetic field. However, most research focuses on MNPs that generate an optimal response once exposed to an external magnetic field, therefore, MNPs typically classified as ferromagnetic and ferrimagnetic are of high interest.[37]

One class of ferromagnetic NPs consists primarily of metallic elemental cores of three main metals: iron, nickel and cobalt. They exhibit high magnetization, but are prone to oxidation and are therefore toxic to biological systems, which limits their direct usefulness in biomedicine. Alloy type MNPs composed of mixtures such as FePt, FeNi, FeCo, CoPt are another class of ferromagnets. They have also found limited use in biomedical applications because of their toxicity and rather poor superparamagnetism. Lastly, a third class of MNPs is represented by oxides of ferrimagnetic elements, such as magnetite (Fe_3O_4) and maghemite (γ-Fe_2O_3).[38] Iron oxide nanoparticles have become the basic component for the most promising magneto-responsive systems in biomedical applications, due to their biocompatibility, tuneable magnetic properties and low cost of production.[40,41] In addition, iron oxide nanoparticles, with small sizes of less than 20-25 nm, are superparamagnetic. This means that each individual nanoparticle behaves as a giant paramagnetic atom with fast response to applied magnetic fields, having a large magnetic moment, but negligible remanence and coercivity at the same time.[42] Some biomedical applications that employ iron oxide NPs are summarized in Figure 1.3.

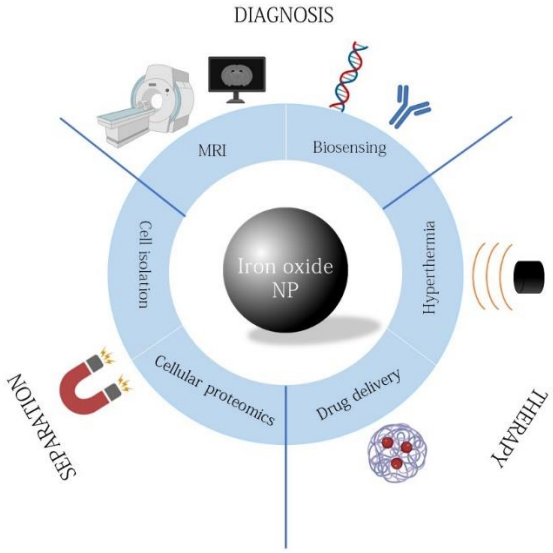

Figure 1.3 Different biomedical applications of iron oxide NPs.

A few sets of iron oxide NPs have already been clinically tested and approved for commercialization as contrast enhancing agents for MRI (Feridex, Ferumoxtran, Resovit) or magnetic hyperthermia therapy (NanoTherm). This laid the foundation for the introduction of inorganic materials into biomedical applications, rather than the well-accepted soft organic compounds such as nano-emulsions and liposomes.[41] Today, the paradigm of research in biomedicine is focusing more on multifunctional NPs, which are superior in comparison to their single-component analogues, since they have the potential to embody the unique properties of two or more modalities in a single entity. Insertion of different metals directly into one MNP endows such hybrid nanomaterial with interesting features. For example, the combination of iron oxide and noble metals in new hybrid NPs enables nanosystems that conduct more than one treatment at the same time, such as magnetic hyperthermia and photothermia.[19]

The properties of nanomaterials are strongly dependent on their size, shape, and other structural characteristics, such as crystallinity, oxidation state, and surface chemistry. Thus, the overall architecture of nanohybrids is one of the crucial factors dictating their physical properties and functional performance. Additionally, the magnetic behaviour exhibited by MNPs is complex and governed by many factors,

which can either improve or disturb the desired magnetic properties. However, reproducible synthesis of such hybrid MNPs, while preserving the desired properties and characteristics is a difficult task. Most of the times it involves complex multistep synthesis, as it is necessary that the conditions for obtaining one material do not interfere with the properties of the second one.[19,28,42] Therefore, a high control over the synthesis during production of such hybrid MNPs is required.

Hybrid NPs can generally be synthesized by physical and chemical methods. The physical methods are simpler in terms of preparation, but the control over the size and shape of the nanohybrids is difficult to achieve. On the other hand, chemical synthesis methods involve more complex procedures, which however offer a higher control over morphology.[19,43] In terms of chemical methods, there are several common ways to fabricate hybrid MNPs.[19,43-45] An overview of the most important routes and the main characteristics of each method are presented in Table 1.1.

Table 1.1 Chemical synthetic routes employed to fabricate hybrid nanoparticles and their characteristics.

Synthesis method	**Main characteristics**	
	Pro's	**Con's**
Co-precipitation	Simple, efficient, fast reaction times	Poor morphological control, broad size-distribution, and possible aggregation
Thermal decomposition	Great morphological control, narrow size-distributions	Multiple synthetic steps, long reaction times and high temperatures. The product is dispersible in organic solvents - exchange steps are required
Hydrothermal	Good morphological control; narrow size distributions	High reaction temperatures and pressure, very long reaction times, high equipment costs
Sonochemical	Fast, safe, less complex, ecological	Low efficiency and yield
Sol-gel	Very good morphological control; low reaction temperatures	Slow hybridization between hybrid nanoparticles, long processing time

As already said, in order to produce hybrid NPs for biomedical applications, it is important to accurately control the size, shape and preserve the desired properties. Biocompatibility, hydrophilicity, and colloidal stability of the NPs can be achieved by coating them either with organic species, such as surfactants or polymers, or with inorganic layers, such as silica or carbon. Therefore, apart from the control over the synthesis method chosen for producing NPs, a very high control over the surface chemistry is also required,[28,38,46] as the (bio)chemical coating plays an additional role in morphology and biodistribution. NPs intended for *in vivo* and *in vitro* biomedical applications must satisfy certain crucial requirements such as stability, nontoxicity and hydrophilicity to be compatible with the living systems. However, little of the synthetic methods ensure these characteristics of NPs directly post-synthesis. For example, NPs synthesized via thermal decomposition, that employs high boiling point organic solvents, are capped with hydrophobic organic molecules, therefore, they need to undergo extra surfactant modification steps to ensure their hydrophilicity. In biomedical applications, the suspension of NPs can be delivered to the site of interest either intravenously or via local injection. In both cases, NPs must not agglomerate and not hinder their own distribution. This may require additional surface modifications that on its turn may strongly influence the performance of the NPs, and therefore, careful design is necessary.

1.3 Nanoscale magnetism

As already explained, MNPs are attractive for biomedicine when they present an instant response to an applied external magnetic field and favourable biocompatibility. Ferrimagnetic materials (magnetite Fe_3O_4 and maghemite γ-Fe_2O_3) are specifically interesting in this respect, as they are composed of Fe-atoms existent at different lattice sites with antiparallel magnetic moments. These magnetic moments being of different magnitudes do not cancel each other out, but generate a net spontaneous magnetic moment.[28,37] As a result, such MNPs exhibit unique magnetic properties compared to those found in their corresponding bulk materials, which typically reach stability by adopting magnetic configurations of multi-domains, separated by domain walls. However, in case of small NPs, the balance of

magnetic interaction changes and single domain becomes the most stable magnetic configuration. The transition point from multi- to single-domain and superparamagnetic regime depends on the size, geometry and composition of the MNPs, as exemplified in Figure 1.4.[37,47]

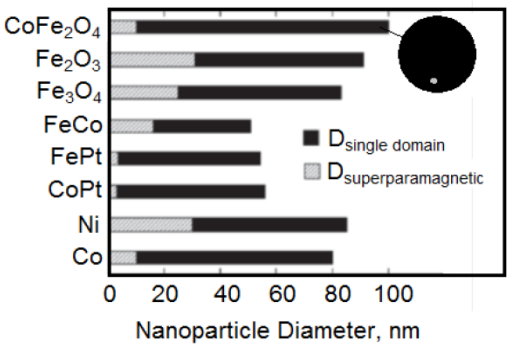

Figure 1.4. Maximum diameters for superparamagnetic and single-domain MNPs of different compositions. Reproduced with permission from [47].

Magnetite and maghemite NPs undergo a transition from multi- to single-domain magnetic structure within sizes of 80-90 nm. In this particular situation, each MNP can be considered as a small magnet, possessing its net magnetic moment. By further size reduction below a critical value of 25-30 nm, and above a temperature known as the blocking temperature (T_B), another phenomenon arises, called the superparamagnetic regime.[41] In this regime, thermal fluctuations tend to dominate the magnetic response of the MNPs, with a zero average magnetic moment in the absence of an external field and a rapidly increasing magnetic moment under the application of an external field.[37,41] This means that MNPs in the superparamagnetic regime exhibit no magnetic properties once the external field is removed, thus, have no attraction for each other, which is one of the reasons that makes them suitable for biomedical applications. Moreover, superparamagnetic NPs enable a better control over the application of their magnetic properties as they provide a strong response to an external magnetic field.[28,37] Overall, most of the MNPs used in biomedical applications are either single-domain or superparamagnetic.[48]

However, nanomagnetism is a complicated matter, and it is important to understand the fundamental magnetic properties, their correlation and dependence on the MNPs characteristics, in order to be able to control and optimize them for particular applications. The performance of MNPs in applications such as thermal ablation/hyperthermia, proton relaxation and contrast-enhancing efficiency in MRI is strongly influenced by the magnetic properties of these NPs, which are dependent on

the various characteristic parameters such as size, shape and composition.[37,49] Analysing the magnetic behaviour of ferro/ferrimagnetic and superparamagnetic NPs under the influence of an applied field, we can study the relevant magnetic data that is important in tuning such NPs for certain applications.

An alternating magnetic field (AMF) can magnetize and demagnetize MNPs in opposite directions in a so-called hysteresis loop. Once an external magnetic field is applied, the material magnetization parallel to the applied field is measured. Figure 1.5 shows a typical magnetization curve for ferro or ferrimagnetic materials (on the left) with the characteristic positions on the curve associated with *saturation magnetization* (M_s) – the maximum magnetization possible, which arises when all the magnetic dipoles are aligned in an external field, *remanent magnetization* (M_r) – the magnetization left after an external field is removed, and *coercivity* (H_c) – the intensity of an external coercive field needed to force the magnetization to zero. In the same figure (on the right), in contrast to the hysteresis loop for ferro or ferrimagnetic materials, is the sigmoid curve to an external field for superparamagnetic nanoparticles, which exhibits no hysteresis.[37,50]

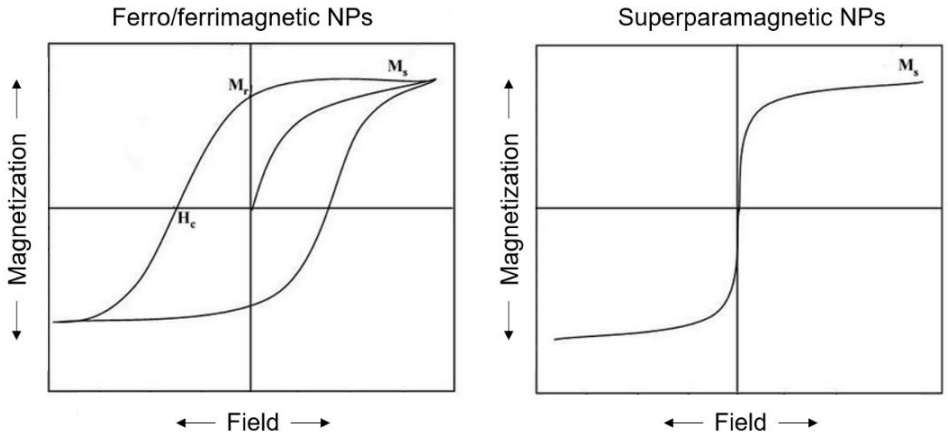

Figure 1.5 Magnetization curves for ferro/ferrimagnetic and superparamagnetic materials.

As we have seen, the size of the MNPs is an extremely important parameter, and based on it, MNPs can exhibit different magnetic properties. For example, in most studies in literature, the value of saturation magnetization increases with size, until it becomes constant and is close to the bulk magnetization value. Therefore,

depending on the desired application for the MNPs, choosing to tailor the size of the MNPs in order to control such magnetic parameters, is important.

Size has also a strong influence on the coercivity exhibited by MNPs. Similar to saturation magnetization, coercivity increases with size until it reaches a maximum. However, after reaching a maximum, the coercivity starts decreasing with further size increase. This phenomenon occurs in MNPs with sizes ranging from superparamagnetic to pseudo single- and multi-domain structures, where the moment of each domain may not be oriented in the same direction. In this particular situation, for the sizes closer to multi-domains, the application of a magnetic field causes the cancellation of the non-parallel moments, resulting in a reduced coercivity required to force magnetization back to zero.[37]

This size-dependence of magnetic properties is, of course, also influencing the thermal performance of the MNPs, since the application of AMF will translate into heating arising from either hysteresis losses or Néel/Brownian relaxation processes, all based on the size of the MNPs. With decreasing the size of the MNPs and passing to single-domain and superparamagnetic regime, hysteresis losses are negligible or non-existent, thus, heating arises from Néel or Brownian relaxation. Néel relaxation refers to the internal friction caused when a particle's magnetic dipole flips between two stable orientations. The relaxation to its natural axis causes energy to be released as heat, occurring without the physical rotation of the MNP itself. Oppositely, Brownian relaxation occurs when the MNP itself changes its orientation, aligning with its changing internal magnetic moment. This triggers physical rotation of the nanoparticle within an AMF, and through its rotation, energy is lost in the form of heat with friction from its surroundings. These internal and external sources of "friction" cause a phase lag between the AMF and the orientation of the magnetic moments, thus generating thermal losses.[21,23,37,51] Both relaxation processes occur simultaneously, but one can dominate the heating effects, however, it is difficult to distinguish the extent of the contribution of each mechanism. In general, Brownian relaxations dominate when the MNPs have sizes larger than 20 nm and Néel relaxations when the MNPs have sizes less than 20 nm.[37]

The efficiency of heating achieved with MNPs is described by the specific absorption rate (SAR) or specific loss power (SLP), which is equal to the rate at which energy is

absorbed per unit of mass of the NPs at a specific frequency. For efficient MNPs heating, a high SAR provided by a minimal amount of MNPs is crucial, which then translates into efficient hyperthermia/thermal ablation with a minimal dose of MNPs required in the body.

Previous studies from literature prove that there is a threshold size of approximatively 9.8 nm, below which the measured SLP is insufficient for hyperthermia/thermal ablation applications, and beyond the optimal diameter of 16 nm, the SLP starts decreasing with particle size.[37,51] Therefore, not only that the size of the MNPs is a crucial parameter for good magnetic properties and performance in heating applications, but there is also a very small size range in which the best performance can be achieved. However, heating performance of MNPs via Néel and Brownian relaxation can also be tuned through changing the viscosity of the suspension medium, in case of Brownian relaxations, or through modulating other factors than size, such as composition and implicitly anisotropy of the MNPs, for enhanced Néel relaxation.[37]

Looking at MRI as an accompanying application of the heat-producing MNPs, it has been shown that that their contrast enhancement ability is directly related to the measured M_s value. As the saturation magnetization exhibited by MNPs is strongly dependent on their size, this means that the efficiency of MNPs as MRI contrast agents is also size dependent.[37]

Overall, even though size is a highly important design parameter that can be manipulated to tune the magnetic properties of saturation magnetization, coercivity, SAR for increased efficiency in MNP heating, and contrast enhancement in MRI, size manipulation alone is not always sufficient and sometimes may fail to produce the desired results.

The shape of the MNPs is another parameter that affects magnetic properties through its influence on the saturation magnetization and magnetic anisotropy. For example, studies of Zhen et al.[52] and Gonzalez-Fernandez et al.[53] observed that cubic MNPs exhibit a higher saturation magnetization when compared to spherical MNPs of the same volume. However, this is not a universal observation, and cubic MNPs do not always present M_s values higher than those of spherical ones.[37] Simply put, it is challenging to draw a correlation between shape and M_s of dissimilar volumes.

Shape also plays a role in the outcome of coercivity. The study of Song et al.[54] found lower coercivity for cubical MNPs compared to spherical ones.

As noted earlier, size influences both the heating and imaging performance of the MNPs. Similar observation concerning NPs shape was done by Zhen et al.[52] who describe cubic magnetite MNPs having four times smaller relaxation times, thus, better image contrast, than spherical magnetite MNPs. In case of heating efficiency, studies in literature also prove that usually certain shapes are better at generating heat than others. For example, it has been shown that cubical nanoparticles exhibit higher heating efficiency than spherical ones.[53,55] Additionally, the heating efficiency of flower-like MNPs has also been investigated, and the nanoflowers exhibited considerably greater heating efficiency than nanocubes of the same size.[56] Overall, no broad conclusion in favour of a particular shape can be drawn based on the current state of the literature, but it is clear that the impact of MNPs shape on magnetic properties is a powerful tool for manipulating these properties and enhancing their performance in particular applications.

Finally, the composition of MNPs has a strong impact on the magnetic properties, as it directly affects both the M_s and coercivity. The magnetic properties arise in the presence or absence of unpaired valence electrons of the metal atoms or metal ions constituting the MNPs. Moreover, the nature and the location of cations within the octahedral and tetrahedral sites of the spinel or inverse spinel crystal structure is influencing the orientation of the magnetic moments, which defines the type of magnetic behaviour.[37] Iron oxide MNPs are most often composed of various ratios of magnetite and maghemite. Even though both have great magnetic properties, magnetite has higher values of saturation magnetization and anisotropy, thus, a better magnetic behaviour can usually be observed in this case. Therefore, the ratio between the two in the composition of the MNPs has an impact on their magnetism and efficiency in various applications.[37,57] Cation exchange in the case of ferrite NPs is especially attractive for tuning the composition through doping iron oxide NPs with metals like Mn, Co or Ni. This has shown promising increase in the magnetic response, and improved efficiency in heat generation and relaxivity.[23,37,57]

As already mentioned, the paradigm of research in biomedical applications switches more and more towards multifunctional nanoparticles. In this case, introducing one

or more components in the MNPs endows such hybrid magnetic nanosystems with interesting features, making them superior candidates for biomedicine. Hybrid MNPs come in various compositions and architectures. It is very common to couple the MNPs with either non-magnetic or magnetic materials. Independent of the type of material introduced, there is usually an effect on the magnetic properties, due to the surface spin effects. For example, Larumbe et al.[58] synthesized Fe_3O_4 NPs with a silica coating and evaluated the effect of the non-magnetic coating on the magnetic response, by comparison with their analogous uncoated Fe_3O_4 NPs. The presence of silica was found to reduce the saturation magnetization of the NPs, thus lowering the heating efficiency. In contrast to most of the studies that show decreased magnetic properties for MNPs coated with a non-magnetic layer, Woo et al.[59] showed a higher M_s for silica-coated Fe_3O_4 MNPs.

Most of the studies that present magnetic behaviour of NPs are based on homogeneous iron oxide nanocrystals. However, hybrid MNPs where a heterometal is directly inserted into the iron oxide core show a disruptor of the lattice, which affects their overall magnetic properties, even though some of the results may be counterintuitive. Additionally, the properties of hybrid MNPs depend on the effectiveness of the employed synthetic procedures to consistently make MNPs with crystal structures of unvarying composition. This aspect makes comparison of hybrid MNPs synthesized by different research groups using different synthetic procedures a challenging task.

In conclusion, there is a strong interplay between the synthetic procedure, the resulting MNPs, their characteristics and the magnetic properties. Therefore, as previously mentioned, it is essential to study and have full control over the synthetic procedure employed to prepare MNPs, to be able to tune the necessary parameters that provide magnetic properties required for the desired theranostic applications, independent of the presence of other components in hybrid MNPs.

1.4 Image-assisted thermo-brachytherapy as alternative minimally invasive cancer treatment

The potential of brachytherapy and thermal ablation/hyperthermia as cancer treatments is incontestable, and both have been employed as cancer therapies with promising results. On top of that, the combination of both methodologies is superior, as there is a strong synergy between the two, reaching a maximum when the treatments are conducted simultaneously. However, both therapies suffer from deficiencies and lack means for an adequate and minimally invasive delivery of radiation and heat with high tumour specificity. Additionally, non-invasive high-resolution imaging techniques such as MRI, would greatly complement the brachytherapy/thermal ablation treatment combination by enabling in situ monitoring of the processes involved.

Fortunately, continuous research focusing on multifunctional nanoparticles has been conducted, leading to nanoparticle systems that can present more than one simultaneous application. This kind of nanomaterials, commonly referred to as theranostic agents, are designed to serve both therapy and imaging applications. Such theranostic agents may hold the key to enabling alternative minimally invasive cancer therapies that have the ability to overcome many of the drawbacks presented by the already existing and intensively clinically used cancer treatments.

Within this framework, a theranostic system for image-assisted thermo-brachytherapy is proposed. The theranostic agent is envisioned as a biocompatible hybrid nanoparticle, graphically shown in Figure 1.6, composed of a ^{103}Pd-seed as the radioactive source, providing the necessary radiation dose for brachytherapy and an iron oxide coating, responsible for hyperthermia/thermal ablation and real-time visualization by MRI during the treatment. Addition of a polymeric surface coating is further expected to improve the stability and biological performance of the designed nanoparticles.

The proposed minimally invasive cancer treatment consists of implantation of the radioactive ^{103}Pd-iron oxide NPs, possibly incorporated in a gel-like matrix, via direct injection into the tumour, while the patient is under light sedation. The hybrid NPs are expected to diffuse inside the tumour, while their distribution is visualized in real-time by MRI. Once the ^{103}Pd-iron oxide NPs are dispersed in the tumour, the

cancer cells will be subjected to simultaneous hyperthermia/thermal ablation and brachytherapy by exposing the nanostructures to a high power – low frequency alternating magnetic field. The heat produced by the NPs will ablate most of the tumour cells, and simultaneously deliver a radiotherapeutic dose to the remaining cells. Additionally, the elevated temperature in the periphery of the cancer tissue is expected to induce a radiosensitizing effect making the entire treatment more efficient. With this approach, the tumour is expected to undergo shrinkage and complete eradication. A graphical representation of the proposed treatment is given in Figure 1.7.

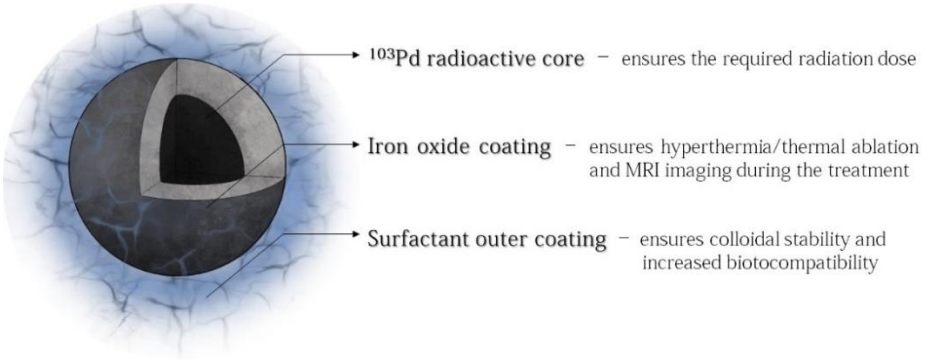

Figure 1.6 ^{103}Pd-iron oxide hybrid nanoparticle as theranostic agent for image-assisted thermo-brachytherapy.

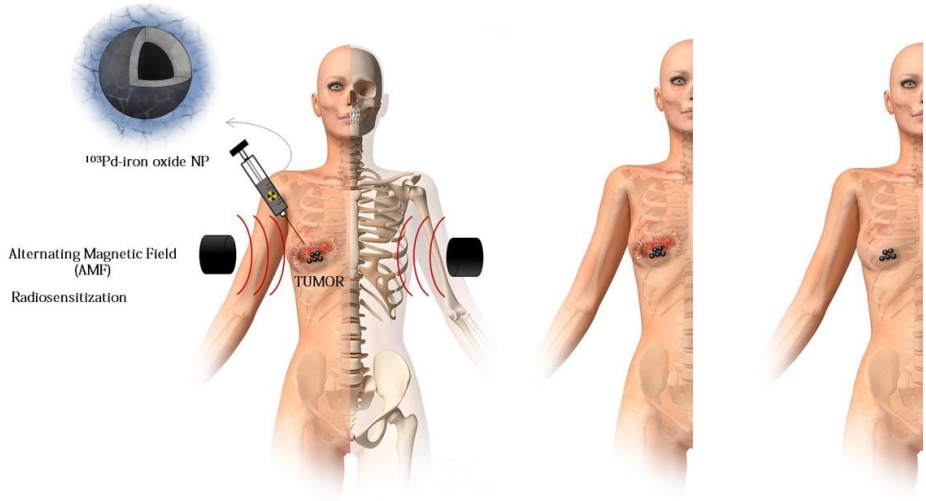

Figure 1.7. Representation of the proposed image-assisted thermo-brachytherapy treatment conducted with ^{103}Pd-iron oxide NPs as theranostic agents.

1.5 Scope and outline of the thesis

This thesis focuses on the development of a theranostic agent, in which both diagnostic and therapeutic modalities are integrated into one unified nanosystem, a hybrid ^{103}Pd-iron oxide nanoparticle for image-assisted thermo-brachytherapy. An alternative minimally invasive form of cancer therapy that overcomes many of the drawbacks presented by the already existent and most clinically employed cancer treatments, such as surgery, chemo- and radiotherapy.

After general introduction given in **Chapter 1,** this thesis continued with **Chapter 2** that described the design and preparation of non-radioactive Pd/Fe-oxide hybrid nanoparticles. An increased attention was paid to the seed-mediated growth thermal decomposition synthesis method, as it produced the desired core-shell hybrid NPs with great uniformity. By systematically investigating the effect of different reaction parameters on the synthesis method, important insights on the synthetic mechanism were unraveled, while variously sized and shaped batches of hybrid Pd/Fe-oxide NPs were produced. In **Chapter 3**, we investigated the magnetic properties of the multiple batches of Pd/Fe-oxide NPs synthesized in the previous chapter and highlighted their dependency on the characteristic parameters of the nanoparticles, focusing also on the influence of the non-magnetic palladium component present in the iron oxide crystal lattice. Additionally, as the NPs post synthesis are functionalized with hydrophobic surfactants, different surfactant modification techniques to render the Pd/Fe-oxide NPs water dispersible with high colloidal stability were assessed. Lastly, the ability of the Pd/Fe-oxide NPs batches with best magnetic properties to perform as hyperthermia/thermal ablation and magnetic resonance imaging agents was tested. Next, **Chapter 4** dealt with boosting the magnetic properties of Pd/Fe-oxide NPs via manganese doping of the iron oxide shell. A seed-mediated thermal decomposition method for synthesis of Pd/Fe-oxide NPs with different amounts of Mn doping was presented first. Subsequently, the effect of manganese doping on the magnetic properties, and their heating and MRI performance was assessed in comparison to Pd/Fe-oxide analogues.

Lastly, **Chapter 5** explored routes for radiolabelling of the previously introduced Pd/Fe-oxide NPs with ^{103}Pd radioisotope. Once a synthesis method able to generate ^{103}Pd radiolabelled hybrid NPs, namely ^{103}Pd:Pd/Fe-oxide NPs, was established, the

radiolabelling efficiency of the method was determined. As these MNPs are intended for biomedical applications, *in vitro* studies on 3D spheroid models of a breast cancer cell line MDA-MB-231 were conducted with Pd/Fe-oxide NPs in their non-radioactive form to assess their toxicity and uptake. Subsequently, the combined therapeutic effects of hyperthermia/thermal ablation together with ^{103}Pd radiation were evaluated on the spheroids via ^{103}Pd:Pd/Fe-oxide MNPs.

Bibliography

1. Organization, W.H. Cancer. Availabe online: https://www.who.int/news-room/fact-sheets/detail/cancer (accessed on 18.9.2023)
2. World Health Organization, I.A.f.R.o.C. Cancer Today. Availabe online: https://gco.iarc.fr/today/online-analysis-pie?v=2020&mode=cancer&mode_population=continents&population=900&populations=900&key=total&sex=0&cancer=39&type=1&statistic=5&prevalence=0&population_group=0&ages_group%5B%5D=0&ages_group%5B%5D=17&nb_items=7&group_cancer=1&include_nmsc=1&include_nmsc_other=1&half_pie=0&donut=0 (accessed on 12.07.2023).
3. Lima-Tenorio, M.K.; Pineda, E.A.; Ahmad, N.M.; Fessi, H.; Elaissari, A. Magnetic nanoparticles: In vivo cancer diagnosis and therapy. *Int J Pharm* **2015**, *493*, 313-327, doi:10.1016/j.ijpharm.2015.07.059.
4. Arruebo, M.; Vilaboa, N.; Saez-Gutierrez, B.; Lambea, J.; Tres, A.; Valladares, M.; Gonzalez-Fernandez, A. Assessment of the evolution of cancer treatment therapies. *Cancers (Basel)* **2011**, *3*, 3279-3330, doi:10.3390/cancers3033279.
5. Nguyen, K. Targeted Nanoparticles for Cancer Therapy: Promises and Challenges. *Journal of Nanomedicine & Nanotechnology* **2011**, *02*, doi:10.4172/2157-7439.1000103e.
6. Nijhawan, G.; Nijhawan, S.S.; Sethi, M. Chapter 12 - Hyperthermia Treatments. In *Noble Metal-Metal Oxide Hybrid Nanoparticles*, Mohapatra, S., Nguyen, T.A., Nguyen-Tri, P., Eds. Woodhead Publishing: 2019; https://doi.org/10.1016/B978-0-12-814134-2.00012-7pp. 241-263.
7. Chu, K.F.; Dupuy, D.E. Thermal ablation of tumours: biological mechanisms and advances in therapy. *Nat Rev Cancer* **2014**, *14*, 199-208, doi:10.1038/nrc3672.
8. van Oossanen, R.; Godart, J.; Brown, J.M.C.; Maier, A.; Pignol, J.P.; Denkova, A.G.; Djanashvili, K.; van Rhoon, G.C. Feasibility Study on the Radiation Dose by Radioactive Magnetic Core-Shell Nanoparticles for Open-Source Brachytherapy. *Cancers (Basel)* **2022**, *14*, doi:10.3390/cancers14225497.
9. Suntharalingam, N.; Podgorsak, E.; Tölli, H. Brachytherapy: Physical and clinical aspects. *Radiation Oncology Physics: A Handbook for Teachers and Students* **2005**.
10. Society, A.C. Radiation Therapy. Availabe online: https://www.cancer.org/treatment/treatments-and-side-effects/treatment-types/radiation.html (accessed on 18.09.2023)
11. Zhivotovsky, B.; Joseph, B.; Orrenius, S. Tumor radiosensitivity and apoptosis. *Exp Cell Res* **1999**, *248*, 10-17, doi:10.1006/excr.1999.4452.
12. Potter, R. Image-guided brachytherapy sets benchmarks in advanced radiotherapy. *Radiother Oncol* **2009**, *91*, 141-146, doi:10.1016/j.radonc.2009.04.011.
13. Habash, R.W.; Bansal, R.; Krewski, D.; Alhafid, H.T. Thermal therapy, part 2: hyperthermia techniques. *Crit Rev Biomed Eng* **2006**, *34*, 491-542, doi:10.1615/critrevbiomedeng.v34.i6.30.

14. Kanikowski, M.; Skowronek, J.; Kubaszewska, M.; ChicheŁ, A.; Milecki, P. Permanent implants in treatment of prostate cancer. *Reports of Practical Oncology & Radiotherapy* **2008**, *13*, 150-167, doi:https://doi.org/10.1016/S1507-1367(10)60006-5.
15. Laprise-Pelletier, M.; Lagueux, J.; Cote, M.F.; LaGrange, T.; Fortin, M.A. Low-Dose Prostate Cancer Brachytherapy with Radioactive Palladium-Gold Nanoparticles. *Adv Healthc Mater* **2017**, *6*, doi:ARTN 1601120 10.1002/adhm.201601120.
16. Yu, Y.; Anderson, L.L.; Li, Z.; Mellenberg, D.E.; Nath, R.; Schell, M.C.; Waterman, F.M.; Wu, A.; Blasko, J.C. Permanent prostate seed implant brachytherapy: report of the American Association of Physicists in Medicine Task Group No. 64. *Med Phys* **1999**, *26*, 2054-2076, doi:10.1118/1.598721.
17. Sharkey, J.; Cantor, A.; Solc, Z.; Huff, W.; Chovnick, S.D.; Behar, R.J.; Perez, R.; Otheguy, J.; Rabinowitz, R. 103Pd brachytherapy versus radical prostatectomy in patients with clinically localized prostate cancer: a 12-year experience from a single group practice. *Brachytherapy* **2005**, *4*, 34-44, doi:10.1016/j.brachy.2004.12.001.
18. Djoumessi, D.; Laprise-Pelletier, M.; Chevallier, P.; Lagueux, J.; Cote, M.F.; Fortin, M.A. Rapid, one-pot procedure to synthesise (103)Pd:Pd@Au nanoparticles en route for radiosensitisation and radiotherapeutic applications. *J Mater Chem B* **2015**, *3*, 2192-2205, doi:10.1039/c4tb01663g.
19. Sanchez, L.M.; Alvarez, V.A. Advances in Magnetic Noble Metal/Iron-Based Oxide Hybrid Nanoparticles as Biomedical Devices. *Bioengineering* **2019**, *6*, doi:10.3390/bioengineering6030075.
20. Dutz, S.; Hergt, R. Magnetic nanoparticle heating and heat transfer on a microscale: Basic principles, realities and physical limitations of hyperthermia for tumour therapy. *Int J Hyperthermia* **2013**, *29*, 790-800, doi:10.3109/02656736.2013.822993.
21. Mornet, S.; Vasseur, S.; Grasset, F.; Duguet, E. Magnetic nanoparticle design for medical diagnosis and therapy. *Journal of Materials Chemistry* **2004**, *14*, 2161-2175, doi:10.1039/B402025A.
22. Overgaard, J. The current and potential role of hyperthermia in radiotherapy. *Int J Radiat Oncol Biol Phys* **1989**, *16*, 535-549, doi:10.1016/0360-3016(89)90470-7.
23. Kaur, P.; Aliru, M.L.; Chadha, A.S.; Asea, A.; Krishnan, S. Hyperthermia using nanoparticles--Promises and pitfalls. *Int J Hyperthermia* **2016**, *32*, 76-88, doi:10.3109/02656736.2015.1120889.
24. Geraldes, C.F.; Laurent, S. Classification and basic properties of contrast agents for magnetic resonance imaging. *Contrast Media Mol Imaging* **2009**, *4*, 1-23, doi:10.1002/cmmi.265.
25. Caravan, P. Strategies for increasing the sensitivity of gadolinium based MRI contrast agents. *Chemical Society Reviews* **2006**, *35*, 512-523, doi:10.1039/B510982P.
26. Hermann, P.; Kotek, J.; Kubicek, V.; Lukes, I. Gadolinium(III) complexes as MRI contrast agents: ligand design and properties of the complexes. *Dalton Trans* **2008**, 10.1039/b719704g, 3027-3047, doi:10.1039/b719704g.
27. Huang, Y.; He, S.; Cao, W.; Cai, K.; Liang, X.J. Biomedical nanomaterials for imaging-guided cancer therapy. *Nanoscale* **2012**, *4*, 6135-6149, doi:10.1039/c2nr31715j.

28. Issa, B.; Obaidat, I.M.; Albiss, B.A.; Haik, Y. Magnetic nanoparticles: surface effects and properties related to biomedicine applications. *Int J Mol Sci* **2013**, *14*, 21266-21305, doi:10.3390/ijms141121266.
29. Lu, A.H.; Schmidt, W.; Matoussevitch, N.; Bonnemann, H.; Spliethoff, B.; Tesche, B.; Bill, E.; Kiefer, W.; Schuth, F. Nanoengineering of a magnetically separable hydrogenation catalyst. *Angew Chem Int Edit* **2004**, *43*, 4303-4306, doi:10.1002/anie.200454222.
30. Tsang, S.C.; Caps, V.; Paraskevas, I.; Chadwick, D.; Thompsett, D. Magnetically separable, carbon-supported nanocatalysts for the manufacture of fine chemicals. *Angew Chem Int Edit* **2004**, *43*, 5645-5649, doi:10.1002/anie.200460552.
31. Gupta, A.K.; Gupta, M. Synthesis and surface engineering of iron oxide nanoparticles for biomedical applications. *Biomaterials* **2005**, *26*, 3995-4021, doi:https://doi.org/10.1016/j.biomaterials.2004.10.012.
32. Vallejo-Fernandez, G.; Whear, O.; Roca, A.G.; Hussain, S.; Timmis, J.; Patel, V.; O'Grady, K. Mechanisms of hyperthermia in magnetic nanoparticles. *J Phys D Appl Phys* **2013**, *46*, Artn 312001, doi: 10.1088/0022-3727/46/31/312001.
33. Hepel, M. Magnetic Nanoparticles for Nanomedicine. *Magnetochemistry* **2020**, *6*, doi:10.3390/magnetochemistry6010003.
34. Thomas, R.; Park, I.-K.; Jeong, Y.Y. Magnetic Iron Oxide Nanoparticles for Multimodal Imaging and Therapy of Cancer. *International Journal of Molecular Sciences* **2013**, *14*, 15910-15930, doi:10.3390/ijms140815910.
35. Taylor, R.; Coulombe, S.; Otanicar, T.; Phelan, P.; Gunawan, A.; Lv, W.; Rosengarten, G.; Prasher, R.; Tyagi, H. Small particles, big impacts: A review of the diverse applications of nanofluids. *J Appl Phys* **2013**, *113*, Artn 011301, doi: 10.1063/1.4754271.
36. Frey, N.A.; Peng, S.; Cheng, K.; Sun, S. Magnetic nanoparticles: synthesis, functionalization, and applications in bioimaging and magnetic energy storage. *Chemical Society Reviews* **2009**, *38*, 2532-2542, doi:10.1039/B815548H.
37. Kolhatkar, A.G.; Jamison, A.C.; Litvinov, D.; Willson, R.C.; Lee, T.R. Tuning the magnetic properties of nanoparticles. *Int J Mol Sci* **2013**, *14*, 15977-16009, doi:10.3390/ijms140815977.
38. Baryeh, K.; Attia, M.; Ulloa, J.C.; Ye, J.Y. 15 - Magnetic nanoparticle-based hybrid materials in the biomedical field: fundamentals and applications. In *Magnetic Nanoparticle-Based Hybrid Materials*, Ehrmann, A., Nguyen, T.A., Ahmadi, M., Farmani, A., Nguyen-Tri, P., Eds. Woodhead Publishing: 2021; https://doi.org/10.1016/B978-0-12-823688-8.00005-3pp. 387-423.
39. Materón, E.M.; Miyazaki, C.M.; Carr, O.; Joshi, N.; Picciani, P.H.S.; Dalmaschio, C.J.; Davis, F.; Shimizu, F.M. Magnetic nanoparticles in biomedical applications: A review. *Applied Surface Science Advances* **2021**, *6*, 100163, doi:https://doi.org/10.1016/j.apsadv.2021.100163.
40. Socoliuc, V.; Peddis, D.; Petrenko, V.I.; Avdeev, M.V.; Susan-Resiga, D.; Szabó, T.; Turcu, R.; Tombácz, E.; Vékás, L. Magnetic Nanoparticle Systems for Nanomedicine—A Materials Science Perspective. *Magnetochemistry* **2020**, *6*, doi:10.3390/magnetochemistry6010002.

41. Piñeiro, Y.; González Gómez, M.; de Castro Alves, L.; Arnosa Prieto, A.; García Acevedo, P.; Seco Gudiña, R.; Puig, J.; Teijeiro, C.; Yáñez Vilar, S.; Rivas, J. Hybrid Nanostructured Magnetite Nanoparticles: From Bio-Detection and Theragnostics to Regenerative Medicine. *Magnetochemistry* **2020**, *6*, doi:10.3390/magnetochemistry6010004.
42. Ma, D. Chapter 1 - Hybrid Nanoparticles: An Introduction. In *Noble Metal-Metal Oxide Hybrid Nanoparticles*, Mohapatra, S., Nguyen, T.A., Nguyen-Tri, P., Eds. Woodhead Publishing: 2019; https://doi.org/10.1016/B978-0-12-814134-2.00001-2pp. 3-6.
43. Nguyen Tri, P.; Ouellet-Plamondon, C.; Rtimi, S.; Assadi, A.A.; Nguyen, T.A. Chapter 3 - Methods for Synthesis of Hybrid Nanoparticles. In *Noble Metal-Metal Oxide Hybrid Nanoparticles*, Mohapatra, S., Nguyen, T.A., Nguyen-Tri, P., Eds. Woodhead Publishing: 2019; https://doi.org/10.1016/B978-0-12-814134-2.00003-6pp. 51-63.
44. Cotin, G.; Perton, F.; Blanco-Andujar, C.; Pichon, B.; Mertz, D.; Bégin-Colin, S. Chapter 2 - Design of Anisotropic Iron-Oxide-Based Nanoparticles for Magnetic Hyperthermia. In *Nanomaterials for Magnetic and Optical Hyperthermia Applications*, Fratila, R.M., De La Fuente, J.M., Eds. Elsevier: 2019; https://doi.org/10.1016/B978-0-12-813928-8.00002-8pp. 41-60.
45. Low, S.S.; Yew, M.; Lim, C.N.; Chai, W.S.; Low, L.E.; Manickam, S.; Tey, B.T.; Show, P.L. Sonoproduction of nanobiomaterials – A critical review. *Ultrasonics Sonochemistry* **2022**, *82*, 105887, doi:https://doi.org/10.1016/j.ultsonch.2021.105887.
46. Sarkar, S.; Pal, T. Chapter 2 - Theoretical Aspects of Synthesis for Controlled Morphological Nanostructures. In *Noble Metal-Metal Oxide Hybrid Nanoparticles*, Mohapatra, S., Nguyen, T.A., Nguyen-Tri, P., Eds. Woodhead Publishing: 2019; https://doi.org/10.1016/B978-0-12-814134-2.00002-4pp. 7-50.
47. Krishnan, K.M. Biomedical Nanomagnetics: A Spin Through Possibilities in Imaging, Diagnostics, and Therapy. *IEEE Transactions on Magnetics* **2010**, *46*, 2523-2558, doi:10.1109/TMAG.2010.2046907.
48. Lavorato, G.C.; Das, R.; Alonso Masa, J.; Phan, M.-H.; Srikanth, H. Hybrid magnetic nanoparticles as efficient nanoheaters in biomedical applications. *Nanoscale Advances* **2021**, *3*, 867-888, doi:10.1039/D0NA00828A.
49. Smolensky, E.D.; Park, H.-Y.E.; Zhou, Y.; Rolla, G.A.; Marjańska, M.; Botta, M.; Pierre, V.C. Scaling laws at the nanosize: the effect of particle size and shape on the magnetism and relaxivity of iron oxide nanoparticle contrast agents. *Journal of Materials Chemistry B* **2013**, *1*, 2818-2828, doi:10.1039/C3TB00369H.
50. Majetich, S.A.; Wen, T.; Mefford, O.T. Magnetic nanoparticles. *MRS Bulletin* **2013**, *38*, 899-903, doi:10.1557/mrs.2013.230.
51. Gazeau, F.; Lévy M Fau - Wilhelm, C.; Wilhelm, C. Optimizing magnetic nanoparticle design for nanothermotherapy.
52. Zhen, G.; Muir, B.W.; Moffat, B.A.; Harbour, P.; Murray, K.S.; Moubaraki, B.; Suzuki, K.; Madsen, I.; Agron-Olshina, N.; Waddington, L., et al. Comparative Study of the Magnetic Behavior of Spherical and Cubic Superparamagnetic Iron Oxide Nanoparticles. *The Journal of Physical Chemistry C* **2011**, *115*, 327-334, doi:10.1021/jp104953z.

53. Gonzalez-Fernandez, M.A.; Torres, T.E.; Andrés-Vergés, M.; Costo, R.; de la Presa, P.; Serna, C.J.; Morales, M.P.; Marquina, C.; Ibarra, M.R.; Goya, G.F. Magnetic nanoparticles for power absorption: Optimizing size, shape and magnetic properties. *Journal of Solid State Chemistry* **2009**, *182*, 2779-2784, doi:https://doi.org/10.1016/j.jssc.2009.07.047.
54. Song, Q.; Zhang, Z.J. Shape Control and Associated Magnetic Properties of Spinel Cobalt Ferrite Nanocrystals. *J Am Chem Soc* **2004**, *126*, 6164-6168, doi:10.1021/ja049931r.
55. Noh, S.-h.; Na, W.; Jang, J.-t.; Lee, J.-H.; Lee, E.J.; Moon, S.H.; Lim, Y.; Shin, J.-S.; Cheon, J. Nanoscale Magnetism Control via Surface and Exchange Anisotropy for Optimized Ferrimagnetic Hysteresis. *Nano Letters* **2012**, *12*, 3716-3721, doi:10.1021/nl301499u.
56. Hugounenq, P.; Levy, M.; Alloyeau, D.; Lartigue, L.; Dubois, E.; Cabuil, V.; Ricolleau, C.; Roux, S.; Wilhelm, C.; Gazeau, F., et al. Iron Oxide Monocrystalline Nanoflowers for Highly Efficient Magnetic Hyperthermia. *The Journal of Physical Chemistry C* **2012**, *116*, 15702-15712, doi:10.1021/jp3025478.
57. Salas, G.; Veintemillas-Verdaguer, S.; Morales, M.d.P. Relationship between physico-chemical properties of magnetic fluids and their heating capacity. *International Journal of Hyperthermia* **2013**, *29*, 768-776, doi:10.3109/02656736.2013.826824.
58. Larumbe, S.; Gómez-Polo C Fau - Pérez-Landazábal, J.I.; Pérez-Landazábal Ji Fau - Pastor, J.M.; Pastor, J.M. Effect of a SiO2 coating on the magnetic properties of Fe3O4 nanoparticles.
59. Woo, K.; Hong, J.; Ahn, J.-P. Synthesis and surface modification of hydrophobic magnetite to processible magnetite@silica-propylamine. *Journal of Magnetism and Magnetic Materials* **2005**, *293*, 177-181, doi:https://doi.org/10.1016/j.jmmm.2005.01.058.

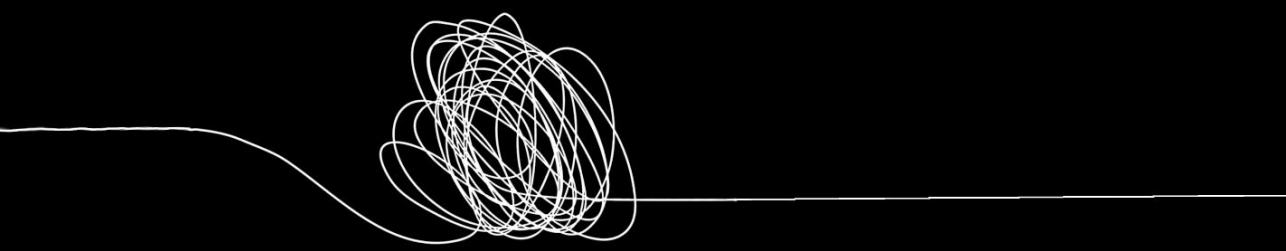

Exploring and understanding the synthesis conditions and mechanistic insights to control the morphology of Pd/Fe-oxide nanoparticles

2

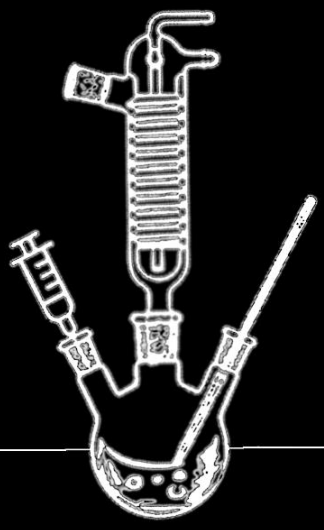

Abstract: Heterostructured magnetic nanoparticles show great potential for numerous applications in biomedicine due to their ability to express multiple functionalities in a single structure. Magnetic properties are generally determined by the morphological characteristics of nanoparticles, such as the size/shape, and composition of the nanocrystals. These in turn are highly dependent on the synthetic conditions applied. Additionally, incorporation of a non-magnetic heterometal influences the final magnetic behaviour. Therefore, construction of multifunctional hybrid nanoparticles with preserved magnetic properties represents a certain nanotechnological challenge. Here, we focus on palladium/iron oxide nanoparticles designed for combined brachytherapy, a type of internal radiotherapy, and MRI-guided hyperthermia/thermal ablation of tumours. The choice of palladium forming the nanoparticle core is envisioned for the eventual radiolabelling with palladium-103 radionuclide to enable the combination of hyperthermia/thermal ablation with brachytherapy, the latter being beyond the scope of this chapter. At this stage, we investigated the synthetic mechanisms and their effects on the final morphology of the hybrid nanoparticles. Thermal decomposition was applied for the synthesis of Pd/Fe-oxide nanoparticles via both, one-pot and seed-mediated processes. The latter method was found to provide better control over morphology of the nanoparticles and was therefore examined closely by varying reaction conditions. This resulted not only in understanding the most relevant synthetic parameters in thermal decomposition synthesis and their interplay, but also in producing multiple batches of Pd/Fe-oxide nanoparticles with different morphologies, which are interesting candidates to be further investigated as theranostic agents.

Keywords: hybrid nanoparticles; iron oxide; palladium; thermal decomposition; one-pot synthesis, seed-mediated growth.

The content of this chapter has been published in:

Maier A, van Oossanen R, van Rhoon GC, Pignol JP, Dugulan I, Denkova AG, Djanashvili K. From Structure to Function: Understanding Synthetic Conditions in Relation to Magnetic Properties of Hybrid Pd/Fe-Oxide Nanoparticles. Nanomaterials (Basel). 2022 Oct 18;12(20):3649.

doi: 10.3390/nano12203649. PMID: 36296839; PMCID: PMC9612236.

2.1. Introduction

Nanomaterials have long been of high scientific interest due to their unique properties arising from the versatile nanoscale structural characteristics, and thus, functional performance. In recent years, research in nanotechnology has increasingly focused on the development of complex heterostructured nanosystems that combine two or more functional species within a single entity. Such hybrid nanoparticles (NPs) have an immense potential for a wide range of applications thanks to the superior inherent properties and the accompanying multifunctionality.

Iron oxide nanoparticles (Fe-oxide NPs) are of particular interest as they exhibit tuneable magnetic properties suitable for various biomedical applications.[1] In their single-domain and superparamagnetic regime, Fe-oxide NPs are able to accelerate the transverse relaxation time (T_2) of bulk water protons in the presence of an external magnetic field and can, therefore, be used as contrast agents in magnetic resonance imaging (MRI).[2] At the same time, they can also generate heat when exposed to an alternating magnetic field (AMF) allowing hyperthermia or thermal ablation of the surrounding tissues.[3] Effectiveness of these performances is highly dependent on the chemical (Fe_2O_3/Fe_3O_4) and morphological (size/shape/composition) characteristics of the Fe-oxide NPs. Additional functionalities, such as drug delivery[4], optical imaging[5], and nuclear imaging[6], are typically realized through appropriate functionalization of the surface. On the other hand, insertion of a heterometal directly into the NPs endows the hybrid materials with interesting features, such as antimicrobial activity (silver/Fe-oxide) and imaging by computed tomography (gold/Fe-oxide)[7], or chelate-free radiolabelling (zirconium-89/Fe-oxide) for Positron Emission Tomography (PET).[8] Since these modifications involve interference with the Fe-oxide lattice, the preservation of magnetic properties becomes a challenge, and extreme caution is needed to precisely control the synthesis of such hybrid nanomaterials.[9]

Among the strategies to produce inorganic metal-based NPs, thermal decomposition (TD) is considered one of the most appropriate methods to generate highly crystalline, monodispersed NPs with good morphology control compared to other traditional wet-chemistry synthesis methods, such as co-precipitation[10], sol-gel[11] or

microemulsion.[12] The TD process consists of thermolysis, in which a metal complex undergoes chemical decomposition in organic solvent with a high-boiling point in the presence of surfactants that stabilize the generated NPs, preventing their aggregation due to van der Waals and dipolar interactions. The process between the start of precursor decomposition and the NPs formation is described by LaMer's theory (Figure 2.1).[13]

The mechanism of NPs formation, according to LaMer's, follows three different stages. In stage I the metal precursor decomposes until the monomer concentration saturates and increases to the nucleation threshold, nuclei starting to form. Stage II implies a "burst nucleation", which results in the formation of nuclei and the simultaneous rapid decrease of monomer concentration, until it drops below the nucleation threshold. Lastly, stage III occurs, where no more nuclei form, but the reaction is at the growth stage, where the free energy of the system drives the attachment of monomers to the preformed nuclei, until the monomers are depleted from solution, dropping again below saturation level. Lastly, for generating monodisperse NPs with narrow size distributions, the key point is to shorten the nucleation process and separate it from the growth phase, which in turn must be maintained at a uniform rate of growth around each nucleus previously formed.[13,14]

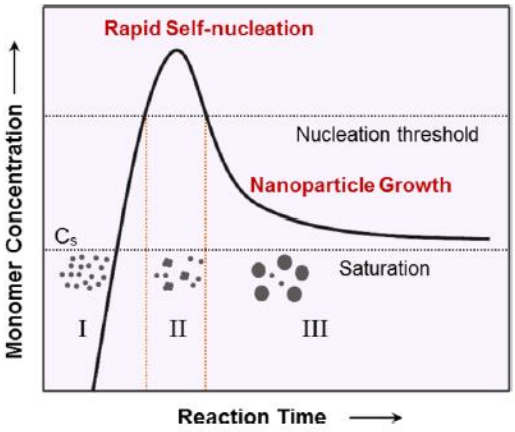

Figure 2.1. LaMer model for the nucleation and growth process. Reproduced with permission from [14], Copyright [2023] American Chemical Society.

A straightforward way to synthesize hybrid metal nanocrystals based on TD is the one-pot approach, where homogeneous nucleation and seed-assisted growth occur simultaneously.[15] On the other hand, the two-step seed-mediated method is considered a better alternative that allows for precise control of size and morphology, relying on the heterogeneous nucleation and growth of a second solid phase on the

surface of the preformed so-called "seeds" introduced into the reaction mixture.[16,17] This method facilitates the separation of nucleation and growth step, the aforementioned key factor in producing NPs with narrow size distributions.[13] The TD synthesis has a multitude of parameters, which enable great freedom in the design of NPs by tuning their size, shape, and composition.[13,18] However, these parameters are co-dependent and, despite the great effort put into the research of synthesizing hybrid nanoparticles via TD, the mechanism of formation and the role of the diverse synthetic parameters to achieve different morphologies are still not fully understood.[19] Thus, even though the concept of thermal decomposition may sound straightforward, its successful operation critically depends on having tight control and full understanding over all the reaction parameters and their interplay, as even a minor variation to the reaction conditions can result in unexpected products.[16] Synthesis of hybrid Fe-oxide NPs containing a non-magnetic heterometal via TD has been extensively described for gold/Fe-oxide,[17,19,20] but there are only a few reports on palladium/Fe-oxide systems,[20-24] with poor to no control over the morphology of the presented hybrid nanostructures. Moreover, these studies focus only on their application for catalysis, attributed to the palladium component, rather than on evaluating and understanding the synthetic mechanisms via the seed-mediated growth process, in order to be able to provide and tailor the necessary properties for other applications based on the inherent magnetic properties of these hybrid NPs, as a result of the iron oxide presence in the composition. Additionally, just because TD has been extensively described for gold/Fe-oxide, does not guarantee that all information gained through those studies can be readily translated to palladium/Fe-oxide NPs obtained in the same manner. Heterogeneous nucleation of iron oxide onto surfaces is not a trivial process and alloying can be different or not valid for all metal combinations, as the two metals involved must conform to certain rules, such as presenting similar crystal structures with closely matching parameters and similar electronegativity.[16,18]

For the aforementioned reasons, we conducted an in-depth study and explored the synthetic conditions for manufacturing Pd/Fe-oxide NPs via TD of iron pentacarbonyl and elucidated the effects of different reaction parameters on the morphological properties of the NPs. Within this frame of reference, both one-pot and

seed-mediated methods were investigated for the controlled production of Pd/Fe-oxide hybrid nanocrystals. Next, the seed-mediated method was studied closely by the systematic variation of the following parameters: the Fe-precursor/Pd-seed ratio, functionalization of the Pd-seeds, surfactant/Fe ratio, heating rate and solvent. As described in the previous chapter, we aim through this thesis at exploring the theranostic potential of Pd/Fe-oxide NPs. Therefore, it is necessary to develop a design which simultaneously enables diagnosis (MRI) and therapy to effectively treat tumours by means of combined hyperthermia/thermal ablation and radiotherapy, after injection of the NPs directly into the tumour mass as an alternative brachytherapy procedure. The latter component can be realized by creating a palladium core in the magnetic Fe-oxide NPs containing its radioisotope (^{103}Pd), which decays with a half-life of 17 days by electron capture, emitting low energy X-rays (21 KeV), ideal for depositing therapeutic radiation dose in tumours.[25-27] Methods to incorporate ^{103}Pd into Pd/Fe-oxide NPs have recently been investigated[28] and will be presented in an upcoming chapter.

As the aim is to employ the Pd/Fe-oxide hybrid NPs in biomedical applications, we need to satisfy a multitude of properties, such as biocompatibility and non-toxicity, which can be increased by encapsulating the palladium component into an iron oxide shell, thus, producing core-shell structures. Moreover, the sizes of these NPs have to be sufficiently small for uncompromised biodistribution and yet large enough to display the desired magnetic properties for MRI and AMF response. All these necessary properties of the NPs for biomedical applications can be controlled and tuned through the synthetic process. Thus, a high control over the synthetic route for Pd/Fe-oxide NPs and understanding the interplay of the parameters governing this process is key. With this study, we reveal the mechanisms and show how the synthetic conditions strongly influence the morphological properties, incl. the overall size and thickness of the iron oxide component in the Pd/Fe-oxide nanohybrids, resulting in both, exotically shaped and core-shell structures, all representing interesting candidates for further investigation as theranostic agents.

2.2 Materials and Methods

Reagents

Pd(II)-acetylacetonate ($Pd(acac)_2$), 1,2-hexadecanediol, 1-octadecene (ODE), oleic acid (OA), oleylamine (OAm), iron pentacarbonyl ($Fe(CO)_5$), ethanol, hexane, chloroform, Palladium (II) acetate, tert-butylamine-borane complex, n-dodecyl sulfide, toluene, diphenyl ether (DBE), dibenzyl ether (DBE). All chemicals were used as received without further purification. All synthetic methods were conducted in a standard airless procedure.

Preparation of Pd/Fe-oxide NPs via a one-pot synthesis method

Flower-like Pd/Fe-oxide NPs. The nanoparticles were synthesized via a one-pot synthesis method following a previously reported protocol.[29] Briefly, $Pd(acac)_2$ (152 mg, 0.5 mmol), 1,2-hexadecanediol (646 mg, 2.5 mmol) and 20 mL octadecene were added to a 3-neck round-bottom flask and purged with nitrogen for 30 min under vigorous stirring. Subsequently, the reaction mixture was heated to 85 °C in approx. 2 min, after which OA (190 μL, 0.5 mmol), OAm (175 μL, 0.5 mmol) and iron pentacarbonyl (263 μL, 2 mmol) were injected via a septum in this exact order. The reaction mixture was further heated to 300 °C under nitrogen blanket and maintained at this temperature for 30 min. After 30 min, the reaction system was left to cool down to room temperature and the Pd/Fe-oxide NPs were collected by addition of 30 mL ethanol and centrifugation at 10500 RPM (11830 ×g) for 4-6 minutes. The procedure was repeated several times with ethanol and one or two times with a combination of ethanol and hexane in equal volumes. Lastly, the Pd/Fe- oxide nanoparticles were dried by a gentle flow of nitrogen/compressed air and stored as such until further use. The final product was redispersible in organic solvents such as toluene, hexane, chloroform.

Popcorn-like Pd/Fe-oxide NPs. The nanoparticles were produced also via the one-pot synthesis method following a previously reported protocol[29] and described above, but with slight modifications. $Pd(acac)_2$ (152 mg, 0.5 mmol), 1,2-hexadecanediol (646 mg, 2.5 mmol) and 20 mL octadecene were added to a 3-neck round bottom flask and

purged with nitrogen for 30 min under vigorous stirring. Subsequently, the reaction mixture was heated to 85 °C in approx. 2 min. At 85 °C, OA (637 μL, 2 mmol), OAm (658 μL, 2 mmol) and iron pentacarbonyl (263 μL, 2 mmol) were injected via a septum in this order. The reaction mixture was further heated to 300 °C with a 5 °C/min heating rate under a nitrogen blanket and maintained at this temperature for 30 min. After 30 min, the reaction system was left to cool down to room temperature and the Pd/Fe-oxide NPs were collected by addition of 30 mL ethanol and centrifugation at 10500 RPM (11830 ×g) for 4-6 minutes. The procedure was repeated several times with ethanol and one or two times with a combination of ethanol and hexane in equal volumes. Lastly, the Pd/Fe-oxide NPs were dried by a gentle flow of nitrogen/compressed air and stored as such until further use. The final product was redispersible in organic solvents such as toluene, hexane, chloroform.

Preparation of Pd-seeds

Preparation of oleylamine capped Pd NPs (seeds). OAm capped Pd-seeds were prepared based on previously published protocols.[30,31] Briefly, palladium (II) acetate (56 mg, 0.249 mmol) was added to 15 mL OAm in a 3-neck round-bottom flask. The reaction mixture was heated to 60 °C in 10 min under a stream of nitrogen gas and vigorous stirring. In parallel, tert-butylamine-borane complex (130 mg, 1.495 mmol) was dissolved in 3 mL OAm and injected into the reaction mixture via a septum, once the temperature reached 60 °C. After addition, the reaction mixture was further heated to 90 °C with a heating rate of 3 °C/min and kept at this temperature for 60 min. After 60 min, the reaction system was left to cool down to room temperature and the Pd NPs were collected by addition of 30 mL ethanol and centrifugation for 8 min at 10500 RPM (11830 ×g). The Pd NPs were stored as such until further use. The final product was redispersible in organic solvents such as toluene, hexane, chloroform.

Preparation of n-dodecyl sulphide capped Pd NPs (seeds). *N*-dodecyl sulfide capped Pd NPs were synthesized following a previously published protocol.[32] Palladium (II) acetate (100 mg, 0.89 mmol) together with n-dodecyl sulphide (0.825 g, 2.23 mmol) were added to a 3-neck round-bottom flask containing 25 mL toluene. The solution was heated to 90 °C under a nitrogen blanket and kept at this temperature for 3h.

After 3h, the reaction system was left to cool down to room temperature and the solvent was removed under vacuum. The resulting precipitate was washed twice with acetone by centrifugation for 5 min at 10500 RPM (11830 ×g). The Pd-seeds were left to dry and kept in a scintillation glass vial until further use. The final product was redispersible in organic solvents such as toluene, hexane, chloroform.

Preparation of Pd/Fe-oxide NPs via a seed-mediated method

For the synthesis of Pd/Fe-oxide NPs, an iron oxide coat was added via a classical thermal decomposition procedure on top of the pre-made Pd-seeds, by following a previously published protocol with slight modifications.[33] OAm capped Pd NPs (20 mg, 0.188 mmol) were dispersed in approximatively 0.5 mL hexane and sonicated for 5 min. Next, the Pd-seeds in hexane were added to a 3-neck round bottom flask containing 20 mL octadecene, OA (1 mL, 3.14 mmol) and OAm (1 mL, 3.14 mmol). The reaction mixture was slowly heated to 120 °C under nitrogen flow and vigorous stirring and left at this temperature for 30 min to ensure the complete removal of hexane. Subsequently, iron pentacarbonyl (150 μL, 1.141 mmol) was injected into the reaction vessel via a septum and the reaction system was heated to 300 °C with a heating rate of 5 °C/ min and kept at this temperature for 30 min. After 30 min, the reaction system was left to cool down to room temperature and the Pd/Fe-oxide NPs were collected by addition of 30 mL ethanol and centrifugation at 10500 RPM (11830 ×g) for 4-6 min. The procedure was repeated several times with ethanol and one or two times with a combination of ethanol and hexane in equal volumes. Lastly, the Pd/Fe-oxide NPs were dried by a gentle flow of nitrogen/compressed air and stored as such until further use. The final product could be redispersed in organic solvents such as toluene, hexane, chloroform.

Characterization

Particle size, size distribution and morphology of the samples were determined by transmission electron microscopy (TEM), using a 120 kV Jeol_JEM1400 microscope. All samples for TEM were prepared by drop-casting a diluted nanoparticle suspension in organic solvents such as hexane on a Quantifoil R1.2/1.3 Cu300 grid and evaporating the solvent at room temperature. The mean diameter and the size

distribution of the samples were obtained by statistical analysis over 500-1000 NPs, by analysing the obtained TEM images with ImageJ software. The elemental mapping analysis was done with an Oxford Instruments EDS detector X-MAX^N 100TLE on the same grids used for TEM.

2.3. Results and Discussion

Nanoparticle synthesis

The preparation of Pd/Fe-oxide NPs was investigated by following two routes: one-pot procedure[29] and seed-mediated synthesis, and the resulting hybrid NPs were compared in terms of their morphology. Generally, the one-pot procedure (Scheme 2.1A) involves in situ formation of metal seeds by means of homogeneous nucleation as a result of thermal decomposition of a precursor, in this case Pd-acetylacetonate ($Pd(acac)_2$). Subsequent injection of the second metal precursor, iron pentacarbonyl ($Fe(CO)_5$), into the reaction mixture and further temperature increase, trigger the second thermal decomposition reaction occurring on the surface of the already formed Pd-seeds. As the result, the final morphology of the hybrid NPs is determined by the second nucleation process in which iron oxide is deposited on the surface of Pd-seeds. For instance, introducing 0.5 mmol OA and 0.5 mmol OAm during the reaction and an instant increase of the temperature to 300 °C (Scheme 2.1A(a)) results in flower-like Pd/Fe-oxide NPs (Figure 2.2A).

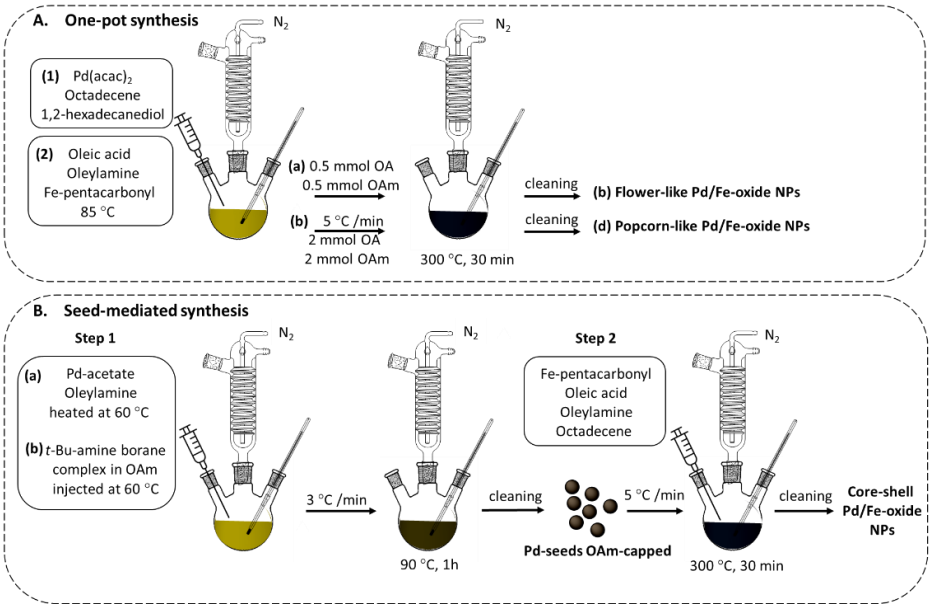

Scheme 2.1. Synthetic routes for the preparation of hybrid Pd/Fe-oxide NPs via **(A)** one-pot procedure and **(B)** seed-mediated synthesis under conditions further notified as Exp_standard.

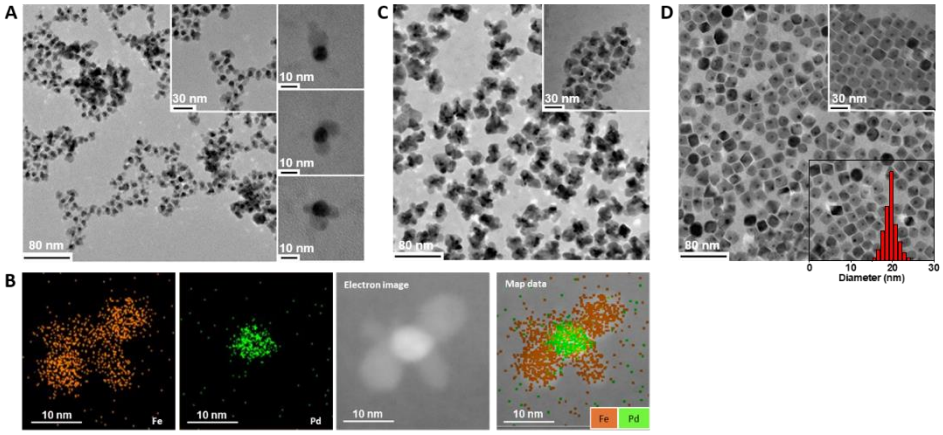

Figure 2.2. Characterization of Pd/Fe-oxide NPs obtained with different synthesis procedures: **(A)** One-pot synthesis resulting in: flower-like NPs – TEM images, incl. the three specific types of shapes they undertook (insets), **(B)** EDS elemental mapping with individual signals for Fe and Pd, **(C)** popcorn-like NPs – TEM images and **(D)** Seed-mediated approach using OAm-capped Pd-seeds (conditions defined as Exp_standard) – TEM images and the corresponding size distribution.

As depicted in the right inset, the NPs exhibit 3 different morphologies as they consist of a 7 nm Pd-core with one, two or three Fe-oxide lobes of approximately 9 nm.

In the bright-field TEM image (Figure 2.2A), the darker areas correspond to palladium, while lighter contrast represents Fe-oxide. This occurs due to the different electron penetration efficiency on the Pd compared to Fe-oxide. To confirm this, EDS elemental mapping was performed on the flower-like Pd/Fe-oxide NPs visualizing the individual signals for Pd and Fe (Figure 2.2B).

To better understand the effect of the synthetic conditions on the morphology of final hybrid Pd/Fe-oxide NPs, the one-pot synthesis was repeated with slight modifications, in which higher amounts of OA (2 mmol) and OAm (2 mmol) were used, and the 300 °C, necessary for the second nucleation reaction, were reached gradually, increasing the temperature by 5 °C/min (Scheme 2.1A(b)). This experiment resulted in Pd/Fe-oxide NPs with popcorn-like morphologies and sizes around 30 nm, as shown in Figure 2.2C. Despite the same principle of NPs formation in both experiments, in the case of popcorn-like heterostructures the Pd-cores were found to be less uniform and completely coated with Fe-oxide (Figure 2.2C), which on its turn resulted in a decreased homogeneity within the sample. Clearly, the simultaneously

occurring homogenous nucleation and seed-assisted growth are two competing processes, which may be integrated under similar experimental conditions, but the individual optimal parameters can differ significantly and the control over the synthesis is challenging. This can lead not only to polydispersity in terms of size and shape, but also to diversity in the crystallinity and internal structure they present. Indeed, as demonstrated, both experiments based on the one-pot procedure resulted in Pd/Fe-oxide NPs with wide variations in size and shape.

The aforementioned uniformity issues could be resolved by separating the nucleation processes of the two metals. This can be achieved by the two-step seed-mediated growth process, which offers the possibility to prevent premature homogeneous nucleation of the second metal, by deposition of its atoms on the preformed seeds with well-defined characteristics.[16] For better understanding, the seeded-growth is based on a key principle of the classical nucleation theory, which states that the energy barrier that needs to be overcome for a certain material to heterogeneously nucleate onto a pre-existing seed is lower than the activation energy necessary to induce the corresponding homogeneous nucleation.[18] In simpler terms, if pre-made seeds are inserted into a reaction mixture during NPs synthesis, it is energetically more favourable for monomers to undergo phase transformation at the surface of a seed, than to self-nucleate. Therefore, a seed-mediated growth process was applied for the synthesis of another batch of Pd/Fe-oxide NPs (Scheme 2.1B) in which the iron precursor ($Fe(CO)_5$) was decomposed and iron atoms were deposited on the surface of the pre-made OAm-capped Pd-seeds with the average diameter of 5 nm (Figure 2.3A).

As the result, the iron-oxide formed a coating on top of the Pd-seeds, leading to monodisperse Pd/Fe-oxide NPs with spherical-squared morphology and sizes around 19 nm, as can be seen in the TEM images presented in Figure 2.2D.

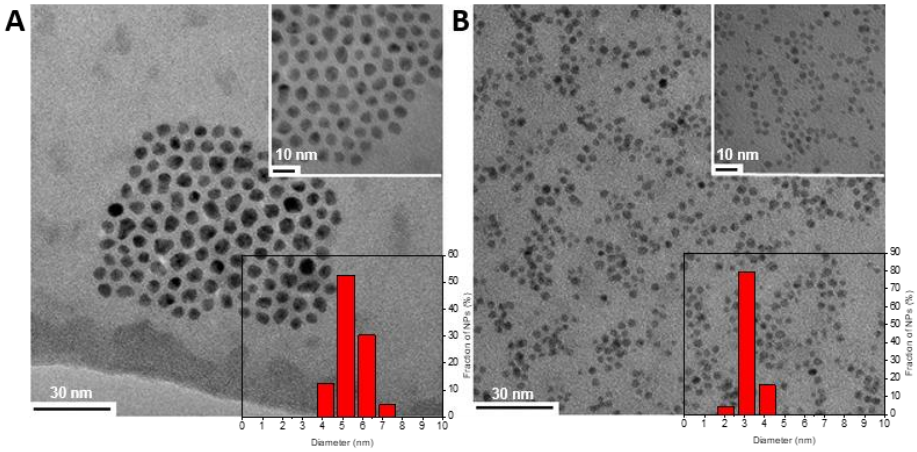

Figure 2.3. TEM images and size distributions of: **(A)** OAm-capped and **(B)** nDS-capped Pd-seeds.

Both, the one-pot synthesis method and the seed-assisted growth method resulted in heterogeneous nucleation of Fe-oxide on the Pd-seeds by TD using $Fe(CO)_5$ in 1-octadecene with OA and OAm added as ligands. However, a lower monodispersity of the nanocrystals synthesized via the one-pot process can be observed when compared to the nanocrystals made via the seed-mediated growth process. This does not come as a surprise, and based on the previously stated principles of TD, the seed-mediated growth procedure was more easily controllable than the one-pot synthesis method, offering hybrid NPs with higher uniformity. Therefore, the one-pot synthesis method was not further investigated, and all efforts were devoted to carefully study the synthetic process of the seed-mediated growth in order to better understand the mechanism and to achieve high control over the morphology of the obtained hybrid nanocrystals. Starting from the reaction conditions depicted in Scheme 2.1B (defined as Exp_standard) that generated the Pd/Fe-oxide NPs presented in Figure 2.2D, different synthetic conditions were investigated to determine the key parameters involved in the control of the nucleation and successive growth of Fe-oxide on top of the Pd-seeds. The overview of the conducted experiments along with the corresponding conditions are summarized in Table 2.1.

Table 2.1. Summary of the synthetic conditions in seed-mediated synthesis of Pd/Fe-oxide NPs and the resulting average sizes.

Sample	Pd-seeds (mg)	Heating rate (°C/min)	[surf]/[Fe] (mol/mol)	Solvent	Average diameter (nm±SD)
Exp_standard	20	5	5.5	ODE	19.5±1.5
Exp_10mg	10	5	5.5	ODE	21.0±2.0
Exp_nDS	20	5	5.5	ODE	14.7±1.8
Exp_3 °C	20	3	5.5	ODE	13.3±2.2
Exp_7 °C	20	7	5.5	ODE	18.9±2.1
Exp_[surf]/[Fe]=2	20	5	2	ODE	9.8±1.1
Exp_[surf]/[Fe]=3.25	20	5	3.25	ODE	16.1±4.3
Exp_[surf]/[Fe]=11	20	5	11	ODE	16.3±1.7
Exp_OAm	20	5	5.5[a]	ODE	– [c]
Exp_OA	20	5	5.5[b]	ODE	– [c]
Exp_DPE	20	5	5.5	DPE	12.1±2.1
Exp_ODE:DPE(1:1)	20	5	5.5	ODE:DPE	15.5±1.8
Exp_DBE	20	5	5.5	DBE	17.9+2.5

[a] 2 mL OAm, w/o OA; [b] 2 mL OA, w/o OAm; [c] not measured; surf = surfactant = [OA] + [OAm]; ODE = 1-octadecene; DPE = diphenyl ether; DBE = dibenzyl ether.

Tuning parameters in the seed-mediated growth procedure

Effect of the [Fe]/[Pd] ratio. The effect of the [Fe]/[Pd] ratio was investigated by conducting an experiment under conditions summarized in Table 2.1 as Exp_10mg, using a smaller amount of pre-made OAm-capped Pd-seeds (10 mg) compared to that used in Exp_standard (20 mg). As the result, Pd/Fe-oxide NPs with spherical-squared morphology and sizes around 21 nm were formed (Figure 2.4). The possibility to tune the size of NPs by varying the precursor/seed ratio, in our case [Fe]/[Pd], is known.[16] Indeed, in the case of Pd/Fe-oxide hybrid nanocrystals obtained using only half of the amount of Pd-seeds compared to Exp_standard, the NPs presented a slight increase in their average size. This can be explained as introducing a lower amount of Pd-seeds into the reaction translates into a smaller surface area available for Fe-oxide deposition forming a thicker Fe-oxide layer, resulting in overall larger sizes of Pd/Fe-oxide NPs.

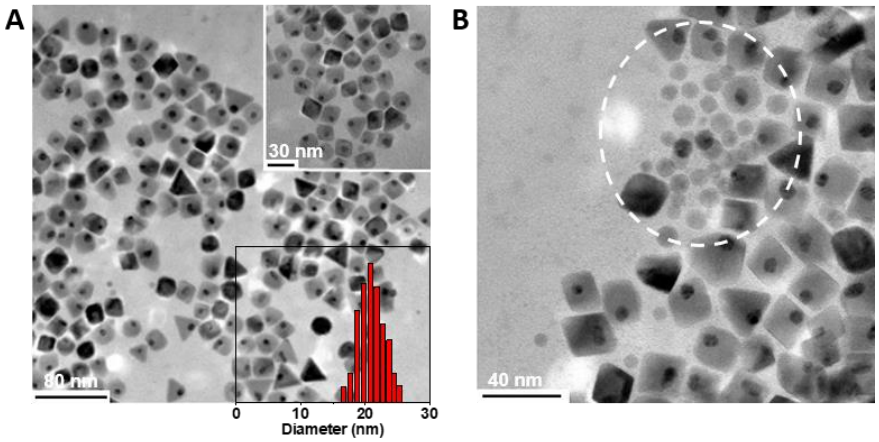

Figure 2.4. Characterization of Pd/Fe-oxide NPs obtained with 10 mg Pd seeds in Exp_10mg: **(A)** TEM images and size distribution of the prepared NPs; **(B)** second population of small iron oxide nanocrystals found in Exp_10mg.

Notably, no major influence on the morphology of the hybrid nanocrystals was observed, meaning that both the thermodynamic and kinetic control of the reaction were ensured in order for the original shape to be maintained.[3] As the overall surface area of the nanocrystals increases with size, more capping agent will be gradually depleted from the solution, therefore, excess of surfactant is often necessary. This was ensured through the experiment, even though the [surf]/[Fe] ratio was not specifically adjusted in this case.

As discussed earlier, seed-mediated growth offers an effective way to avoid homogeneous nucleation by deposition of the atoms on preformed seeds because of the lower energy barrier. However, when the monomer concentration exceeds a certain threshold, both homogeneous and heterogeneous nucleation can occur concomitantly, leading to nanocrystals with diverse morphologies, sizes, shapes and internal structures.[3] In the specific case of Exp_10mg, next to the Pd/Fe-oxide NPs, a second population of small Fe-oxide nanocrystals with the diameter of around 9 nm could be found (Figure 2.4B).

Effect Pd-seeds coating layer. Surfactants play a crucial role in the formation of the intermediate complexes during the synthesis of nanocrystals by TD. These ligands protect the surface and confine the size of the obtained nanostructures to nanoscale

by forming a dynamic layer, which not only allows to control the growth of the primary nanocrystals, but also the nucleation of another inorganic phase onto their surface, leading to hybrid NPs.[19] Therefore, requirements for the surface ligand include compatibility with growth-conditions and the nature of its binding to the surface of the primary seeds, which should generally not be too strong.[34] In order to investigate how different surfactant layers of the Pd-seeds, used during the seed-mediated growth synthesis, influence the final morphology of Pd/Fe-oxide NPs, Exp_standard was repeated using Pd-seeds with *n*-dodecyl sulphide (nDS) instead of OAm as a capping agent under synthetic conditions summarized in Table 2.1 as Exp_nDS. These nDS-coated Pd-seeds have spherical shapes, but smaller sizes (3 nm) (Figure 2.3B) compared to OAm-coated Pd-seeds (5 nm) used for Exp_standard (Figure 2.3A).

As presented in Figure 2.5, Pd/Fe-oxide NPs with an average size of 15 nm were obtained employing nDS coated Pd-seeds, compared to the 20 nm Pd/Fe-oxide NPs obtained using OAm coating of Pd-seeds in Exp_standard. Besides the decrease in size, the final NPs also exhibited a large diversity in morphology. The nanocrystals undertook spherical, squared, triangled, and flower-like morphologies, which ultimately translates in higher size distribution.

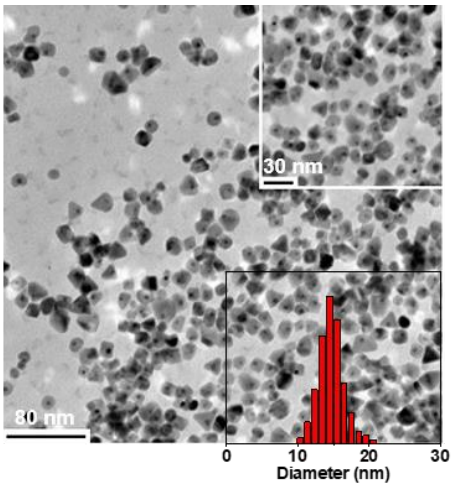

Figure 2.5. TEM image and size distribution of Pd/Fe-oxide NPs prepared with nDS coated Pd-seeds (Exp_nDS).

As all other reaction conditions were kept the same during the synthesis, it is obvious that the new ligand nDS present on the Pd-seeds either affected the growth-phase, or played a role in limiting the access to Pd-seeds due to the strong binding to their surface. Similar effects of the sulphur-containing ligands hindering the epitaxial overgrowth of metal oxides on noble metal nanocrystals have been reported in literature.[34] In contrast, as a weak ligand, OAm is known to bind less strongly to the surface of noble metals, presumably facilitating

the growth-phase more than the nDS ligand, which on its turn explains the smaller sizes of the NPs obtained with the latter surfactant.

Ligands also play an important role in the shape-control of the NPs, modulating the surface energy of a specific facet and favoring growth in certain crystallographic planes. The strength of binding of each capping agent is different for various facets, and in some cases, an exclusive facet is preferred over another. Lastly, a facet that is selectively capped will result in its dominant expression during growth. This means that a certain morphology will be preferred over others.[16] One of the examples of capping ligands determining the morphology of NPs is the combination of carboxylic acid/amine ligands, known to yield cubic structures.[34] Since such great diversity in shape was noted for the Pd/Fe-oxide NPs obtained with nDS-capped Pd-seeds, this ligand most likely has neither an exclusive facet for binding, nor a clear effect on specific morphology, as OAm does.

Effect heating rate. As nanoparticle synthesis based on TD requires high temperatures to trigger the decomposition of the iron precursor, the rate of temperature increase is another important parameter among the wide range of variables that can influence this process. Cotin et al. considered that the heating rate used to reach the growth-temperature is probably even more important than the boiling temperature of the solvent in which the synthesis is conducted.[13] During this study, the influence of the heating rate was investigated by running experiments with two variable rates implemented to reach 300 °C, one lower and one higher than 5 °C/min applied in Exp_standard. The experimental details for these batches of Pd/Fe-oxide NPs are summarized in Table 2.1 as Exp_3 °C and Exp_7 °C for experiments with the heating rates of 3 °C/min and 7 °C/min, respectively.

The Pd/Fe-oxide NPs resulted from the experiment with a heating rate of 3 °C/min exhibited an average size of 13 nm (Figure 2.6A), which is smaller than the average size of the Pd/Fe-oxide nanoparticles obtained through the experiments in which higher heating rates were employed. A change in morphology was also noted in this case, as most of the NPs undertook a dumbbell-like shape, and irregular shapes were more frequently encountered than in the other samples synthesized with higher heating rates. This also explains the broader size distribution found in Exp_3 °C

(Figure 2.6A). All these results are in agreement with those from other studies by Lassenberger et al.[35] and Cotin et al.[13], who also noted smallest core sizes and broadest size distribution for the NPs synthesized at low heating rates. Similar to these observations, our results suggest that the probable reason for this inhomogeneity comes either from multiple nucleation steps or as a consequence of the nucleation step not being quick enough due to the lower heating rate. Additionally, Ostwald ripening may also be the reason for the presence of both small and large NPs within the same sample. In this case, the smallest nanocrystals with the higher surface energy start to dissolve and the created monomers diffuse to the surface of larger NPs and participate in their growth further on.

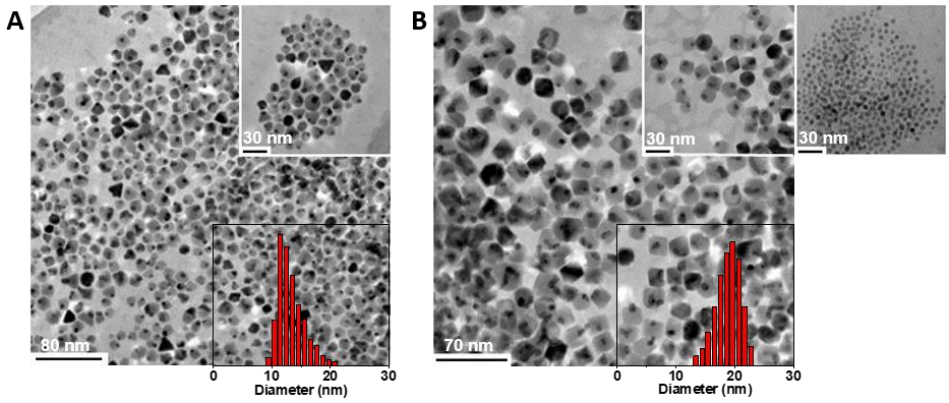

Figure 2.6. TEM images and size distributions of Pd/Fe-oxide NPs obtained with different heating rates to reach growth temperature of 300 °C: (**A**) heating rate 3 °C /min (Exp_3 °C), and (**C**) heating rate 7 °C /min (Exp_7 °C), and second population of small iron oxide nanocrystals found in Exp_7 °C (inset on the right).

On the other hand, the nanocrystals produced via Exp_7 °C were found to be very similar in average size, shape, and size distribution (Figure 2.6B) to the Pd/Fe-oxide NPs obtained from Exp_standard. The average size of the Pd/Fe-oxide NPs from Exp_7 °C was 19 nm, retaining a round-squared morphology. However, the fast heating rate causes production of many monomers, surpassing the minimum number necessary for nucleation and possibly overcoming the threshold for homogeneous nucleation.[13] As the result, this high burst of monomers compared to slower heating rates causes the undesired homogeneous nucleation in the form of Fe-oxide NPs within the sample (Figure 2.6B, inset).

Effect surfactant to iron ratio. It is known that the surfactant/metal ratio ([surf]/[Fe]) has an influence on the size of the final NPs, and specifically, that a decrease in the amount of surfactant for the same iron precursor concentration is expected to produce smaller nanoparticles.[30] To investigate this, experiments were conducted under standard conditions, but varying the amount of surfactant introduced in the reaction mixture. Two experiments with a lower and one experiment with a higher [surf]/[Fe] ratio than that used for Exp_standard were performed. The synthetic conditions are summarized in Table 2.1 as Exp_[surf]/[Fe]=2, Exp_[surf]/[Fe]=3.25 and Exp_[surf]/[Fe]=11.

The experiment in which a [surf]/[Fe] ratio of 2 was employed resulted in Pd/Fe-oxide NPs with 10 nm average size and a fraction of Fe-oxide nanocrystals around 4 nm (Figure 2.7A). Increasing the [surf]/[Fe] ratio to 3.25, resulted in an increase in the average size of Pd/Fe-oxide NPs to 16 nm, but no homogeneous nucleation was noticed in this case (Figure 2.7B). As expected, both experiments with [surf]/[Fe] ratios being smaller compared to those in Exp_standard (5.5) yielded Pd/Fe-oxide NPs with average sizes smaller than 20 nm. Interestingly, doubling the [surf]/[Fe] ratio from 5.5 in Exp_standard to 11 (Exp_[surf]/[Fe]=11), led to Pd/Fe-oxide NPs with a lower average size of 16 nm (Figure 2.7C).

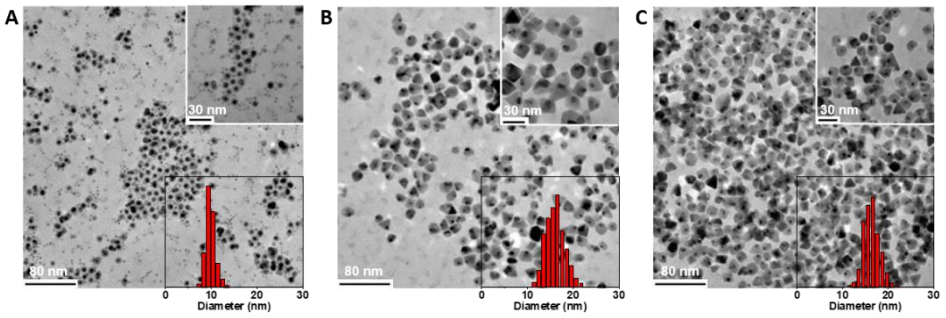

Figure 2.7. TEM images and size distributions of **(A)** Exp_[surf]/[Fe]=2, **(B)** Exp_[surf]/[Fe]=3.25, and **(C)** Exp_[surf]/[Fe]=11.

Possibly, a larger amount of ligand used in Exp_[surf]/[Fe]=11 increased the stability of the iron precursor, and consequently the decomposition temperature. Additionally, increased surfactant concentration may also mean that there are simply more ligand molecules at the surface and around the formed nuclei, which also

contributes to either slowing down or inhibiting the growth-process. Consequently, this increase in amount of surfactant influences the growth-time, which also translates into a lower concentration of monomers available for the growth-step compared to Exp_standard.

Notably, the Pd/Fe-oxide NPs obtained from Exp_[surf]/[Fe]=11 had an average size very close to those obtained from Exp_[surf]/[Fe]=3.25. However, the experiment with a [surf]/[Fe] ratio of 11 offered a better size distribution, while NPs prepared using a [surf]/[Fe] ratio of 3.25 exhibited high polydispersity. These observations are in agreement with Lassenberger et al.[35], who observed that the temperature for onset of rapid growth decreases with decreased surfactant concentration. Moreover, an increase in the polydispersity during the growth-phase was observed when using smaller amounts of surfactant compared to the cases when NPs were synthesized with higher [surf]/[Fe] ratios. [30]

Based on the results obtained from this series of experiments, it can be hypothesized that the mean size of the NPs does increase with the amount of ligand up to a critical value, after which the behaviour fails (Figure 2.8). The mechanism underlying this phenomenon is however still not clearly formulated and conflicting results obtained through numerous studies on the stoichiometric ratio ligand/precursor with similar reaction mixtures make it difficult to compare our results with those from literature.[13] The chemical nature of the ligand has also a direct effect on the reaction mechanism[13], and in order to study this, an experiment was conducted in the presence of OAm only with [OAm]/[Fe]=5.5, as in Exp_standard. The experiment resulted in a product composed of large aggregates, from which the majority is Fe-oxide NPs (Figure 2.9A). In parallel, an experiment in the presence of OA only with [surf]/[Fe]=5.5, as in Exp_standard was conducted in order to study the influence of

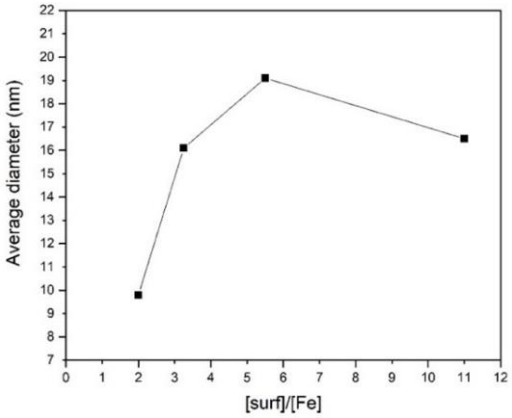

Figure 2.8. Average diameter of the Pd/Fe-oxide hybrid NPs as a function of the ligand/precursor molar ratio.

OA only on the NPs outcome. The experiment resulted in no core-shell Pd/Fe-oxide NPs either (Figure 2.9B). Amines are known to ease the decomplexation of the oleates coordinated to the iron, while the influence of carboxylic acid ligands can be quite complex as they can stabilize the precursors and have an effect of the monomer formation.[13,36] The results obtained in experiment Exp_OAm and Exp_OA suggest that using OAm or respectively, OA as the only ligand is not sufficient for obtaining well-formed Pd/Fe-oxide NPs. Therefore, we can conclude that both OAm and OA are necessary for the formation of well-defined Pd/Fe-oxide hybrid NPs, with both surfactants playing a role against aggregation and in the control of the iron oxide domains.

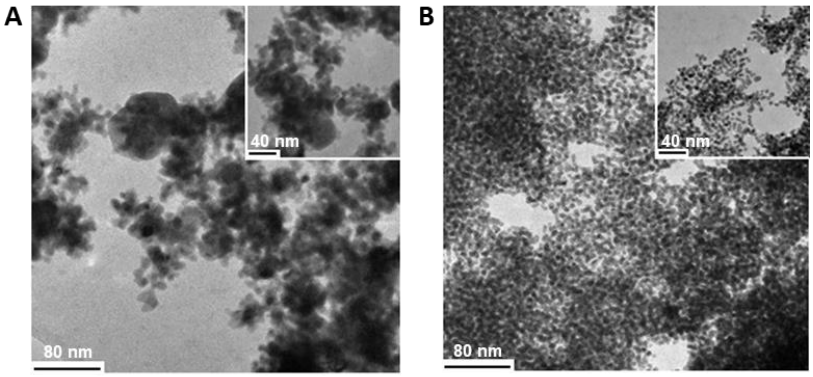

Figure 2.9. TEM images of NPs prepared with **(A)** only OAm (Exp_OAm) and **(B)** only OA **(**Exp_OA).

Effect solvent/temperature. The iron precursor decomposes at a wide range of temperatures, meaning, the higher the temperature during synthesis, the more monomers are formed, which results in bigger NPs. Therefore, the NPs size depends on and increases with the boiling point of the solvent, as demonstrated in literature.[36-39] In order to verify this phenomenon for our hybrid NPs, the growth-mediated synthesis was conducted under standard conditions, but using solvents with boiling temperatures lower than that of ODE (315 °C) used in Exp_standard. Three batches of NPs were prepared in DBE (b.p. 298 °C), a mixture of ODE:DPE (1:1, b.p. ± 270 °C), and DPE (b.p. 258 °C). The corresponding TEM images and size distributions are depicted in Figure 2.10 (A-C), respectively.

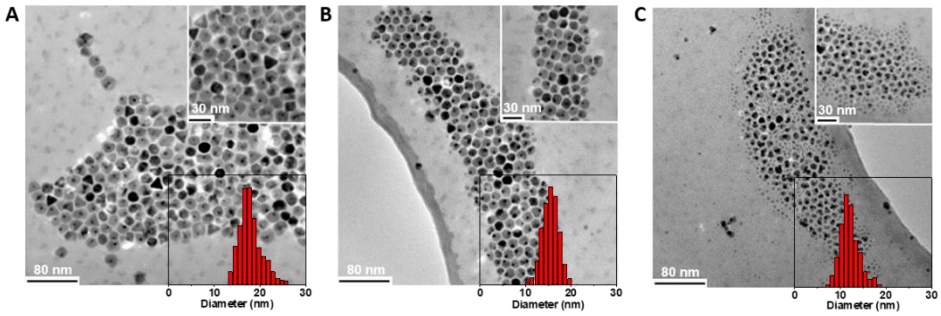

Figure 2.10. TEM images and size distributions of Pd/Fe-oxide NPs prepared in different solvents: (**A**) dibenzyl ether (Exp_DBE), (**B**) 1-octadecene:diphenyl ether 1:1 (Exp_ODE:DPE(1:1)), and (**C**) diphenyl ether (Exp_DPE).

As expected, the mean diameter of the Pd/Fe-oxide NPs decreased with the decrease of the boiling point of the solvent (Table 2.2), confirming that the growth rate essentially depends on the temperature in which the reaction is conducted. However, the final size of the NPs is also dependent on the nature of the solvent. Observations by Cotin et al. reveal that the solvent is able to interact with the metal precursor and affect the monomer formation rate depending on its chemical properties.[13] Thereby, a polar solvent is more likely to destabilize the formed complex and yield smaller NPs, while the non-polar solvents stabilize the complex and condition larger NPs. Baaziz et al. drew the same conclusion about the nature of the solvent governing the nucleation temperatures, and therefore, it is fair to assume that the solvent plays a key role in the stability of the complex and its decomposition kinetics.[36] Our results confirm these observations, as the largest NPs were formed in Exp_standard, with the least polar solvent, ODE. Oppositely, DPE, the most polar solvent out of the four used through this study, led to the smallest Pd-Fe/oxide NPs (Figure 2.10C).

Another aspect presented in literature is that the polarity of the solvent can influence the morphology of the NPs. It is suggested that multinucleation may be favoured by the use of slightly polar solvents, such as diphenyl ether or benzyl ether. However, in non-polar solvents, such as ODE, the Fe-oxide domain drains electrons from the seeds on which it grows and disables them from potential polynucleation, resulting in a single Fe-oxide domain.[17,20,40] Contrastingly, the results of the experiments performed in different solvents presented by Wei et al.[20] suggest that neither the polarity of the solvent, nor the saturation of the solvent molecules play a role in the

final morphologies of the synthesized hybrid NPs. The reason behind this phenomenon is the crystallinity of the seeds on which the Fe-oxide was grown.

However, most of the Pd/Fe-oxide NPs obtained from Exp_DPE do indeed present multiple iron domains, undertaking a flower-like shape (Figure 2.10C), as expected from a solvent with higher polarity.[40] Homogeneous Fe-oxide, found within Exp_DPE, is most likely formed due to the lower b.p. of DPE and, hence, the lower reaction temperature. These iron oxide species seem to have an amorphous character. However, complete crystallization of the Fe-oxide using DPE as a solvent seems to be possible with reaction time increased from 45 min to 3h.[41] For comparison, we conducted Exp_ODE:DPE(1:1), in which a mixture of ODE and DPE in 1:1 ratio was used as solvent. Due to addition of non-polar ODE, the solvent mixture had a decreased polarity compared to DPE only, and the polynucleation was not favoured anymore. Consequently, core-shell Pd/Fe-oxide NPs were obtained instead of flower-like (Figure 2.10B).

Interestingly, core-shell NPs obtained from both, Exp_ODE:DPE(1:1) and Exp_DBE, were similar to those of Exp_standard. In the case of the former experiment, the Pd/Fe-oxide tended to undertake hexagonal shapes, while the latter one resulted in various shapes like spheres, triangles and even isolated flowers. This difference in shape-control can again be explained by the higher polarity of the ODE:DPE solvent mixture, compared to ODE. Based on the results obtained through this study, it is clear that the solvent has a significant effect on the outcome of the reaction by influencing the physical properties of the reaction surrounding media (e.g. polarity) and the stabilities of different reactants and intermediate species. This is generally in agreement with the studies conducted by others as mentioned earlier.

Table 2.2. Dependence of the average diameter of Pd/Fe-oxide NPs on the b.p. of the solvent in which the experiment was conducted.

Solvent	ODE	DBE	ODE:DPE(1:1)	DPE
Boiling point (°C)	315 °C	298 °C	± 270 °C	258 °C
Average diameter (nm)	19.5±1.5	17.9±2.5	15.5+1.8	12.1±2.1

2.4. Conclusion

We successfully synthesized Pd/Fe-oxide hybrid NPs with sizes between 9 and 30 nm via both, one-pot synthesis method and seed-mediated growth thermal decomposition procedures. As the hybrid nanocrystals obtained via the one-pot synthesis method presented less uniformity in terms of size and morphology, we focused on systematically investigating the seed-mediated growth procedure by varying one parameter at a time. These experiments offered important insights on the synthetic mechanism and shed light over the effect of different reaction parameters, enabling the production of variously sized and shaped hybrid Pd/Fe-oxide NPs. We saw that the [Fe]/[Pd] ratio parameter can be successfully used in tuning the size of the nanoparticles, but with certain limitations, as a too high ratio can overcome the critical concentration that leads to homogeneous nucleation in the form of a second population of small iron oxide NPs. An effect on the size and shape of the Pd/Fe-oxide NPs was observed when differently capped Pd-seeds were used as a surface for iron oxide nucleation and growth, thus confirming that ligands play an important role during the synthesis by modulating the surface energy of specific facets and favoring growth in certain crystallographic planes over others. The heating rate chosen for the experiments was discovered as another important tuning parameter. Hence, a low heating rate enabled Ostwald ripening processes, which has led to hybrid NPs with multiple morphologies and broad size distributions. On the other hand, even though a fast heating rate did not have a huge impact on the morphology and size distribution of the obtained Pd/Fe-oxide NPs, homogeneous nucleation of iron oxide as a consequence of the high burst of monomers was observed. In the case of surfactant to iron ratio, we noticed a linear correlation between the two, as the size of the hybrid NPs increased with the increase of the [surf]/[Fe] ratio. However, this behavior holds until a critical value only, above which the size of the NPs decreases. Additionally, it was clear that the combination of surfactants is essential for the formation of well-defined Pd/Fe-oxide nanostructures. Lastly, the interplay between the boiling point and the polarity of the solvent used during the thermal decomposition synthesis is highly important as it affects both size and shape of the obtained NPs.

Therefore, from the multitude of batches obtained, the core-shell Pd/Fe-oxide NPs with sizes around 15-21 nm and narrow size distributions are considered the most promising candidates for potential biomedical applications and investigation of their magnetic properties will be presented in the following chapter of this thesis.

Bibliography

1. Vangijzegem, T.; Stanicki, D.; Laurent, S. Magnetic iron oxide nanoparticles for drug delivery: applications and characteristics. *Expert Opinion on Drug Delivery* **2019**, *16*, 69-78, doi:10.1080/17425247.2019.1554647.
2. Gossuin, Y.; Gillis, P.; Hocq, A.; Vuong, Q.L.; Roch, A. Magnetic resonance relaxation properties of superparamagnetic particles. *WIREs Nanomedicine and Nanobiotechnology* **2009**, *1*, 299-310, doi:https://doi.org/10.1002/wnan.36.
3. Blanco-Andujar, C.; Walter, A.; Cotin, G.; Bordeianu, C.; Mertz, D.; Felder-Flesch, D.; Begin-Colin, S. Design of iron oxide-based nanoparticles for MRI and magnetic hyperthermia. *Nanomedicine (Lond)* **2016**, *11*, 1889-1910, doi:10.2217/nnm-2016-5001.
4. Laurent, S.; Saei, A.A.; Behzadi, S.; Panahifar, A.; Mahmoudi, M. Superparamagnetic iron oxide nanoparticles for delivery of therapeutic agents: opportunities and challenges. *Expert Opinion on Drug Delivery* **2014**, *11*, 1449-1470, doi:10.1517/17425247.2014.924501.
5. Sharma, S.; Lamichhane, N.; Parul; Sen, T.; Roy, I. Iron oxide nanoparticles conjugated with organic optical probes for in vivo diagnostic and therapeutic applications. *Nanomedicine* **2021**, *16*, 943-962, doi:10.2217/nnm-2020-0442.
6. Torres, M.d.R.R.; Tavare, R.; Paul, R.L.; Jauregui-Osoro, M.; Protti, A.; Glaria, A.; Varma, G.; Szanda, I.; Blower, P.J. Synthesis of 64Cu(II)-bis(dithiocarbamatebisphosphonate) and its conjugation with superparamagnetic iron oxide nanoparticles: in vivo evaluation as dual-modality PET-MRI agent. *Angew Chem Int Ed Engl* **2011**, *50*, 5509-5513.
7. Sanchez, L.M.; Alvarez, V.A. Advances in Magnetic Noble Metal/Iron-Based Oxide Hybrid Nanoparticles as Biomedical Devices. *Bioengineering (Basel)* **2019**, *6*, doi:10.3390/bioengineering6030075.
8. Boros, E.; Bowen, A.M.; Josephson, L.; Vasdev, N.; Holland, J.P. Chelate-free metal ion binding and heat-induced radiolabeling of iron oxide nanoparticles. *Chemical Science* **2015**, *6*, 225-236, doi:10.1039/C4SC02778G.
9. Ma, D. Chapter 1 - Hybrid Nanoparticles: An Introduction. In *Noble Metal-Metal Oxide Hybrid Nanoparticles*, Mohapatra, S., Nguyen, T.A., Nguyen-Tri, P., Eds. Woodhead Publishing: 2019; https://doi.org/10.1016/B978-0-12-814134-2.00001-2pp. 3-6.
10. Wu, S.; Sun, A.; Zhai, F.; Wang, J.; Xu, W.; Zhang, Q.; Volinsky, A.A. Fe3O4 magnetic nanoparticles synthesis from tailings by ultrasonic chemical co-precipitation. *Materials Letters* **2011**, *65*, 1882-1884, doi:https://doi.org/10.1016/j.matlet.2011.03.065.
11. Qi, H.; Yan, B.; Li, C.; Lu, W. Synthesis and characterization of water-soluble magnetite nanocrystals via one-step sol-gel pathway. *Science China Physics, Mechanics and Astronomy* **2011**, *54*, 1239-1243, doi:10.1007/s11433-011-4375-0.
12. Jarzyna, P.A.; Skajaa, T.; Gianella, A.; Cormode, D.P.; Samber, D.D.; Dickson, S.D.; Chen, W.; Griffioen, A.W.; Fayad, Z.A.; Mulder, W.J.M. Iron oxide core oil-in-water emulsions as a multifunctional nanoparticle platform for tumor targeting and imaging. *Biomaterials* **2009**, *30*, 6947-6954, doi:https://doi.org/10.1016/j.biomaterials.2009.09.004.
13. Cotin, G.; Perton, F.; Blanco-Andujar, C.; Pichon, B.; Mertz, D.; Bégin-Colin, S. Chapter 2 - Design of Anisotropic Iron-Oxide-Based Nanoparticles for Magnetic Hyperthermia. In *Nanomaterials for Magnetic and Optical Hyperthermia Applications*,

Fratila, R.M., De La Fuente, J.M., Eds. Elsevier: 2019; https://doi.org/10.1016/B978-0-12-813928-8.00002-8pp. 41-60.
14. Wu, L.; Mendoza-Garcia, A.; Li, Q.; Sun, S. Organic Phase Syntheses of Magnetic Nanoparticles and Their Applications. *Chemical Reviews* **2016**, *116*, 10473-10512, doi:10.1021/acs.chemrev.5b00687.
15. Chai, Y.; Feng, F.; Li, Q.; Yu, C.; Feng, X.; Lu, P.; Yu, X.; Ge, M.; Wang, X.; Yao, L. One-Pot Synthesis of High-Quality Bimagnetic Core/Shell Nanocrystals with Diverse Exchange Coupling. *Journal of the American Chemical Society* **2019**, *141*, 3366-3370, doi:10.1021/jacs.8b12888.
16. Xia, Y.; Gilroy, K.D.; Peng, H.-C.; Xia, X. Seed-Mediated Growth of Colloidal Metal Nanocrystals. *Angewandte Chemie International Edition* **2017**, *56*, 60-95, doi:https://doi.org/10.1002/anie.201604731.
17. Tancredi, P.; da Costa, L.S.; Calderon, S.; Moscoso-Londoño, O.; Socolovsky, L.M.; Ferreira, P.J.; Muraca, D.; Zanchet, D.; Knobel, M. Exploring the synthesis conditions to control the morphology of gold-iron oxide heterostructures. *Nano Research* **2019**, *12*, 1781-1788, doi:10.1007/s12274-019-2431-7.
18. Carbone, L.; Cozzoli, P.D. Colloidal heterostructured nanocrystals: Synthesis and growth mechanisms. *Nano Today* **2010**, *5*, 449-493, doi:https://doi.org/10.1016/j.nantod.2010.08.006.
19. Fantechi, E.; Roca, A.G.; Sepúlveda, B.; Torruella, P.; Estradé, S.; Peiró, F.; Coy, E.; Jurga, S.; Bastús, N.G.; Nogués, J., et al. Seeded Growth Synthesis of Au–Fe3O4 Heterostructured Nanocrystals: Rational Design and Mechanistic Insights. *Chemistry of Materials* **2017**, *29*, 4022-4035, doi:10.1021/acs.chemmater.7b00608.
20. Wei, Y.; Klajn, R.; Pinchuk, A.O.; Grzybowski, B.A. Synthesis, Shape Control, and Optical Properties of Hybrid Au/Fe3O4 "Nanoflowers". *Small* **2008**, *4*, 1635-1639, doi:https://doi.org/10.1002/smll.200800511.
21. Jang, Y.; Chung, J.; Kim, S.; Jun, S.W.; Kim, B.H.; Lee, D.W.; Kim, B.M.; Hyeon, T. Simple synthesis of Pd–Fe3O4 heterodimer nanocrystals and their application as a magnetically recyclable catalyst for Suzuki cross-coupling reactions. *Physical Chemistry Chemical Physics* **2011**, *13*, 2512-2516, doi:10.1039/C0CP01680B.
22. Lee, J.; Chung, J.; Byun, S.M.; Kim, B.M.; Lee, C. Direct catalytic C–H arylation of imidazo[1,2-a]pyridine with aryl bromides using magnetically recyclable Pd–Fe3O4 nanoparticles. *Tetrahedron* **2013**, *69*, 5660-5664, doi:10.1016/j.tet.2013.04.031.
23. Jang, S.; Hira, S.A.; Annas, D.; Song, S.; Yusuf, M.; Park, J.C.; Park, S.; Park, K.H. Recent Novel Hybrid Pd–Fe3O4 Nanoparticles as Catalysts for Various C–C Coupling Reactions. *Processes* **2019**, *7*, doi:10.3390/pr7070422.
24. Lee, W.-S.; Byun, S.; Kwon, J.; Kim, B.M. Magnetic Pd–Fe3O4 Heterodimer Nanocrystals as Recoverable Catalysts for Ligand-Free Hiyama Cross-Coupling Reactions. *Bulletin of the Korean Chemical Society* **2016**, *37*, 1992-1997, doi:https://doi.org/10.1002/bkcs.11013.
25. Yu, Y.; Anderson, L.L.; Li, Z.; Mellenberg, D.E.; Nath, R.; Schell, M.C.; Waterman, F.M.; Wu, A.; Blasko, J.C. Permanent prostate seed implant brachytherapy: Report of the American Association of Physicists in Medicine Task Group No. 64. *Medical Physics* **1999**, *26*, 2054-2076, doi:https://doi.org/10.1118/1.598721.
26. Sharkey, J.; Cantor, A.; Solc, Z.; Huff, W.; Chovnick, S.D.; Behar, R.J.; Perez, R.; Otheguy, J.; Rabinowitz, R. 103Pd brachytherapy versus radical prostatectomy in patients with clinically localized prostate cancer: A 12-year experience from a single group practice. *Brachytherapy* **2005**, *4*, 34-44, doi:https://doi.org/10.1016/j.brachy.2004.12.001.

27. Kainz, K. Radiation Oncology Physics: A Handbook for Teachers and Students. *Medical Physics* **2006**, *33*, 371-396, doi:https://doi.org/10.1118/1.2201870.
28. Maier, A.; Djanashvili, K.; Denkova, A.G.; van Rhoon, G.C.; Pignol, J.-P.; van Oossanen, R. Synthesis of Hybride Palladium(103)/Iron Oxide Nanoparticles for Thermobrachy Therapy. *European Patent Application No. 2029314* **2021**.
29. Chen, S.; Si, R.; Taylor, E.; Janzen, J.; Chen, J. Synthesis of Pd/Fe3O4 Hybrid Nanocatalysts with Controllable Interface and Enhanced Catalytic Activities for CO Oxidation. *The Journal of Physical Chemistry C* **2012**, *116*, 12969-12976, doi:10.1021/jp3036204.
30. Lin, F.-h.; Chen, W.; Liao, Y.-H.; Doong, R.-a.; Li, Y. Effective approach for the synthesis of monodisperse magnetic nanocrystals and M-Fe3O4 (M = Ag, Au, Pt, Pd) heterostructures. *Nano Research* **2011**, *4*, 1223-1232, doi:10.1007/s12274-011-0173-2.
31. Mazumder, V.; Sun, S. Oleylamine-Mediated Synthesis of Pd Nanoparticles for Catalytic Formic Acid Oxidation. *J Am Chem Soc* **2009**, *131*, 4588-4589, doi:10.1021/ja9004915.
32. Ganesan, M.; Freemantle, R.G.; Obare, S.O. Monodisperse Thioether-Stabilized Palladium Nanoparticles: Synthesis, Characterization, and Reactivity. *Chemistry of Materials* **2007**, *19*, 3464-3471, doi:10.1021/cm062655q.
33. Liu, S.; Guo, S.; Sun, S.; You, X.-Z. Dumbbell-like Au-Fe3O4 nanoparticles: a new nanostructure for supercapacitors. *Nanoscale* **2015**, *7*, 4890-4893, doi:10.1039/C5NR00135H.
34. Wang, C.; Yin, H.; Dai, S.; Sun, S. A General Approach to Noble Metal−Metal Oxide Dumbbell Nanoparticles and Their Catalytic Application for CO Oxidation. *Chemistry of Materials* **2010**, *22*, 3277-3282, doi:10.1021/cm100603r.
35. Lassenberger, A.; Grünewald, T.A.; van Oostrum, P.D.J.; Rennhofer, H.; Amenitsch, H.; Zirbs, R.; Lichtenegger, H.C.; Reimhult, E. Monodisperse Iron Oxide Nanoparticles by Thermal Decomposition: Elucidating Particle Formation by Second-Resolved in Situ Small-Angle X-ray Scattering. *Chemistry of Materials* **2017**, *29*, 4511-4522, doi:10.1021/acs.chemmater.7b01207.
36. Baaziz, W.; Pichon, B.P.; Fleutot, S.; Liu, Y.; Lefevre, C.; Greneche, J.-M.; Toumi, M.; Mhiri, T.; Begin-Colin, S. Magnetic Iron Oxide Nanoparticles: Reproducible Tuning of the Size and Nanosized-Dependent Composition, Defects, and Spin Canting. *The Journal of Physical Chemistry C* **2014**, *118*, 3795-3810, doi:10.1021/jp411481p.
37. Maity, D.; Choo, S.-G.; Yi, J.; Ding, J.; Xue, J.M. Synthesis of magnetite nanoparticles via a solvent-free thermal decomposition route. *Journal of Magnetism and Magnetic Materials* **2009**, *321*, 1256-1259, doi:https://doi.org/10.1016/j.jmmm.2008.11.013.
38. Sun, S.; Zeng, H.; Robinson, D.B.; Raoux, S.; Rice, P.M.; Wang, S.X.; Li, G. Monodisperse MFe2O4 (M = Fe, Co, Mn) Nanoparticles. *J Am Chem Soc* **2004**, *126*, 273-279, doi:10.1021/ja0380852.
39. Xie, J.; Peng, S.; Brower, N.; Pourmand, N.; Wang, S.X.; Sun, S. One-pot synthesis of monodisperse iron oxide nanoparticles for potential biomedical applications. *Pure and Applied Chemistry* **2006**, *78*, 1003-1014, doi:doi:10.1351/pac200678051003.
40. Yu, H.; Chen, M.; Rice, P.M.; Wang, S.X.; White, R.L.; Sun, S. Dumbbell-like bifunctional Au-Fe3O4 nanoparticles. *Nano Lett* **2005**, *5*, 379-382, doi:10.1021/nl047955q.
41. Efremova, M.V.; Naumenko, V.A.; Spasova, M.; Garanina, A.S.; Abakumov, M.A.; Blokhina, A.D.; Melnikov, P.A.; Prelovskaya, A.O.; Heidelmann, M.; Li, Z.-A., et al. Magnetite-Gold nanohybrids as ideal all-in-one platforms for theranostics. *Scientific Reports* **2018**, *8*, 11295, doi:10.1038/s41598-018-29618-w.

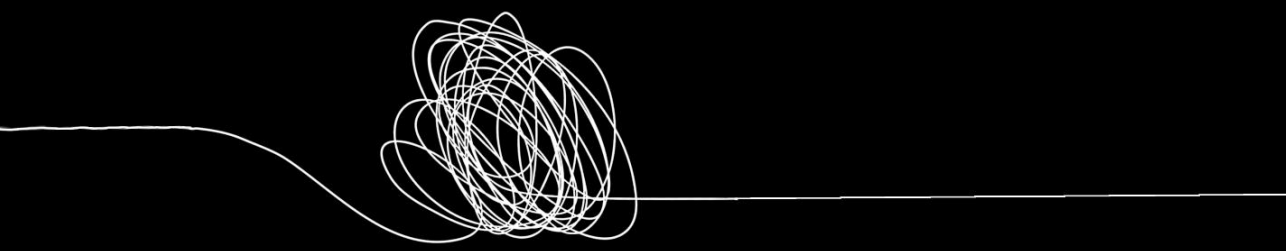

Tuning the magnetic properties and surface functionalization of Pd/Fe-oxide nanoparticles towards application in image-assisted thermo-brachytherapy

3

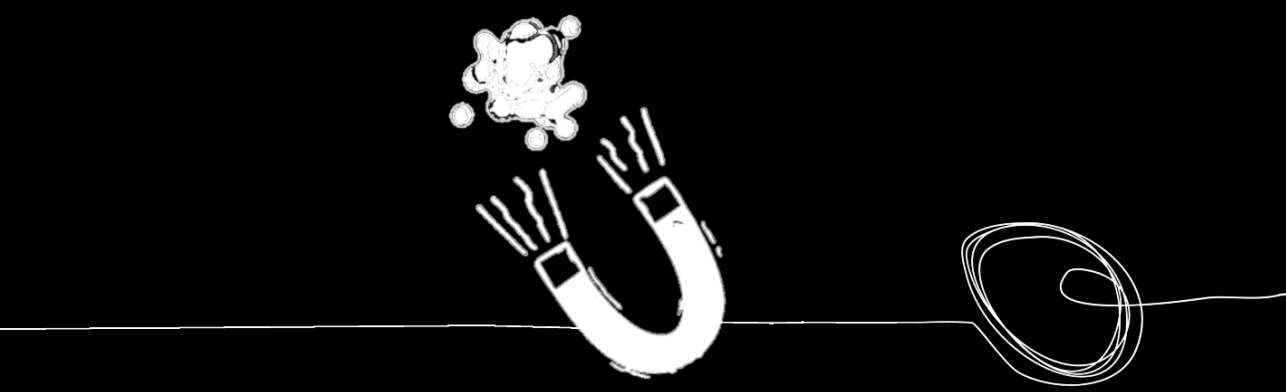

Abstract: Hybrid magnetic nanoparticles have been of high interest for biomedical applications, due to their ability to incorporate multiple functionalities in a single nanostructure, which makes them promising candidates for revolutionizing the field of theranostics for cancer treatment. Such magnetic hybrid NPs can simultaneously deliver therapy and allow following the treatment effects by imaging. However, they must possess specific magnetic properties for the desired applications, non-toxicity and stability in biologic environments. The magnetic properties are dependent on the characteristic parameters of the hybrid MNPs, and their non-toxicity and stability on their functionalization, therefore, an increased attention to the design of hybrid MNPs must be paid. Here, we investigated the magnetic properties via SQUID measurements of multiple batches of hydrophobic Pd/Fe-oxide NPs previously synthesized. Subsequently, we looked at the dependency of the magnetic parameters such as saturation magnetization, coercivity, and blocking temperature on the characteristics of the hybrid MNPs, with increased attention to the influence of the non-magnetic Pd component that disrupts the iron oxide lattice. Additionally, different surfactant modification techniques were assessed to render the Pd/Fe-oxide NPs water dispersible with satisfying colloidal stability. The Pd/Fe-oxide NPs modified via an additional molecular layer with a PEG-surfactant (DSPE-PEG_{2000}-COOH) provided the best results. Lastly, the performance in magnetic hyperthermia/thermal ablation and magnetic resonance imaging of the Pd/Fe-oxide NPs batches with the best magnetic properties in terms of saturation magnetization were tested and Pd/Fe-oxide NPs with sizes around 21 nm were deemed as best candidates.

Keywords: hybrid magnetic nanoparticles, iron oxide, palladium, superparamagnetism, surface exchange, heating power, relaxivity.

The content of this chapter has been published in:

Maier A, van Oossanen R, van Rhoon GC, Pignol JP, Dugulan I, Denkova AG, Djanashvili K. From Structure to Function: Understanding Synthetic Conditions in Relation to Magnetic Properties of Hybrid Pd/Fe-Oxide Nanoparticles. Nanomaterials (Basel). 2022 Oct 18;12(20):3649.

doi: 10.3390/nano12203649. PMID: 36296839; PMCID: PMC9612236.

3.1 Introduction

Magnetic nanoparticles (MNPs) represent an important branch of nanomaterials that enable interesting applications in many fields, and especially, in biomedicine.[1,2] The main research on MNPs concerns their analytical and therapeutic applications, such as separation and purification,[3-5] biosensing,[6-8] magnetic resonance imaging (MRI),[9-13] delivery of targeted drugs and active biocompounds,[14-18] and hyperthermia/thermal ablation.[12,19-21] Small sized MNPs translate into large surface-to-volume ratios, which is the reason behind their unique magnetic properties compared to those found in the corresponding bulk materials.[1,22] Consequently, the inherent magnetism and behaviour under the influence of an external magnetic field, is what makes them particularly attractive for biomedical applications.[23] The key challenge in design of such MNPs is not only to endow them with the desired magnetic properties, but not less importantly, to ensure their non-toxicity and stability in biological environment.[24] From this point of view, magnetic iron oxide NPs (usually magnetite Fe_3O_4 or maghemite γ-Fe_2O_3) are of high interest because of their interesting magnetic properties, non-toxicity and high biocompatibility. Iron oxide NPs, especially in their superparamagnetic regime (SPIONs), i.e., no magnetism once the external field is removed, are increasingly prominent in the biomedical field.[1,25]

The magnetic properties of iron oxide NPs govern their heating efficiency for hyperthermia/thermal ablation as well as their relaxivities (relaxation rate enhancement per mM of iron) and hence the efficacy as contrast agents for MRI.[26-28] Importantly, these magnetic properties of MNPs are determined by the characteristic parameters, such as size, shape and composition,[1,26,28] which must be considered during the design of materials for an intended application, bearing in mind that all these parameters are interdependent.

Nowadays, the paradigm of research in biomedicine is switching its focus towards hybrid MNPs, composed of two or more distinctive parts in a single entity with the potential to gain superior performances that are difficult to achieve by simply mixing the individual constituents. The final properties of hybrid MNPs are again dependent on the aforementioned parameters (size, shape, composition), but additionally, on the

spatial organization, distribution of each constituent, and the interface between the components.[29,30] Coupling of MNPs with both magnetic and non-magnetic components inevitably affects the magnetic properties. Thus, rational design and well-regulated synthesis of hybrid MNPs are essential in facilitating the fine-tuning of their functional properties. Among possible chemical routes for production of hybrid MNPs, thermal decomposition methods are usually preferred, as they provide great morphological control and narrow size-distributions. However, the as-obtained products are usually capped with hydrophobic ligands, such as oleic acid, hence dispersion in aqueous media necessary for biomedical use is limited, and the MNPs require additional manipulation at their surface, that leads to improved biocompatibility.[22]

In this thesis, we focus on multifunctional, biocompatible, theranostic MNPs composed of non-magnetic Pd-core and magnetic iron oxide shell. This hybrid magnetic nanosystem is intended to simultaneously enable diagnosis (MRI) and therapy to effectively treat tumours by means of combined hyperthermia/thermal ablation and ^{103}Pd-based radiotherapy. Investigation of synthetic routs leading to hybrid NPs with various morphological features was described in chapter 2. This chapter describes the magnetic properties of the multiple batches of Pd/Fe-oxide NPs and discusses the correlations with the characteristic parameters of these MNPs, paying specific attention to the presence of the non-magnetic Pd-core. The Pd/Fe-oxide NPs are hydrophobic post synthesis, hence, different functionalization methods were investigated to render the hybrid MNPs water dispersible and the effects of surface functionalization were assessed. Lastly, the magnetic properties were brought in relation with the best performance in magnetic hyperthermia/thermal ablation and MRI, determining the best Pd/Fe-oxide NPs candidates for image-assisted thermo-brachytherapy.

3.2 Materials and methods

Reagents

Hexane, acetone, trimethylamine, 2,3-dimercaptosuccinic acid (DMSA). 1,2-distearoyl-sn-glycero-3-phosphoethanolamine-N-[carboxy(polyethylene glycol)-2000] (sodium salt) DSPE-PEG$_{2000}$-COOH, powder; 1,2-distearoyl-sn-glycero-3-phosphoethanol amine-N-[methoxy(polyethylene glycol)-2000], DSPE-mPEG$_{2000}$ (ammonium salt), chloroform solution 25 mg/mL; 1,2-distearoyl-sn-glycero-3-phosphoethanolamine-N-[amino(polyethylene glycol)-2000] (ammonium salt), DSPE-PEG$_{2000}$-NH$_2$, powder; 1,2-distearoyl-sn-glycero-3-phosphoethanolamine-N-[amino(polyethylene glycol)-5000] (ammonium salt), DSPE-PEG$_{5000}$-NH$_2$, powder, were purchased from Avanti Lipids.

Preparation of water-dispersible Pd/Fe-oxide NPs

Dispersion of Pd/Fe-oxide NPs in aqueous media with DMSA. The previously synthesized Pd/Fe-oxide NPs were transferred into water by functionalization with DMSA following a slightly modified protocol presented elsewhere.[2] Briefly, 10 mg dry powder of oleic acid (OA) capped Pd/Fe-oxide NPs dispersed in 3.3 mL hexane and 10 mg DMSA dispersed in 3.3 mL acetone were added into a three-neck round bottom flask together with 5 μL trimethylamine. The mixture was brought to reflux in nitrogen atmosphere under stirring and kept under reflux for 4 h at 44 °C. Black precipitate that appeared at the bottom of the flask was collected by disposing the solvent and drying the precipitate with gentle nitrogen flow. The remaining dried NPs powder was redispersed in 20 mL deionized water and further purified by dialysis (MW cutoff 12-15 kDa) against deionized water for 1 day.

Dispersion of Pd/Fe-oxide NPs in aqueous media with DSPE-PEG$_{2000}$-COOH. The previously synthesized Pd/Fe-oxide NPs were transferred into water by means of functionalization with DSPE-PEG$_{2000}$-COOH/DSPE-mPEG$_{2000}$/DSPE-PEG$_{2000}$-NH$_2$/ DSPE-PEG$_{5000}$-NH$_2$ following a slightly modified protocol presented elsewhere.[31] Briefly, 1 mg of OA-capped Pd/Fe-oxide NPs were dispersed via ultrasonication in 1 mL chloroform containing 1.5 mg of PEG surfactant. The vial containing the mixture

was then left open for 24–48 h for the slow evaporation of the solvent, until a pasty precipitate remained at the bottom of the vial. The residual solid was heated to 80 °C for 10 min in a vacuum oven to ensure complete removal of chloroform. Next, 1 mL of Milli-Q water was added to the precipitate and sonicated for 15 min until a colloidal suspension in aqueous media was obtained. The colloidal suspension of NPs was pipetted into Eppendorf vials and the unbound polymer and excess lipids were removed by centrifugation for 1 h at 19,600 RPM (30,000 ×*g*) and subsequent removal of the supernatant. This procedure was repeated twice. Lastly, the NPs were collected in 1–2 mL of Milli-Q water in an Eppendorf and kept as such for further use.

Characterization

Magnetic characterization by superconducting quantum interference device (SQUID), was carried out on an MPMS XL magnetometer from Quantum Design, using about 1–2 mg of dried NPs powder. The hysteresis loops M(H) obtained under continuously varying applied magnetic field up to a maximum of ±50 kOe at 5 K and 300 K were used for evaluation of saturation magnetization (M_s) and coercivity (H_c). Zero-field-cooling (ZFC) and field-cooling (FC) magnetization curves were measured at 1 kOe in the temperature range 5–370 K. The sample was cooled from 370 K down to 5 K in the absence of magnetic field. Once the lowest temperature was reached, magnetic field was set to 1 kOe and magnetization was measured as the temperature was increased to obtain the ZFC curve. When back at high temperatures, the sample was cooled down again while a magnetic field was applied. The magnetic NPs were progressively blocked along the magnetic field axis, and the FC magnetization was measured. The blocking temperature (T_B) was determined as the maximum on the ZFC curve.

Transmission ^{57}Fe Mössbauer spectra were collected at 300 K with a conventional constant-acceleration spectrometer using a ^{57}Co (Rh) source. Velocity calibration was done using an α-Fe foil. The spectra were fitted using the Mosswinn 4.0 program.[32]

The heating power measurements were performed using the Magnetherm Digital, manufactured by Nanotherics, using a 50 mm coil device. All SLP values were measured using an alternating magnetic field with a frequency of 346 kHz and a field strength of 23 mT. Two glass-fibre optic thermometers were used for temperature

measurement [Osensa PRB-G40_2.0M-STM-MRI] to measure both the core and bottom temperature of the sample. The core temperature measured was used for SLP calculations. For determination of SLP, a sample of 1 mL of NPs in suspension was inserted in an isolated sample holder, to reduce heat loss to the environment, and placed in the middle of the coil. The temperature was equilibrated until it varied less than 0.05 °C/min before the measurement was conducted. The sample was then exposed to the magnetic field.

The hydrodynamic radius of the differently PEG-functionalized Pd/Fe-oxide NPs was determined by dynamic light scattering (DLS) which consisted of a JDS uniphase 633 nm 35 mW laser source, an ALV sp 125 s/w 93 goniometer, a fibre detector and a Perkin Elmer photo counter.

Thermogravimetric analysis (TGA) was performed on a Perkin Elmer thermogravimetric analyser from 30 to 850 °C (heating rate 10 °C/min) under air atmosphere on approx. 2 mg powder NPs obtained via freeze-drying of aqueous dispersions of PEG-functionalized Pd/Fe-oxide NPs.

Transversal relaxation times (R_2) of water protons in the presence of magnetic NPs were measured on a Bruker Avance-300 NMR using Carr-Purcell-Meiboom-Gill (CPMG) pulse sequence with variable spin-echo train and echo time of 0.5 ms.

The SLP-values and r_2-relaxivities of the samples were calculated using the concentrations of iron obtained from the ICP-OES data performed on the same samples after destruction of NPs.

3.3 Results and discussion

Magnetic properties of Pd/Fe-oxide NPs as a function of their morphology

Defining the optimal synthetic conditions leading to hybrid Pd/Fe-oxide nanocrystals with characteristics suitable for hyperthermia and MR imaging involves understanding the associated magnetic properties, and especially, their correlation with geometric data. Not less important is the possibility of the NPs to interact with each other due to magnetic dipole interactions, which can impact the collective magnetic response.[33] The static magnetic behaviour of the prepared NPs was investigated by SQUID magnetometry. The measurements were conducted on the batches of hybrid NPs as-obtained from the thermal decomposition synthesis and subsequent cleaning procedure (see Table 2.1), hence coated with OA and in powder form. Magnetization curves resulting from alignment of NPs in the presence of an increasing magnetic field (up to 50 kOe) were measured at 300 and 5K, as presented in Figures 3.1A and 3.1B, respectively. The saturation magnetization (M_S) could be determined by extrapolating the highest magnetization values to the ordinate axis, where the field approaches zero (Table 3.1). These values were found to be lower compared to the bulk magnetite (92 emu/g)[34] but corresponding to those of the NPs with sizes around 20 nm,[35] and close to the value of 84.5 emu/g measured from commercial magnetite fine powder.[36] The presence of Pd-core and organic layer at the surface were not accounted for, and therefore, it should be noted that the real M_S values expressed in emu/g of NPs should actually be higher. The magnetization curves measured at 5K display a hysteretic behaviour with substantial coercivities and remanence (Figure 3.1A-inset and Table 3.1). This indicates typical behaviour of superparamagnetic NPs below their blocking temperature (T_B), above which the thermal fluctuations randomize magnetic moments leading to decreased M_S values as well as coercivities (Figure 3.1B-inset). As the result, at 300K the NPs exhibit characteristics of the superparamagnetic state, while the presence of some remained coercivities (Table 3.1) can be attributed to the complex interactions, such as frustrated order or spin canting phenomena, described for the surface functionalized core–shell structures.[37]

Furthermore, the saturation magnetization of Pd/Fe-oxide NPs increases with the size of the nanocrystals (Figure 3.1C), which agrees with the literature.[1] Notably, this behaviour fails for certain Pd/Fe-oxide batches, which can be explained by the shape variations of these NPs. Therefore, the M_S values for the 'exotically' shaped Exp_flower-like and Exp_popcorn-like NPs were excluded from comparison, as it is hard to determine their relevant average size. Moreover, it is challenging to draw an exact correlation between M_S and shape for the NPs with dissimilar volumes of Fe-oxide content.[1]

Table 3.1. Overview of the magnetic properties of Pd/Fe-oxide NPs (batches prepared as presented in Table 2.1). Saturation magnetization (M_S) at 50 kOe, T = 5 K and 300 K, coercivity (H_C) at T = 5 K and 300 K, and determined blocking temperature (T_B). Calculated SLP, ILP and r_2 values.

Sample	**Saturation Magnetization (M_S) (emu/g)**		**Coercivity (H_C) (Oe)**		**T_B (K)**	**SLP [a] (W/g_{Fe})**	**ILP (nHm^2/kg)**	**r_2 [b] ($mM^{-1}\ s^{-1}$)**
	5K	**300K**	**5K**	**300K**				
Exp_standard	67.9	58.7	20	8	180	113	0.975	220
Exp_flower-like	53.1	45.4	270	31	120	-[c]	-[c]	-[c]
Exp_popcorn-like	58.5	49.0	427	6	>370	-[c]	-[c]	-[c]
Exp_10 mg	69.2	61.4	67	12	200	233	2.011	440
Exp_nDS	62.7	56.3	26	8	100	-[c]	-[c]	-[c]
Exp_3 °C	52.1	45.1	287	8	40	-[c]	-[c]	-[c]
Exp_7 °C	63.7	57.5	213	6	130	102	0.880	90
Exp_[surf]/[Fe] = 2	26.4	20.5	466	10	30	2	0.017	-[c]
Exp_[surf]/[Fe] = 11	62.4	55.8	81	4	120	-[c]	-[c]	-[c]
Exp_DPE	36.9	28.1	236	19	23	-[c]	-[c]	-[c]
Exp_ODE:DPE (1:1)	46.5	39.9	56	9	120	-[c]	-[c]	-[c]
Exp_DBE	63.6	55.4	13	4	160	-[c]	-[c]	-[c]

[a] Measured at 346 kHz, 23 mT; SLP error ≤ 5%; [b] measured at 9.4 T and 25 °C; [c] not measured.

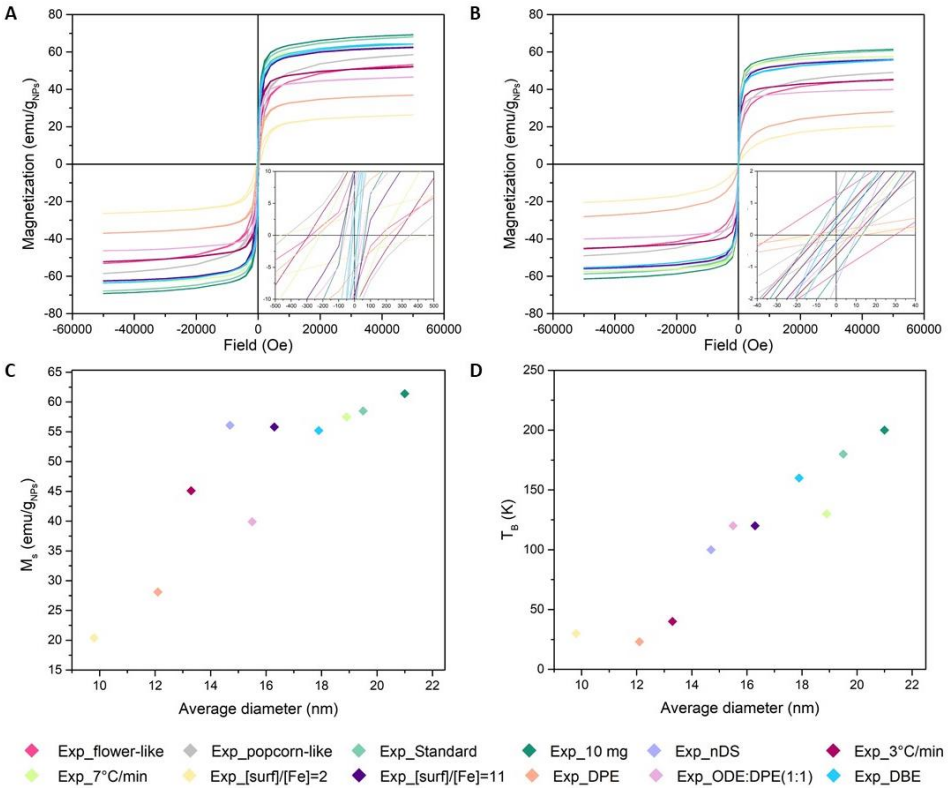

Figure 3.1. SQUID magnetometry of dry Pd/Fe-oxide NPs batches prepared under conditions summarized in Table 3.1: (**A**) M(H)$_T$ curves measured at T = 5 K; the inset represents 120× magnification of the *x*-axis showing coercivities (H_c); **(B)** M(H)$_T$ curves measured at T = 300 K; the inset represents 1500× magnification of the *x*-axis showing coercivities (H_c); (**C**) derived M_S at 300 K as a function of the average diameter; (**D**) T_B as a function of the average diameter of NPs.

Similarly, T_B (vide infra) is generally found to be proportional to the NPs volume/size.[1] This is a trend that we generally observe for our Pd/Fe-oxide NPs (Figure 3.1D) but once again, with certain exceptions. Moreover, we also need to consider the effect of dipolar interactions on the determined T_B, as the NPs cannot be assumed to be fully isolated.

More insights into the interparticle dipolar interactions could be obtained by measuring magnetization as a function of temperature under zero-field-cooling (ZFC) and field-cooling (FC) conditions (Figure 3.2). The Pd/Fe-oxide NPs were cooled from 370 K to 5 K in the absence of magnetic field after which a small magnetic field (1 kOe) was applied.

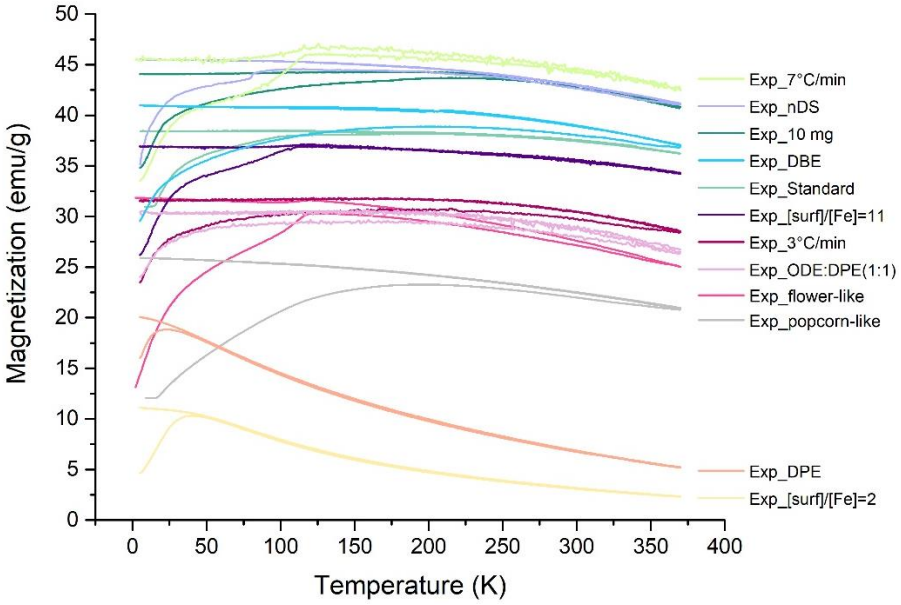

Figure 3.2. ZFC/FC-curves of the Pd/Fe-oxide NPs samples (abbreviations explained in Table 3.1) measured at 1 kOe.

As the temperature increased ($T < T_B$), the magnetic moments aligned along the direction of the field and the maximum magnetization was reached. This typical maximum in the ZFC-curve lays around the T_B, which can then be calculated as the first derivative of zero magnetization (Table 3.1).[38]

In some cases, such as for Exp_flower-like and Exp_popcorn-like NPs, the T_B is distributed over a certain temperature range, due to the size irregularities and interparticle interaction. The latter can also be concluded from the bifurcation of ZFC/FC curves above the T_B observed in several batches, except for Exp_standard, Exp_[surf]/[Fe] = 2, Exp_[surf]/[Fe] = 11, and Exp_DPE. At $T > T_B$, the thermal energy exceeds that of the magnetic field, causing a random flip of magnetic moments, hindering a further increase in the measured magnetization. Thereby, the profiles of superparamagnetic NPs are characterized with a steep decrease in magnetization (e.g., Exp_DPE and Exp_[surf][Fe] = 2).

As the transition magnetic NPs from single to multi-domain is expected at a critical diameter of 30–90 nm, depending on the size, shape, and magneto-crystalline anisotropy[39], we expect all batches of Pd/Fe-oxide, with Exp_popcorn-like as a possible exception, to be superparamagnetic/single domain. Indeed, all NPs present

T_B much smaller than room temperature, therefore, all Pd/Fe-oxide batches synthesized are in their superparamagnetic/single domain regime at room temperature.

It is important to note that most studies presenting magnetic behaviour of NPs are based on homogeneous Fe-oxide nanocrystals. Magnetic properties arise in the presence or absence of unpaired valence electrons and the distribution of cations in tetrahedral (A) and octahedral (B) sites within the inverse spinel crystal structures, such as magnetite (Fe_3O_4) and maghemite (Fe_2O_3).[1] The presence of a second element, Pd in our case, influences the magnetic properties,[40] and can be another reason why typical correlations fail for certain Pd/Fe-oxide NPs. Therefore, at this point it becomes interesting to take a closer look at the composition/crystallinity of the NPs, as magnetic properties can be influenced by (i) the ratio of low-magnetization maghemite to high-magnetization magnetite, and (ii) alteration of the chemical composition caused by OA bound strongly via its two carboxylic oxygen atoms leading to magnetically inhomogeneous surface.[41]

The Mössbauer spectroscopy conducted on the NPs at 300K (Figure 3.3) reveals the hyperfine parameters determined by the position of Fe-ions within different lattice positions (Table 3.2). The first indication on the chemical composition at the A- and B-sites of magnetite can be derived from the isomeric shifts (IS). The charges of Fe^{2+} and Fe^{3+} ions at the octahedral B-site are delocalized and averaged to $Fe^{2.5+}$ with IS of 0.67 mm s^{-1} expected for bulk magnetite. Therefore, the IS values measured for B-sites within the lattice that deviate downwards directly indicate the substitution of Fe^{2+} by Pd^{2+}. With increasing Pd substitution levels (and decreasing B-site IS values)—the spectral contribution of the octahedral site is expected to decrease compared to the measured value in bulk magnetite (67%). This is indeed observed with samples Exp_10mg, Exp_nDS and Exp_7 °C, although the presence of small amounts of maghemite (overlapping with the A-site) cannot be excluded at this stage. In samples Exp_standard and Exp_flower-like the opposite effect is detected (in correlation with higher B-site IS values)—indicating substitution of Pd also at the A-site (preferentially). As the Mössbauer parameters do not directly correlate to the observed magnetic properties—it is conceivable that an optimum Pd substitution degree is achieved in the better performing Pd/Fe-oxide NPs. The presence of

magnetite in sample Exp_nDS rather than maghemite detected for Exp_ODE:DPE(1:1) can explain the higher saturation magnetization of the smaller NPs (56.1 emu/g, 15 nm) compared to the bigger ones (39.9 emu/g, 16 nm). Additionally, the magnetite composition of the largest NPs (Exp_10mg (21 nm), Exp_standard (20 nm), and Exp_7 °C (19 nm) was confirmed based on the spectral contribution values (Table 3.2).

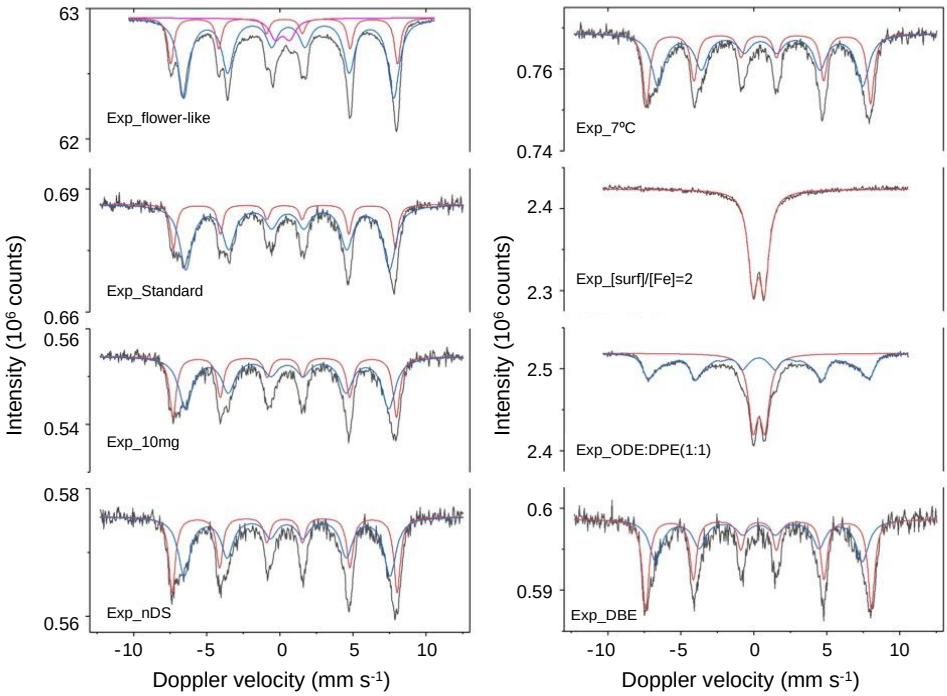

Figure 3.3. Mössbauer spectra of Pd/Fe-oxide NPs at 300 K.

Finally, the high crystallinity derived from the small Mössbauer line widths (Γ), the reasonably high M_S values saturating at relatively low fields, and the favourable hysteresis loops (especially of Exp_10mg, Exp_standard and Exp_7 °C NPs) suggest that the samples are of high magnetic quality, making them well suited for potential biomedical applications.[42]

Table 3.2. The Mössbauer fitted parameters of Pd/Fe-oxide NPs at 300 K.

Sample	Phase	IS (mm s^{-1})	QS (mm s^{-1})	Hyperfine Field (T)	Γ (mm s^{-1})	Spectral Contribution (%)
Exp_standard	Fe^{3+} (Fe_3O_4, A)	0.32	−0.01	47.2	0.46	24
	$Fe^{2.5+\delta}$ (Fe_3O_4, B)	0.54	−0.01	43.3	1.03	76
Exp_flower-like	Fe^{3+} (Fe_3O_4, A)	0.31	−0.02	48.2	0.50	22
	$Fe^{2.5+\delta}$ (Fe_3O_4, B)	0.60	0.02	44.6	0.93	70
	Fe^{3+} (SPM)	0.19	0.98	-	0.95	8
Exp_10mg	Fe^{3+} (Fe_3O_4, A)	0.34	−0.02	47.5	0.57	38
	$Fe^{2.5+\delta}$ (Fe_3O_4, B)	0.50	−0.01	43.2	1.12	62
Exp_nDS	Fe^{3+} (Fe_3O_4, A)	0.33	−0.01	47.8	0.53	41
	$Fe^{2.5+\delta}$ (Fe_3O_4, B)	0.49	0.02	43.7	0.99	59
Exp_7 °C	Fe^{3+} (Fe_3O_4, A)	0.34	−0.02	47.7	0.56	42
	$Fe^{2.5+\delta}$ (Fe_3O_4, B)	0.46	−0.03	43.6	1.07	58
Exp_[surf]/[Fe] = 2	Fe^{3+} (SPM)	0.33	0.79	-	0.78	100
Exp_ODE:DPE(1:1)	Fe^{3+} (SPM)	0.36	0.80	-	0.74	41
	Fe^{3+} (γ-Fe_2O_3)	0.34	−0.02	45.6	0.68	59
Exp_DBE	Fe^{3+} (γ-Fe_2O_3)	0.33	−0.01	48.1	0.55	53
	Fe^{3+} (γ-Fe_2O_3)	0.36	−0.01	44.0	1.04	47

Experimental uncertainties: Isomer shift: I.S. ± 0.02 mm s^{-1}; Quadrupole splitting: Q.S. ± 0.02 mm s^{-1}; Line width: Γ ± 0.03 mm s^{-1}; Hyperfine field: ± 0.1 T; Spectral contribution: ± 3%.

Surface modification of Pd/Fe-oxide NPs and resulting magnetic properties

The surface effects on magnetic properties of NPs become more significant with decrease of their sizes, as the fraction of surface atoms vs bulk atoms increases, hence enhanced attention is required during surface functionalization procedures.[43] As previously shown, the investigation of magnetic properties for multiple batches of Pd/Fe-oxide NPs was conducted on the NPs in powder form, as obtained from the thermal decomposition synthesis and the subsequent cleaning procedure, functionalized with OA-molecules. Oleic acid surfactant is widely employed in the preparation of ferrite NPs, as it can form a dense protective monolayer during the synthesis, which leads to highly uniform and monodisperse particles. Studies of Wu et al.[44] and Zhang et al.[45] showed that OA is chemisorbed on the particle surface via carboxylates with non-polar methyl end-groups exposed in the solution. This surface arrangement endows the OA-capped NPs with hydrophobicity that explains the

excellent dispersibility in non-polar solvents. Enabling the final NPs for *in vitro* and *in vivo* studies requires aqueous media. Therefore, the hydrophobic NPs must be chemically functionalized with hydrophilic inorganic compounds (e.g., silica) or organic functional polymers, such as polyethylene glycol (PEG), polyvinyl alcohol (PVA), polylactic acid (PLA), polyvinylpirrolidone (PVP) in order to facilitate their dispersion and stability in aqueous media and minimize aggregation. For such phase-transfer of NPs to aqueous media three strategies are generally employed, namely (i) ligand exchange, (ii) ligand modification, and (iii) additional coating layers.[46] Next to improving colloidal stability, the surface-active compounds play an important role in determining the biocompatibility and non-toxicity of the NPs, their *in vivo* biodistribution and in preventing their premature biological clearance after intravenous or intratumoral administration.[22] All these benefits of surface modification come with one key requirement: preservation of magnetic properties responsible for heating and imaging performance, which are known to be affected by the coating, regardless of its type.[22,24,47,48] The magnetic structure present at the nanoparticles' surface layer is usually significantly different from that in the nanoparticles' core. It is suggested that the total magnetization of the nanoparticle is comprised of a component due to the core of the particle and one due to the surface spins.[22] On the surface of the nanoparticle, the organic ligands are changing the anisotropy and the magnetic moments. Therefore, as the chemical environment of the coating shell influences the magnetic properties of the surface ions, i.e. it could have a notable effect on the overall magnetic performance.[49-51] Plenty of the studies in literature report a reduced magnetization for NPs coated with non-magnetic layers.[1,26,28,52]

To transfer the OA-capped Pd/Fe-oxide NPs into water-phase, a well-known ligand exchange method was adopted in the first place. The principle behind ligand exchange is that the molecules stabilizing the NPs in the original phase are replaced by other, ideally more strongly binding ligand molecules that would enable the transfer to the desired phase and provide high colloidal stability. In our case, the hydrophobic OA ligand molecules present on the surface of Pd/Fe-oxide NPs as-obtained from a batch of Exp_standard, were replaced by hydrophilic DMSA surfactant molecules through ligand exchange strategy, following a slightly modified

procedure presented by Song et al.[2] After the ligand exchange with DMSA procedure was performed, the Pe/Fe-oxide NPs were dispersed in water. As a first step, the shelf-life of the NPs was checked, by leaving the colloidal water dispersion in a glass vial overnight without stirring or moving. As no obvious precipitation was noticed by naked eye, the surfactant exchange step was considered satisfactory. Further on, investigation of magnetic properties via SQUID magnetometry was conducted on the DMSA-capped Pd/Fe-oxide NPs to assess the magnetic properties after the ligand exchange procedure. For comparison, hysteresis loops of a batch of Pd/Fe-oxide NPs from Exp_standard, coated with OA and DMSA, respectively, were recorded at 5K. The measurements were performed on the NPs in powder form in both cases, as obtained post-cleaning after the thermal decomposition synthesis of OA-capped hybrid NPs, and after freeze-drying the DMSA-capped Pd/Fe-oxide NPs suspension in water. As a result, a sharp decrease in the M_s value from 64.7 emu/g_{NPs} to 35.5 emu/g_{NPs} was recorded for DMSA-capped Pd/Fe-oxide NPs when compared to the as-synthesized OA-capped Pd/Fe-oxide NPs (Figure 3.4A).

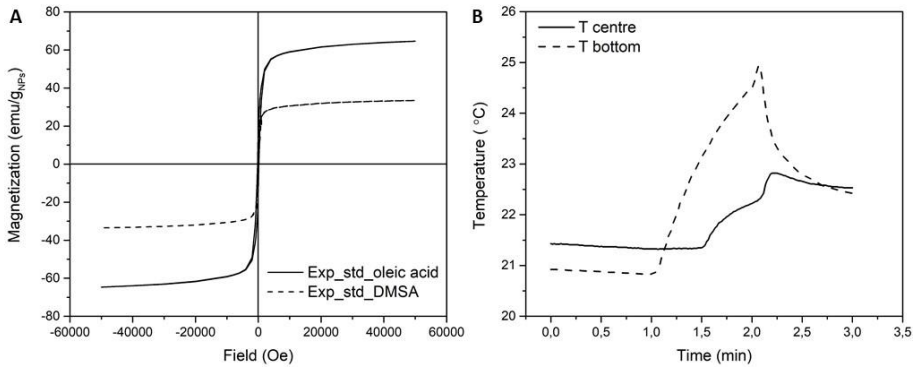

Figure 3.4. (**A)** SQUID magnetometry of dry Pd/Fe-oxide NPs from a batch of Exp_standard before and after ligand exchange, $M(H)_T$ curves measured at 5 K; **(B)** Heating profile (AMF of 346 kHz, 23 mT) of DMSA-capped Pd/Fe-oxide NPs from a batch of Exp_Standard.

These findings agree with literature reporting a decrease in M_s post surface modification for phase transfer of NPs to aqueous media.[1,26,28,52]

Nevertheless, the next step was to assess the heating capability of the DMSA-coated Pd/Fe-oxide NPs. A sample containing the hybrid NPs dispersed in water was exposed to AMF at the frequency of 346 kHz and a field strength of 23 mT, while the

temperature profile over time (Figure 3.4B) was recorded for three-time intervals: before (0-1 min), during (1-2 min) and post AMF exposure (2-3 min). During the heating measurement, the temperature was recorded by two different probes, one placed in the centre of the sample, and one at the bottom of the vial. In case of a good colloidal dispersion, the temperatures recorded in both points of the sample should coincide, as the NPs concentration is consistent throughout the sample. However, this was not the case, as the temperature recorded at the bottom was considerably higher than that at the centre, which is a strong indication of NPs sedimentation. The stability of a colloidal system is defined by its resistance to aggregate and remain in suspension, defined by the balance between the attractive and repulsive forces once the NPs come in close proximity to each other.[53] When the attractive forces overcome the repulsive ones, the NPs will aggregate and sediment. To tackle this problem, the DMSA-capped Pd/Fe-oxide NPs were dispersed in water containing either 0.5% xanthan or 2% agar, both added to increase sample viscosity and prevent agglomeration and subsequent sedimentation of the NPs. From the temperature profiles recorded during exposure of the NPs dispersion with xanthan at the same conditions as before, it can be concluded that addition of xanthan was not sufficient to prevent sedimentation as the temperature at the bottom of the sample was still increasing at a higher rate than that recorded at the centre (Figure 3.5A).

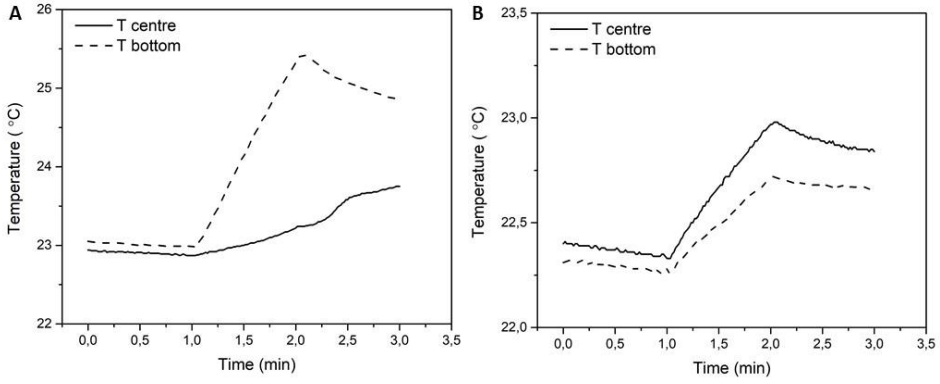

Figure 3.5. Heating graphs (346 kHz, 23 mT) of DMSA-capped Pd/Fe-oxide NPs from a batch of Exp_standard in water **(A)** with 1 mL of 0.5% xanthan solution and **(B)** with 2% agar solution.

In contrast, the presence of 2% agar facilitated stable dispersion of NPs, evident from the heating profiles where the temperature in the centre is higher than that measured at the bottom of the sample vial (Figure 3.5B). However, the maximum temperature rise was very low (23 °C), which may be because of the aggregation that occurs immediately after dispersion of DMSA-capped Pd/Fe-oxide NPs in water and before addition of agar, or because of the too high viscosity of the sample. Additionally, a significant decrease in M_s recorded for the DMSA-capped Pd/Fe-oxide NPs was observed, and it is known that heating efficiency is proportional to the NPs magnetic properties. Overall, considering the sharp decrease in M_s value and the poor colloidal stability in water of the resulted NPs post DMSA ligand exchange, it was concluded that the DMSA-capped Pd/Fe-oxide NPs are not satisfactory for the desired applications of this thesis, and another surfactant modification technique was investigated.

The next surfactant modification strategy for Pd/Fe-oxide NPs (batch of Exp_10mg) involved introduction of an additional molecular layer, that adsorbs on the original ligand molecules (OA) and changes the surface properties accordingly. In this manner, a ligand bilayer is formed, which allows the transfer of the hydrophobic nanoparticles from organic solvents to aqueous media. This procedure requires an amphiphilic molecule, comprised of both hydrophobic and hydrophilic parts, acting as a phase-transfer agent. The hydrophobic tail intercalates in between the OA surfactant molecules bound to the NPs, leaving the hydrophilic part exposed, thereby rendering the NPs dispersible in water.[28] As PEG-coating strategies are the most used for biomedical applications,[50] DSPE-PEG_{2000}-COOH consisting of hydrophobic lipid and hydrophilic PEG-chains and polar carboxylic end-group was the first amphiphilic PEG surfactant used. The same NPs (Exp_10mg) were functionalized with three additional surfactants (DSPE-$mPEG_{2000}$, DSPE-PEG_{2000}-NH_2 and DSPE-PEG_{5000}-NH_2) and compared with DSPE-PEG_{2000}-COOH (see Figure 3.6 for the chemical structures) to identify the best performance in terms of colloidal stability, preservation of magnetic properties and heating ability. The shelf-life of the surface modified NPs was assessed visually and by DLS over the period of 1 week (Figure 3.7).

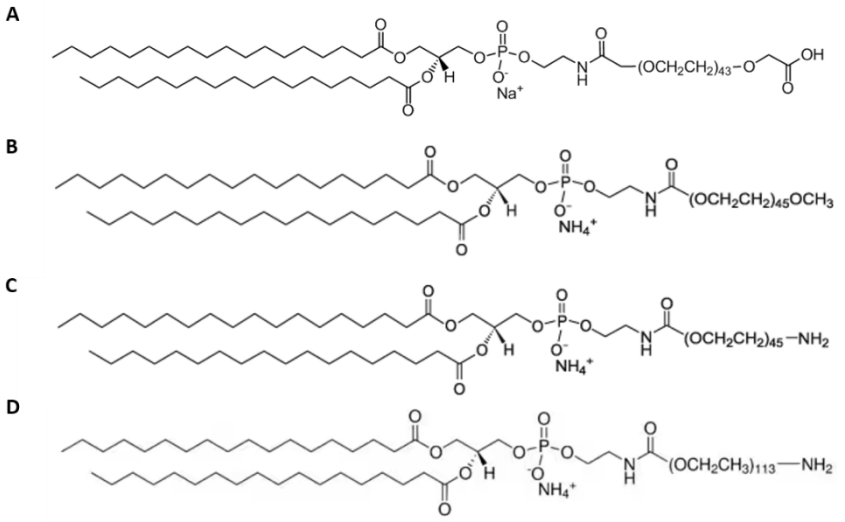

Figure 3.6. Chemical structures of the PEG-polymers used to functionalize the Pd/Fe-oxide NPs: **(A)** DSPE-PEG$_{2000}$-COOH; **(B)** DSPE-mPEG$_{2000}$; **(C)** DSPE-PEG$_{2000}$-NH$_2$; **(D)** DSPE-PEG$_{5000}$-NH$_2$.

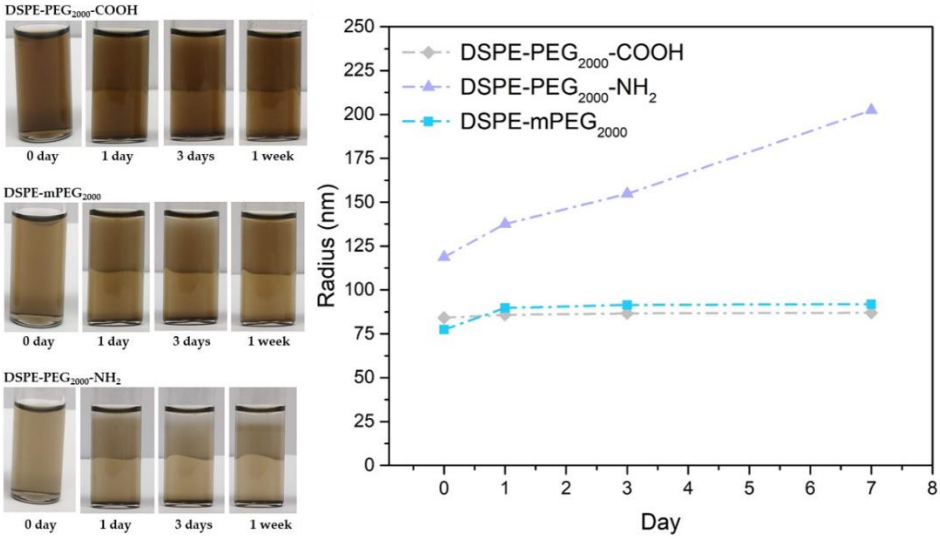

Figure 3.7. Shelf-life (left, photographic images (the apparent phase-separation is actually the paper/table background transition)) and DLS measurements (right) of aqueous suspensions of Pd/Fe-oxide NPs (Exp_10mg) functionalized with different surfactants, monitored over 7 days.

The colloidal systems looked overall stable, with DSPE-PEG$_{2000}$-NH$_2$ as an exception, where minor NPs sedimentation could be noticed over time. Another problem was noticed for DSPE-PEG$_{5000}$-NH$_2$-capped Pd/Fe-oxide NPs that became unstable and

quite viscous at higher concentrations, which is not surprising considering the increase from 2000 to 5000 PEG-units. The satisfactory visual colloidal stability of the PEG-functionalized Pd/Fe-oxide NPs was further confirmed by DLS measurements (Figure 3.7). No increase in size was found for Pd/Fe-oxide NPs functionalized with DSPE-PEG_{2000}-COOH and DSPE-$mPEG_{2000}$, while the DSPE-PEG_{2000}-NH_2 functionalized NPs showed an increase in size over time, indicating unsatisfactory colloidal stability and sedimentation, as it was noticed in the shelf-life images. Looking at the chemical structures of these PEG surfactants (Figure 3.6), the main difference between the implemented polymers stands in the functional groups that are exposed to aqueous solution, namely carboxyl-, methoxy- and amino-groups. In aqueous media at neutral pH, the negatively charged carboxylates stabilize the NPs better due to strong electrostatic repulsions, which is not the case for the amino-groups containing polymers. This results in a weaker electrostatic repulsion and a higher chance for NPs aggregation, which translates into possibly larger sized NPs and subsequent sedimentation. This is in line with the visually less satisfactory shelf-life results and DLS measurements (Figure 3.7) obtained for DSPE-PEG_{2000}-NH_2 functionalized Pd/Fe-oxide NPs in comparison to the DSPE-PEG_{2000}-COOH functionalized analogues.

To investigate the magnetic properties of Pd/Fe-oxide NPs after modification of their surface with the aforementioned amphiphilic PEG-polymers, water dispersions of the NPs were freeze-dried and the SQUID measurements were conducted on the obtained powder. The magnetic hysteresis loops obtained at 300 K (Figure 3.8A) displayed no coercivity and remanence (Table 3.3, Exp_10mg) indicating typical superparamagnetic behaviour above blocking temperature independent of the amphiphilic PEG-surfactant.

The M_s values recorded were lower for all the PEG-functionalized Pd/Fe-oxide NPs in comparison to the M_s value obtained for OA-capped Pd/Fe-oxide NPs, but as mentioned already, a diamagnetic/non-magnetic polymer layer at the surface of NPs can reduce their magnetization. The highest M_s value of 51.1 emu/g_{NPs} was recorded for the NPs modified with DSPE-PEG_{2000}-COOH, followed by DSPE-$mPEG_{2000}$, for which a reduced M_s value of 44.9 emu/g_{NPs} was obtained (Table 3.3).

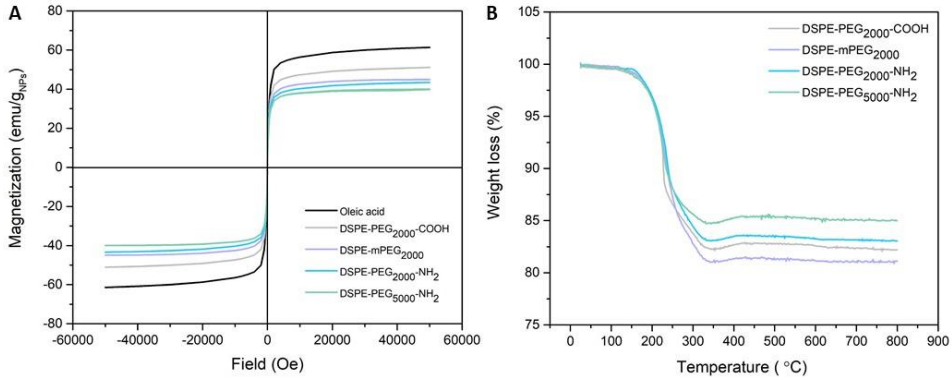

Figure 3.8. Analysis of Pd/Fe-oxide NPs from Exp_10mg with various PEG-functionalization: (**A**) M(H)$_T$ curves measured at T = 300 K; **(B)** Thermogravimetric analysis (TGA).

Table 3.3. Overview of the magnetic properties of Pd/Fe-oxide NPs from Exp_10mg with different PEG functionalization.

Surfactant	Saturation magnetization (M_s)[a] (emu/g_{NPs})	Coercivity (H_c)[b] (Oe)	Weight Loss[c] (%)	SLP (W/g_{Fe})[d]
Oleic acid	61.4	12	-	-
DSPE-PEG$_{2000}$-COOH	51.1	5.23	17.8	233
DSPE-mPEG$_{2000}$	44.9	4.95	18.9	205
DSPE-PEG$_{2000}$-NH$_2$	43.4	4.00	16.9	203
DSPE-PEG$_{5000}$-NH$_2$	39.8	2.85	15.0	201

[a]Measured at 50 kOe and T = 300 K; [b]Measured at 300 K; [c]Obtained from TGA; [d]Measured at 346 kHz, 23 mT; Error ≤ 5%.

It is expected that variations in surface coverage density (based on TGA) create differences in surface environments and introduce uncertainty to the magnetic response of NPs after surface modification.[45] This explains the slightly lower M_s-value of the NPs functionalized with DSPE-mPEG$_{2000}$ in comparison to DSPE-PEG$_{2000}$-COOH, as a the corresponding weight loses are 18.9 and 17.8%, respectively (Figure 3.8B, Table 3.3)

Considering that all PEG is decomposed at 800 °C and palladium/magnetite are thermally stable in the measured temperature range, the difference between the remaining weight can be related to the extent of bound PEG, meaning a higher number of DSPE-mPEG$_{2000}$ molecules were present on the surface of NPs, resulting in decreased M_s, which is in agreement with literature.[54,55] However, for the NPs

functionalized with DSPE-PEG$_{2000/5000}$-NH$_2$-polymers the opposite was found: lower weight loss (16.9 and 15%, respectively) did not result in increased M_s-values. It is important to stress that there are multiple factors regarding functionalization found to significantly affect the saturation magnetization and anisotropy, such as the type of functional group of the ligands, the nature and the strength of the bonds, the surfactant chain length, the packing density of the coating molecules. Because of this complexity and the number of factors involved, in some cases contradictory results can be observed.[48] Possibly, during the functionalization procedure with DSPE-PEG$_{2000}$-NH$_2$, more oleic acid surfactant molecules were stripped, higher number of strong covalent O-Fe bonds formed at the surface of the particles being disrupted, leading to changes in magnetic moment due to an increased spin disorders and a decrease in saturation magnetization.

For Pd/Fe-oxide NPs modified with the higher molecular weight (M_w) DSPE-PEG$_{5000}$-NH$_2$ surfactant, a small decrease in the absorbed amount of ligand molecules on the surface of the NPs was determined via TGA measurements in comparison to the other three PEG polymers with lower M_w. This is in agreement with the TGA results reported by other studies, which show that larger polymers lead to lower amounts adsorbed on the surface of the NPs.[54,56,57] On the other hand, Hong et al. concludes that the actual molecular weight of the polymer has little effect on the coating efficiency,[55] which corresponds to our case considering the small differences in weight loss (%) obtained via TGA for all PEG polymers.

The M_s value recorded for Pd/Fe-oxide NPs functionalized with DSPE-PEG$_{5000}$-NH$_2$ was the lowest (39.8 emu/g$_{NPs}$). Even though it is expected that less surfactant adsorbed on the surface leads to better M_s values, the effect of the surfactant on the magnetic properties of the NPs is also dependent on the balance between the amount of polymer adsorbed on the surface and the length of the polymer chain employed through functionalization. In this case, considering the small differences between TGA results, the increased number of PEG units plays the determining role, and the decrease in M_s does not come as a surprise but is in agreement with other studies like the ones of Józefczak et al.[58] and Hong et al.[55]

Lastly, the scope of the abovementioned surface functionalization experiments was to transfer the hydrophobic Pd/Fe-oxide NPs to aqueous media in a way that ensures

good colloidal stability and preservation of magnetic properties, rather than conducting a comprehensive study on the effects of surface functionalization and the crystal distortions that may arise as a consequence. Hence, functionalization with DSPE-PEG_{2000}-COOH leading to NPs with the highest saturation magnetization and excellent colloidal stability was chosen as the best functionalization route for transferring the initially hydrophobic Pd/Fe-oxide NPs to aqueous media for further testing their performance as heating/thermal ablation and MR imaging agents.

Pd/Fe-oxide nanoparticles as magnetic hyperthermia/thermal ablation agents

Heat treatments entail either hyperthermia, increasing the in vivo temperature to a level that either sensitizes other therapies, such as chemo- or radiotherapy (41–46 °C), or thermal ablation, that causes a targeted ablation and cell death (>46 °C).[21] Magnetic nanoparticles can generate heat via different mechanisms in the surrounding regions when submitted to an alternating magnetic field. Depending on the size of the NPs, the heating can arise from hysteresis losses or, as in the case of Pd/Fe-oxide superparamagnetic nanoparticles presented in this study, the effects are attributed to Néel and Brownian relaxation mechanisms.[1,59]

To evaluate the heating efficiency, we chose four of the Pd/Fe-oxide NPs batches previously introduced through this study: Exp_10mg, Exp_standard and Exp_7 °C with the highest values of saturation magnetization and, oppositely, Exp_[surf]:[Fe] = 2 with the smallest size and M_s value. As previously discussed, the as-prepared hybrid nanocrystals were hydrophobic post thermal decomposition synthesis, thus, the hybrid NPs were first transferred to aqueous media by providing their surface with hydrophilic DSPE-PEG_{2000}-COOH. Next, samples containing approximatively 10 mg of Pd/Fe-oxide NPs dispersed in 1 mL of water were used while applying an AMF at the frequency of 346 kHz and a field strength of 23 mT. The efficiency of heating, expressed as specific loss power (SLP)[60], was calculated for each batch of Pd/Fe-oxide NPs based on the following equation:

$$\mathrm{SLP}\ [\mathrm{W/g_{Fe}}] = \frac{\mathrm{C}}{\mathrm{m_{Fe}}}\frac{\Delta \mathrm{T}}{\Delta \mathrm{t}} \qquad (1)$$

where C is the heat capacity of the sample, m_{Fe} is the mass of iron in the colloidal solution determined by ICP-OES, and $\Delta T/\Delta t$ is the measured temperature increase with time.

As the properties of the externally applied magnetic field influence the extent of heating resulted from the magnetic NPs, it has been proposed to use intrinsic loss power (ILP) to enable comparison of heating power measurements made at different magnetic field strengths/frequencies[61], which can be derived from SLP using Equation (2), in which SLP is in W/kg, *f* is the frequency of the alternating magnetic field in kHz and H is the magnetic field strength in kA/m.

$$\mathrm{ILP} = \frac{\mathrm{SLP}}{f \cdot \mathrm{H}^2} \qquad (2)$$

The superparamagnetic Pd/Fe-oxide NPs from Exp_[surf]:[Fe] = 2 presented an SLP value of only 2 W/g_{Fe} (Table 3.1). This value is below the detection limit of the machine, meaning, no heat was generated by these NPs. This is in agreement with the study of Jeun et al., that established a threshold size (approx. 10 nm) below which the measured SLP is insufficient for hyperthermia applications.[62] Generally, the SLP values of magnetic Fe-oxide NPs are known to be proportional to the saturation magnetization of these NPs.[63] In our case, even with the inclusion of Pd as a second metal and the Fe-oxide as a coating, we noticed the same correlation of increasing SLP values with M_S as the Pd/Fe-oxide NPs with sizes of 19, 20 and 21 nm from Exp_7 °C, Exp_standard and Exp_10 mg, which produced SLP values of 102 W/g_{Fe}, 113 W/g_{Fe}, and 233 W/g_{Fe}, respectively (Table 3.1). Of course, we are interested in the highest SLP values possible for efficient hyperthermia/thermal ablation with a minimal dose of magnetic NPs introduced into the body, therefore, Exp_10mg had the most promising results.

The SLP and ILP values are extensively used to characterize the heat generation ability of magnetic systems. The SLP is directly influenced by both intrinsic parameters such as size, magnetocrystalline/shape anisotropy and surface functionalization of the nanoparticles, as well as extrinsic parameters like frequency, amplitude of the magnetic field applied and the viscosity of the media.[64] As SLP is dependent on the frequency and strength of the magnetic field employed during the

measurement, the ILP value is commonly used for comparison between magnetic nanoparticle heating powers measured at different laboratories.[61] However, it has been shown that ILP values of the same sample measured at several laboratories can differ up to 40% because of large systematic errors and lack of agreement in magnetic heating characterization.[12,65] Equation (1) used in this research to calculate the SLP is based on the assumption that all energy dissipated goes into a temperature increase of the sample. In reality, as the system is not perfectly adiabatic, some of the energy is lost to the environment. However, as the cooling rate is very low in comparison to the heating rate, the heat loss to the environment is negligible compared to the sample heating. Multiple calculation methods have been developed to estimate SLP from heating data, and such examples with more detailed decription are reported in studies of Soetaert et al.[66] and Wells et al.[65]

As there is currently no consensus on "best practice" to measure temperatue and calculate SLP, it makes it hard to directly compare the results between our experiments and other different experimental setups.

Once more, the presence of Pd in the composition of the NPs makes it hard to compare our results with those presented in literature on homogeneous Fe-oxides, and, to the best of our knowledge, there are no other Pd/Fe-oxide NPs on which the heating efficiency has been investigated. However, there are studies on Au/Fe-oxide NPs synthesized via thermal decomposition, such as the those reported by Efremova et al.[67] in which they present similar hybrid nanoparticles along with analogous method for transferring the hybrid nanoparticles in aqueous solution. Converting their maximum reported SLP value of Au/Fe-oxide NPs to the ILP results into 1.410 nHm^2/kg, which is comparable to our results with a slightly higher ILP value (2.011 nHm^2/kg) calculated for Exp_10mg. Still, this comparison is not fully relevant, as an AMF with different frequency and amplitude was applied during their heating studies, which still leads to differences in heating results.[65]

As shown before, the heating efficiency of Pd/Fe-oxide NPs functionalized with DSPE-PEG_{2000}-COOH was satisfactory, but NPs functionalized with other PEG-polymers that led to lower saturation magnetization values were also tested under the same AMF conditions (346 kHz and a field strength of 23 mT) and the corresponding SLP values were calculated (Table 3.3). The SLP values recorded for

DSPE-PEG$_{2000}$-COOH, DSPE-mPEG$_{2000}$, DSPE-PEG$_{2000}$-NH$_2$ and DSPE-PEG$_{5000}$-NH$_2$ functionalized NPs did not exhibit significant differences and were determined to be 233, 205, 203 and 201 W/g$_{Fe}$, respectively. These results are consistent with the theoretical prediction for such small NPs in their superparamagnetic/single-domain regime, where Neél relaxation is thought to be the predominant mechanism, which is unaffected by the coating of the NPs.[68]

Pd/Fe-oxide nanoparticles as MR imaging agents

MRI is a well-known diagnostic technique in medicine, and it is mostly applied to generate high-resolution anatomic images of organs and tissues. The principle is based on the nuclear magnetic resonance of the protons, whose relaxation can be altered by administration of contrast agents, which leads to contrast enhancement of the images. Superparamagnetic Fe-oxide NPs are superior candidates to decrease the transversal T_2-relaxation times of the protons in their proximity through generation of large magnetic field gradients resulting in a dark contrast in T_2-weighted images.[1,69]

As the Pd/Fe-oxide NPs presented promising magnetic properties, we performed T_2-relaxation measurements to gain insight into the r_2 relaxivity (relaxation rate enhancement per mM of magnetic species). In accordance with the theory, only ultra-small Fe-oxide NPs (<10 nm) exhibit a T_1-effect,[70] which was not the case for the presented Pd/Fe-oxide NPs, thus the r_1-measurements were omitted in this study. It has been shown that the contrast enhancement effects are directly related to the saturation magnetization value,[1] thus the Pd/Fe-oxide NPs from Exp_[surf]:[Fe] = 2 were excluded, as their M_S was the lowest and the SLP value was insufficient for heating. Instead, we focused on the three Pd/Fe-oxide batches with the highest M_S values: Exp_10mg, Exp_standard and Exp_7 °C in aqueous suspensions, after surface modification with DSPE-PEG$_{2000}$-COOH, and investigated their impact on the T_2 relaxation time. The resulting transverse relaxivities r_2 measured for these three batches are summarized in Table 3.1. A typical increase in r_2 values with increasing NPs size was observed[71] with the highest value of 440 mM^{-1} s^{-1} for Exp_10mg, making these NPs the most promising T_2 contrast agents candidates, as the higher the relaxivity, the smaller the amount of NPs to be injected in the patient for high quality

imaging. An inverse of the T_2-relaxation time as a function of iron concentration for Exp_10mg can be found in Figure 3.9.

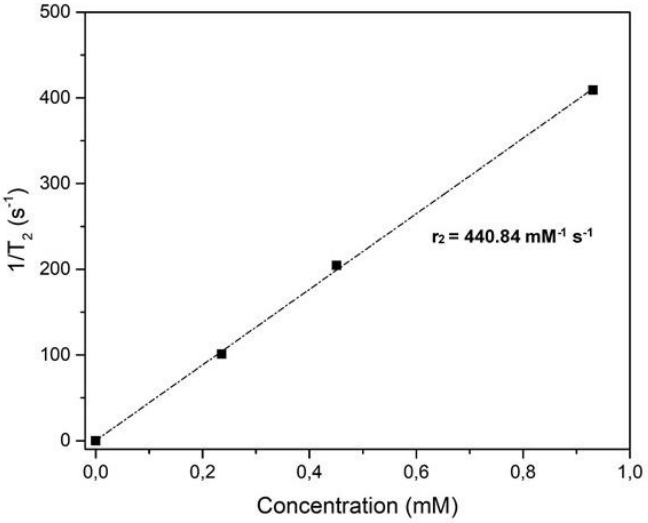

Figure 3.9. Inverse of the T_2-relaxation times as a function of iron concentration (determined by ICP-OES) for Pd/Fe-oxide NPs from Exp_10mg and functionalized with DSPE-PEG_{2000}-COOH.

3.4 Conclusion

The magnetic properties of the multiple batches of Pd/Fe-oxide NPs synthesized and presented in the previous chapter of this thesis were investigated. For this, SQUID magnetometry was conducted on hydrophobic Pd/Fe-oxide NPs in powder form. It was noticed that the magnetic behaviour of NPs is strongly dimension-dependent, and size is indeed one of the parameters that can be manipulated to tune the magnetic properties like saturation magnetization, coercivity, blocking temperature, etc. However, most of the trends on magnetic properties of NPs presented in literature are based on homogeneous Fe-oxide nanocrystals. Moving towards hybrid NPs and more complicated nanosystems leads to even more variables that influence the magnetic properties. This becomes extremely challenging, especially without a reliable basis for comparison with other magnetic nanoparticles presented in literature that are synthesized by various research groups via different synthetic routes. In any case, the presence of the non-magnetic Pd in the core of Fe-oxide NPs complicates the size-dependence due to variations in the volume of magnetic shell. Therefore, parameters, such as shape, composition, anisotropy, surface functionalization, etc., need to be considered to achieve complete control over the magnetic properties.

Nevertheless, the reasonably high saturation magnetization values obtained in this study with Pd/Fe-oxide NPs indicate that high-temperature synthesis via thermal decomposition is a suitable method to produce magnetic hybrid NPs. Majority of the hysteresis loops presented by the various batches of Pd/Fe-oxide NPs suggests that the samples are in their superparamagnetic regime, with low coercivity and remanence, and saturation magnetization occurs at relatively low fields.

The Pd/Fe-oxide NPs are meant to be used as theranostic agents, but the as-synthesized hybrid NPs are hydrophobic, hence surface modification was required in order to transfer the hybrid NPs to aqueous media. For making the NPs hydrophilic, a ligand exchange procedure with DMSA was conducted first, but the results were unsatisfactory in terms of colloidal stability and preservation of magnetic properties. A second attempt at making the NPs water-dispersible was by introducing an additional PEG layer on the Pd/Fe-oxide NPs. Four PEG-surfactants with different functional groups or M_w were employed, but DSPE-PEG_{2000}-COOH

offered the best results, as the Pd/Fe-oxide NPs were stable in water for long periods of time and presented the highest saturation magnetization value.

Lastly, the best combination of SLP values and r_2-relaxivities in water were obtained for Exp_standard and Exp_10mg. These batches present efficient heating and transversal relaxation rate enhancement, which makes them the best candidates for further investigation on their application for MR-image assisted hyperthermia/thermal ablation and radiotherapy.

Bibliography

1. Kolhatkar, A.G.; Jamison, A.C.; Litvinov, D.; Willson, R.C.; Lee, T.R. Tuning the magnetic properties of nanoparticles. *Int J Mol Sci* **2013**, *14*, 15977-16009, doi:10.3390/ijms140815977.
2. Song, M.; Zhang, Y.; Hu, S.; Song, L.; Dong, J.; Chen, Z.; Gu, N. Influence of morphology and surface exchange reaction on magnetic properties of monodisperse magnetite nanoparticles. *Colloids and Surfaces A: Physicochemical and Engineering Aspects* **2012**, *408*, 114-121, doi:https://doi.org/10.1016/j.colsurfa.2012.05.039.
3. Safarik, I.; Safarikova, M. Magnetic techniques for the isolation and purification of proteins and peptides.
4. Wilhelm, C.; Billotey C Fau - Roger, J.; Roger J Fau - Pons, J.N.; Pons Jn Fau - Bacri, J.C.; Bacri Jc Fau - Gazeau, F.; Gazeau, F. Intracellular uptake of anionic superparamagnetic nanoparticles as a function of their surface coating.
5. Yang, P.-F.; Lee, C.-K. Hyaluronic acid interaction with chitosan-conjugated magnetite particles and its purification. *Biochemical Engineering Journal* **2007**, *33*, 284-289, doi:https://doi.org/10.1016/j.bej.2006.11.010.
6. Megens, M.; Prins, M. Magnetic biochips: a new option for sensitive diagnostics. *Journal of Magnetism and Magnetic Materials* **2005**, *293*, 702-708, doi:https://doi.org/10.1016/j.jmmm.2005.02.046.
7. Graham, D.L.; Ferreira Ha Fau - Freitas, P.P.; Freitas, P.P. Magnetoresistive-based biosensors and biochips.
8. Colombo, M.; Carregal-Romero, S.; Casula, M.F.; Gutiérrez, L.; Morales, M.P.; Böhm, I.B.; Heverhagen, J.T.; Prosperi, D.; Parak, W.J. Biological applications of magnetic nanoparticles. *Chemical Society Reviews* **2012**, *41*, 4306-4334, doi:10.1039/C2CS15337H.
9. Neuberger, T.; Schöpf, B.; Hofmann, H.; Hofmann, M.; von Rechenberg, B. Superparamagnetic nanoparticles for biomedical applications: Possibilities and limitations of a new drug delivery system. *Journal of Magnetism and Magnetic Materials* **2005**, *293*, 483-496, doi:https://doi.org/10.1016/j.jmmm.2005.01.064.
10. Lacava, L.M.; Lacava Zg Fau - Da Silva, M.F.; Da Silva Mf Fau - Silva, O.; Silva O Fau - Chaves, S.B.; Chaves Sb Fau - Azevedo, R.B.; Azevedo Rb Fau - Pelegrini, F.; Pelegrini F Fau - Gansau, C.; Gansau C Fau - Buske, N.; Buske N Fau - Sabolovic, D.; Sabolovic D Fau - Morais, P.C., et al. Magnetic resonance of a dextran-coated magnetic fluid intravenously administered in mice.
11. Kim, D.K.; Mikhaylova, M.; Wang, F.H.; Kehr, J.; Bjelke, B.; Zhang, Y.; Tsakalakos, T.; Muhammed, M. Starch-Coated Superparamagnetic Nanoparticles as MR Contrast Agents. *Chemistry of Materials* **2003**, *15*, 4343-4351, doi:10.1021/cm031104m.
12. Blanco-Andujar, C.; Walter, A.; Cotin, G.; Bordeianu, C.; Mertz, D.; Felder-Flesch, D.; Begin-Colin, S. Design of iron oxide-based nanoparticles for MRI and magnetic hyperthermia. *Nanomedicine (Lond)* **2016**, *11*, 1889-1910, doi:10.2217/nnm-2016-5001.
13. Huh, Y.-M.; Jun, Y.-w.; Song, H.-T.; Kim, S.; Choi, J.-s.; Lee, J.-H.; Yoon, S.; Kim, K.-S.; Shin, J.-S.; Suh, J.-S., et al. In Vivo Magnetic Resonance Detection of Cancer by Using

Multifunctional Magnetic Nanocrystals. *J Am Chem Soc* **2005**, *127*, 12387-12391, doi:10.1021/ja052337c.

14. Arruebo, M.; Fernández-Pacheco, R.; Ibarra, M.R.; Santamaría, J. Magnetic nanoparticles for drug delivery. *Nano Today* **2007**, *2*, 22-32, doi:https://doi.org/10.1016/S1748-0132(07)70084-1.
15. Kami, D.; Takeda S Fau - Itakura, Y.; Itakura Y Fau - Gojo, S.; Gojo S Fau - Watanabe, M.; Watanabe M Fau - Toyoda, M.; Toyoda, M. Application of magnetic nanoparticles to gene delivery.
16. Dobson, J. Magnetic nanoparticles for drug delivery. *Drug Development Research* **2006**, *67*, 55-60, doi:https://doi.org/10.1002/ddr.20067.
17. Chertok, B.; Moffat Ba Fau - David, A.E.; David Ae Fau - Yu, F.; Yu F Fau - Bergemann, C.; Bergemann C Fau - Ross, B.D.; Ross Bd Fau - Yang, V.C.; Yang, V.C. Iron oxide nanoparticles as a drug delivery vehicle for MRI monitored magnetic targeting of brain tumors.
18. Jain, T.K.; Morales Ma Fau - Sahoo, S.K.; Sahoo Sk Fau - Leslie-Pelecky, D.L.; Leslie-Pelecky Dl Fau - Labhasetwar, V.; Labhasetwar, V. Iron oxide nanoparticles for sustained delivery of anticancer agents.
19. Gazeau, F.; Lévy M Fau - Wilhelm, C.; Wilhelm, C. Optimizing magnetic nanoparticle design for nanothermotherapy.
20. Gupta, A.K.; Gupta, M. Synthesis and surface engineering of iron oxide nanoparticles for biomedical applications. *Biomaterials* **2005**, *26*, 3995-4021, doi:https://doi.org/10.1016/j.biomaterials.2004.10.012.
21. Mornet, S.; Vasseur, S.; Grasset, F.; Duguet, E. Magnetic nanoparticle design for medical diagnosis and therapy. *Journal of Materials Chemistry* **2004**, *14*, 2161-2175, doi:10.1039/B402025A.
22. Issa, B.; Obaidat, I.M.; Albiss, B.A.; Haik, Y. Magnetic nanoparticles: surface effects and properties related to biomedicine applications. *Int J Mol Sci* **2013**, *14*, 21266-21305, doi:10.3390/ijms141121266.
23. Baryeh, K.; Attia, M.; Ulloa, J.C.; Ye, J.Y. 15 - Magnetic nanoparticle-based hybrid materials in the biomedical field: fundamentals and applications. In *Magnetic Nanoparticle-Based Hybrid Materials*, Ehrmann, A., Nguyen, T.A., Ahmadi, M., Farmani, A., Nguyen-Tri, P., Eds. Woodhead Publishing: 2021; https://doi.org/10.1016/B978-0-12-823688-8.00005-3pp. 387-423.
24. Hepel, M. Magnetic Nanoparticles for Nanomedicine. *Magnetochemistry* **2020**, *6*, doi:10.3390/magnetochemistry6010003.
25. Materón, E.M.; Miyazaki, C.M.; Carr, O.; Joshi, N.; Picciani, P.H.S.; Dalmaschio, C.J.; Davis, F.; Shimizu, F.M. Magnetic nanoparticles in biomedical applications: A review. *Applied Surface Science Advances* **2021**, *6*, 100163, doi:https://doi.org/10.1016/j.apsadv.2021.100163.
26. Salas, G.; Veintemillas-Verdaguer, S.; Morales, M.d.P. Relationship between physico-chemical properties of magnetic fluids and their heating capacity. *International Journal of Hyperthermia* **2013**, *29*, 768-776, doi:10.3109/02656736.2013.826824.

27. Baaziz, W.; Pichon, B.P.; Fleutot, S.; Liu, Y.; Lefevre, C.; Greneche, J.-M.; Toumi, M.; Mhiri, T.; Begin-Colin, S. Magnetic Iron Oxide Nanoparticles: Reproducible Tuning of the Size and Nanosized-Dependent Composition, Defects, and Spin Canting. *The Journal of Physical Chemistry C* **2014**, *118*, 3795-3810, doi:10.1021/jp411481p.
28. Smolensky, E.D.; Park, H.-Y.E.; Zhou, Y.; Rolla, G.A.; Marjańska, M.; Botta, M.; Pierre, V.C. Scaling laws at the nanosize: the effect of particle size and shape on the magnetism and relaxivity of iron oxide nanoparticle contrast agents. *Journal of Materials Chemistry B* **2013**, *1*, 2818-2828, doi:10.1039/C3TB00369H.
29. Tan, C.; Junze, C.; Wu, X.-J.; Zhang, H. Epitaxial growth of hybrid nanostructures. *Nature Reviews Materials* **2018**, *3*, 17089, doi:10.1038/natrevmats.2017.89.
30. Zeng, J.; Gong, M.; Wang, D.; Li, M.; Xu, W.; Li, Z.; Li, S.; Zhang, D.; Yan, Z.; Yin, Y. Direct Synthesis of Water-Dispersible Magnetic/Plasmonic Heteronanostructures for Multimodality Biomedical Imaging. *Nano Letters* **2019**, *19*, 3011-3018, doi:10.1021/acs.nanolett.9b00171.
31. Jin, Y.; Jia, C.; Huang, S.-W.; O'Donnell, M.; Gao, X. Multifunctional nanoparticles as coupled contrast agents. *Nature Communications* **2010**, *1*, 41, doi:10.1038/ncomms1042.
32. Klencsár, Z. Mössbauer spectrum analysis by Evolution Algorithm. *Nuclear Instruments and Methods in Physics Research Section B: Beam Interactions with Materials and Atoms* **1997**, *129*, 527-533, doi:https://doi.org/10.1016/S0168-583X(97)00314-5.
33. Morup, S.; Hansen, M.F.; Frandsen, C. Magnetic interactions between nanoparticles. *Beilstein J Nanotechnol* **2010**, *1*, 182-190, doi:10.3762/bjnano.1.22.
34. Han, D.H.; Wang, J.P.; Luo, H.L. Crystallite size effect on saturation magnetization of fine ferrimagnetic particles. *Journal of Magnetism and Magnetic Materials* **1994**, *136*, 176-182, doi:https://doi.org/10.1016/0304-8853(94)90462-6.
35. Vargas, J.M.; Lawton, J.; Vargas, N.M.; Schuller, I.K.; Sowko, N.J.; Huang, M.-X.; Zhang, M. Temperature trends and correlation between SQUID superparamagnetic relaxometry and dc-magnetization on model iron-oxide nanoparticles. *Journal of Applied Physics* **2020**, *127*, 044304, doi:10.1063/1.5131012.
36. Sun, S.; Zeng, H.; Robinson, D.B.; Raoux, S.; Rice, P.M.; Wang, S.X.; Li, G. Monodisperse MFe2O4 (M = Fe, Co, Mn) Nanoparticles. *J Am Chem Soc* **2004**, *126*, 273-279, doi:10.1021/ja0380852.
37. Skumryev, V.; Stoyanov, S.; Zhang, Y.; Hadjipanayis, G.; Givord, D.; Nogués, J. Beating the superparamagnetic limit with exchange bias. *Nature* **2003**, *423*, 850-853, doi:10.1038/nature01687.
38. Saragi, T.; Sinaga, H.D.; Rahmi, F.; Pramesti, G.A.; Sugiarto, A.; Therigan, A.; Syakir, N.; Hidayat, S.; Risdiana, R. Blocking Temperature of Magnetite Nanoparticles Fe3O4 Encapsulated Silicon Dioxide SiO2. *Key Engineering Materials* **2020**, *855*, 172-176, doi:10.4028/www.scientific.net/KEM.855.172.
39. Majetich, S.A. Magnetic Nanoparticles. In *Handbook of Magnetism and Magnetic Materials*, Coey, M., Parkin, S., Eds. Springer International Publishing: Cham, 2020; 10.1007/978-3-030-63101-7_20-1pp. 1-36.

40. Mohapatra, J.; Mitra, A.; Bahadur, D.; Aslam, M. Surface controlled fabrication of MFe2O4 (M = Mn, Fe, Co, Ni and Zn) nanoparticles and their magnetic properties. *CrystEngComm* **2012**, *15*, 524-532.
41. Nedelkoski, Z.; Kepaptsoglou, D.; Lari, L.; Wen, T.; Booth, R.A.; Oberdick, S.D.; Galindo, P.L.; Ramasse, Q.M.; Evans, R.F.L.; Majetich, S., et al. Origin of reduced magnetization and domain formation in small magnetite nanoparticles. *Scientific Reports* **2017**, *7*, 45997, doi:10.1038/srep45997.
42. Guardia, P.; Labarta, A.; Batlle, X. Tuning the Size, the Shape, and the Magnetic Properties of Iron Oxide Nanoparticles. *The Journal of Physical Chemistry C* **2011**, *115*, 390-396, doi:10.1021/jp1084982.
43. De Palma, R.; Peeters, S.; Van Bael, M.J.; Van den Rul, H.; Bonroy, K.; Laureyn, W.; Mullens, J.; Borghs, G.; Maes, G. Silane Ligand Exchange to Make Hydrophobic Superparamagnetic Nanoparticles Water-Dispersible. *Chemistry of Materials* **2007**, *19*, 1821-1831, doi:10.1021/cm0628000.
44. Wu, N.; Fu, L.; Su, M.; Aslam, M.; Wong, K.C.; Dravid, V.P. Interaction of Fatty Acid Monolayers with Cobalt Nanoparticles. *Nano Letters* **2004**, *4*, 383-386, doi:10.1021/nl035139x.
45. Zhang, L.; He, R.; Gu, H.-C. Oleic acid coating on the monodisperse magnetite nanoparticles. *Applied Surface Science* **2006**, *253*, 2611-2617, doi:https://doi.org/10.1016/j.apsusc.2006.05.023.
46. Sperling, R.; Parak, W. Surface modification, functionalization and bioconjugation of colloidal Inorganic nanoparticles. *Philosophical transactions. Series A, Mathematical, physical, and engineering sciences* **2010**, *368*, 1333-1383, doi:10.1098/rsta.2009.0273.
47. Majetich, S.A.; Wen, T.; Mefford, O.T. Magnetic nanoparticles. *MRS Bulletin* **2013**, *38*, 899-903, doi:10.1557/mrs.2013.230.
48. Abdolrahimi, M.; Vasilakaki, M.; Slimani, S.; Ntallis, N.; Varvaro, G.; Laureti, S.; Meneghini, C.; Trohidou, K.N.; Fiorani, D.; Peddis, D. Magnetism of Nanoparticles: Effect of the Organic Coating. *Nanomaterials (Basel)* **2021**, *11*, doi:10.3390/nano11071787.
49. Haracz, S.; Hilgendorff, M.; Rybka, J.D.; Giersig, M. Effect of surfactant for magnetic properties of iron oxide nanoparticles. *Nuclear Instruments and Methods in Physics Research Section B: Beam Interactions with Materials and Atoms* **2015**, *364*, 120-126, doi:https://doi.org/10.1016/j.nimb.2015.08.035.
50. Piñeiro, Y.; González Gómez, M.; de Castro Alves, L.; Arnosa Prieto, A.; García Acevedo, P.; Seco Gudiña, R.; Puig, J.; Teijeiro, C.; Yáñez Vilar, S.; Rivas, J. Hybrid Nanostructured Magnetite Nanoparticles: From Bio-Detection and Theragnostics to Regenerative Medicine. *Magnetochemistry* **2020**, *6*, doi:10.3390/magnetochemistry6010004.
51. Vestal, C.R.; Zhang, Z.J. Effects of Surface Coordination Chemistry on the Magnetic Properties of MnFe2O4 Spinel Ferrite Nanoparticles. *J Am Chem Soc* **2003**, *125*, 9828-9833, doi:10.1021/ja035474n.

52. Lavorato, G.C.; Das, R.; Alonso Masa, J.; Phan, M.-H.; Srikanth, H. Hybrid magnetic nanoparticles as efficient nanoheaters in biomedical applications. *Nanoscale Advances* **2021**, *3*, 867-888, doi:10.1039/D0NA00828A.
53. Koper, G. *An introduction to interfacial engineering*; VSSD: Delft, 2007.
54. Strbak, O.A.-O.; Antal, I.; Khmara, I.; Koneracka, M.; Kubovcikova, M.; Zavisova, V.; Molcan, M.; Jurikova, A.; Hnilicova, P.A.-O.; Gombos, J., et al. Influence of Dextran Molecular Weight on the Physical Properties of Magnetic Nanoparticles for Hyperthermia and MRI Applications. LID - 10.3390/nano10122468 [doi] LID - 2468.
55. Hong, R.Y.; Feng, B.; Chen, L.L.; Liu, G.H.; Li, H.Z.; Zheng, Y.; Wei, D.G. Synthesis, characterization and MRI application of dextran-coated Fe3O4 magnetic nanoparticles. *Biochemical Engineering Journal* **2008**, *42*, 290-300, doi:https://doi.org/10.1016/j.bej.2008.07.009.
56. Butterworth, M.D.; Illum, L.; Davis, S.S. Preparation of ultrafine silica- and PEG-coated magnetite particles. *Colloids and Surfaces A: Physicochemical and Engineering Aspects* **2001**, *179*, 93-102, doi:https://doi.org/10.1016/S0927-7757(00)00633-6.
57. Jurikova, A.; Csach, K.; Miskuf, J.; Koneracka, M.; Zavisova, V.; Kubovcikova, M.; Kopcansky, P.; Muckova, M. Thermal Properties of Magnetic Nanoparticles Modified With Polyethylene Glycol. *IEEE Transactions on Magnetics* **2013**, *49*, 236-239, doi:10.1109/TMAG.2012.2224322.
58. Józefczak, A.; Hornowski, T.; Skumiel, A.; Závišová, V.; Koneracká, M.; Tomašovičová, N.; Timko, M.; Kopčanský, P.; Kelani, H.N. Effect of the Molecular Weight of Poly(ethylene glycol) on the Properties of Biocompatible Magnetic Fluids. *International Journal of Thermophysics* **2012**, *33*, 640-652, doi:10.1007/s10765-011-1061-4.
59. Gazeau, F.; Levy, M.; Wilhelm, C. Optimizing magnetic nanoparticle design for nanothermotherapy. *Nanomedicine (Lond)* **2008**, *3*, 831-844, doi:10.2217/17435889.3.6.831.
60. Natividad, E.; Castro, M.; Mediano, A. Adiabatic vs. non-adiabatic determination of specific absorption rate of ferrofluids. *Journal of Magnetism and Magnetic Materials* **2009**, *321*, 1497-1500, doi:https://doi.org/10.1016/j.jmmm.2009.02.072.
61. Wildeboer, R.R.; Southern, P.; Pankhurst, Q.A. On the reliable measurement of specific absorption rates and intrinsic loss parameters in magnetic hyperthermia materials. *Journal of Physics D: Applied Physics* **2014**, *47*, doi:10.1088/0022-3727/47/49/495003.
62. Jeun, M.; Lee, S.; Kyeong Kang, J.; Tomitaka, A.; Wook Kang, K.; Il Kim, Y.; Takemura, Y.; Chung, K.-W.; Kwak, J.; Bae, S. Physical limits of pure superparamagnetic Fe3O4 nanoparticles for a local hyperthermia agent in nanomedicine. *Applied Physics Letters* **2012**, *100*, 092406, doi:10.1063/1.3689751.
63. Filippousi, M.; Angelakeris, M.; Katsikini, M.; Paloura, E.; Efthimiopoulos, I.; Wang, Y.; Zamboulis, D.; Van Tendeloo, G. Surfactant Effects on the Structural and Magnetic Properties of Iron Oxide Nanoparticles. *The Journal of Physical Chemistry C* **2014**, *118*, 16209-16217, doi:10.1021/jp5037266.
64. Cotin, G.; Perton, F.; Blanco-Andujar, C.; Pichon, B.; Mertz, D.; Bégin-Colin, S. Chapter 2 - Design of Anisotropic Iron-Oxide-Based Nanoparticles for Magnetic

Hyperthermia. In *Nanomaterials for Magnetic and Optical Hyperthermia Applications*, Fratila, R.M., De La Fuente, J.M., Eds. Elsevier: 2019; https://doi.org/10.1016/B978-0-12-813928-8.00002-8pp. 41-60.

65. Wells, J.; Ortega, D.; Steinhoff, U.; Dutz, S.; Garaio, E.; Sandre, O.; Natividad, E.; Cruz, M.M.; Brero, F.; Southern, P., et al. Challenges and recommendations for magnetic hyperthermia characterization measurements. *International Journal of Hyperthermia* **2021**, *38*, 447-460, doi:10.1080/02656736.2021.1892837.
66. Soetaert, F.; Kandala, S.K.; Bakuzis, A.; Ivkov, R. Experimental estimation and analysis of variance of the measured loss power of magnetic nanoparticles. *Scientific Reports* **2017**, *7*, 6661, doi:10.1038/s41598-017-07088-w.
67. Efremova, M.A.-O.; Nalench, Y.A.-O.; Myrovali, E.; Garanina, A.S.; Grebennikov, I.S.; Gifer, P.K.; Abakumov, M.A.; Spasova, M.; Angelakeris, M.; Savchenko, A.G., et al. Size-selected Fe(3)O(4)-Au hybrid nanoparticles for improved magnetism-based theranostics.
68. Quinto, C.A.; Mohindra P Fau - Tong, S.; Tong S Fau - Bao, G.; Bao, G. Multifunctional superparamagnetic iron oxide nanoparticles for combined chemotherapy and hyperthermia cancer treatment.
69. Ganapathe, L.S.; Mohamed, M.A.; Mohamad Yunus, R.; Berhanuddin, D.D. Magnetite (Fe3O4) Nanoparticles in Biomedical Application: From Synthesis to Surface Functionalisation. *Magnetochemistry* **2020**, *6*, doi:10.3390/magnetochemistry6040068.
70. Jeon, M.; Halbert, M.V.; Stephen, Z.R.; Zhang, M. Iron Oxide Nanoparticles as T1 Contrast Agents for Magnetic Resonance Imaging: Fundamentals, Challenges, Applications, and Prospectives. *Advanced Materials* **2021**, *33*, 1906539, doi:https://doi.org/10.1002/adma.201906539.
71. Laurent, S.; Forge, D.; Port, M.; Roch, A.; Robic, C.; Vander Elst, L.; Muller, R.N. Magnetic Iron Oxide Nanoparticles: Synthesis, Stabilization, Vectorization, Physicochemical Characterizations, and Biological Applications. *Chemical Reviews* **2008**, *108*, 2064-2110, doi:10.1021/cr068445e.

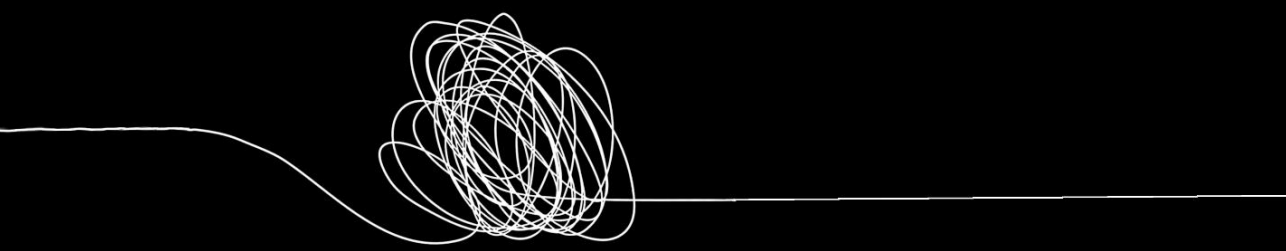

Boosting the heating and imaging performance of Pd/Fe-oxide NPs via manganese doping

4

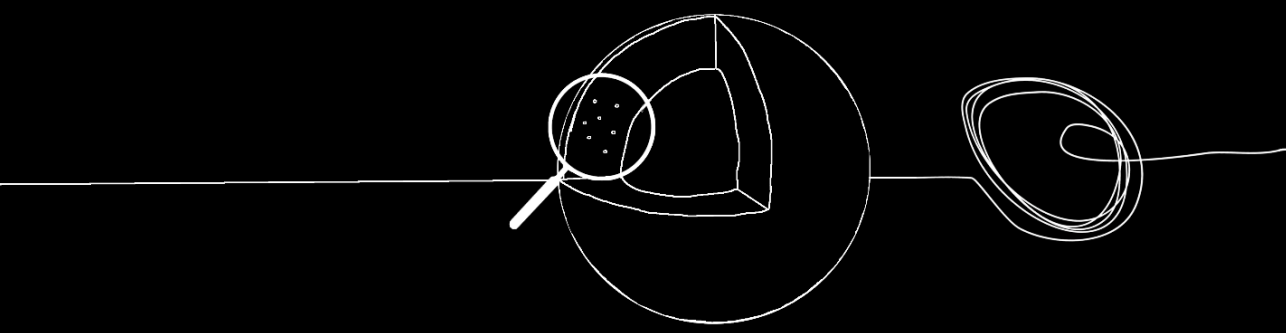

Abstract: Multifunctional biocompatible magnetic nanoparticles (MNPs) are highly researched for biomedical applications, especially in the fields of diagnosis (e.g. MRI imaging) and therapy (e.g. hyperthermia/thermal ablation) for cancer treatment. A crucial requirement for such theranostic nanoparticles meant as thermal and contrast agents is to endow them with magnetic properties, while retaining small sizes to ensure superparamagnetism. This would provide high heating efficiency at clinically relevant doses and contrast enhancement under application of an external magnetic field. The magnetic properties of nanoparticles are strongly related to their characteristic parameters such as size, shape and magnetocrystalline anisotropy. However, size has its limitations as MNPs move from superparamagnetic regime to pseudo single-domain and then multi-domain with size increase. Tuning the magnetocrystalline anisotropy can be an alternative strategy to increase the magnetic properties, for e.g. via doping by introducing different cations in the crystal lattice. Ferrite nanoparticles with the general formula MFe_2O_4 (M = Mn, Co, Ni) are a great inspiration, as their magnetic properties can be altered and enhanced by introducing the desired number of dopants in the nanoparticles composition. The idea of this study was to generate nanoparticles comprised of a Pd core, envisioned for the eventual radiolabelling with ^{103}Pd to enable brachytherapy, and an iron oxide coating doped with Mn, responsible for hyperthermia/thermal ablation and MR-imaging. Therefore, we established a synthesis method for Pd-core-iron oxide manganese doped shell nanoparticles (Pd/Fe|Mn-oxide NPs), investigated their magnetic properties, and tested their performance as theranostic agents. Lastly, a better performance in comparison to analogue Pd/Fe-oxide NPs previously presented in this thesis was demonstrated, including additionally enabled beneficial T_1 contrast.

Keywords: hybrid nanoparticles, palladium, iron oxide, manganese doping, magnetic properties, hyperthermia/thermal ablation, dual MR-contrast.

4.1. Introduction

One of the most challenging innovations in medicine stands in multifunctional biocompatible magnetic nanoparticles (MNPs), that have the ability to revolutionize the field of diagnosis and therapy of cancer.[1] The magnetic properties of MNPs are crucial for their successful performance in biomedical applications, such as drug delivery, cell marking, magnetic hyperthermia/thermal ablation (MH/TA) or magnetic resonance imaging (MRI).[2,3] For example, one of the limitations of conventional MNPs in thermal treatments is their low heating power, which requires local injection of MNPs in large quantities.[1] However, it is difficult to inject high volumes in tumours, plus the recommended dose of magnetic iron oxide NPs (Ferumoxytol) approved by the FDA is 510 mg (<10 mg per kg). Hence, to fully exploit the therapeutic potential of thermal treatments, it is crucial to design MNPs with high heating efficiency at clinically relevant doses (<10 mg per kg) to ensure generation of high intratumoral and intralesional temperatures required for sensitization or complete eradication of cancer tissues.[2,4] Therefore, design optimization of the nanoagents for MH/TA, while keeping an efficient heating power, has become a truly important challenge in biomedicine. At the same time, optimized magnetic properties designed for thermal treatments may also lead to improved MRI performance, as both heating performance and contrast enhancement are directly related to saturation magnetization (M_s).[2,5] These objectives can be achieved by tuning the MNPs parameters, such as size, shape and magnetocrystalline anisotropy.[1]

Saturation magnetization (M_s) varies with the size of the MNPs until a threshold size beyond which the magnetization value reaches a plateau and approaching the bulk magnetization value. At the same time, with size increase, the balance of magnetic interaction changes, and the MNPs move from superparamagnetic regime to single- and eventually multi-domain regimes.[5] However, the MNPs preferred in biomedical applications are sufficiently small to ensure the superparamagnetic regime, where magnetism disappears after removal of applied magnetic field, ensuring colloidal stability and resistance towards aggregation.[6,7] Lastly, it seems that MNPs with an optimal size limit between superparamagnetic and single-domain behaviour are optimal for thermal treatment.[1,8] Therefore, tuning the efficiency of MNPs via their

size has limitations. On the other hand, tuning the anisotropy of the NPs is a very promising alternative strategy to increase M_s, and to enhance MNPs heating efficiency and relaxivities (relaxation rate enhancement per concentration of magnetic component).[1,8] The effective anisotropy of MNPs can be tuned via changes on shape anisotropy, or on magnetocrystalline anisotropy by doping or synthesizing core-shell MNPs.[1,9] In the last years, ferrite nanoparticles with the general formula MFe_2O_4 (M = Fe, Mn, Co, Ni) have gained the spotlight due to their potential applications in biomedicine, and due to their remarkable magnetic properties, which can be tuned by introducing the desired composition of the dopants.[10,11] For example, the saturation magnetization of $MnFe_2O_4$ NPs was enhanced to 110 emu/mass of magnetic atoms from 101 emu/g of magnetic atoms presented by Fe_3O_4 NPs of the same size, via magnetic engineering of the iron oxide nanocrystal by replacement of Fe^{2+} with Mn^{2+}.[8,12]

Lastly, the nanomedicine paradigm is moving towards design of dual T_1/T_2 contrast agents. Such nanomaterials are developed through different approaches, one example being doping iron oxide NPs with paramagnetic ions, as Mn^{2+}.[1] In accordance to literature, only ultra-small iron oxide NPs (<10 nm) exhibit a T_1-effect.[13] However, such small sized MNPs are not able to generate heat sufficient for HT/TH applications.[14] Therefore, engineering of magnetization values via the MNPs composition is critical for developing sensitive magnetic probes for biomedical applications.[8]

In the previous chapter of this thesis, core-shell Pd/Fe-oxide NPs, with sizes around 20 nm, were deemed as best candidates for both MH/TA and MR-imaging. Therefore, we wanted to investigate the possibility of boosting their efficiency as theranostic agents even further. As previously mentioned, tuning the magnetic properties of NPs via their size, while ensuring superparamagnetism, has limitations, hence, anisotropy becomes a great alternative. For this, we attempted to boost the magnetic properties of Pd/Fe-oxide NPs by tuning their magnetocrystalline anisotropy via doping the iron oxide coating with manganese. Firstly, a seed-mediated thermal decomposition method for synthesis of Pd/Fe-oxide NPs with different amounts of manganese-doped iron oxide coatings (Pd/Fe|Mn-oxide NPs) was investigated. These hybrid MNPs were synthesized with similar sizes and shapes as the Pd/Fe-oxide NPs, in

order to study the effect of doping on magnetic properties, heating and imaging performance in comparison to their Pd/Fe-oxide analogues.

4.2 Materials and methods

Reagents

Palladium (II) acetate, oleylamine (OAm), tert-butylamine-borane complex, ethanol, hexane, Iron (III) acetylacetonae ($Fe(acac)_3$), Manganese (II) acetylacetonate ($Mn(acac)_2$), 1,2-hexadecanediol, 1-oxtadecene (ODE), oleic acid (OA), chloroform, 1,2-distearoyl-sn-glycero-3-phosphoethanolamine-*N*-[carboxy(polyethylene glycol)-2000] sodium salt, powder (DSPE-PEG_{2000}-COOH), ethylenediaminetetraacetic acid disodium salt dihydrate (EDTA), sodium hydroxide (NaOH).

Preparation of oleylamine capped Pd NPs (seeds)

OAm capped Pd-seeds were prepared based on previously published protocols.[15,16] Briefly, palladium (II) acetate (56 mg, 0.249 mmol) was added to 15 mL OAm in a 3-neck round-bottom flask. The reaction mixture was heated to 60 °C in 10 min under a stream of nitrogen gas and vigorous stirring. In parallel, tert-butylamine-borane complex (130 mg, 1.495 mmol) was dissolved in 3 mL OAm and injected into the reaction mixture via a septum, once the temperature reached 60 °C. After addition, the reaction mixture was further heated to 90 °C with a heating rate of 3 °C/min and kept at this temperature for 60 min. After 60 min, the reaction system was left to cool down to room temperature and the Pd NPs were collected by addition of 30 mL ethanol and centrifugation for 8 min at 10500 RPM (11830 ×g). The Pd NPs were stored as such until further use. The final product was redispersible in organic solvents such as toluene, hexane, chloroform.

Preparation of Mn doped Pd/Fe-oxide NPs (Pd/Fe|Mn-oxide) via a seed-mediated method

The synthesis employed to prepare Pd/Fe|Mn-oxide NPs for this study was adjusted from protocols presented in previously published articles.[17,18] Iron(III) acetylacetonate ($Fe(acac)_3$) (23.5 mg, 0.066 mmol) together with Mn(II) acetylacetonate ($Mn(acac)_2$) (8 mg, 0.033 mmol), and 1,2-hexadecanediol (50 mg) were

added to a 3-neck round bottom flask containing 20 mL octadecene (ODE), oleic acid (OA, 660 μL), and oleylamine (OAm, 65 μL). OAm capped Pd NPs (5.3 mg, 0.05 mmol) were dispersed in approximatively 0.4 mL hexane and sonicated for 5 min. Next, the Pd-seeds in hexane were added to the 3-neck round bottom flask. The reaction mixture was slowly heated to 120 °C under nitrogen flow and vigorous stirring and left at this temperature for 20 min to ensure the complete removal of hexane. Subsequently, the reaction mixture was further heated to 205 °C with a heating rate of 5 °C/ min and kept at this temperature for 120 min. After 120 min, the reaction mixture was further heated to 315 °C with a heating rate of 5 °C and kept at this temperature for 60 min. Next, the reaction system was left to cool down to room temperature and the Mn-dopped Pd/Fe-oxide NPs were collected by addition of 30 mL ethanol and centrifugation at 10500 RPM (11830 ×g) for 4-6 min. The procedure was repeated several times with ethanol and one or two times with a combination of ethanol and hexane in equal volumes. Lastly, the NPs were dried by a gentle flow of nitrogen/compressed air and stored as such until further use. The final product could be redispersed in organic solvents such as toluene, hexane, chloroform.
The experiment was conducted with 1[Mn]:4[Fe] ratio as well.

Dispersion of Pd/Fe-oxide NPs in aqueous media with DSPE-PEG$_{2000}$-COOH

The synthesized Pd/Fe|Mn-oxide NPs were transferred into water by means of functionalization with DSPE-PEG$_{2000}$-COOH following a slightly modified protocol presented elsewhere.[19] Firstly, 2 mg of Pd/Fe|Mn-oxide NPs were dispersed via ultrasonication in 1 mL chloroform containing 1.5 mg of PEG surfactant. The vial containing the mixture was left open for 24 h for the slow evaporation of the solvent, until a pasty precipitate remained at the bottom of the vial. The residual solid was heated to 80 °C for 10 min in a vacuum oven and subsequently flushed with a gentle flow of nitrogen, to ensure complete removal of chloroform. Next, 1 mL of Milli-Q water was added to the precipitate and sonicated for 15 min until a colloidal suspension in aqueous media was obtained. The colloidal suspension of NPs was pipetted into Eppendorf vials and the unbound polymer and excess lipids were removed by two rounds of centrifugation for 1 h at 19,600 RPM (30,000 xg) and

subsequent removal of the supernatant. Lastly, the NPs were collected in 1-2 mL of Milli-Q water in an Eppendorf and kept as such for further use.

Pd, Mn leakage study

Pd/Fe|Mn-oxide MNPs (2.5 mg) were transferred into an aqueous media with DSPE-PEG_{2000}-COOH surfactant. Subsequently, the MNPs were resuspended in 0.5 mL 1 mM ethylenediaminetetraacetic acid disodium salt dihydrate (EDTA) solution, previously brought to pH 7.4 with 0.1 M sodium hydroxide (NaOH) solution. The NPs were left for 24 h in suspension, after which they were added to an Amicon Ultra Centrifugal tube with a centrifugal concentrator Ultracel - 30 kDa MWCO regenerated cellulose membrane and centrifuged for 20 min at 4200 RPM. Lastly, the filtrate was collected and analysed on ICP-MS to check the Pd and Mn content. The 2.5 mg of Pd/Fe|Mn-oxide NPs were resuspended in 0.5 mL EDTA solution and the same procedure was repeated after 48h and 7 days.

Characterization

Particle size, size distribution and morphology of the samples were determined by transmission electron microscopy (TEM), using a 120 kV Jeol_JEM1400 microscope. All samples for TEM were prepared by drop-casting a diluted nanoparticle suspension in organic solvents such as hexane on a Quantifoil R1.2/1.3 Cu300 grid and evaporating the solvent at room temperature. The mean diameter and the size distribution of the samples were obtained by statistical analysis over 500-1000 NPs, by analysing the obtained TEM images with ImageJ software. The elemental mapping analysis was done with an Oxford Instruments EDS detector X-MAX^N 100TLE on the same grids used for TEM.

Magnetic characterization by superconducting quantum interference device (SQUID), was carried out on an MPMS XL magnetometer from Quantum Design, using about 1–2 mg of dried NPs powder. The hysteresis loops M(H) obtained under continuously varying applied magnetic field up to a maximum of ±50 kOe at 5 K and 300 K were used for evaluation of saturation magnetization (M_s) and coercivity (H_c). The heating power measurements were performed using the Magnetherm Digital, manufactured by Nanotherics, using a 50 mm coil device. All SLP values were

measured using an alternating magnetic field with a frequency of 346 kHz and a field strength of 19.1 mT. Two glass-fiber optic thermometers were used for temperature measurement [Osensa PRB-G40_2.0M-STM-MRI] to measure both the core and bottom temperature of the sample. The core temperature measured was used for SLP calculations. For determination of SLP, a sample of 1 mL of NPs in suspension was inserted in an isolated sample holder, to reduce heat loss to the environment, and placed in the middle of the coil. The temperature was equilibrated until it varied less than 0.05 °C/min before the measurement was conducted. The sample was then exposed to the magnetic field.

The longitudinal (T_1) and transverse (T_2) MR relaxation times of the phantoms were evaluated at 1.5 T, using a 450W MR scanner (GE Healthcare, Waukesha, WI, USA). T_1 relaxation times were measured with an inversion recovery (IR) turbo spin echo sequence with the following parameters: repetition time (TR) = 3000 ms, inversion time (TI) = 50, 100, 250, 200, 250, 500, 750, 1000, and 1500 ms, echo time (TE) = 11.2 ms, field of view (FOV) = 192 x 192 mm^2, slice thickness = 4 mm, acquisition matrix = 192 x 192, and number of excitations (NEX) = 1.[20] The T_1 relaxometry data were analysed using MATLAB script (R2018b, The MathWorks INC, Natick, USA) developed by Barral et al.[21] T_2 relaxation times were measured with a spin echo sequence with the following parameters: TR = 2000 ms, TE = 9, 15, 25, 35, 55, and 75 ms, FOV = 192 x 192 mm^2, slice thickness = 4 mm, acquisition matrix = 128 x 128, and NEX = 1. The T_2 relaxation rates were calculated by fitting a mono-exponential signal decay model using the nonlinear curve fitting function lsqcurvefit of MATLAB with an in-house developed script. Relaxation measurements were repeated once. The measured values were calculated per voxel and reported as the mean and standard deviation over approx. 120 voxels per sample.

The SLP-values and r_2-relaxivities of the samples were calculated using the concentrations of iron obtained from the ICP-OES data performed on the same samples after destruction of NPs.

4.3 Results and Discussion

Pd/Fe|Mn-oxide NPs synthesis

Cation exchange (CE) processes consist in partial or total replacement of cations from a nanocrystal structure with other cations. A typical CE process is conducted by mixing pre-made nanoparticles with additional metal precursors and surfactants and subsequent heating of the mixtures.[7] Even though post-synthetic cation exchange is an elegant method to introduce doping, as presented in the study of Sytnyk et al.[22], conventional seeded-growth method was preferred in this case, as it spares an extra step in the procedure, highly important in the view of the eventual radiolabelling of these MNPs with ^{103}Pd radionuclide.

The synthesis of iron oxide NPs via reductive thermal decomposition of $Fe(acac)_3$ iron precursor is highly popular, and it can be easily extended to the preparation of MFe_2O_4 by simply adding $Mn(acac)_2$ in the reaction mixture, together with the $Fe(acac)_3$ precursor.[8] Therefore, the $Fe(CO)_5$ precursor previously employed through the synthesis of Pd/Fe-oxide NPs was replaced with $Fe(acac)_3$, as acetylacetonate groups coordinate to a range of metals, including iron and manganese, both precursors being readily available and with decomposition temperatures around 200 °C.[8,18,23] The synthesis method adopted for generating Pd/Fe|Mn-oxide MNPs was a seed-mediated thermal decomposition, similar to the one employed for Pd/Fe-oxide NPs, in which pre-made OAm-capped Pd NPs were introduced in the reaction mixture to act as seeds on which the iron|manganese-oxide simultaneously nucleate and grow as a coating. However, the change in precursor introduced new challenges in the synthesis as experiments failed to consistently display core-shell structures. $Fe(acac)_3$ and $Mn(acac)_2$ have different nucleation/growth regimes than $Fe(CO)_5$, arising from their different chemistries and reactivities. While $Fe(CO)_5$ favours heterogeneous nucleation onto seeds surface and successive growth over homogeneous nucleation, $Fe(acac)_3$ does not exhibit the same preference, homogeneous nucleation being favoured in this case. During the synthesis, this resulted into a mixture of single iron|manganese-oxide NPs, uncoated Pd-seeds and incomplete core-shell morphologies, as reported elsewhere.[17] Therefore, new measures were employed during the synthesis with $Fe(acac)_3$ and $Mn(acac)_2$

precursors, in order to promote heterogeneous nucleation and formation of Pd/Fe|Mn-oxide MNPs. Such measures included i) a decrease in the iron|manganese precursor quantity present in the reaction, to avoid supersaturation conditions promoting homogeneous nucleation, ii) a lower amount of OAm-surfactant introduced during the reaction, iii) introducing an intermediate temperature step at approximatively 200 °C during a prolonged time to stimulate the formation of Fe(III)-complex with surfactants, iv) the use of a long-chain diol (1,2-hexadecanediol) to act both as accelerant in the formation of Fe-O-Fe bonds and mild reducing agent, and v) an increased temperature of 315 °C for the growth stage. Similar measures that promoted the heterogeneous nucleation of $Fe(acac)_3$ on pre-made seeds were proposed in other studies.[17]

After tuning the synthesis in accordance to the aforementioned measures, Pd/Fe|Mn-oxide NPs were successfully prepared via thermal decomposition of acetylacetonate precursors of iron and manganese on preformed OAm-capped Pd NPs with an average diameter of 5 nm. As the result, the iron|manganese-oxide heterogeneously nucleated and formed a coating on top of the Pd-seeds, leading to hybrid MNPs with spherical-squared morphology and sizes around 22 nm, as can be seen in the TEM images presented in Figure 4.1.

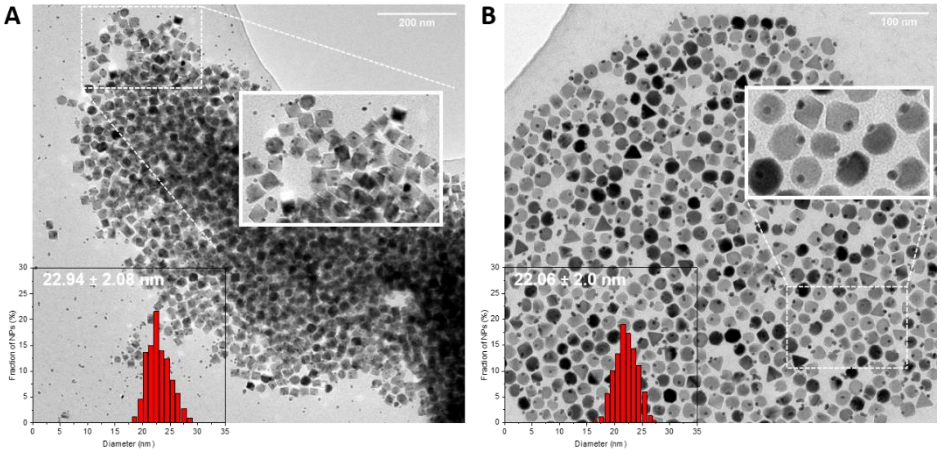

Figure 4.1. TEM images and corresponding size distributions of Pd/Fe|Mn-oxide MNPs synthesized with the following precursor ratios: **(A)** Pd/Fe|(0.5 Mn)-oxide and **(B)** Pd/Fe|(0.25 Mn)-oxide.

Two experiments were conducted, in which different amounts of manganese precursor $Mn(acac)_2$ in relation to iron precursor $Fe(acac)_3$ (1[Mn]:2[Fe] and 1[Mn]:4[Fe]) were employed during the synthesis. The two batches of NPs are to be referred as Pd/Fe|(0.5 Mn)-oxide and Pd/Fe|(0.25 Mn)-oxide, respectively. Independent of the precursor ratio introduced in the reaction, the hybrid MNPs undertook the same spherical-squared morphology (Figure 4.1A,B).

In the bright-field TEM images, the darker areas correspond to Pd, whereas lighter contrast represents Fe|Mn-oxide, as a result of the different electron penetration efficiency on Pd compared to Fe|Mn-oxide. However, Fe and Mn have similar electron densities, and cannot be differentiated via different contrast in TEM images, making it impossible to confirm the presence of the two metals in the composition of the hybrid MNPs. For this, EDS elemental mapping analysis was performed on the two batches of synthesized Pd/Fe|Mn-oxide NPs visualizing the individual signals for Pd, Fe, and Mn to confirm their position within the coating (Figure 4.2).

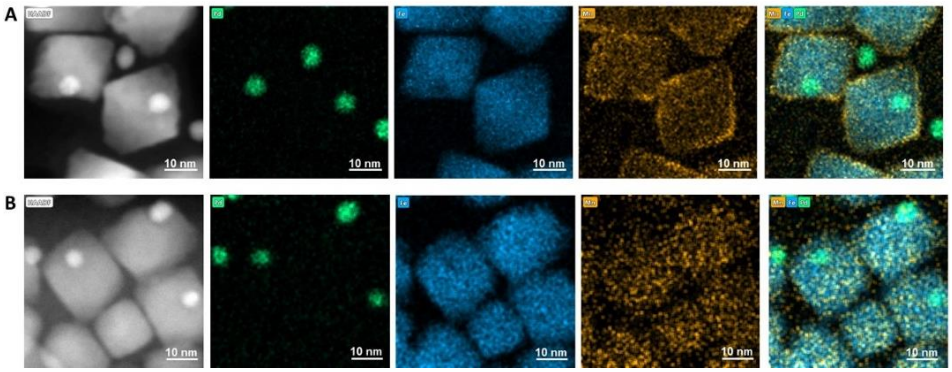

Figure 4.2. HR-TEM and EDS elemental mapping with individual signals for Pd (green), Fe (blue), and Mn(orange) of **(A)** Pd/Fe|(0.5 Mn)-oxide and **(B)** Pd/Fe|(0.25 Mn)-oxide.

Interestingly, the experiment conducted with a higher Mn amount, generated Pd/Fe|Mn-oxide NPs with a portion of the Mn atoms permeating the iron oxide coating. However, the majority of the Mn atoms was residing at the surface, generating an outer rim on the hybrid MNPs (Figure 4.2A). On the other hand, for the experiment conducted with lower Mn amount, the Mn atoms were found to be permeating the iron oxide coating (Figure 4.2B), but no outer rim was formed, possibly due to insufficient amount of Mn atoms. The EDS mapping analysis

confirmed the successful synthesis of Pd/Fe|Mn-oxide hybrid MNPs, with spherical-square morphologies, relevant sizes around 22 nm and different Mn-doping amounts, which increased with the higher [Mn]:[Fe] precursor ratio introduced in the synthesis.

Magnetic properties of Pd/Fe|Mn-oxide MNPs

The static magnetic behaviour of the two aforementioned batches of Pd/Fe|Mn-oxide MNPs was investigated by SQUID magnetometry. The MNPs were coated with OA, as-obtained from the thermal decomposition synthesis and subsequent cleaning procedure. The magnetization curves resulting from the alignment of the MNPs in the presence of an increasing magnetic field (up to 50 kOe) were measured at 5 K and 300 K, as shown in Figures 4.3A and 4.3B, respectively.

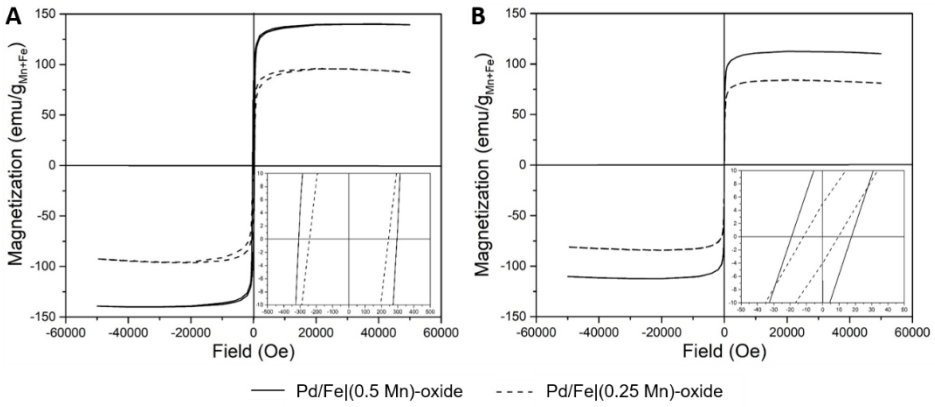

Figure 4.3. SQUID magnetometry of Pd/Fe|Mn-oxide MNPs: **(A)** $M(H)_T$ curves at T = 5 K; the inset represents 120x magnification of the x-axis showing coercivities (H_c); **(B)** $M(H)_T$ curves at T = 300 K; the inset represents 1200x magnification of the x-axis showing coercivities (H_c).

It is important to mention that the hysteresis loops present small dips at high fields, as a consequence of the strong diamagnetic interaction of the plastic capsule used during the measurements. The saturation magnetization (M_s) was determined by extrapolating the highest magnetization values (40 kOe) to the ordinate axis, where the field approaches zero (Table 4.1). The M_s values obtained for the two batches of Pd/Fe|Mn-oxide MNPs were corrected for the presence of Pd-core and organic layer at the surface, hence expressed in emu/g_{Fe+Mn}. For both temperatures, 5 K and 300 K

the saturation magnetization values were higher for the Pd/Fe|(0.5 Mn)-oxide MNPs, with higher content of Mn in their composition (Figure 4.3, Table 4.1).

As both batches of MNPs possess similar sizes, the differences in M_s values can be attributed to the content of doping material in their composition. According to multiple studies in literature,[10,11,22,24] doping iron oxide crystal structures with paramagnetic cations, such as manganese or cobalt, results in magnetic anisotropy increase, due to the replacement of Fe^{2+}/Fe^{3+} cations with more anisotropic Mn^{2+} or Co^{2+}. Additionally, the same studies observed that an increased magnetic anisotropy ensures higher M_s values, which translates in better magnetic properties. This confirms that tuning the composition of the MNPs can be indeed used as an alternative strategy to increase the M_s of the nanoparticles, instead of size. Unfortunately, as the M_s value obtained for Pd/Fe-oxide NPs described previously (Chapter 2) was not corrected for Pd-core and surfactants, a relevant comparison could not be made in this case.

Table 4.1. Overview of the magnetic properties of Pd/Fe|Mn-oxide and Pd/Fe-oxide (Exp_10mg) NPs: saturation magnetization (M_s) at 40 kOe, T = 5 K and 300 K, coercivity (H_c) at T = 5 K and 300 K, and calculated SLP, r_1 and r_2 values.

MNPs	M_s (emu/g_{Fe+Mn})		H_c (Oe)		SLP [b] (W/g_{Fe+Mn})	r_1 [c] (mM_{Fe+Mn}^{-1} s^{-1})	r_2 [c] (mM_{Fe+Mn}^{-1} s^{-1})
	5K	300K	5K	300K			
Pd/Fe|(0.5 Mn)-oxide	140	112	308	20	386	8.74 ± 0.3	443
Pd/Fe|(0.25 Mn)-oxide	95	83	240	12	352	5.95± 0.4	404
Pd/Fe-oxide[a]	-[c]	-[c]	67	12	233	-[d]	440

[a] from Exp_10mg, [b] measured at 346 kHz, 19.1 mT, SLP error ≤ 5-10%, [c] measured at 1.5 T and 25 °C; [d] not measured.

Both magnetization curves at 5 K display a hysteretic behaviour with substantial coercivity (Table 4.1), which indicates a typical behaviour of superparamagnetic MNPs below their blocking temperature. On the other hand, the MNPs exhibit characteristics of the superparamagnetic state at 300 K, with some low remained coercivity that can be attributed to complex interactions, such as frustrated order or spin canting phenomena.[25] Interestingly, the coercivity values at both 5 K and 300 K are also higher for the Pd/Fe|(0.5 Mn)-oxide MNPs, with higher content of Mn in their

composition. Coercivity, like saturation magnetization, is mainly related to the increase of anisotropy, which in turn is higher for higher Mn-doping contents. The same trend of coercivity with doping amount was also recorded in the studies of Jalili et al.,[10] Fantechi et al.,[11] and Sytnyk et al.[22]

Pd/Fe|Mn-oxide MNPs as hyperthermia/thermal ablation agents

Thermal therapies in oncology refer to hyperthermia, which entails an in vivo temperature increase that sensitizes (41-46 °C) other therapies like chemo- and radiotherapy or thermal ablation (>46 °C), which causes a targeted ablation and cell death, and is meant as surgery replacement.[1,26] There are two main mechanisms responsible for the heat dissipated by MNPs exposed to an alternating magnetic field (AMF), dependent on their sizes. At large enough sizes, the MNPs are in multi-domain regime, and the heating arises from hysteresis losses. For small sizes that ensure superparamagnetism, as is the current case of Pd/Fe|Mn-oxide MNPs, the heating effects are attributed to Néel and Brownian relaxation mechanisms.[1,5,27]

It is known that magnetic anisotropy plays a critical role in SLP enhancement,[8] thus, the heating efficacy of the two Pd/Fe|Mn-oxide NPs batches with different Mn doping amounts was tested. For this, the MNPs were first transferred to aqueous media by providing their surface with hydrophilic DSPE-PEG_{2000}-COOH surfactant. Subsequently, the samples containing Pd/Fe|Mn-oxide MNPs dispersed in approx. 1 mL of water were subjected to an alternating magnetic field at the frequency of 346 kHz and a field strength of 19.1 mT. The ability of MNPs to generate heat under AMF exposure is characterized by the specific loss power (SLP).[1,28] Hence, the heating efficiency expressed as SLP was determined for both batches of Pd/Fe|Mn-oxide NPs based on the Eq.1:

$$\mathrm{SLP}\ [\mathrm{W/g_{Fe+Mn}}] = \frac{\mathrm{C}}{\mathrm{m_{Fe+Mn}}}\frac{\Delta \mathrm{T}}{\Delta \mathrm{t}} \quad (1)$$

where C is the heat capacity of the sample, m_{Fe+Mn} is the sum of the masses of Fe and Mn in the colloidal NPs suspension, determined by ICP_OES, and $\Delta T/\Delta t$ is the temperature increase measured with time.

The Pd/Fe|(0.5 Mn)-oxide exhibited an SLP value of 386 W/g_{Fe+Mn}, while Pd/Fe|(0.25 Mn)-oxide MNPs generated a lower value of 352 W/g_{Fe+Mn}. However, both SLP values obtained are higher in comparison to the SLP of 233 W/g_{Fe} obtained for Pd/Fe-oxide NPs (Exp_10mg). The SLP is directly influenced by both extrinsic parameters such as frequency, amplitude of the magnetic field applied and media viscosity,[9] as well as intrinsic parameters like size, magnetocrystalline/shape anisotropy, and surface functionalization, as the latter creates changes in local magnetization at the surface of the MNPs.[9] The three aforementioned batches of MNPs presented similar sizes/shapes and were transferred to aqueous media by functionalization via the same procedure using the same hydrophilic surfactant. Additionally, the heating efficiency for all batches was assessed similarly, via MNPs exposure to the same AMF (346 kHz, 19.1 mT). Therefore, the better heating efficiency of Pd/Fe|Mn-oxide NPs over the Pd/Fe-oxide NPs can be attributed to the Mn doping of the Fe-oxide coating and the doping amount. These results are in agreement with the consensus in literature that doping increases the crystalline anisotropy, playing a critical role in SLP enhancement.[1,8,9]

Pd/Fe|Mn-oxide MNPs as MR imaging agents

MRI is a well-known, non-invasive high-resolution imaging technique in medicine that generates anatomical images based on the differences in relaxation of water protons around solid tissue and the surrounding biological media in the presence of magnetic field. The proton relaxation rates can be altered by administration of contrast agents, generating improved MRI sensitivity and contrast enhancement of the images. MRI contrast agents function by reducing either the longitudinal (T_1) or the transversal (T_2) relaxation times of protons in the target tissue, generating T_1-weighted images that give positive (bright) image contrast and T_2-weighted images that result in negative (dark) contrast, respectively.[5,8,29] T_1 contrast agents are mostly based on paramagnetic ions like Gd^{3+} and Mn^{2+} in the form of ion-complexes, while T_2 contrast agents are mainly based on superparamagnetic NPs. The efficacy of contrast agents is evaluated in terms of relaxivities (r_1 or r_2).[8] Doping of Pd/Fe-oxide with paramagnetic manganese renders these MNPs interesting candidates for generating both T_1 and T_2 contrast. To evaluate this, T_1 and T_2 measurements were

performed on the two batches of Pd/Fe|Mn-oxide NPs after their transfer to aqueous media with DSPE-PEG$_{2000}$-COOH. Results summarized in Table 4.1 demonstrate that both MNPs batches express r_2-relaxivities comparable to those of Pd/Fe-oxide NPs and additional increased r_1-relaxivities. Interestingly, the r_1 value is higher for Pd/Fe|(0.5 Mn)-oxide (8.74 mM_{Fe+Mn} s^{-1}) compared to Pd/Fe|(0.25 Mn)-oxide (5.95 mM_{Fe+Mn} s^{-1}), which is expected since former MNPs contain a higher amount of paramagnetic Mn. Additionally, according to Li et al.[30], T_1-effect is dominated by the presence of Mn^{2+}-ions at the surface of the MNPs, which is the exact case of the MNPs from the Pd/Fe|(0.5 Mn)-oxide batch, as confirmed by the EDS analysis. Figure 4.4 demonstrates an indication of the T_1 contrast enhancement generated by both Pd/Fe|Mn-oxide NPs, with a higher contrast measured for Pd/Fe|(0.5 Mn)-oxide NPs.

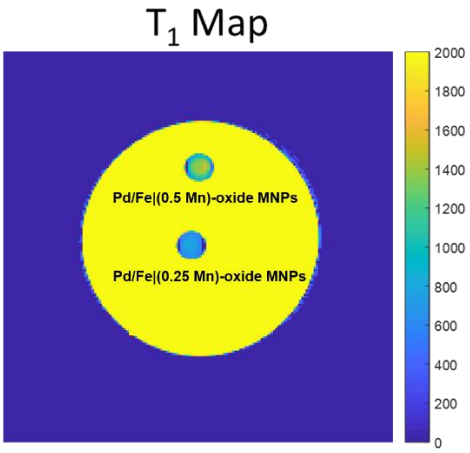

Figure 4.4. T_1 mapping measured at 1.5T and 25 °C on agar phantoms containing Pd/Fe|(0.25 Mn)-oxide (top) and Pd/Fe|(0.5 Mn)-oxide (bottom) nanoparticles.

To gain more insight into the interplay of the magnetic components constituting the MNPs (i.e. Fe and Mn), electron paramagnetic resonance (EPR) spectra of dry Pd/Fe|Mn-oxide NPs with different Mn-content were recorded at room temperature and the obtained parameters are summarized in Table 4.2. As shown in Figure 4.5A, the EPR active spins of both samples resulted in broad spectra ranging from 1500 to 4500 Gauss.

Table 4.2. The EPR parameters of Pd/Fe|(0.5 Mn)-oxide and Pd/Fe|(0.25 Mn)-oxide NPs.

MNPs	H_r[a] (mT)	ΔH_{pp}[b] (mT)	P_{asy}[c]	g_{peak}[d]	$g_{crossover}$[f]	g_{valley}[g]
Pd/Fe|(0.25 Mn)-oxide	250	147	2.03	3.35	2.44	1.96
Pd/Fe|(0.5 Mn)-oxide	326	155	0.82	2.78	2.07	1,72

[a] resonance field; [b] line width; [c] the ratio of the amplitude of the peak above and below the baseline; [d] g-factor at the positive peak the EPR signal; [f] g-factor at H_r; [g] g-factor at the negative peak the EPR signal. $g = \frac{h \cdot \nu}{\mu_B \cdot B}$ with h = Planck constant, ν = microwave frequency (9.78 Hz), μB = Bohr magneton, B = magnetic field (T). The g-factor for a free electron in vacuum g_e = 2.00232.

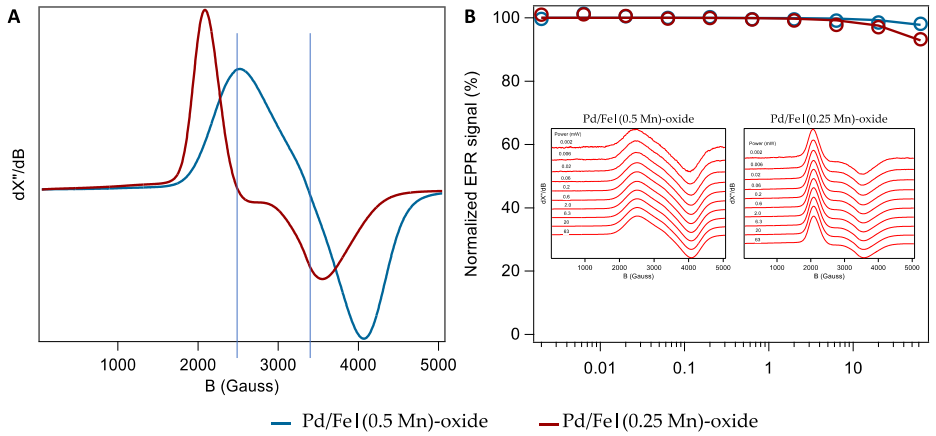

Figure 4.5. EPR date obtained on superparamagnetic hybrid nanoparticles with different Mn-content Pd/Fe|(0.5 Mn)-oxide and Pd/Fe|(0.25 Mn)-oxide: **A**) EPR spectra of the powder samples. The signal intensity of the two spectra were normalized to their maximal signal amplitude. EPR conditions: microwave frequency, 9.78 GHz; microwave power, 20 mW, modulation frequency, 100 kHz, modulation amplitude, 5 Gauss; room temperature.; **B**) Power saturation curves, with insets representing the spectra corresponding to each power data point. EPR conditions: microwave frequency, 9.78 GHz; microwave power, 0.002-63 mW, modulation frequency, 100 kHz, modulation amplitude, 2.5 Gauss; room temperature.

The power saturation behaviour of the EPR signals in both cases shows almost no saturation, confirming the fast relaxation of the spins (Figure 4.5B). The slight decrease in signal intensity at maximal power (200 mW), being more pronounced for Pd/Fe|(0.25 Mn)-oxide NPs, indicates slower relaxation for the less Mn-containing MNPs. This is consistent with the larger ΔH_{pp} for Pd/Fe|(0.5 Mn)-oxide NPs, which represents a shorter spin lifetime for the more Mn-containing NPs.

The line shape of Pd/Fe|(0.25 Mn)-oxide NPs nanoparticles corresponds to a so-called Dysonian line, which is determined by the diffusion of electrons, the penetration

depth of the microwaves and relaxation time, while the more symmetrical line shape of Pd/Fe|(0.25 Mn)-oxide NPs resembles those observed for superparamagnetic iron oxide NPs.[31] According to Dyson theory, the symmetry parameter P_{asy} is correlated with the ratio of electron diffusion and spin lifetime T_D/T_{spin}. Since the spin lifetime T_{spin} (inversely proportional to the ΔH_{pp}) contains both T_1 and T_2 relaxation in metals, the calculated P_{ass} value for Pd/Fe|(0.5 Mn)-oxide is significantly lower compared to the less Mn-containing NPs.

Finally, for the nanoparticles to be either positive or dual T_1/T_2 contrast agents, the ratio r_2/r_1 should be close to 1, whereas larger values generally mean the preference for a T_2 contrast.[32] However, as they are meant for intratumoural injection, high concentrations required for thermal treatments in combination with high r_2-relaxivities may cause artefacts during the T_2-weighted imaging. Therefore, the T_1 contrast can be helpful until the MNPs start diffusing.

Pd- and Mn-leakage studies

Since the designed Pd/Fe|Mn-oxide NPs are intended for biomedical applications, a primordial requirement is their biocompatibility. Palladium is considered toxic for the human body, being hypothesized that the effects of Pd metal are mediated via the presence or release of Pd ions, which are capable of eliciting a series of cytotoxic effects *in vitro*.[33] Manganese toxicity (manganism) is rarely encountered but represents a serious health hazard, resulting in severe pathologies of the central nervous system.[34,35] The manganese cytotoxicity arises from the triggering of apoptosis in cells accumulating toxic doses of Mn. Depending on the comorbid disease state or dietary variation, bodily efflux and pancreatic elimination may be dysfunctional, in which case, the cellular efflux of Mn may also be affected. Changes in glutamate and glutamine metabolism and use, mitochondrial function, and triggering of cellular apoptosis and necrosis comprise the cellular responses to manganism, which eventually result in the neuropsychiatric manifestations of Mn toxicity.[34] Therefore, with biomedical applications in mind, a study was conducted to simulate and determine the amount of Pd and Mn leak from the MNPs. To assess this, Pd/Fe|Mn-oxide NPs functionalised with DSPE-PEG_{2000}-COOH were dispersed

in 1 mM EDTA solution, a widely used compound in leakage studies as it binds to di- and trivalent metal ions.[36] The MNPs after 24 h, 48 h and 7 days were filtered in an Amicon tube with a 30 kDa MWCO membrane and the filtrates were analysed by ICP-MS for both palladium and manganese content (Table 4.3).

Table 4.3. Pd and Mn leakage from Pd/Fe|Mn-oxide NPs at different time points.

Time	Pd (μg)	% Pd leaked from total amount of NPs	Mn (μg)	% Mn leaked from total amount of NPs
24 h	0.019	0.00081	0.196	0.0081
48 h	0.017	0.00071	0.113	0.0047
7 d	0.016	0.00066	0.096	0.0039

Negligible amounts of Pd and Mn (μg), close to the detection limit of the ICP-MS were found in the supernatants. The iron oxide coating encapsulating the Pd-core and the surfactant layers create a sufficient barrier to prevent any Pd or Mn leakage, and therefore, the Pd/Fe|Mn-oxide NPs can be considered stable for the biomedical use.

4.4 Conclusion

This chapter focused on the assessment of the effects of manganese doping on the properties and performance of Pd/Fe-oxide NPs as thermal and MR-imaging agents. For this, a seed-mediated thermal decomposition method that generated Pd/Fe|Mn-oxide with different Mn-doping amounts was established. Subsequently, the presence and position of Pd, Fe, and Mn in the composition of the MNPs and the doping amounts were confirmed through EDS mapping analysis. The Pd/Fe|Mn-oxide MNPs were synthesized with similar sizes and shapes to Pd/Fe-oxide NPs, in order to enable their comparison. Via SQUID magnetometry, the Mn-doped MNPs were identified as superparamagnetic, with high saturation magnetization values and low coercivities. An increase in both M_s and H_c with Mn-content in the composition of the hybrid MNPs was recorded, in accordance with other literature studies. To test their performance in hyperthermia/thermal ablation, the Pd/Fe|Mn-oxide MNPs were transferred to aqueous media with DSPE-PEG_{2000}-COOH surfactant, exposed to AMF, and their SLPs values were calculated. The hybrid MNPs doped with the highest Mn amount performed best as thermal agent, with highest SLP value recorded. The SLP values obtained for the two batches of Pd/Fe|Mn-oxide MNPs were higher in comparison to the one of their Pd/Fe-oxide analogues. Lastly, the performance of these hybrid MNPs as T_1 and T_2 contrast agents was assessed via MRI measurements. Both Pd/Fe|Mn-oxide MNPs batches showed r_2-relaxivities comparable to those of Pd/Fe-oxide NPs and additional increased r_1-relaxivities, with higher T_1 contrast enhancement measured for Pd/Fe|(0.5 Mn)-oxide MNPs compared to their non-doped analogues. Therefore, the possibility of boosting the magnetic properties of NPs via increasing their magnetocrystalline anisotropy through Mn-doping was showed.

Bibliography

1. Blanco-Andujar, C.; Walter, A.; Cotin, G.; Bordeianu, C.; Mertz, D.; Felder-Flesch, D.; Begin-Colin, S. Design of iron oxide-based nanoparticles for MRI and magnetic hyperthermia.
2. Jang, J.T.; Nah, H.; Lee, J.H.; Moon, S.H.; Kim, M.G.; Cheon, J. Critical enhancements of MRI contrast and hyperthermic effects by dopant-controlled magnetic nanoparticles. *Angew Chem Int Ed Engl* **2009**, *48*, 1234-1238, doi:10.1002/anie.200805149.
3. Song, L.; Yan, C.; Zhang, W.; Wu, H.; Jia, Z.; Ma, M.; Xie, J.; Gu, N.; Zhang, Y. Influence of Reaction Solvent on Crystallinity and Magnetic Properties of MnFe₂O₄ Nanoparticles Synthesized by Thermal Decomposition. *Journal of Nanomaterials* **2016**, *2016*, 4878935, doi:10.1155/2016/4878935.
4. Park, Y.; Demessie, A.A.; Luo, A.; Taratula, O.R.; Moses, A.S.; Do, P.; Campos, L.; Jahangiri, Y.; Wyatt, C.R.; Albarqi, H.A., et al. Targeted Nanoparticles with High Heating Efficiency for the Treatment of Endometriosis with Systemically Delivered Magnetic Hyperthermia. *Small* **2022**, *18*, e2107808, doi:10.1002/smll.202107808.
5. Kolhatkar, A.G.; Jamison, A.C.; Litvinov, D.; Willson, R.C.; Lee, T.R. Tuning the magnetic properties of nanoparticles. *Int J Mol Sci* **2013**, *14*, 15977-16009, doi:10.3390/ijms140815977.
6. Issa, B.; Obaidat, I.M.; Albiss, B.A.; Haik, Y. Magnetic nanoparticles: surface effects and properties related to biomedicine applications. *Int J Mol Sci* **2013**, *14*, 21266-21305, doi:10.3390/ijms141121266.
7. Lavorato, G.C.; Das, R.; Alonso Masa, J.; Phan, M.-H.; Srikanth, H. Hybrid magnetic nanoparticles as efficient nanoheaters in biomedical applications. *Nanoscale Advances* **2021**, *3*, 867-888, doi:10.1039/D0NA00828A.
8. Wu, L.; Mendoza-Garcia, A.; Li, Q.; Sun, S. Organic Phase Syntheses of Magnetic Nanoparticles and Their Applications. *Chemical Reviews* **2016**, *116*, 10473-10512, doi:10.1021/acs.chemrev.5b00687.
9. Cotin, G.; Perton, F.; Blanco-Andujar, C.; Pichon, B.; Mertz, D.; Bégin-Colin, S. Chapter 2 - Design of Anisotropic Iron-Oxide-Based Nanoparticles for Magnetic Hyperthermia. In *Nanomaterials for Magnetic and Optical Hyperthermia Applications*, Fratila, R.M., De La Fuente, J.M., Eds. Elsevier: 2019; https://doi.org/10.1016/B978-0-12-813928-8.00002-8pp. 41-60.
10. Jalili, H.; Aslibeiki, B.; Ghotbi Varzaneh, A.; Chernenko, V.A. The effect of magneto-crystalline anisotropy on the properties of hard and soft magnetic ferrite nanoparticles. *Beilstein Journal of Nanotechnology* **2019**, *10*, 1348-1359, doi:10.3762/bjnano.10.133.
11. Fantechi, E.; Campo, G.; Carta, D.; Corrias, A.; de Julián Fernández, C.; Gatteschi, D.; Innocenti, C.; Pineider, F.; Rugi, F.; Sangregorio, C. Exploring the Effect of Co Doping

in Fine Maghemite Nanoparticles. *The Journal of Physical Chemistry C* **2012**, *116*, 8261-8270, doi:10.1021/jp300806j.

12. Lee, J.-H.; Huh, Y.-M.; Jun, Y.-w.; Seo, J.-w.; Jang, J.-t.; Song, H.-T.; Kim, S.; Cho, E.-J.; Yoon, H.-G.; Suh, J.-S., et al. Artificially engineered magnetic nanoparticles for ultra-sensitive molecular imaging. *Nature Medicine* **2007**, *13*, 95-99, doi:10.1038/nm1467.
13. Jeon, M.; Halbert, M.V.; Stephen, Z.R.; Zhang, M. Iron Oxide Nanoparticles as T(1) Contrast Agents for Magnetic Resonance Imaging: Fundamentals, Challenges, Applications, and Prospectives. *Adv Mater* **2021**, *33*, e1906539, doi:10.1002/adma.201906539.
14. Jeun, M.; Lee, S.; Kyeong Kang, J.; Tomitaka, A.; Wook Kang, K.; Il Kim, Y.; Takemura, Y.; Chung, K.-W.; Kwak, J.; Bae, S. Physical limits of pure superparamagnetic Fe3O4 nanoparticles for a local hyperthermia agent in nanomedicine. *Applied Physics Letters* **2012**, *100*, 092406, doi:10.1063/1.3689751.
15. Lin, F.-h.; Chen, W.; Liao, Y.-H.; Doong, R.-a.; Li, Y. Effective approach for the synthesis of monodisperse magnetic nanocrystals and M-Fe3O4 (M = Ag, Au, Pt, Pd) heterostructures. *Nano Research* **2011**, *4*, 1223-1232, doi:10.1007/s12274-011-0173-2.
16. Mazumder, V.; Sun, S. Oleylamine-Mediated Synthesis of Pd Nanoparticles for Catalytic Formic Acid Oxidation. *J Am Chem Soc* **2009**, *131*, 4588-4589, doi:10.1021/ja9004915.
17. Fantechi, E.; Roca, A.G.; Sepúlveda, B.; Torruella, P.; Estradé, S.; Peiró, F.; Coy, E.; Jurga, S.; Bastús, N.G.; Nogués, J., et al. Seeded Growth Synthesis of Au–Fe3O4 Heterostructured Nanocrystals: Rational Design and Mechanistic Insights. *Chemistry of Materials* **2017**, *29*, 4022-4035, doi:10.1021/acs.chemmater.7b00608.
18. Sun, S.; Zeng, H.; Robinson, D.B.; Raoux, S.; Rice, P.M.; Wang, S.X.; Li, G. Monodisperse MFe2O4 (M = Fe, Co, Mn) Nanoparticles. *J Am Chem Soc* **2004**, *126*, 273-279, doi:10.1021/ja0380852.
19. Jin, Y.; Jia, C.; Huang, S.-W.; O'Donnell, M.; Gao, X. Multifunctional nanoparticles as coupled contrast agents. *Nature Communications* **2010**, *1*, 41, doi:10.1038/ncomms1042.
20. Thangavel, K.; Saritas, E.U. Aqueous paramagnetic solutions for MRI phantoms at 3 T: A detailed study on relaxivities. *Turk J Electr Eng Co* **2017**, *25*, 2108-2121, doi:10.3906/elk-1602-123.
21. Barral, J.K.; Gudmundson, E.; Stikov, N.; Etezadi-Amoli, M.; Stoica, P.; Nishimura, D.G. A robust methodology for in vivo T1 mapping. *Magn Reson Med* **2010**, *64*, 1057-1067, doi:10.1002/mrm.22497.
22. Sytnyk, M.; Kirchschlager, R.; Bodnarchuk, M.I.; Primetzhofer, D.; Kriegner, D.; Enser, H.; Stangl, J.; Bauer, P.; Voith, M.; Hassel, A.W., et al. Tuning the Magnetic Properties of Metal Oxide Nanocrystal Heterostructures by Cation Exchange. *Nano Letters* **2013**, *13*, 586-593, doi:10.1021/nl304115r.
23. Song, Q.; Ding, Y.; Wang, Z.L.; Zhang, Z.J. Tuning the Thermal Stability of Molecular Precursors for the Nonhydrolytic Synthesis of Magnetic MnFe2O4 Spinel Nanocrystals. *Chemistry of Materials* **2007**, *19*, 4633-4638, doi:10.1021/cm070990o.

24. Mahmood, A.; Maqsood, A.; Abdi, A. Effect of manganese doping on the structural, mechanical, optical, and magnetic properties of zinc ferrite nanoparticles. *Physica Scripta* **2022**, *97*, 065707, doi:10.1088/1402-4896/ac6f2a.
25. Skumryev, V.; Stoyanov, S.; Zhang, Y.; Hadjipanayis, G.; Givord, D.; Nogués, J. Beating the superparamagnetic limit with exchange bias. *Nature* **2003**, *423*, 850-853, doi:10.1038/nature01687.
26. Mornet, S.; Vasseur, S.; Grasset, F.; Duguet, E. Magnetic nanoparticle design for medical diagnosis and therapy. *Journal of Materials Chemistry* **2004**, *14*, 2161-2175, doi:10.1039/B402025A.
27. Gazeau, F.; Lévy M Fau - Wilhelm, C.; Wilhelm, C. Optimizing magnetic nanoparticle design for nanothermotherapy.
28. Natividad, E.; Castro, M.; Mediano, A. Adiabatic vs. non-adiabatic determination of specific absorption rate of ferrofluids. *Journal of Magnetism and Magnetic Materials* **2009**, *321*, 1497-1500, doi:https://doi.org/10.1016/j.jmmm.2009.02.072.
29. Ganapathe, L.S.; Mohamed, M.A.; Mohamad Yunus, R.; Berhanuddin, D.D. Magnetite (Fe3O4) Nanoparticles in Biomedical Application: From Synthesis to Surface Functionalisation. In *Magnetochemistry*, 2020; Vol. 6.
30. Li, M.; Bao, J.; Zeng, J.; Huo, L.; Shan, X.; Cheng, X.; Qiu, D.; Miao, W.; Zhu, X.; Huang, G., et al. Engineering manganese ferrite shell on iron oxide nanoparticles for enhanced T1 magnetic resonance imaging. *Journal of Colloid and Interface Science* **2022**, *626*, 364-373, doi:https://doi.org/10.1016/j.jcis.2022.06.118.
31. Stefani, C.; Langenberg, E.; Cordero-Edwards, K.; Schlom, D.G.; Catalan, G.; Domingo, N. Mechanical reading of ferroelectric polarization. *J Appl Phys* **2021**, *130*, 074103, doi:10.1063/5.0059930.
32. Peters, J.A.; Djanashvili, K. Lanthanide Loaded Zeolites, Clays, and Mesoporous Silica Materials as MRI Probes. *European Journal of Inorganic Chemistry* **2012**, *2012*, 1961-1974, doi:https://doi.org/10.1002/ejic.201101195.
33. Kielhorn, J.; Melber, C.; Keller, D.; Mangelsdorf, I. Palladium--a review of exposure and effects to human health. *Int J Hyg Environ Health* **2002**, *205*, 417-432, doi:10.1078/1438-4639-00180.
34. Evans, G.R.; Masullo, L.N. Manganese Toxicity. In *StatPearls*, Treasure Island (FL) ineligible companies. Disclosure: Lawrence Masullo declares no relevant financial relationships with ineligible companies., 2023.
35. Keen, C.L.; Zidenberg-Cherr, S. MANGANESE. In *Encyclopedia of Food Sciences and Nutrition (Second Edition)*, Caballero, B., Ed. Academic Press: Oxford, 2003; https://doi.org/10.1016/B0-12-227055-X/00732-Xpp. 3686-3691.
36. Mohammadi, Z.; Shalavi, S.; Jafarzadeh, H. Ethylenediaminetetraacetic acid in endodontics. *Eur J Dent* **2013**, *7*, S135-S142, doi:10.4103/1305-7456.119091.

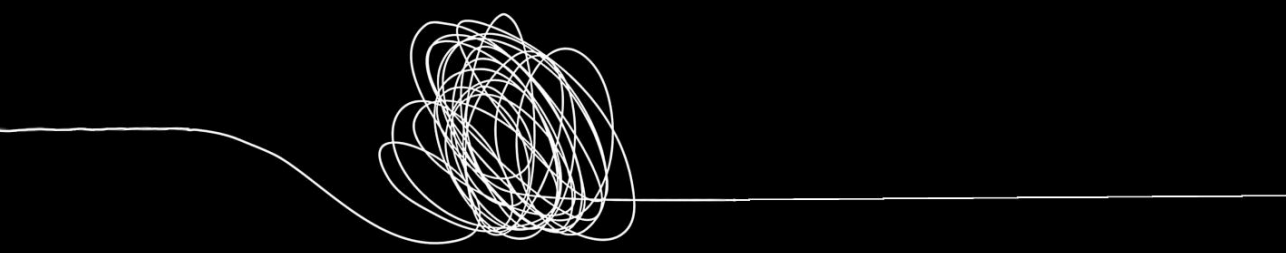

Synthesis and preliminary biological evaluation of theranostic ^{103}Pd:Pd/Fe-oxide nanoparticles

5

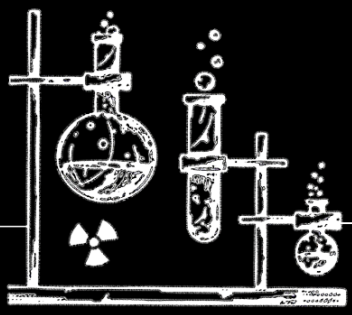

Abstract: To this day, cancer remains one of the leading causes of death worldwide. Surgery, chemotherapy and radiotherapy are the most common cancer treatments used in clinical practices, with associated limitations and multiple side effects. However, the current advances in nanotechnology, specifically on multi-functional theranostic NPs that can simultaneously deliver therapy and enable follow-up of the effect via imaging, in combination with the more common early detection of cancer, open the possibility for alternative treatments, that can offer more precise diagnostic and therapeutic regimes. Nanobrachytherapy is conducted via injection of radioactive NPs into the tumour and its great advantages are the preservation of the characteristics of brachytherapy, such as precise and targeted dose delivery, while allowing less invasive administration. The main disadvantage, the radioresistance exhibited by tumour cells, can be overcome via combination with hyperthermia, a heating treatment. Thermal ablation, heating treatment with even higher temperatures, is proposed as a surgery replacement. Due to the advances in nanotechnology, magnetic nanoparticles can deliver heat when exposed to an alternating magnetic field. Hence, the synergy between these two treatments and the possibility for both to be delivered via NPs stands as the basis for the superior hybrid magnetic NPs that we envision as theranostic agents for cancer treatment. In this study, we explore the synthetic conditions for manufacturing novel ^{103}Pd:Pd/Fe-oxide theranostic nanoparticles, composed of a palladium core containing its ^{103}Pd radioisotope, meant to deliver the required dose for nanobrachytherapy, and an iron oxide shell responsible for generation of heat for hyperthermia/thermal ablation and contrast enhancement in magnetic resonance imaging (MRI). In this chapter, we developed routes for radiolabelling Pd/Fe-oxide hybrid nanoparticle with ^{103}Pd radioisotope and investigated the radiolabelling efficiency. Subsequently, *in vitro* studies on spheroids of the breast cancer cell line MDA-MB-231 were conducted with the non-radioactive NPs to assess their biocompatibility and determine uptake. Lastly, the efficacy of the ^{103}Pd:Pd/Fe-oxide MNPs as nanobrachytherapy and hyperthermia/thermal ablation agents were assessed on the same 3D models.

Keywords: hybrid nanoparticles, ^{103}Pd radionuclide, iron oxide, nanobrachytherapy, hyperthermia/thermal ablation, theranostics

---

The content of this chapter was partially filed for:

EU-patent, *No. 2029314*, "Synthesis of Hybrid Palladium (103)/iron Oxide Nanoparticles for Thermo-brachy Therapy", **2021.**

5.1 Introduction

To this day, cancer remains one of the leading causes of death worldwide and the survival rates have only been improved slightly over the past few decades.[1,2] Despite advances in oncology, treatments such as surgery, chemotherapy, and radiotherapy are still the most commonly used clinical practices, with associated limitations and multiple side effects.[3,4] However, biocompatible, multifunctional nanosystems, which represent the most challenging innovation in medicine, are capable of revolutionizing the fields of imaging and therapy, allowing their simultaneous application for cancer treatment, namely theranostics. Such multi-functional theranostic nanoparticles (NPs) can simultaneously treat and enable following up the therapeutic effect through imaging. Being able to combine the two functionalities in one entity, while avoiding the side effects presented by the conventional cancer therapies employed in clinics, may boost the emerging market of nanotechnology in biomedicine.[5] Additionally, the number of patients diagnosed with cancer in incipient stages is constantly increasing.[6,7] Therefore, the advances in nanotechnology for cancer treatment along with its increasingly accessible early detection open the possibility for alternative treatments, which can develop more precise diagnostic and therapeutic regimens, thus, specifically treat the cancerous cells while reducing the damage to the surrounding areas. Such therapies bear an enormous potential for tailored treatments according to the patient needs.

Radiotherapy (RT) is a well-established method for treating cancer and in current practice, more than half of cancer patients receive RT either as a primary treatment or an adjuvant mode along with other therapies.[4] Particularly interesting is a type of internal RT, known as brachytherapy (BT), conducted by placing the radiation sources inside or in close proximity to the tumour, enabling delivery of high radiation doses precisely to the tumour volume, while minimizing radiation exposure of the healthy tissues and organs at risk. For BT, implants containing radionuclides that ensure a low/high-dose rate are widely used in the treatment of prostate and breast cancers and preclinical and clinical studies employing BT have reported promising results.[4,8] However, the treatment necessitates the insertion of tens of seeds per tumour, and the logistical and operational difficulties associated with seed placement

have impeded its fully successful application. Moreover, the millimetric seeds are relatively big compared to the dimensions of an incipient tumour, thus, insertion causes trauma and edema, which results in inaccurate or off-target placement of the seeds and high discomfort for the patient. Additionally, in BT, the dose gradients are very steep, and the dose delivered to tumours falls off sharply with increasing distance from the seeds, which can lead to either inhomogeneous dose distribution to the tumour, or exposure of the surrounding normal tissues to high doses of radiation.[4,8]

Based on the aforementioned advances in nanotechnology, preclinical studies on localized delivery of radioactive NPs into the tumour, analogous to BT, have been reported in literature.[9-11] This technique is termed as nanobrachytherapy, in which injection of the radioactive NPs is used as an alternative to the radioactive seed implantation. Such an unconventional BT procedure has great advantages as it retains the characteristics of BT, such as precise and targeted dose delivery while allowing less invasive administration by intratumoral injection. In this way, the radiation dose can be delivered in several fractions, convenient for patient-specific treatments. Once injected, due to their nanometre size, the NPs can diffuse and improve the homogeneity of the dose distribution within the tumour volume. Lastly, such strategy would also alleviate inflammation, often caused by insertion of multiple millimetric-sized radioactive seeds within the tumour.[4,8]

Successful nanobrachytherapy relies on the same criteria handled for the conventional seed-based approach: precise placement of the radiation source and the right choice of the radionuclide. For small tumours in incipient stages or cluster tumour cells, radionuclides emitting Auger electrons are considered to be beneficial, especially for the treatment of solid tumours like breast and prostate cancers. The reason behind is the higher cytotoxicity caused by these low-energy electrons (few keV) with short range in the biological tissues (few nm).[4] ^{103}Pd radionuclide has been long used in seed-based BT, and recent preclinical studies with tumour-bearing xenograft models showed its potential for nanobrachytherapy.[4] This radionuclide decays by electron capture (EC) emitting Auger electrons according to Scheme 5.1.

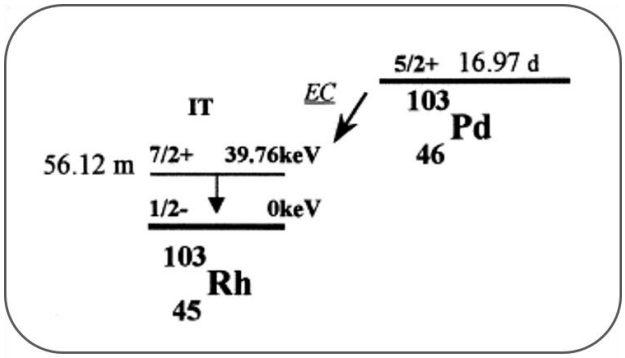

Scheme 5.1. Decay scheme for ^{103}Pd.[12]

The low-energy X-ray (21 keV) photons emitted by ^{103}Pd are attenuated by a few mm of biological tissue, which is a great advantage over high-energy emitters, since it confines the radiation inside the tumour.[4,9,12]

With such short penetration depth, patients are not required to be isolated and admitted in the hospital to minimize the risk of radiation exposure to the general public, as there is none.[13] Moreover, the half-life of 17 days makes ^{103}Pd radionuclide a great candidate for low dose rate BT, as it is able to deliver the dose with an acceptable dose rate for such application while, at the same time, enables shipping and storage. Lastly, the ^{103}Pd-NPs are expected to diffuse slowly inside the tumour and eventually be cleared from the area at a much slower pace than the half-life of the radionuclide. Overall, ^{103}Pd is a perfect candidate for depositing therapeutic radiation in tumours.

Even though brachytherapy is such a promising tool for cancer treatment, it may not always be enough to affect the tumour completely as the poorly vascularized hypoxic core of the tumour exhibits resistance to ionizing radiation, which limits, at times, BT to be used as the main therapeutic modality. However, the cancerous cells residing in the hypoxic core of tumours being more acidotic, and thus, less sensitive to radiation, can actually be more sensitive to thermal damage. From the available heating treatments, hyperthermia, procedure in which the temperature of a part or the body is increased up to 44-46 °C, is already used as adjunctive therapy with established cancer treatments such as external radiotherapy, to boost the therapeutic effects.[14] It has great potential to sensitize tumour cells to be killed by ionizing

radiation, attributed to the fact that heat is a pleiotropic damaging agent, affecting multiple cell components to different degrees by altering protein structures, hence influencing the DNA damage response. Overall, there is great synergy between hyperthermia and radiation as cancer treatment modalities, as the intent of hyperthermia is to raise the temperature of the target tissue to alter its physiology and biology, which in practice translates to a greater response of the tumours to other therapeutic modalities, such as radiation.[15-17] From the heating medical treatments, apart from hyperthermia, thermal ablation has also great potential as adjuvant therapy together with radiation, being an effective surgery replacement, as elevated temperatures above 48-50 °C cause direct tissue necrosis.[7,16] For example, nowadays, the treatment for early-stage detected breast tumours often includes surgery, where most of the tumour is removed, followed by external beam radiotherapy applied to the whole breast to kill any remaining cancer cells. This treatment is effective, but also comes with significant side effects. Therefore, replacing surgery with thermal ablation, which would enable minimally invasive tumour eradication, followed by BT as an alternative to the external beam radiation, to ensure the full elimination of any remaining tumour cells post-ablation, would offer a superior treatment with fewer side effects and improved well-being for patients.[6]

Despite the clear advantage of heating treatments, the current methods of attaining, maintaining and monitoring such treatments suffer from inadequacies.[15] As other therapies, heating treatments also require to be tumour-focused, minimally invasive and more uniform in heat generation. In this direction, same as for BT, current developments in nanotechnology make possible to employ heat-generating NPs that can be activated by an external magnetic field. These nanometre scale heat sources have decisive advantages, as they can be injected directly into tumour through a variety of non-invasive techniques, plus they generate heat homogeneously.[16] Among the different nanostructures designed for therapeutic uses, magnetic NPs (MNPs) generate heat efficiently when subjected to an alternating magnetic field. From this category, iron oxide NPs that are nontoxic, nonimmunogenic, biocompatible and stable, are exceptional candidates. Moreover, iron oxide NPs also enable diagnosis via magnetic resonance imaging (MRI) through acceleration of transversal relaxation times of water protons in their proximity, resulting in

darkening of the contrast. Taking into consideration the previously discussed synergistic effects between heating and radiation treatments and the great opportunities coming from the developments in hybrid NPs, designing such multi-functional nanosystems capable of two treatments and imaging, can be the key to enable a superior image-assisted cancer treatment avoiding most of the side effects typical for conventional therapies.

Based on the study of van Oossanen et al.,[6] the dose distribution of such a hybrid MNP is comparable with current commercial brachytherapy seeds, while anisotropy of the dose distribution is reduced. This decreases the dependence of dose distribution on seed orientation, simplifying surgical placement of MNPs. Lastly, the same study explained that variations in shell thickness only led to changes in the dose profile between 2×10^{-4} mm and 3×10^{-4} mm radial distance to the hybrid NP, therefore, not affecting the long-range dose. This offers great flexibility in tuning the size of the iron oxide shell in which ^{103}Pd is encapsulated to satisfy the necessary requirements for high heat generation and imaging, without influencing the dose distribution.

In this chapter, we explore the synthetic conditions for manufacturing Pd/Fe-oxide hybrid nanoparticles in their radioactive form (^{103}Pd:Pd/Fe-oxide NPs) and investigate their effect using 3D models of spheroids from MDA-MB-231 cell line, derived from human breast adenocarcinoma. Two different approaches for radiolabelling of the hybrid nanoparticles with the ^{103}Pd radionuclide were tested, and the radiolabelling efficiency was investigated for the successful method. Subsequently, *in vitro* studies were conducted first, with the hybrid NPs in their non-radioactive form in order to determine their biocompatibility and uptake by spheroids. Lastly, the combined therapeutic effects of ^{103}Pd radiation and hyperthermia/thermal ablation delivered via ^{103}Pd:Pd/Fe-oxide NPs on the same 3D models were investigated. To the best of our knowledge, this is a novel proposal for combining radiotherapy, heating and imaging in a single nanoparticle design.

5.2 Materials and methods

Reagents

[^{102}Pd]Pd metallic powder 90% enriched purchased from Buyisotope.com, Neonest AB. Glacial acetic acid, nitric acid 69% (HNO_3), palladium powder, Pd(II)-acetylacetonate ($Pd(acac)_2$), 1-octadecene (ODE), oleic acid (OA), oleylamine (OAm), iron pentacarbonyl ($Fe(CO)_5$), ethanol, hexane, chloroform, palladium (II) acetate, tert-butylamine-borane complex (BTB), 1,2-distearoyl-sn-glycero-3-phosphoethanolamine-*N*-[carboxy(polyethylene glycol)-2000] sodium salt, powder ($DSPE\text{-}PEG_{2000}\text{-}COOH$), ethylenediaminetetraacetic acid disodium salt dehydrate (EDTA), and sodium hydroxide (NaOH) were obtained from Sigma Aldrich. All chemicals were used as received without further purification.

Pd(II) acetate synthesis

Synthesis of Pd(II) acetate was conducted according to a procedure presented by Cotton et al.[18] Briefly, 0.3 g palladium powder were suspended in 20 mL glacial acetic acid and 300 μL concentrated HNO_3 (69%) were slowly added under stirring. Next, the reaction mixture was heated to reflux (b.p. acetic acid 118 °C) and kept for 30 min, while stirring and bubbling nitrogen through the mixture. The reaction mixture was cooled to room temperature and the obtained product was isolated via filtration and evaporation.

^{103}Pd radionuclide

The [^{103}Pd]Pd metallic powder was obtained by exposure of 0.5 mg of purchased [^{102}Pd][Pd] 90% enriched powder in a quartz vial to thermal neutron flux at the TU Delft Reactor Institute: thermal flux 4.9 x 10^{16} $s^{-1}m^{-2}$, epithermal flux 9.3 x 10^{14} $s^{-1}m^{-2}$ and fast neutrons flux 3.6 x 10^{15} $s^{-1}m^{-2}$. The obtained [^{103}Pd]Pd metallic powder was used as such without further purification.

Synthesis of ^{103}Pd:Pd NPs

The palladium-103 radionuclide available as a powder was converted into its ionic form prior to the synthesis by solubilisation in aqua regia to obtain a ^{103}Pd stock

solution. ^{103}Pd:Pd NPs were synthesized by following a similar procedure, based on previously published protocols,[19,20] as applied for the synthesis of cold OAm-capped Pd NPs, with slight modifications. Briefly, Pd(II) acetate (56 mg, 0.249 mmol) was added to 15 mL OAm in a 3-neck round-bottom flask and the volume (μL) of ^{103}Pd stock solution in aqua regia necessary to achieve the desired activity in the yielding NPs was added to the mixture. The reaction mixture was next heated to 60 °C in 10 min under a stream of nitrogen gas and vigorous stirring. In parallel, tert-butylamine-borane complex (130 mg, 1.495 mmol) was dissolved in 3 mL OAm and injected into the reaction mixture via a septum, once the temperature reached 60 °C. After addition, the reaction mixture was further heated to 90 °C with a heating rate of 3 °C/min and kept at this temperature for 60 min. After 60 min, the reaction system was left to cool down to room temperature and the ^{103}Pd nanoparticles were collected by addition of 30 mL ethanol and centrifugation for 8 min at 10500 RPM (11830 ×g) multiple times. The ^{103}Pd:Pd NPs were stored as such until further use. The final product was redispersible in organic solvents such as toluene, hexane, and chloroform.

Synthesis of ^{103}Pd:Pd/Fe-oxide NPs

For the synthesis of ^{103}Pd:Pd/Fe-oxide NPs, an iron oxide shell was added via the same classical thermal decomposition procedure on top of the pre-made radioactive ^{103}Pd:Pd-seeds, by following a previously published protocol with slight modifications.[21] OAm-capped ^{103}Pd:Pd NPs (10 or 20 mg, 0.094/0.188 mmol) were dispersed in approximatively 0.5 mL hexane and sonicated for 5 min. Next, the ^{103}Pd:Pd-seeds in hexane were added to a 3-neck round bottom flask containing 20 mL ODE, OA (1 mL, 3.14 mmol) and OAm (1 mL, 3.14 mmol). The reaction mixture was slowly heated to 120 °C under nitrogen flow and vigorous stirring and left at this temperature for 30 min to ensure the complete removal of hexane. Subsequently, iron pentacarbonyl (150 μL, 1.141 mmol) was injected into the reaction vessel via a septum and the reaction system was heated to 300 °C with a heating rate of 5 °C/ min and kept at this temperature for 30 min. After that, the reaction system was left to cool down to room temperature and the ^{103}Pd:Pd/Fe-oxide nanoparticles were collected by addition of 30 mL ethanol and centrifugation at 10500 RPM (11830 ×g) for 4-6 min.

The procedure was repeated several times with ethanol and one or two times with a combination of ethanol and hexane in equal volumes. Lastly, the ^{103}Pd:Pd/Fe-oxide nanoparticles were dried by a gentle flow of nitrogen/compressed air and stored as such until further use. The final product could be redispersed in organic solvents such as toluene, hexane, and chloroform.

Dispersion of ^{103}Pd:Pd/Fe-oxide NPs in aqueous media with DSPE-PEG$_{2000}$-COOH

The synthesized ^{103}Pd:Pd/Fe-oxide NPs were transferred into water by modification with DSPE-PEG$_{2000}$-COOH following a slightly modified protocol presented elsewhere.[22] Firstly, the ^{103}Pd/Fe-oxide NPs were dispersed in the necessary amount of chloroform to obtain a concentration of 1 mg NPs/mL. After addition of chloroform, the solution was stirred and sonicated to ensure a good colloidal system. Next, 1 mg ^{103}Pd:Pd/Fe-oxide NPs in 1 mL chloroform were pipetted into a glass vial containing 1.5 mg DSPE-PEG$_{2000}$-COOH. The vials were sonicated for 5-10 minutes and left open for 24 h for slow evaporation of the solvent, until a pasty precipitate remained at the bottom. The residual solid was additionally flushed with nitrogen for 1-2 minutes, to ensure complete removal of chloroform. Next, 1 mL of Milli-Q water was added to the precipitate and sonicated for 15 min until a colloidal suspension in aqueous media was obtained. The colloidal suspension of NPs was transferred into Eppendorf vials and the unbound polymer, excess lipids were removed by centrifugation for 1h at 19600 RPM (30000 ×g), and the supernatant was removed. This procedure was repeated twice. Lastly, the NPs were collected in 1-2 mL of Milli-Q water in an Eppendorf and kept as such for further use.

Pd leakage study

Pd/Fe-oxide NPs (1 mg) were transferred into aqueous media with DSPE-PEG$_{2000}$-COOH. Subsequently, the NPs were resuspended in 0.5 mL 1 mM EDTA solution, previously brought to pH 7.4 with 0.1 M NaOH solution. The NPs were left in suspension for 24h, after which they were added to an Amicon Ultra Centrifugal tube with a centrifugal concentrator Ultracel - 30 kDa MWCO regenerated cellulose membrane and centrifuged for 20 min at 4200 RPM. Lastly, the filtrate was collected and analysed on ICP-MS to check the Pd content. The 1 mg of Pd/Fe-oxide NPs were

resuspended in 0.5 mL EDTA solution, and the same procedure was repeated after 48h and 7 days.

Characterization

IR spectroscopy was conducted on the powder using KBr pellets. Approximatively 0.5 g KBr and 1 mg product powder were mixed and pulverized into small granular powder. Next, the powder was inserted into a pellet-forming dye and was subjected to 10 tons pressure in vacuum, resulting in a transparent cylindrical pellet. The same procedure was carried out for pure KBr powder to produce a blank pellet for background measurement.

^{1}H NMR analysis was performed on Agilent 400-MR DD2, operating at the frequency of 399.7 MHz. The samples were prepared in deuterated chloroform ($CDCl_3$) in 5 mm NMR tubes.

Particle size, size distribution and morphology of the Pd-seeds and Pd/Fe-oxide NPs samples were determined by transmission electron microscopy (TEM), using a 120 kV Jeol_JEM1400 microscope. All samples for TEM were prepared by drop-casting a diluted nanoparticle suspension in organic solvents such as hexane on a Quantifoil R1.2/1.3 Cu300 grid and evaporating the solvent at room temperature. The mean diameter and the size distribution of the samples were obtained by statistical analysis of around 200-300 NPs, by analyzing the obtained TEM images with ImageJ software.

The count rates of ^{103}Pd were determined with a Perkin Elmer 2480 automated γ-counter WALLAC for multiple supernatants obtained through the ^{103}Pd:Pd-seeds and ^{103}Pd:Pd/Fe-oxide nanoparticles cleaning procedure.

Magnetic characterization by superconducting quantum interference device (SQUID), was carried out on an MPMS XL magnetometer from Quantum Design, using about 1–2 mg of dried Pd/Fe-oxide NPs powder. The hysteresis loops M(H) obtained under continuously varying applied magnetic field up to a maximum of ±50 kOe at 5 K and 300 K were used for evaluation of saturation magnetization (M_s) and coercivity (H_c).

The heating power measurements were performed using the Magnetherm Digital, manufactured by Nanotherics, using a 50 mm coil device. An alternating magnetic field (AMF) was applied on the samples containing 1 mL suspension of Pd/Fe-oxide

or ^{103}Pd:Pd/Fe-oxide NPs placed in the middle of the coil in an isolated sample holder to reduce heat loss to the environment. The temperature was equilibrated until it varied less than 0.05 °C/min before the measurement was conducted. The sample was then exposed to a magnetic field with a frequency of 346 kHz and a field strength of 19.1 mT. Two glass-fiber optic thermometers [Osensa PRB-G40_2.0M-STM-MRI] were used to monitor the temperature at the bottom as well as at the core of the sample. The latter was used to calculate specific loss power (SLP) produced by nanoparticles expressed in W/g_{Fe}. The concentration of iron was determined by the ICP-OES or ICP-MS on the same samples after destruction of the NPs in aqua regia (HNO_3 + 3HCl).

***In vitro* studies**

Cell culture. Breast cancer cell line (MDA-MB-231) was kindly provided by the Department of Genetics, Erasmus MC. The cells were cultured in high glucose (4.5 g/L) Dulbecco's Modified Eagle's Medium (DMEM) with 10% fetal bovine serum and 1% penicillin (6 mg/L) and streptomycin (10 mg/L) (Biowest). The cells were incubated at 37 °C and 5% CO_2. Cells were counted using the automated Luna2 cell counter (Westburg) to determine the cell concentration.

Preparation of MDA-MB-231 spheroids. MDA-MB-231 spheroids were produced using the liquid overlay technique in cell repellent U-shaped 96-well plates (Greiner Bio-one GmbH, CELLSTAR®). Cells were seeded in concentrations of 2000 cells/well in DMEM culture medium with 3.5% Matrigel, followed by centrifugation (1000 RPM for 10 min at 10 °C) (Eppendorf centrifuge 5810 R). Each treatment group consisted of 6 spheroids.

Spheroid viability assay. The viability of the spheroids was determined by Glo3D viability assay (Promega), a method that determines the number of viable cells in 3D cultures by quantifying the concentration of ATP. A Glo3D reagent caused cell lysis by breaking down cell membranes leading to release of ATP, which in presence of the enzyme luciferase and substrate luciferin emitted luminescence signal. The

viability of the cells was determined based on the linear relationship between the luminescence signal and the cell number.

Characterization of spheroid growth rate. The spheroids were imaged using a 12 MP camera mounted on a binocular microscope using automated imaging software (SampleScan). The diameter of the spheroids was measured using the open-source image processing software ImageJ. The diameter and volume were hence determined based on the 2D area measurement, with the assumption that the spheroid is a perfect sphere.

Biocompatibility of Pd and Pd/Fe-oxide NPs with MDA-MB-231 spheroids. The biocompatibility of Pd NPs was tested in the concentration range of 10 - 250 μg/mL, whereas the biocompatibility of Pd/Fe-oxide MNPs was tested in the concentration range of 125 - 1000 μg/mL NPs for 7 days after MDA-MB-231 spheroid formation. Both NPs solutions were prepared from a stock of 10 mg/mL NPs, freshly prepared in MilliQ water before use. Suspensions with different concentrations of Pd NPs (10, 50 and 250 μg/mL) and Pd/Fe-oxide MNPs (125, 250, 500 and 1000 μg/mL) were freshly prepared in cell culture medium prior to the treatment of spheroids. Spheroids in only medium were used as positive control, whereas spheroids in 10% DMSO were used as negative control. Each treatment group consisted of 6 spheroids. The NPs were incubated with the spheroids on day 7 and the spheroids viability and growth rate (diameter and volume) were assessed at day 14 post incubation.

Uptake of Pd/Fe-oxide MNPs by MDA-MB-231 spheroids. Pd/Fe-oxide MNPs uptake in MDA-MB-231 spheroids was followed over a period of 7 days. Each spheroid was exposed to 100 μL of a 500 μg/mL concentration Pd/Fe-oxide NPs in each well. The spheroids were collected at different time points namely, 1h, 3h, 24h, 72h and 168h. Each spheroid was washed gently twice with phosphate buffer saline (PBS) and collected in a vial for quantification of Fe and Pd elements by ICP-MS. The obtained amounts were used to determine the percentage of Pd/Fe-oxide NPs uptake in the spheroids at different time intervals.

Spheroid processing and embedding for histology. Spheroids were slowly collected by aspiration in a 1.5 mL Eppendorf vial and rinsed with PBS. 4% cold paraformaldehyde was used to fix the spheroids for 30 min at room temperature. Post-fixation, spheroids were rinsed in PBS (twice) by slow aspiration. Using wide bore pipet tips, spheroids were transferred to the centre of a disposable biopsy mould, covered with a few drops of molten HistoGel, and then transferred to a cold surface for rapid solidification for 5 min. Solidified HistoGel with spheroids was demoulded, transferred to a labelled tissue cassette and placed in a container with 70% alcohol. HistoGel embedded spheroids were later processed into paraffin in an automated tissue processor. After paraffin infiltration, each cassette was placed in a molten paraffin to embed in desired orientations and then transferred to cold plate.

Prussian blue staining protocol. Spheroids embedded in paraffin were cut in 4 μm slices using microtome and placed on microscope slides (Ultra). Next, they were deparaffinised (3 × 3 min xylene), rehydrated (ethanol series, 1 min each: 100%, 100%, 95%, 95%, 80%, 79%, 50%) and incubated for 1 min in demi-water. A mixture of potassium ferrocyanide and hydrochloric acid solutions in equal volumes was prepared to obtain the iron staining solution (one use only). Subsequently, the slides were incubated in the iron staining solution for 5 min at room temperature. After the incubation, the slides were rinsed gently with distilled water and dehydrated (ethanol series, 1 min each: 95%, 100%, 100%). Each slice was cleared using xylene for 3 min (twice) and mounted using Pertex mouting medium.

Radiotherapeutic effect of ^{103}Pd. The radiotherapeutic effect of ^{103}Pd was investigated by exposure of MDA-MB-231 spheroids to a varying range of ^{103}Pd radioactivities, namely, 50 kBq, 100 kBq, 200 kBq and 400 kBq. Based on the biocompatibility study conducted on Pd NPs, a concentration of 50 μg/mL [^{103}Pd]Pd metallic powder was chosen, to avoid interference of palladium toxicity itself with the results. Similarly, as a control, spheroids were also exposed to non-radioactive Pd solutions with the same concentration of 50 μg/mL Pd metallic powder. The ^{103}Pd/Pd stock solutions were prepared using ^{103}Pd/Pd in aqua regia (54 μL) neutralized to pH 7.2 using sodium hydroxide (NaOH, 10M and 0.1M) and diluted with sterile PBS. The ^{103}Pd/Pd treatment solutions were freshly prepared using neutralized ^{103}Pd/Pd stock in cell

culture medium, made prior to the treatment of spheroids. Each treatment group consisted of 6 spheroids. Different radiation doses of ^{103}Pd or non-radiation doses of Pd were introduced in each spheroid on day 6. Subsequently, the spheroids viability and growth rate (diameter and volume) were determined at day 13 post incubation.

^{103}Pd:Pd/Fe-oxide NPs as thermo-brachytherapy agents. Spheroids were treated using ^{103}Pd:Pd/Fe-oxide MNPs with 1 mg/mL (approx. 50 kBq) or 10 mg/mL (approx. 500 kBq) concentration. The following thermal doses were selected based on clinical relevance and thermal ablation reference, which were delivered via heating with the two concentrations of radioactive MNPs.

Table 5.1. Thermal doses delivered to MDA-MB-231 spheroids via ^{103}PdPd/Fe-oxide NPs.

	Temperature (˚C)	**Time (min)**	**CEM43 °C[b]**
Control	37	-	0
42˚C	42	60	15 CEM43 °C
43˚C	43	30	30 CEM43 °C
45 ˚C	45	30	120 CEM43 °C
50 ˚C	50	22/7[a]	-

[a]22 and 7 minutes were required to reach thermal ablation (50 ˚C) with 1 mg/mL and 10 mg/mL ^{103}Pd:Pd/Fe-oxide MNPs concentration, respectively. [b]CEM43 °C was determined according to the formula $CEM43\,°C = \sum_{i=1}^{n} t_i \cdot R^{(43-T_i)}$, where CEM43 °C is the cumulative number of equivalent minutes at 43 °C, t_i is the i-th time interval, R is related to the temperature dependence of the rate of cell death (R = 0.25 for T < 43 °C, R = 0.5 for T > 43 °C and T_i is the average temperature during time interval t_i.[23]

The NP heating experiments were performed using the MagneTherm Digital device, manufactured by NanoTherics Ltd, with a 50 mm diameter coil. The device was connected to a water cooler/heater and the coil cooling water temperature was set to 37 °C. The experiments were conducted with a frequency of 346 kHz and a maximum magnetic field strength of 19.1 mT.

It is important to mention the limit on the maximum magnetic field strength and frequency of an AMF that can be safely applied to patients. The reported AMF limit is around $5{\cdot}10^9$ $Am^{-1}s^{-1}$ for hyperthermia applications using coils of around 10 cm.[24,25] This AMF limit is expressed as the product of magnetic field strength (*H*-field) and frequency (s^{-1}). As our setup is calibrated using the magnetic flux density field (*B*-field), closely related to *H*-field as follows from equation $B = \mu_0\mu_r H$, the AMF limit

can be rewritten as approximatively $6.3 \cdot 10^9$ Ts^{-1}, assuming $\mu_r \approx 1$ for air. If the AMF limit is exceeded, eddy currents might be induced in healthy tissue, causing unwanted and unselective heating, and eventually burns. Through this study , we are very close to the less rigid Hergt-Dutz limit mentioned above.

Inside the coil, an isolating sample holder made of polystyrene was placed to prevent heat losses of the sample to the environment. The sample holder was also necessary to ensure the sample was positioned in the centre of the coil, where the magnetic field strength was maximal. Just before heating, the spheroids were transferred to a vial containing 1 mL colloidal solution of 1 or 10 mg ^{103}Pd:Pd/Fe-oxide MNPs in cell medium and placed in the incubator at 37 °C. The plastic vial had a total volume of 2 mL and a screw cap with 1 mm hole. A glass fibre thermometer (Osensa PRB-G40_2.0M-STM-MRI sensor, compatible with strong magnetic fields) was carefully inserted through the hole in the cap. The thermometer was placed at the bottom of the vial, next to the spheroids. The initial field strength was set to maximum to bring the sample to the programmed temperature as fast as possible. After reaching the desired temperature, the MagneTherm was changed to temperature control mode, in which the software automatically changed the field strength to maintain a constant temperature. The sample was kept at the desired temperature for the set time, after which the field was turned off. Immediately after, the sample was taken out to enable fast cooling. Subsequently, the spheroids were carefully washed with PBS and transferred to a 96-well plate. The spheroids treated with 1 or 10 mg/mL ^{103}Pd:Pd/Fe-oxide MNPs were divided into two groups, namely, Group I, not exposed to MNPs post thermal dose or Group II, exposed to 200 µL of 1 mg/mL ^{103}Pd:Pd/Fe-oxide MNPs colloidal solution post thermal dose. Each treatment group consisted of 6 spheroids. The treatment was initiated on spheroids between day 5 to day 8 and incubated post application of thermal doses. The spheroids viability was determined 3 and 7 days post incubation, whereas the growth rate (diameter and volume) was determined only on day 7 post incubation.

Statistical analysis. Quantitative results were assessed with ANOVA to show the statistical significance within groups of spheroids. For all statistical analyses, a value of p was considered significantly different if $*p \leq 0.05$; $**p \leq 0.01$; $***p \leq 0.001$; $****p \leq 0.0001$ and a 95% confidence interval.

5.3 Results and discussion

Synthesis of ^{103}Pd(II)-acetate

Since the ^{103}Pd radionuclide is supplied in powder form, but the synthesis of OAm-capped Pd NPs employs a palladium precursor in the form of Pd(II)-acetate salt, the [^{103}Pd]Pd metallic powder cannot be used as such and extra steps need to be taken prior to the synthesis. The full procedure is shown in Scheme 5.2A. The first step in this approach consists of the synthesis of the Pd(II)-acetate salt in its radioactive form, starting from the available [^{103}Pd]Pd metallic powder. The synthesized ^{103}Pd(II)-acetate precursor is then used in the following step for preparation of ^{103}Pd NPs. These ^{103}Pd NPs are to be used as seeds to grow an iron oxide coating through the seed-mediated growth synthesis as described and conducted before (Chapter 2). Therefore, we started with the search for a good method to synthesize Pd(II)-acetate, first in its non-radioactive form, starting from Pd-powder similar to the one used as a ^{103}Pd-source. Wilkinson et al.[26] was the first reporting on synthesis of Pd(II)-acetate, and even though it is an old method, it is still the most commercially used route for producing Pd(II)-acetate.[27] Briefly, glacial acetic acid containing palladium powder is heated to reflux in the presence of a minimal amount of nitric acid, until the formation of brown NO_x fumes ceases, conform the reaction:

$$3\ Pd + 6\ HNO_3 + 6\ HOAc \longrightarrow Pd_3(OAc)_6 + 6\ NO_2 + 6\ H_2O \qquad (1)$$

Even though the synthesis seems trivial, it is not, and several studies in literature[18,27] corroborate that next to the desired Pd(II)-acetate, two common impurities $Pd_3(OAc)_5(NO_2)$, and the insoluble polymeric $[Pd(OAc)_2]_n$ are often present (Figure 5.1).

Formation of $Pd_3(OAc)_5(NO_2)$ by-product can be attributed to the attack of nitrogen oxides on the formed Pd(II)-acetate molecules. These oxides are generated during the oxidation of Pd-powder with nitric acid.[18]

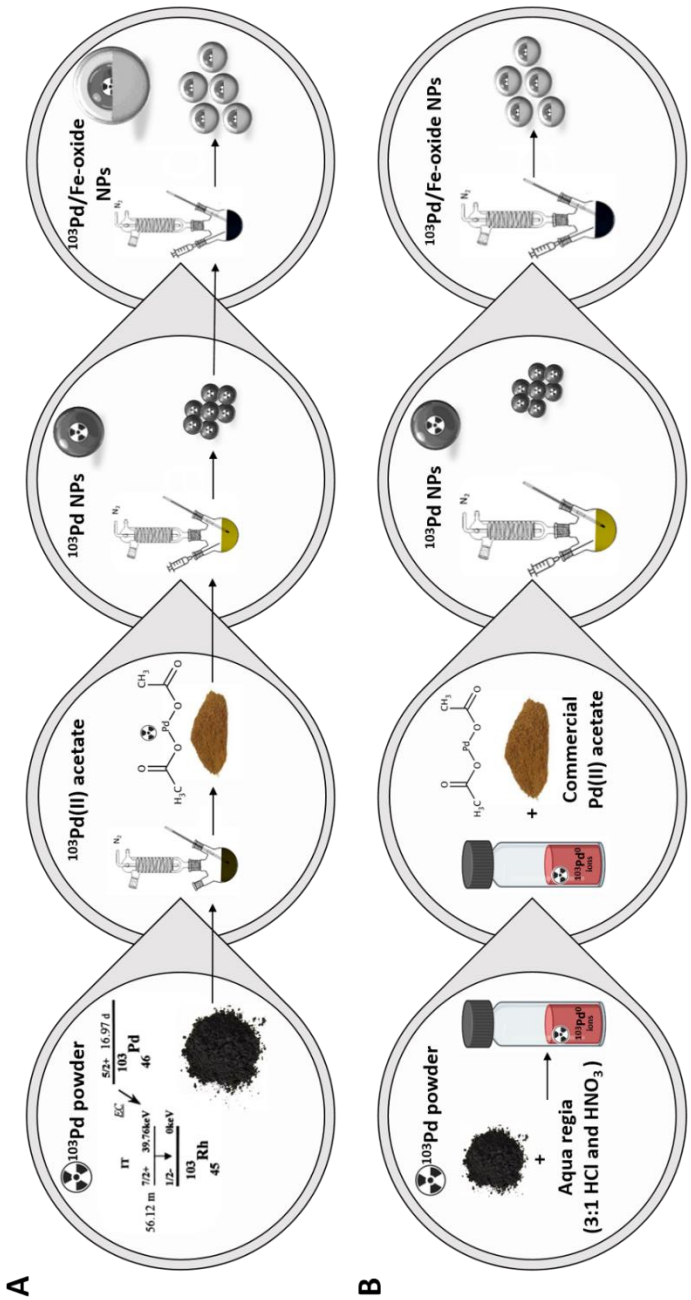

Scheme 5.2. Routes for preparation of ^{103}Pd radiolabelled Pd/Fe-oxide NPs via **(A)** ^{103}Pd(II)-acetate and **(B)** ^{103}Pd-powder solubilized in aqua regia.

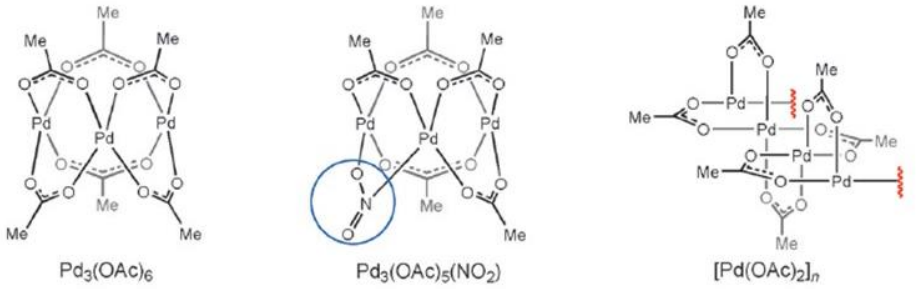

Figure 5.1. (A) Pd (II) species, identified as by-products originated from the Pd(II)-acetate formation reaction.[27]

However, Cotton's group reported a modified Wilkinson method in which nitrogen gas is bubbled through the reaction mixture in order to rapidly eliminate the formed NO_x fumes and prevent the formation of the two side-products mentioned above.[18] In this direction, we tried to mimic the synthesis method for Pd(II)-acetate reported by Cotton et al. Their synthesis follows a two-step procedure starting from palladium chloride ($PdCl_2$). First, the palladium chloride salt is transformed to palladium powder following the reaction:

$$PdCl_2 + NaO_2CH + NaOH \longrightarrow Pd + CO_2 + 2NaCl + H_2O \qquad (2)$$

Subsequently, the palladium powder is separated by filtration, washed with acetone and dried under vacuum. They report almost 100% yield, with a production of 0.3 g palladium powder from 0.5 g $PdCl_2$ starting material. The next step of the synthesis follows reaction (1).

As the radionuclide is available as powder, we skipped the first step of the procedure presented by Cotton et al. Initially, the synthesis was performed starting from palladium powder in its non-radioactive form and 0.3 g palladium powder were added to a reaction vessel containing acetic acid. Next, concentrated nitric acid was slowly added while stirring. The first problem noticed was the lack of solubility of the palladium powder precursor in the used solvents, even after slow addition of HNO_3. Nevertheless, the reaction was continued with heating the mixture to reflux (b.p. acetic acid is 118 °C) under continuous stirring, nitrogen atmosphere, and nitrogen bubbling. Cotton et al. describe that the solution is brought to reflux for 30

min and the volume of the solution is then reduced to a third of the original volume by slow evaporation using mild heating, with no specific instruction about the time or temperature used during the mild heating. As instructed, the reaction was brought to reflux and kept for 30 min, after which the temperature was decreased below the b.p. of acetic acid and left for several hours. However, no change in volume was observed during the heating step. Additionally, the Pd powder did not seem to solubilize even after reflux and long exposure to elevated temperature. By the end of the experiment, a black powder remained, clearly indicating the unreacted precursor, as the Pd(II)-acetate salt has typically an orange colour.

As solubility was a problem in the previously conducted experiment, we ran a second experiment following the same procedure, but with an excess of nitric acid, as an attempt to improve the solubility of the Pd-powder in the reaction mixture. After heating to reflux and maintaining the reaction for 30 min under reflux, an orange powder appeared on the edges of the liquid. After the 30 min, the temperature was decreased below reflux and maintained for several hours. Yet again, the volume was not reduced to a third as described by Cotton et al., thus, the reaction mixture was left overnight. The next day, the volume was still not reduced, but a brown liquid was formed and collected. By filtration, an orange-coloured powder was isolated from the reaction mixture. However, only 21.6 mg were collected as powder, and assuming this was pure Pd(II)-acetate, it would entail a yield of only 7.2 %. Despite the low yield, next step was to check if the produced powder was indeed Pd(II)-acetate. For this, IR analysis was carried out on a sample of commercially available Pd(II)-acetate and on the powder collected from the experiment described above. An overlay of the two spectra can be seen in Figure 5.2 for a direct comparison. From literature,[18] Pd(II)-acetate shows characteristic peaks in IR spectrum at the following wavelengths: 1600, 1430, 1350, 1157, 1047, 951, 696 and 625 cm^{-1}. As the spectrum is strongly muddled from noise between 400 and 900 cm^{-1}, the characteristic wavelengths at 625 and 696 cm^{-1} for Pd(II) acetate are not visible. Both commercial Pd(II)-acetate and the as-obtained powder clearly present the peak at 951 cm^{-1}. Not as clear, but visible, are small dips at 1350 cm^{-1} and broad dips at 1430 and 1600 cm^{-1} for both spectra. However, only the commercial Pd(II)-acetate showed peaks at the characteristic 1157 and 1047 cm^{-1}. Overall, it was concluded that the product powder

isolated from the experiment has a somehow similar structure to Pd(II)-acetate, but the absence of peaks at 1157 and 1047 cm^{-1} indicates that the desired product can either be in extremely low quantity, or one of the by-products was produced. Presence of the nitrate coupled by-product is, however, not a surprise, as the reaction was performed with an excess of HNO_3, in an attempt to increase the palladium powder solubility.

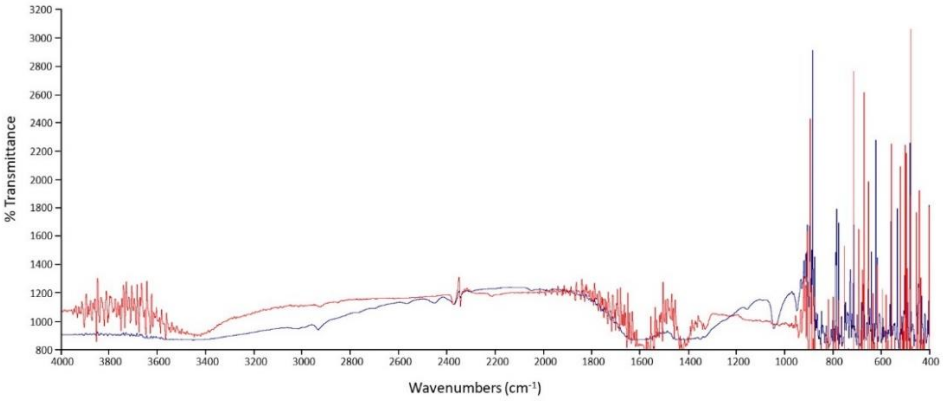

Figure 5.2. Overlay of commercial Pd(II)-acetate IR spectra (blue) and as-obtained powder from the experiment following Cotton et al. procedure, but conducted with HNO_3 excess.

As additional confirmation, ^1H NMR analysis was performed on the obtained powder solubilized in deuterated chloroform ($CDCl_3$). The obtained spectrum is shown in Figure 5.3A and was compared to available spectra of commercial Pd(II)-acetate, $Pd(OAc)_5(NO_2)$ by-product, where one acetate group is replaced by a nitrite group, and in-house prepared Pd(II)-acetate from the study of Cotton et al. (Figure 5.3B). The high peak at 2.10 ppm from the ^1H NMR spectrum of our powder product indicates the presence of acetic acid. The peak at 2 ppm is the characteristic peak for Pd(II)-acetate. This is indeed confirmation that Pd(II)-acetate was synthesized during the experiment, however, additional prominent peaks present at 2.07, 2.03 and 1.95 ppm indicate the presence of the nitrate coupled by-product, confirmed by the presence of similar peaks on the ^1H NMR spectrum (Figure 5.3B) of the $Pd_3(OAc)_5(NO_2)$ by-product from Cotton et al. Seemingly, the by-product was present in higher quantities than the desired product, which can be once again explained by the excess HNO_3 used during the experiment for boosting the solubility of the palladium powder.

Despite the excess of nitric acid used to perform the reaction, the high amount of by-product formed can also be due to a too low N_2 bubbling present during the experiment. With a closed system in nitrogen atmosphere, the pressure of the nitrogen for bubbling from outside through a needle was indeed very small. Additionally, the lack of specificity regarding the parameters used by Cotton et al., such as the temperature used during the mild heating phase and the time exposure that caused the reaction volume to decrease by up to a third, was puzzling, as in our case, the volume of the reaction mixture never dropped to one third of the initial amount.

In a third experiment, no excess of nitric acid was used, and the same precursor quantities, as used by Cotton et al., were employed. However, this time the reaction was brought to reflux, kept for 30 min under nitrogen atmosphere, and post reflux, the experiment was continued in open system, which allowed vigorous nitrogen bubbling and solvent evaporation. As a result, an oil-like substance was formed, rather than a powder, leaving again most of the palladium powder precursor unreacted. An attempt to remove the acetic acid under vacuum in a rotary evaporator was made, but the substance remained a viscous liquid that did not turn into a powder. Even so, the viscous liquid product obtained was solubilized in $CDCl_3$ and analysed. The obtained ^1H NMR spectrum is shown in Figure 5.3C. The presence of the peak at approx. 2 ppm is an indication that some Pd(II)-acetate was formed, but it is hugely overshadowed by the acetic acid peak at 2.10 ppm. The 1.88 ppm peak can be indication of a hydrolysed version of the Pd(II)-acetate salt, while the peak at 1.95 ppm corresponds again to the $Pd_3(OAc)_5(NO_2)$ by-product. Even though none of the other correspondent peaks for the by-product can be seen, it can simply be that they are completely overshadowed by the large acetic acid peak. Thus, this third attempt in synthesizing Pd(II)-acetate with high yield and purity was again unsuccessful. Several other experiments with minor variations were performed, however, the desired product was never obtained in a satisfactory manner and, even though, Cotton et al. reported production of pure Pd(II)-acetate in 94% yield, we were unable to reproduce this result. Similar to our study, there are other examples in literature such as by Carole et al.[27] and Stolyarov et al.[28] that were also unable to reproduce the results of Cotton et al.

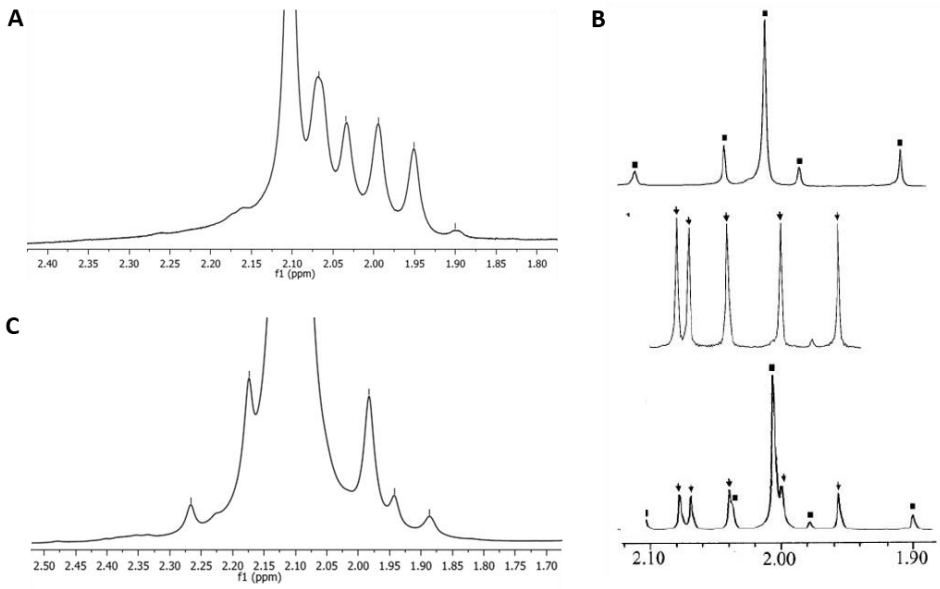

Figure 5.3. (A) ^{1}H NMR spectrum in $CDCl_3$ of the as-obtained powder from the experiment following Cotton et al. procedure, but conducted with HNO_3 excess; **(B)** ^{1}H NMR spectrum in $CDCl_3$ of commercial Pd(II)-acetate (top), by-product $Pd(OAc)_5(NO_2)$ (middle) and in-house prepared Pd(II)-acetate (bottom) by Cotton et al. Reproduced with permission from [18]; **(C)** ^{1}H NMR spectrum in $CDCl_3$ of the as-obtained powder from the experiment following Cotton et al. procedure, but conducted in open system post reflux.

As previously explained, the Pd(II)-acetate synthesis employed by Cotton et al. is a two-step procedure, starting with a first reaction in which $PdCl_2$ is used as precursor to generate Pd-powder, which is further employed as precursor to synthesize the Pd(II)-acetate salt in a second reaction step. As the ^{103}Pd radionuclide is available as a powder, in our case the first reaction step had to be skipped through the experiments and a commercially available Pd-powder was used as precursor, similar to the radioactive palladium. Therefore, the inability to solubilize the employed Pd-powder in the reaction mixture is a highlight on the importance of the palladium source. The same observation was also made by Carole et al. in his study after multiple attempts to mimic the system and obtain the same palladium source failed.

Even though the excess of nitric acid helps to improve solubility, it also leads to generation of more NO_x fumes, which results in undesired by-products. Therefore, what seemed to be a solution for one problem, only generated another.

Lastly, there are other methods in literature presenting synthesis of Pd(II)-acetate from different starting materials. However, as the radioactive material is available in the form of [^{103}Pd]Pd metallic powder, it is futile to investigate such attempts, as it implies conversion of the radioactive palladium source to a Pd-salt, meaning extra steps with increased risk of contamination. Therefore, another route was developed in order to synthesize the Pd NPs in their radioactive form.

Synthesis of ^{103}Pd:Pd NPs

As production of palladium precursor salt in its radioactive form was not successful, a different approach (Scheme 5.2B) to introduce the desired radionuclide in the reaction mixture was designed. The concept behind this approach was to integrate the palladium radionuclide into the composition of the nanoparticles without converting it to a palladium salt first. During the procedure, the [^{103}Pd]Pd metallic powder was first solubilized in aqua regia and introduced as such in the reaction mixture together with the commercially available Pd(II)-acetate, both intended to work as palladium precursors during the synthesis. The radioactive palladium in aqua regia was fully solubilized, thus in the form of $^{103}Pd^{2+}$ ions. During the synthesis, in the presence of the OAm weak reductant, together with the co-reductant BTB and the temperature increase, thermal decomposition is triggered and the Pd(II)-acetate salt decomposes, releasing Pd^{2+} ions. The free $^{103}Pd^{2+}$ and Pd^{2+} ions existent in the reaction mixture and surrounded by surfactant molecules act as monomers and start the nucleation and subsequent growth process, in accordance with LaMer's theory, resulting in radioactive palladium nanoparticles consisting of both radioactive and non-radioactive palladium.

As [^{103}Pd]Pd metallic powder is introduced during the synthesis as solubilized in aqua regia, the presence of such strong acid is a new parameter that could influence the reaction mechanism. However, because the as-synthesized ^{103}Pd:Pd NPs could not be visualized via TEM while still radioactive, a study on the effect of aqua regia on the synthesis was first conducted by synthesizing two non-radioactive Pd NPs batches under previously described conditions, with addition of 15 and 100 μL aqua regia, respectively. Subsequently, the Pd NPs synthesized in the presence of aqua regia were visualized via TEM (Figure 5.4A,B) and their size and morphology were assessed.

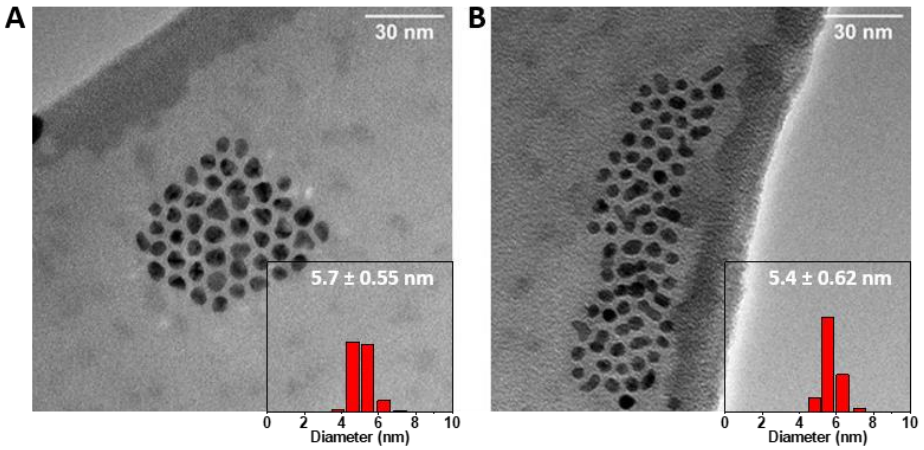

Figure 5.4. OAm-capped Pd NPs synthesized in presence of **(A)** 15 μL and **(B)** 100 μL aqua regia.

As the result, the Pd NPs synthesized with different volumes of aqua regia presented the same spherical morphology, independent of the quantity of aqua regia added during the experiment. Most probably, the high acidity of aqua regia assisted the breakdown of the Pd(II)-acetate precursor, without later interference with the growth-process. The presence of an acid is known to play a role in precursor reduction, meaning an excess of reducing power can increase the rate of monomer generation during the nucleation phase. Excess of monomers usually translates into more nucleation centres, which can lead to smaller sized nanoparticles.[29,30] However, this was not reflected through the aforementioned experiments, and the Pd NPs retained the same 5 nm size they had as a result of thermal decomposition conducted without aqua regia. Overall, no obvious influence on the outcome of the Pd NPs using different quantities of aqua regia in the synthesis was noticed from the TEM images. The presence of acid could also influence the surface charges of the nanoparticles, which may play a role in stabilizing the formed monomer-ligand complexes during the nucleation phase. If the presence of acid has an effect on the surface charges during the synthesis, the functionalization of the Pd NPs post-synthesis may differ when the synthesis is conducted in presence of aqua regia. In order to confirm that the surface of the Pd-seeds is preserved and behaves similarly to those prepared without aqua regia, the Pd-seeds synthesized in the presence of 15 μL aqua regia were used to conduct Exp_Standard, as presented in Chapter 2 of this thesis, in which an

iron oxide shell was grown on top of the pre-formed Pd-seeds via thermal decomposition. Additionally, it was highly important to understand if there is any influence on the nucleation or growth processes of iron oxide during the synthesis, by verifying if the resulting Pd/Fe-oxide NPs retain same sizes, morphology, magnetic properties and heating ability. Figure 5.5 displays the Pd/Fe-oxide NPs obtained via thermal decomposition (Exp_standard procedure) by employing Pd-seeds synthesized with 15 μL aqua regia. As shown, the hybrid nanoparticles maintained the same spherical-squared morphology and sizes as the NPs from Exp_standard presented in Chapter 2 of this thesis.

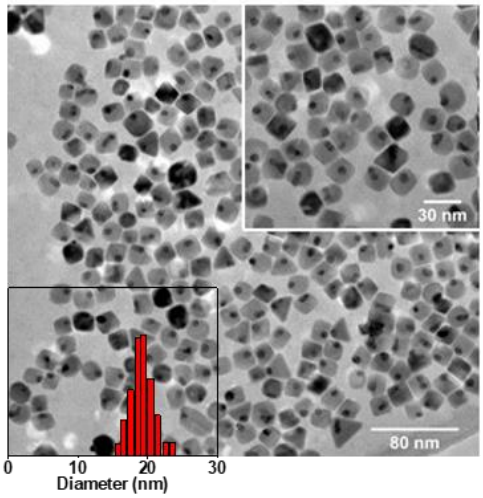

Figure 5.5. TEM image and size distribution of Pd/Fe-oxide obtained via thermal decomposition using Pd-seeds synthesized in the presence of 15 μL aqua regia.

However, even though the synthesized NPs are very similar in terms of size and morphology, the most important aspect is their final heating performance. Therefore, the magnetic properties were investigated next (Figure 5.6A,B) and the results of this experiment and classical Exp_standard conducted with OAm-capped Pd seeds synthesized without aqua regia were compared. As shown in Table 5.2, the magnetic properties of both types of nanoparticles are nearly the same, and negligible differences are within the experimental variation range.

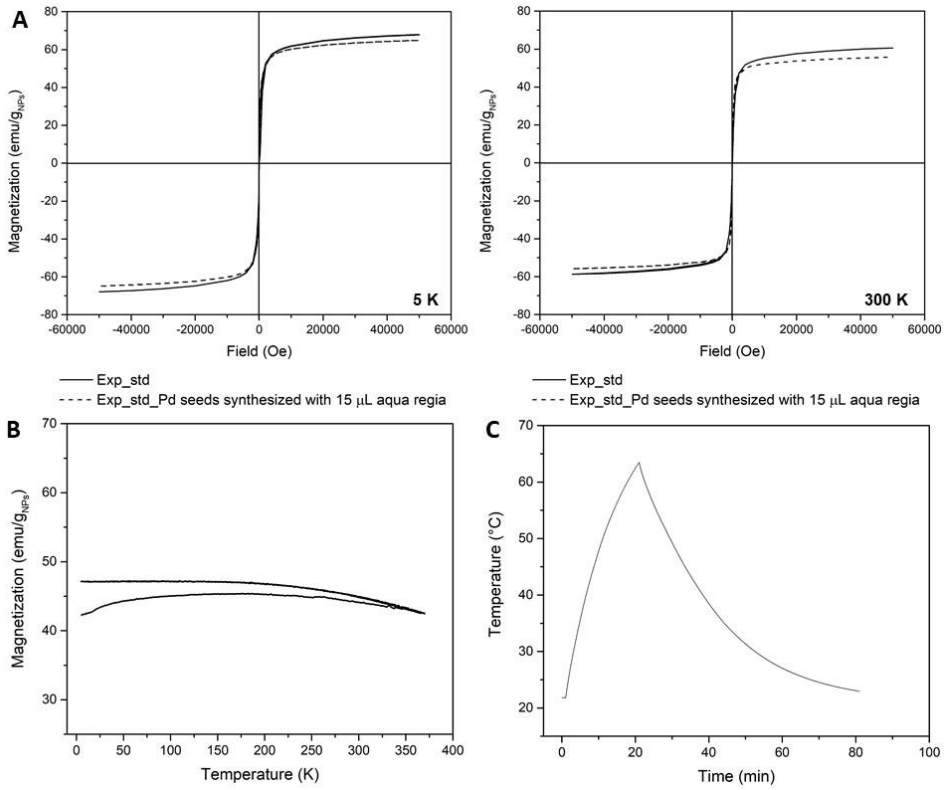

Figure 5.6. SQUID magnetometry of dry Pd/Fe-oxide NPs: **(A)** $M(H)_T$ curves measured at 5 and 300 K; **(B)** ZFC/FC-curve; **(C)** heating graph of the Pd/Fe-oxide NPs with Pd-seeds synthesized in presence of 15 μL aqua regia.

Table 5.2. Overview of the magnetic properties of Pd/Fe-oxide NPs produced with/without aqua regia introduced during the synthesis of the Pd-seeds.

Pd/Fe-oxide NPs from:	**Size**	**M_s[a]**		**T_B[b]**	**SLP (W/g_{Fe})**
	(nm)	**5 K**	**300 K**	**(K)**	
Pd NPs - no aqua regia	19.5 ± 1.5	67.9	58.7	180	113
Pd NPs - 15 μL aqua regia	19.2 ± 1.7	64.9	55.8	178	102

[a] Found at 50 kOe; [b] determined from ZFC/FC curves; [c] measured at 346 kHz, 19.1 mT; Error ≤ 5%, and calculated using the concentration of Fe determined by ICP-OES.

We can conclude that introduction of aqua regia during the synthesis of Pd seeds has no influence on the synthetic procedure resulting in Pd NPs with same properties as those synthesized without aqua regia. Moreover, the seeds in their radioactive form can be further used as surface to grow the iron oxide shell and obtain hybrid ^{103}Pd:Pd/Fe-oxide NPs with preserved morphology and magnetic properties.

Lastly, the Pd/Fe-oxide NPs synthesized from Pd-seeds produced in the presence of aqua regia were taken to water phase through the same surfactant modification step with DSPE-PEG$_{2000}$-COOH, as presented before. Heating measurements were conducted next and the SLP was determined. The SLP value obtained was 102 W/g$_{Fe}$, very similar to the value of 113 W/g$_{Fe}$ presented by Exp_standard from Chapter 3, this thesis. The small difference between the SLP values that can be accounted to the slightly lower M_s or to the small variations during the functionalization step, are in any case within the experimental error range. Most importantly, the heating temperature as high as 60 °C during 20 min exposure of these Pd/Fe-oxide NPs to AMF (346 kHz and 19.1 mT) could be reached (Figure 5.6C), which confirms their suitability to be used as agents for both hyperthermia and thermal ablation. As the Pd-seeds synthesized in presence of aqua regia and the from obtained Pd/Fe-oxide NPs maintained all necessary properties, we proceeded to synthesize them in their radioactive form.

Radiolabelling Pd-seeds and Pd/Fe-oxide NPs with ^{103}Pd

As previously explained, the procedure for synthesizing radioactive ^{103}Pd:Pd-seeds was conducted by using [^{103}Pd]Pd metallic powder solubilized in aqua regia as a precursor, together with the commercially available Pd(II)-acetate. An important step was to investigate how much of the activity introduced in the reaction can actually be incorporated in the synthesized nanoparticles. To do this, several experiments were conducted by varying ^{103}Pd-activities and amounts of aqua regia added to the reaction mixture. Post synthesis, the activity in the supernatants obtained from the two centrifugation rounds during the cleaning procedure was measured to verify how much of the activity stayed in the supernatant and how much was actually incorporated in the synthesized nanoparticles.

In the first two experiments, similar activities of 359 and 331 kBq were added to the precursors after dissolving [^{103}Pd]Pd metallic powder in 15 μL of aqua regia, resulting in very similar radiolabelling efficiency of 98.09% and 98.86%, respectively (Table 5.3). Increasing the amount of aqua regia to 100 μL for 359 kBq ^{103}Pd activity resulted in similar radiolabelling efficiency (97.69%). Overall, it is safe to conclude that this synthetic approach offers high and consistent efficiency for the preparation of ^{103}Pd:Pd NPs. Lastly, the fact that neither the amount of activity, nor the volumes of aqua regia introduced in the reaction mixture have an effect on the radiolabelling efficiency, translates into a great flexibility in tuning the amount of activity with which the NPs are radiolabelled, by simply varying the amount of activity introduced in the experiment, independent of the aqua regia volume.

Table 5.3. ^{103}Pd radiolabelling efficiency for Pd-seeds and Pd/Fe-oxide NPs.

Nanoparticles	**Aqua regia (μL)**	**^{103}Pd activity introduced (kBq)**	**Total activity lost in the supernatants (kBq)**	**Radiolabeling efficiency (%)**
^{103}Pd-seeds	15	359	6.83	98.09 %
^{103}Pd-seeds	15	331	3.75	98.86 %
^{103}Pd-seeds	100	359	8.30	97.69 %
^{103}Pd:Pd/Fe-oxide NPs	-	93	1.33	98.56 %

The next step was to use the ^{103}Pd:Pd NPs in the seed-mediated growth synthesis and coat them with iron oxide to produce ^{103}Pd:Pd/Fe-oxide NPs. As this reaction takes place at very high temperatures, it was important to check if any of the radioactivity incorporated in the ^{103}PdPd NPs was lost. Therefore, the synthesis was ran as described, and 93 kBq were introduced via the synthesized ^{103}Pd:Pd seeds. Post the experiment, during the cleaning procedure, the activity in the supernatants obtained after each centrifugation round (6 in total) was measured. Only 1.33 kBq were lost in the supernatants, meaning 98.56% of the activity introduced with the ^{103}Pd:Pd-seeds stayed in the precipitated ^{103}Pd:Pd/Fe-oxide NPs.

Additionally, valid for both synthesis of ^{103}Pd:Pd-seeds and ^{103}Pd:Pd/Fe-oxide NPs, during the cleaning procedure some of the nanoparticles were lost in the supernatant. Figure 5.7 shows the 6 supernatants obtained through the cleaning process for isolating the as-synthesized ^{103}Pd:Pd/Fe-oxide NPs and the recorded activities. As it

can be seen, the clear coloured supernatants (S1-S4) have very little activity, while supernatants S5 and S6, which clearly contain lost NPs due to the darker colour of the suspension, showed also the highest activity. Therefore, it is reasonable to assume 100% incorporation of the introduced radionuclide in the synthesized ^{103}Pd:Pd-seeds and implicitly in the ^{103}Pd:Pd/Fe-oxide NPs.

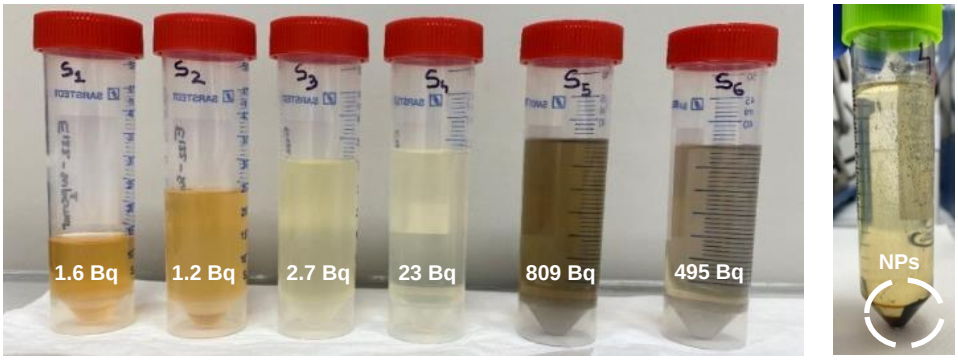

Figure 5.7. Falcon tubes containing the 6 supernatants collected post each round of centrifugation during the cleaning procedure of the ^{103}Pd:Pd/Fe-oxide NPs, and the recorded activities for each supernatant.

Pd leakage study

As the Pd/Fe-oxide NPs in their radioactive form are intended for biomedical applications, a primordial requirement is their biocompatibility. Palladium is considered toxic for the human body, being hypothesized that the effects of Pd metal are mediated via the presence or release of Pd ions. Pd ions are capable of eliciting a series of cytotoxic effects in vitro.[31] A study was conducted to determine the amount of Pd that leaks from the hybrid NPs. For this, Pd/Fe-oxide NPs functionalized with DSPE-PEG$_{2000}$-COOH were dispersed in 1 mM EDTA solution, a widely used compound in leakage studies as it binds to di- and trivalent metal ions.[32] The NPs after 24 h, 48 h and 7 days were filtered in an Amicon tube with a 30 kDa MWCO membrane and the filtrates were analysed via ICP-MS for palladium content (Table 5.4). As for the results, the Pd amount (μg) recorded was almost zero, close to the detection limit of the device. It can be concluded that there is no leakage of Pd from Pd/Fe-oxide NPs. Therefore, as expected, the iron oxide coating and the surfactant layer encapsulating the Pd core create a barrier sufficient to prevent any Pd leakage.

Table 5.4. Pd leakage from Pd/Fe-oxide NPs at different times.

Time	Pd (μg)	% Pd leaked from total amount of NPs
24 h	0.101	0,0092
48 h	0.072	0,0065
7 days	0.057	0,0052

In vitro evaluation of Pd/Fe-oxide and ^{103}Pd:Pd/Fe-oxide NPs

Typical *in vitro* studies with NPs are tested on 2D cancer cell cultures. This conventional model is relatively simple, cheap and provides a reliable tool for biomedical research. However, it comes with several limitations, most importantly their inability to effectively mimic the interactions between cells of real physiological tissues and the tumour microenvironment (TME), as a result of insufficient structural, mechanical, and biochemical attributions. Because 2D models cannot mimic crucial tumour aspects to accurately emulate *in vivo* conditions, they can negatively influence tested therapies, and lead to poor prediction of the real *in vivo* effect.[33] Employment of 3D cellular models can bridge the gap towards *in vivo* and ease the development and screening of new theranostic nanosystems.[33] Multicellular tumour spheroids (MCTS) are the most commonly used 3D tumour models, comprised of spherical cellular self-aggregates that can produce their own extracellular matrix (ECM), being recognized as non-vascularized tumour models. The MCTS exhibit a similar growth kinetics to real tumours, forming a gradient of oxygen, nutrients and metabolic waste. This translates into a hypoxic core with necrotic cells and an outer rim formed by proliferative cells in the outer layer and quiescent cells in the inner layer (Figure 5.8). The structures are estimated to be formed in spheroids with diameter over 400-500 μm, with the outer rim having usually 100–220 μm of thickness. Therefore, all the *in vitro* studies were conducted in a 3D model of spheroids from a MDA-MB-231 cell line, derived from human breast adenocarcinoma, with sizes around 400 or 500 μm.

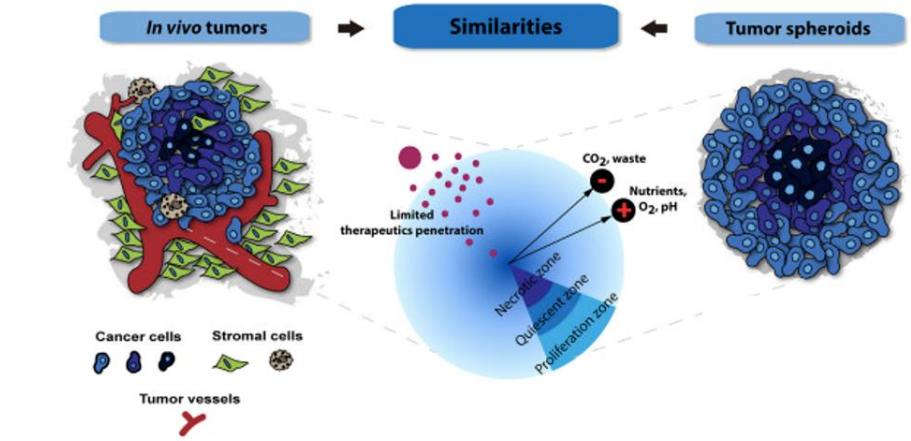

Figure 5.8. Common structural features displayed by solid tumours and tumour spheroids. Reproduced with permission from [34], 2023-Copyright Elsevier.

Biocompatibility of Pd/Fe-oxide hybrid MNPs and Pd seeds.

The ^{103}Pd:Pd/Fe-oxide hybrid NPs are meant to be used as theranostic agents, hence, to estimate their suitability for biomedical applications, we first assessed their cytotoxicity. The study was conducted with non-radioactive Pd/Fe-oxide NPs functionalized with DSPE-PEG$_{2000}$-COOH surfactant. The water-dispersible MNPs were incubated in graded concentrations of 125 – 1000 μg/mL for 7 days with spheroids obtained from a MDA-MB-231 cell line. In parallel, a control consisted of spheroids where no MNPs were incubated, while incubation with 10% DMSO acts as a negative control. Subsequently, the cell viability was evaluated (Figure 5.9A).

The lower concentrations of MNPs maintained the same cell viability as the control, with only the highest concentration of 500 and 1000 μg/mL Pd/Fe-oxide NPs resulting in 19 ± 4.5% and 22 ± 9.2% viability loss, respectively. However, the percentage of size increase after the incubation period (Figure 5.9B) is similar or greater to the control for all concentrations. It can be concluded that Pd/Fe-oxide MNPs exhibit no significant toxicity in the employed concentration range, confirmed also via images of the spheroids exposed to different concentrations of MNPs (Figure 5.9C). Such a result is not unexpected, as the toxic palladium core is encapsulated by biocompatible/non-toxic iron oxide and PEG-surfactant. However, as it is possible during the synthesis of Pd/Fe-oxide NPs for certain Pd cores to remain uncoated, the

cytotoxicity of Pd NPs was investigated as well. For this, OAm-capped Pd NPs were transferred to water phase by functionalization with DSPE-PEG$_{2000}$-COOH and different concentrations in the 10-250 μg/mL range were incubated with the spheroids for 7 days.

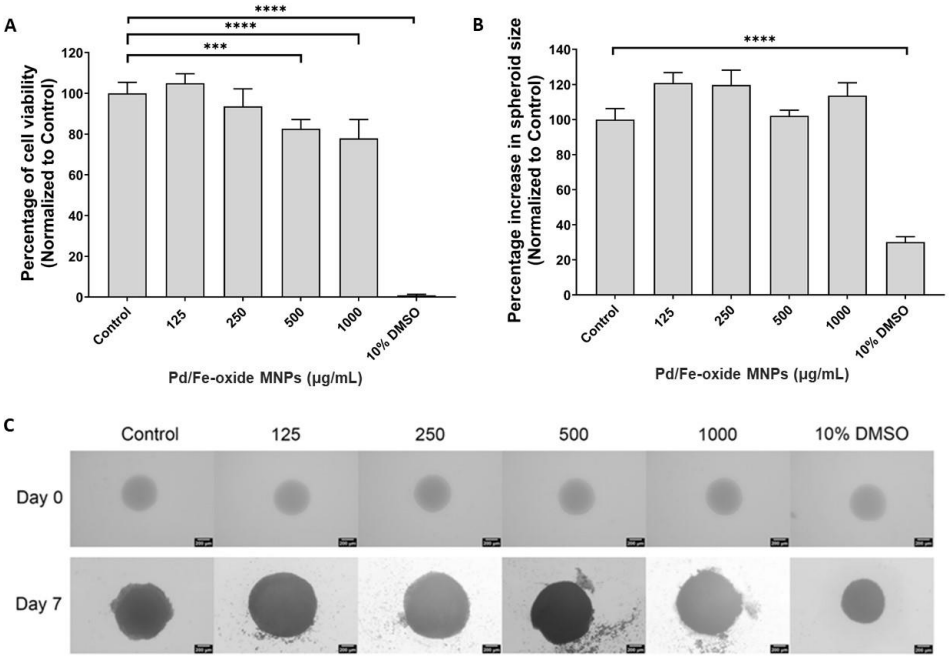

Figure 5.9. *In vitro* toxicity induced by Pd/Fe-oxide NPs on MDA-MB-231 spheroids on day 7: **(A)** cell viability, **(B)** spheroid growth rate, and **(C)** representative images of the spheroids treated with different MNPs concentrations. Scalebars are 200 μm.

The cell viability assay (Figure 5.10A) showed no toxic effect for the lower 10 and 50 μg/mL Pd NPs concentrations used through the study, with 100 ± 3.8% spheroid viability recorded in both cases. However, a strong toxic effect with a viability loss of 81 ± 17.5% was recorded for the highest concentration of 250 μg/mL Pd NPs. This was also confirmed by the percentage of size increase in the spheroids (Figure 5.10B), as 40 ± 9.6% of the spheroid size was reduced for the highest Pd NPs concentration employed as shown in the representative images of MDA-MB-231 spheroids treated with different Pd NPs concentrations (Figure 5.10C).

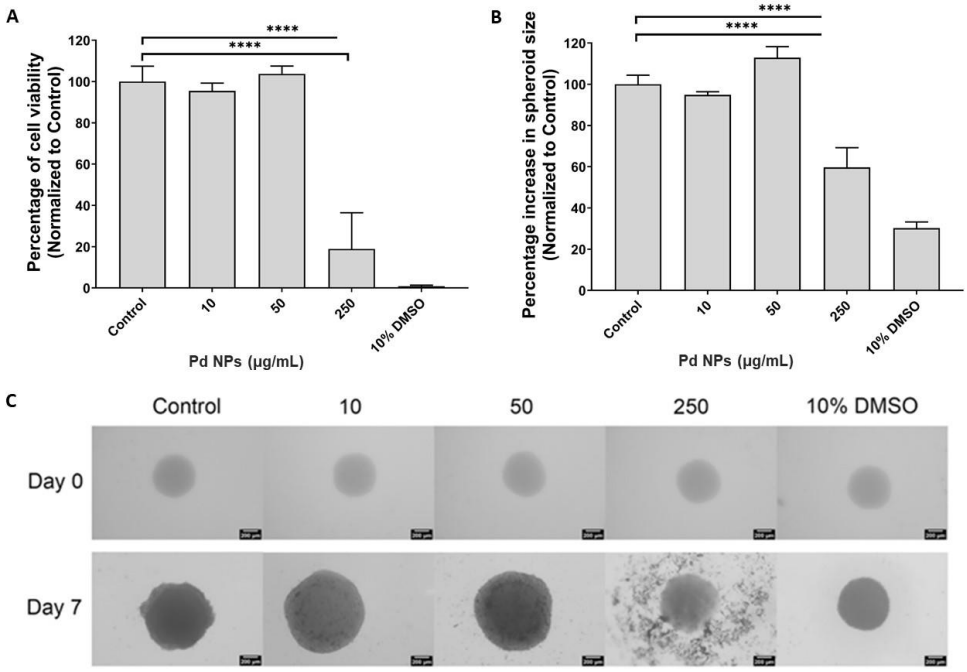

Figure 5.10. *In vitro* toxicity induced by Pd NPs on MDA-MB-231 spheroids on day 7: **(A)** cell viability, **(B)** spheroid growth rate, and **(C)** representative images of the spheroids treated with different Pd NPs concentrations. Scalebars are 200 μm.

Uptake of Pd/Fe-oxide MNPs

An important element in the selection of the radionuclide for radiation therapy is the energy of the emitted particles and the tissue penetration range.[35] As discussed, ^{103}Pd decays by electron capture (EC) emitting low energy X-rays and Auger electrons (AEs). The AEs are attractive for radiation treatment of cancer, especially when emitted in close proximity to cell sensitive targets such as DNA and the cell membrane.[35] As the AEs of the ^{103}Pd are highly efficient in such close proximity to cell sensitive targets, it is important to investigate the uptake of the Pd/Fe-oxide NPs by the spheroids. Additionally, the internalization of the MNPs in the spheroids can impact the heating efficiency, as this can impact the Brownian relaxation events leaving Néel relaxation as the only available mechanism after internalization of NPs.[36] However, based on the small sizes presented by the Pd/Fe-oxide NPs and the results obtained in Chapter 3, it is expected that Néel relaxation is anyway the predominant mechanism via which the Pd/Fe-oxide hybrid MNPs produce heat.

To investigate the uptake, we used the same 3D tumour model based on spheroids composed of MDA-MB-231 cells. The spheroids were incubated with a concentration of 500 μg/mL Pd/Fe-oxide NPs and collected after 1, 3, 24, 72 and 168 hours. The uptake of MNPs by spheroids was assessed based on the iron content determined via ICP-MS. Based on the results, a slight increase in uptake was recorded with time, resulting in the highest value of 8 ± 0.4% internalization of the introduced Pd/Fe-oxide NPs for the 7-day incubation period (Figure 5.11A).

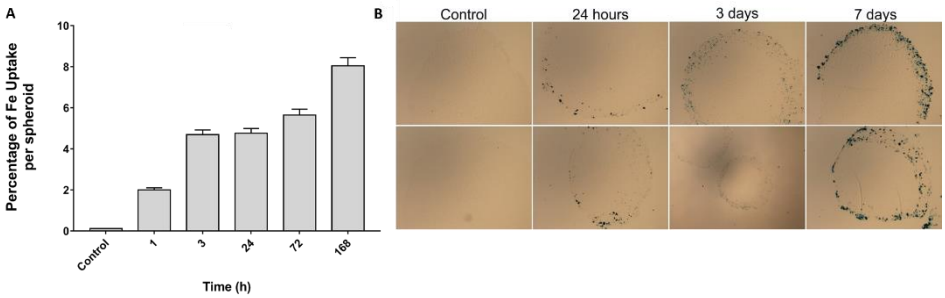

Figure 5.11. (A) Uptake percentage of DSPE-PEG$_{2000}$-COOH functionalized Pd/Fe-oxide NPs by MDA-MB-231 spheroids as obtained from ICP-MS and **(B)** Prussian Blue staining showing cells and Pd/Fe-oxide NPs (blue) at different incubation times.

Prussian blue staining confirmed just a little uptake of Pd/Fe-oxide NPs by the spheroids, with the NPs being deposited only in the proliferation zone of the spheroids (Figure 5.11B). As mentioned, the MNPs are functionalized with DSPE-PEG$_{2000}$-COOH polymer. Surface modification of the NPs via PEGylation is known for shielding the surface from aggregation, opsonisation, and phagocytosis, prolonging systemic circulation times.[37] While PEGylation renders the colloidal system of MNPs stable and highly reduces systemic toxicity of the MNPs that could arise from their injections, it also has an apparent effect of limited uptake of the MNPs by spheroids.

On this basis, the goal of the *in vitro* studies was to assess the effect of ^{103}Pd:Pd/Fe-oxide MNPs surrounding the spheroids. It should be noted that under clinical conditions, the radioactive hybrid MNPs are to be administered locally via injection in the centre of the tumour, aiming to specifically target the peripheral region of the tumour after hyperthermia/thermal ablation treatment. The fact that the MNPs are

not taken up becomes an advantage in this case, as they are expected to stay longer at the tumour site, thus, enabling the possibility of heat treatments with longer intervals as well as continuous localized radiation exposure.

Radioactivity effect of [^{103}Pd]Pd

To investigate the *in vitro* efficiency of ^{103}Pd:Pd/Fe-oxide NPs as thermo-brachytherapy agents, we first needed to validate and confirm a minimum ^{103}Pd activity that provides a therapeutic effect on MDA-MB-231 spheroids. For this, a study of the effect of [^{103}Pd]Pd metallic powder on MDA-MB-231 spheroids was conducted. From the investigations on Pd NPs cytotoxicity, 50 μg/mL non-radioactive Pd/[^{103}Pd]Pd metallic powder stock solution was chosen as a suitable concentration for the study, to avoid interference of palladium toxicity itself.

A range of 50-400 kBq of ^{103}Pd activity was employed through the investigation, and a strong effect was seen only for the highest activity of 400 kBq. In this case, the cell viability decreased to 58 ± 6% (Figure 5.12A) and 66 ± 18.9% of the spheroids size was reduced (Figure 5.12B) compared to the control, demonstrating the therapeutic effect of ^{103}Pd and the minimum necessary ^{103}Pd activity to be radiolabeled on the hybrid MNPs.

However, due to constraints encountered during the radiolabelling synthesis procedure, a radiolabelling to achieve 400 kBq activity could not be performed for a concentration of 1 mg/mL ^{103}Pd:Pd/Fe-oxide NPs.

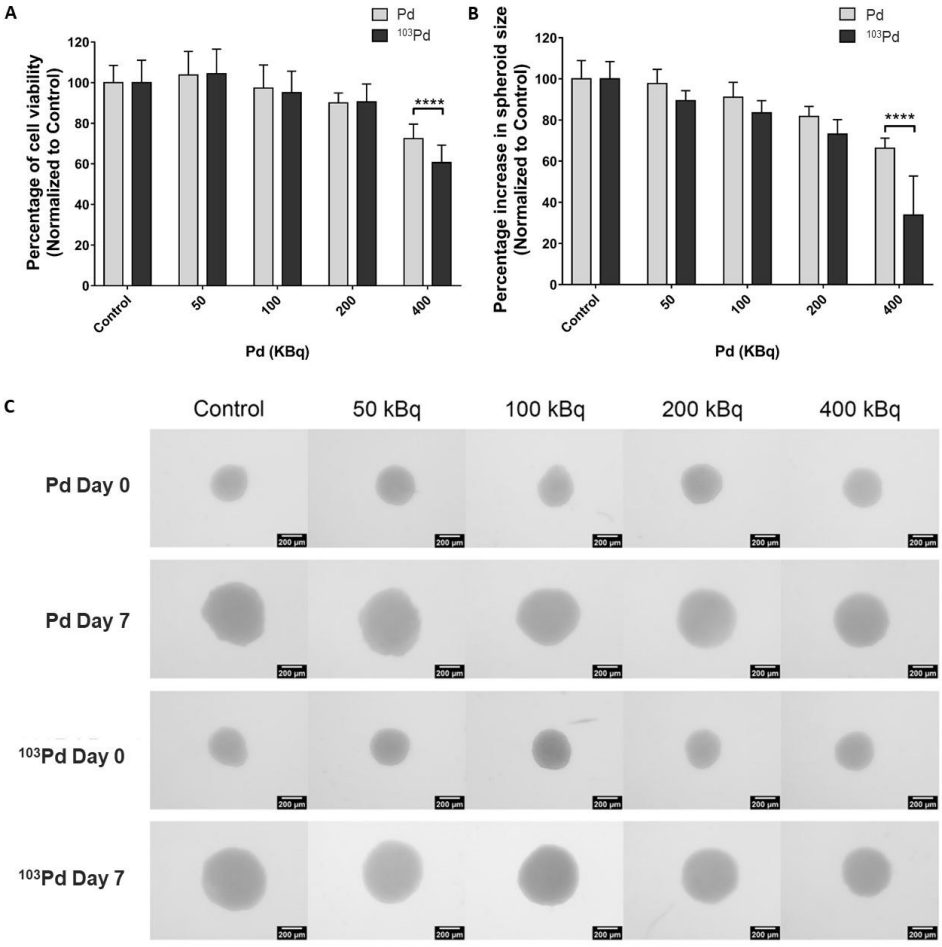

Figure 5.12. Study of [^{103}Pd]Pd radioactivity (50 – 400 kBq) therapeutic effect on MDA-MB-231 spheroids: **(A)** cell viability, **(B)** spheroid growth rate, and **(C)** representative images of the spheroids treated with different Pd/[^{103}Pd]Pd doses. Scalebars are 200 μm.

Investigation of ^{103}Pd:Pd/Fe-oxide NPs as thermo-brachytherapy agents

To evaluate *in vitro* the combined therapeutic effects of hyperthermia/thermal ablation and ^{103}Pd radiation, MDA-MB-231 spheroids were treated with ^{103}Pd:Pd/Fe-oxide NPs. A concentration of 1 mg/mL MNPs was the minimum required to deliver effective heat doses. However, the synthetic procedure and permit limitations hindered the radiolabelling of the hybrid MNPs with the minimum 400 kBq ^{103}Pd activity that showed therapeutic effect on MDA-MB-231 spheroids. An activity of

only approx. 50 kBq was achieved with a 1 mg/mL ^{103}Pd:Pd/Fe-oxide NPs concentration. Hence, it was decided to study and compare the therapeutic effects of hyperthermia/thermal ablation at 10 mg/mL ^{103}Pd:Pd/Fe-oxide NPs also, to reach an activity of approx. 500 kBq. The treatment applied was conducted as shown in Scheme 5.3.

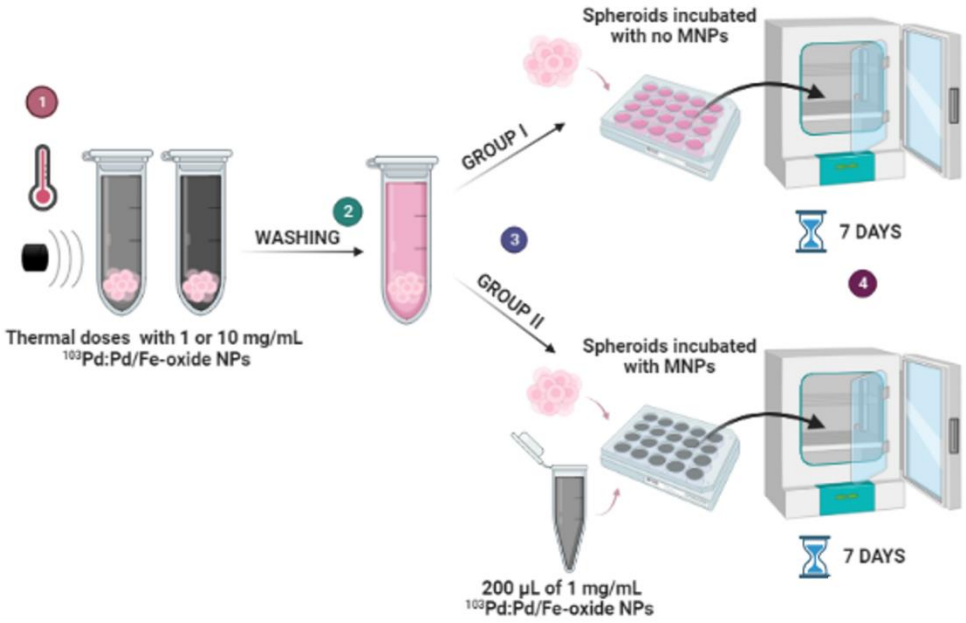

Scheme 5.3. Procedure followed to evaluate the combined therapeutic effects of hyperthermia/thermal ablation and ^{103}Pd radiation via ^{103}Pd:Pd/Fe-oxide NPs on MDA-MB-231 spheroids.

Samples of spheroids in colloidal solutions of 1 mg/mL or 10 mg/mL ^{103}Pd:Pd/Fe-oxide NPs were exposed to AMF, subjecting the spheroids to different thermal doses. Subsequently, the MNPs colloidal solution was gently aspirated and the spheroids were washed carefully. Next, the treated spheroids were divided into two groups, namely, Group I, where the spheroids were not exposed to MNPs after the treatment, and Group II, in which the treated spheroids were incubated with 200 µL of 1 mg/mL radioactive MNPs colloidal solution. The latter group treatment was supposed to better simulate the *in vivo* conditions, where the MNPs will be distributed locally to deliver radiation post hyperthermia/thermal ablation treatment.

1 mg/mL ^{103}Pd:Pd/Fe-oxide NPs – Group I – day 3 vs day 7 post treatment

For Group I spheroids treated with 1 mg/mL ^{103}Pd:Pd/Fe-oxide NPs (approx. 50 kBq) and no MNPs incubation after heat exposure, the thermal doses delivered via hyperthermia at 42 °C (60 min) and 43 °C (30 min), together with the low radioactivity dose to which the spheroids were exposed during heating, did not show a therapeutic effect at day 3 post treatment (Figure 5.13A). The cell viability (> 80%) remained similar to the control (Figure 5.13A). Similar results were also observed for day 7 post treatment.

On the other hand, cell viability losses of 54 ± 5.3% and 78 ± 2.2% were recorded 3 days post treatment for hyperthermia at 45 °C (30 min) and thermal ablation (TA_50 °C), respectively (Figure 5.13A). However, the spheroids treated via hyperthermia at 45 °C (30 min) showed on day 7 post treatment an increase in cell viability from 46 ± 5.3% to 67 ± 5.9%, indicating spheroid recovery. It is well-known that hyperthermia alone is not always efficient in completely killing the cancerous cells, being mainly used as an adjuvant to radiotherapy or other treatments. However, the low radioactivity dose received via 1 mg/ml ^{103}Pd:Pd/Fe-oxide MNPs was also not enough to create cytotoxic effects, regardless the radiosensitization triggered by hyperthermia. Interestingly, the spheroids treated via thermal ablation (TA_50 °C) recorded further decrease in cell viability 7 days post treatment, suggesting spheroid eradication. Same conclusions can be drawn from the size growth rate of the spheroids (Figure 5.13B).

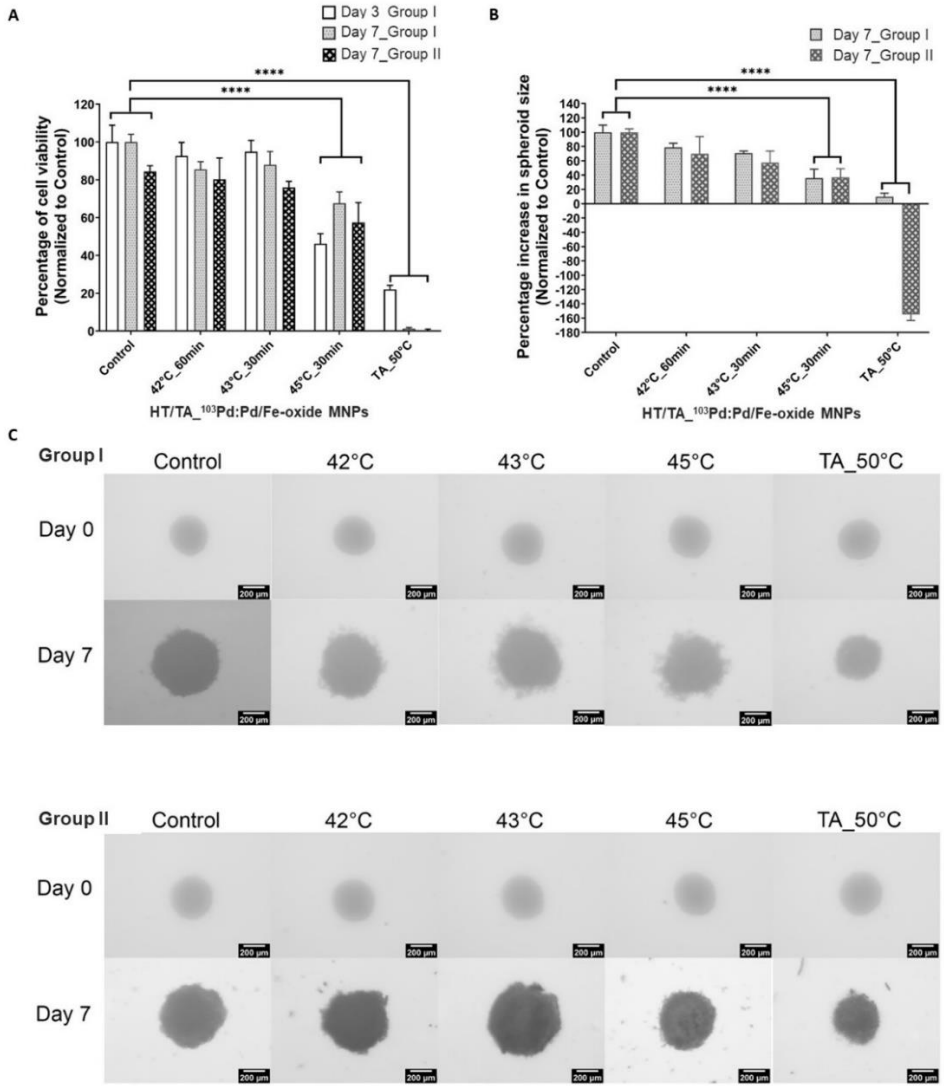

Figure 5.13. *In vitro* combined therapeutic effects of ^{103}Pd radiation (approx. 50 kBq) and hyperthermia/thermal ablation via 1 mg/mL ^{103}Pd:Pd/Fe-oxide MNPs on MDA-MB-231 spheroids: **(A)** cell viability at day 3 and 7 post treatment for Group I and at day 7 post treatment for Group II, **(B)** size growth rate, and **(C)** representative images of the spheroids for all treatment groups at day 0 and 7 post treatment administration. Scalebars are 200 µm.

1 mg/mL ^{103}Pd:Pd/Fe-oxide NPs – Group I vs. Group II – day 7 post treatment

For the treatment applied with 1 mg/mL ^{103}Pd:Pd/Fe-oxide NPs, the difference between Group I and Group II stayed only in incubation of the spheroids with 200 μL of 1 mg/mL MNPs colloidal solution post heat treatment in the case of Group II, as a trial in better mimicking *in vivo* conditions. As the same MNPs concentration was employed during the treatment of both groups, the thermal and radioactive doses received by the spheroids were the same during heating. Looking at the cell viability (Figure 5.13A), independent of the thermal dose applied, the results recorded were similar for both groups, with only thermal ablation showing a strong therapeutic effect. As previously mentioned, hyperthermia alone is usually not sufficient to completely eradicate tumours, plus the ^{103}Pd activity to which the spheroids were exposed was much lower than the 400 kBq ^{103}Pd activity that was determined to show a therapeutic effect. Nevertheless, looking at the spheroids size growth (Figure 5.13B), we do notice an interesting effect for thermal ablation. Even though the spheroids from Group I indicate a minimal size increase, hence possible slight recovery, this is not the case for Group II, where the spheroids were completely destroyed. This can stand as an indication that MNPs presence post heat treatment, and possibly even such small radioactivity, can have a therapeutic effect in combination with thermal ablation.

10 mg/mL ^{103}Pd:Pd/Fe-oxide NPs – Group I – day 3 vs day 7 post treatment

For Group I spheroids treated with 10 mg/mL ^{103}Pd:Pd/Fe-oxide NPs (approx. 500 kBq) and no MNPs incubation after heat exposure, a significant cell viability loss 3 days post treatment was observed in all cases (Figure 5.14A). The strongest effects, approx. 90% viability loss in both cases, were obtained with hyperthermia at 45 °C (30 min) and thermal ablation (TA_50 °C). Interestingly, for this treatment scenario, an increase in cell viability, indicating spheroid recovery, was noticed 7 days post treatment only for the spheroids subjected to hyperthermia at 42 °C (60 min) and 43 °C (30 min), respectively. Possibly, the therapeutic effect of moderate hyperthermia together even with high radioactivity dose (approx. 500 kBq ^{103}Pd during heating), was still insufficient to generate complete spheroid destruction. On the other hand, hyperthermia at 45 °C (30 min) and thermal ablation (TA_50 °C), together with

exposure to high ^{103}Pd activity, were highly efficient in killing the cancer cells. Analysis of the spheroids size growth (Figure 5.14B) 7 days post treatment confirms these results. Lastly, the best therapeutic effect of this group was actually achieved via hyperthermia at 45 °C (30 min) instead of thermal ablation. For a concentration of 10 mg/mL MNPs colloidal solution employed for delivering the established thermal doses, the heating rate to achieve the desired temperature is high. Therefore, in case of thermal ablation, the spheroids were exposed to heat for 7 minutes only, whereas hyperthermia was delivered for 30 min at 45 °C. This concludes that apart the radioactivity and the temperature at which the spheroids are exposed during the treatment, the time exposure to a certain temperature is another important factor in ensuring an efficient treatment.

10 mg/mL ^{103}Pd:Pd/Fe-oxide NPs – Group I vs. Group II – day 7 post treatment

For the treatment applied via 10 mg/mL ^{103}Pd:Pd/Fe-oxide NPs, the difference between the treatment groups stays only in the incubation of the spheroids with 200 μL of 1 mg/mL MNPs colloidal solution post treatment in the case of Group II, as a trial to better mimic *in vivo* conditions. In case of thermal doses delivered via hyperthermia at 42 °C (60 min) and 43 °C (30 min), Group II showed a much stronger therapeutic effect compared to Group I , with lower cell viability recorded in both cases (Figure 5.14A). Additionally, complete spheroid destruction was achieved (Figure 5.14B). Therefore, the combination of high radiation dose and hyperthermia, followed by spheroid incubation with MNPs post treatment administration, to better simulate *in vivo* conditions, effectively results in complete cancer cell destruction, with better results than Group I.

In case of the spheroids that received thermal doses delivered via hyperthermia at 45 °C (30 min) and thermal ablation (TA_50 °C), both Group I and II showed strong heat and radiation dose damage, with complete loss of cell viability (Figure 5.14A).

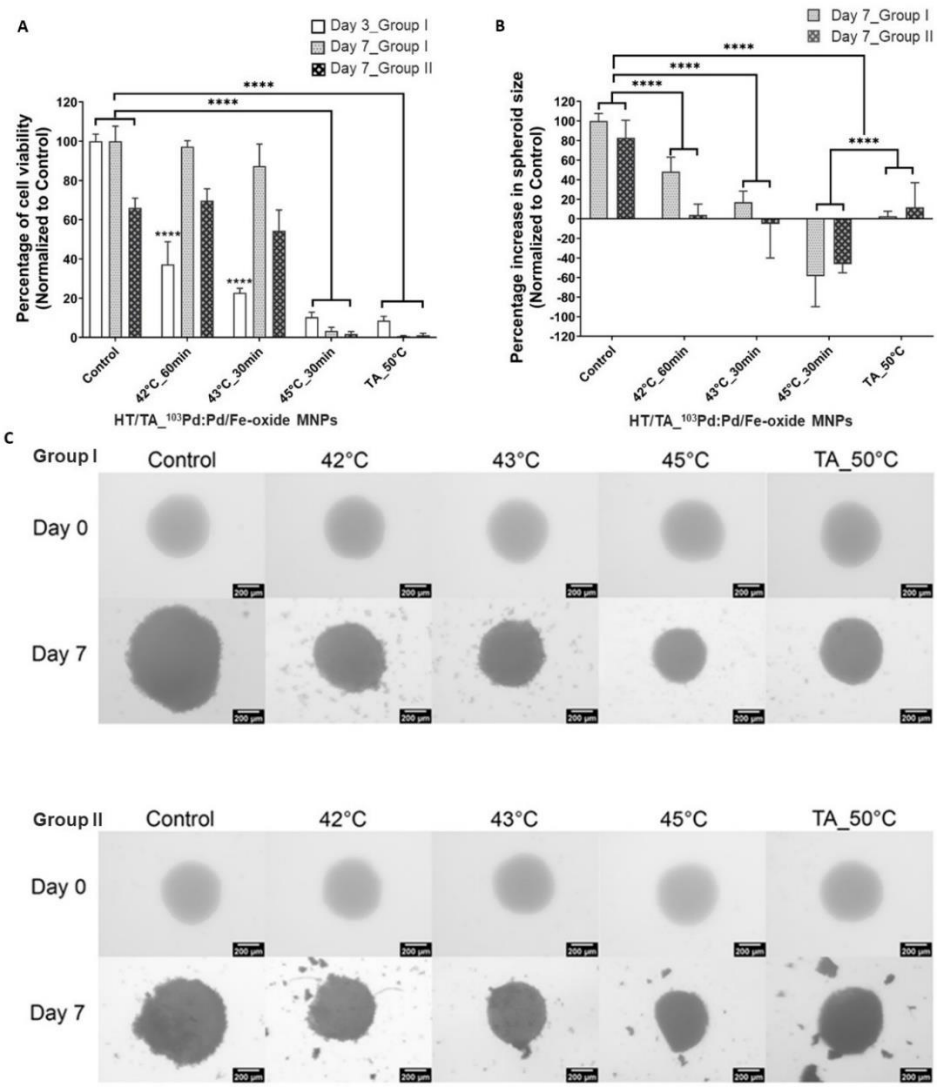

Figure 5.14. *In vitro* combined therapeutic effects of ^{103}Pd radiation (approx. 500 kBq) and hyperthermia/thermal ablation via 10 mg/mL ^{103}Pd:Pd/Fe-oxide MNPs on MDA-MB-231 spheroids: **(A)** cell viability at day 3 and 7 post treatment for Group I and at day 7 post treatment for Group II, **(B)** size growth rate, and **(C)** representative images of the spheroids for all treatment groups at day 0 and 7 post treatment administration. Scalebars are 200 μm.

It is important to mention that when the treatment effects are very strong, little of the spheroids is left behind. In such cases, the spheroids are not alive, as confirmed by the cell viability assays, but some structures are still maintained. This occurs especially in case of incubation with nanoparticles, as the MNPs surround the spheroids and are able to maintain their structure.

1 vs 10 mg/mL ^{103}Pd:Pd/Fe-oxide NPs – Group I – day 7 post treatment

The combined effect and synergy between hyperthermia/thermal ablation and radiation can be best seen for the spheroids treated with 10 mg/mL ^{103}Pd:Pd/Fe-oxide NPs in comparison to 1 mg/mL ^{103}Pd:Pd/Fe-oxide NPs. The 10 times higher ^{103}Pd activity (approx. 500 kBq) achieved with 10 mg/mL MNPs showed much stronger therapeutic effects, especially with the spheroids that underwent hyperthermia at 45 °C (30 min) and thermal ablation (TA_ 50 °C). The cell viability (Figure 5.15A) and size growth (Figure 5.15B) results stand as confirmation that the therapeutic effects obtained via higher radiation doses led to better spheroid destruction. It is interesting to mention that a stronger effect was recorded in case of hyperthermia at 45 °C (30 min) over thermal ablation (TA_ 50 °C). However, as explained before, conducting the treatment with a 10 mg/mL ^{103}Pd:Pd/Fe-oxide MNPs concentration ensures faster heating rates, therefore, the spheroids were exposed to heating significantly shorter times in case of thermal ablation.

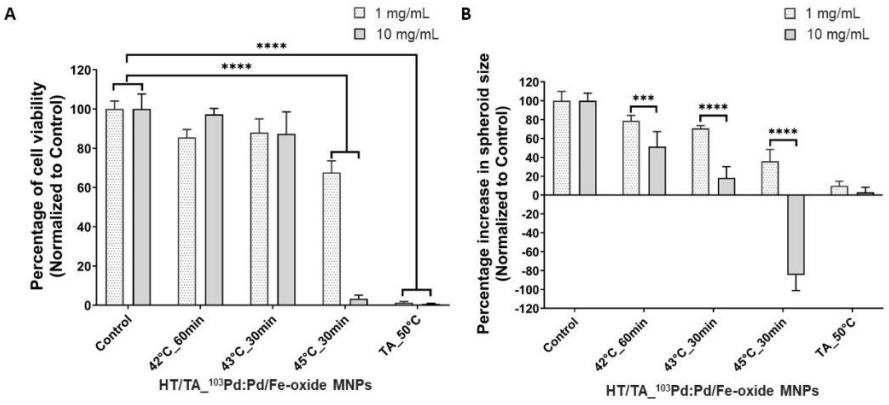

Figure 5.15. *In vitro* therapeutic effects of ^{103}Pd:Pd/Fe-oxide MNPs on Group I MDA-MB-231 spheroids assessed on day 7 after the treatment and subsequent washing removal of MNPs: **(A)** cell viability, and **(B)** size growth rate.

1 vs 10 mg/mL ^{103}Pd:Pd/Fe-oxide MNPs – Group II – day 7 post treatment

For Group II, where the spheroids were incubated with MNPs post treatment administration, the same effects as for Group I presented earlier were seen for almost all thermal doses applied (Figure 5.16A,B). However, it is important to discuss the stronger therapeutic effect shown by the spheroids treated with 1 mg/mL ^{103}Pd:Pd/Fe-oxide MNPs and thermally ablated, in comparison to the spheroids thermally ablated with 10 mg/mL ^{103}Pd:Pd/Fe-oxide NPs (Figure 5.16B). The spheroids were exposed to a 10-fold higher dose in case of 10 mg/mL ^{103}Pd:Pd/Fe-oxide NPs concentration, however, it took only 7 min to reach the thermal ablation temperature, compared to 22 min that were required in case of the 1 mg/mL MNPs concentration. Hence, this shows again the importance of the exposure time to a certain temperature, apart from the radiation and thermal doses received during the treatment.

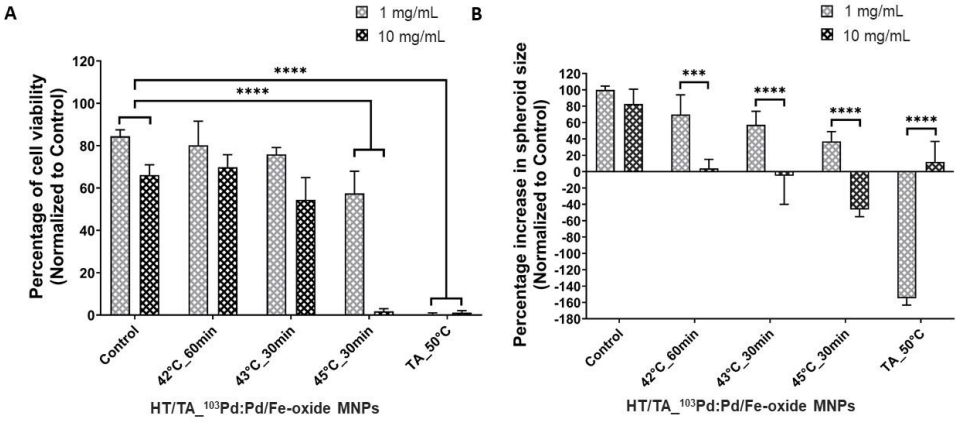

Figure 5.16. *In vitro* therapeutic effects of ^{103}Pd:Pd/Fe-oxide MNPs on Group II MDA-MB-231 spheroids assessed on day 7 after the treatment and subsequent incubation with same amount of MNP: **(A)** cell viability, and **(B)** size growth rate.

5.4 Conclusion

This chapter started with investigation of different radiolabelling routes for obtaining ^{103}Pd-labelled Pd/Fe-oxide NPs (^{103}Pd:Pd/Fe-oxide NPs). The concept behind the radiolabelling route that proved successful stood in insertion of the [^{103}Pd]Pd metallic powder solubilized in aqua regia in the synthesis reaction mixture, together with available non-radioactive palladium precursor. As radioactive nanoparticles could not be imaged via TEM, Pd NPs were first synthesized in their non-radioactive form in order to assess if the presence of different aqua regia quantities has an influence on the outcome of the Pd NPs. As no obvious influence was recorded, with the NPs maintaining the same morphology, independent of the aqua regia quantity employed, they were further used as seeds to verify that the same nucleation and growth processes of iron oxide during thermal decomposition was enabled. Pd/Fe-oxide NPs obtained from Pd-seeds synthesized with aqua regia exhibited same morphology, magnetic properties and heating ability as previously presented Pd/Fe-oxide NPs. As the radiolabelling method proved to generate nanoparticles with conserved properties, the ^{103}Pd-labelling efficiency was next assessed by synthesizing the nanoparticles with several ^{103}Pd activities and aqua regia quantities. All trials resulted in very high radiolabelling efficiency, close to 100%.

The biocompatibility of the designed nanoparticles was assessed first in their non-radioactive form by monitoring the *in vitro* toxicity effects of Pd and Pd/Fe-oxide NPs in different concentration ranges on MDA-MB-231 spheroids. Pd NPs showed no toxic effect until a concentration of 250 μg/mL, whereas Pd/Fe-oxide NPs showed no significant toxicity in the employed concentration range, being established that the highest concentration of 1000 μg/mL MNPs could be used for further studies. Subsequently, investigation of the uptake of Pd/Fe-oxide NPs by spheroids resulted in very low uptake, with only 8 ± 0.4% internalization of the introduced MNPs for the 7-day incubation period. Prussian blue staining confirmed this result, showing that the MNPs were taken up only in the proliferation zone of the spheroids. The radioactivity effects of ^{103}Pd were also assessed, to confirm a minimum activity that provides a therapeutic effect on MDA-MB-231 spheroids. From the range of 50-400 kBq ^{103}Pd activity employed through the study, a strong effect was seen only for the highest activity, in this case the cell viability decreasing to 58 ± 6% and 66 ± 18.9% of

the spheroids size being reduced. The next step was to evaluate *in vitro* the combined therapeutic effects of hyperthermia/thermal ablation and ^{103}Pd radiation on the same 3D cell model. As it was not possible to achieve the minimum ^{103}Pd activity (400 kBq) that showed a therapeutic effect with 1 mg/mL ^{103}Pd:Pd/Fe-oxide NPs concentration, the same study was also conducted with 10 mg/mL MNPs concentration. After delivery of thermal dose with the two MNPs concentrations, the spheroids were split in treatment groups, namely Group I, where the treated spheroids were not exposed to MNPs and Group II, in which the spheroids were incubated with MNPs, to better simulate *in vivo* conditions. In case of Group I treated with 1 mg/mL ^{103}Pd:Pd/Fe-oxide NPs concentration only thermal ablation in combination with the low ^{103}Pd dose seemed to have good therapeutic effect, whereas the hyperthermia treatments together with the low ^{103}Pd dose showed spheroid recovery on day 7 post treatment compared to day 3. In case of Group II treated with 1 mg/mL ^{103}Pd:Pd/Fe-oxide NPs concentration, complete spheroid destruction was achieved in case of thermal ablation, being an indication of how the presence of MNPs post thermal dose, as it is the case *in vivo*, has an effect. Overall, it can be concluded that hyperthermia with such low ^{103}Pd radiation dose cannot produce satisfactory therapeutic effects, whereas thermal ablation, even in combination with low doses, can lead to spheroid eradication. In case of treatments applied with 10 mg/mL ^{103}Pd:Pd/Fe-oxide NPs concentration, the combination of high ^{103}Pd dose with all thermal doses showed great therapeutic effects in all cases, with strongest effects for hyperthermia at 45 °C (30 min) and thermal ablation, where complete loss of cell viability was recorded. A very interesting result worth mentioning was the stronger therapeutic effect obtained for the spheroids of Group II treated with 1 mg/mL ^{103}Pd:Pd/Fe-oxide MNPs and thermally ablated, in comparison to the spheroids of Group II thermally ablated with 10 mg/mL ^{103}Pd:Pd/Fe-oxide NPs. Due to the lower concentration in case of 1 mg/mL MNPs concentration, a slower heating rate was employed, hence the spheroids were exposed longer to higher temperatures, which resulted in a stronger therapeutic effect.

Overall, through the *in vitro* studies, we managed to confirm that the combination of high ^{103}Pd dose together with strong thermal dose is able to generate spheroid destruction, and additionally, the time exposure to a certain temperature is a very important factor. Lastly, this preliminary biological evaluation conducted showed the

great potential of ^{103}Pd:Pd/Fe-oxide NPs in cancer therapeutics, which should be further complemented with *in vivo* assessments.

Bibliography

1. Aly, H.A. Cancer therapy and vaccination.
2. Song, G.; Cheng, L.; Chao, Y.; Yang, K.; Liu, Z. Emerging Nanotechnology and Advanced Materials for Cancer Radiation Therapy. *Advanced Materials* **2017**, *29*, 1700996, doi:https://doi.org/10.1002/adma.201700996.
3. Arruebo, M.; Vilaboa, N.; Saez-Gutierrez, B.; Lambea, J.; Tres, A.; Valladares, M.; Gonzalez-Fernandez, A. Assessment of the evolution of cancer treatment therapies. *Cancers (Basel)* **2011**, *3*, 3279-3330, doi:10.3390/cancers3033279.
4. Seniwal, B.; Thipe, V.C.; Singh, S.; Fonseca, T.C.F.; Freitas de Freitas, L. Recent Advances in Brachytherapy Using Radioactive Nanoparticles: An Alternative to Seed-Based Brachytherapy.
5. Blanco-Andujar, C.; Walter, A.; Cotin, G.; Bordeianu, C.; Mertz, D.; Felder-Flesch, D.; Begin-Colin, S. Design of iron oxide-based nanoparticles for MRI and magnetic hyperthermia.
6. van Oossanen, R.; Godart, J.; Brown, J.M.C.; Maier, A.; Pignol, J.P.; Denkova, A.G.; Djanashvili, K.; van Rhoon, G.C. Feasibility Study on the Radiation Dose by Radioactive Magnetic Core-Shell Nanoparticles for Open-Source Brachytherapy. *Cancers (Basel)* **2022**, *14*, doi:10.3390/cancers14225497.
7. Chu, K.F.; Dupuy, D.E. Thermal ablation of tumours: biological mechanisms and advances in therapy. *Nat Rev Cancer* **2014**, *14*, 199-208, doi:10.1038/nrc3672.
8. Djoumessi, D.; Laprise-Pelletier, M.; Chevallier, P.; Lagueux, J.; Côté, M.F.; Fortin, M.A. Rapid, one-pot procedure to synthesise 103Pd:Pd@Au nanoparticles en route for radiosensitisation and radiotherapeutic applications. *Journal of Materials Chemistry B* **2015**, *3*, 2192-2205, doi:10.1039/C4TB01663G.
9. Laprise-Pelletier, M.; Lagueux, J.; Cote, M.F.; LaGrange, T.; Fortin, M.A. Low-Dose Prostate Cancer Brachytherapy with Radioactive Palladium-Gold Nanoparticles. *Adv Healthc Mater* **2017**, *6*, ARTN 1601120, doi: 10.1002/adhm.201601120.
10. Khan, M.K.; Minc Ld Fau - Nigavekar, S.S.; Nigavekar Ss Fau - Kariapper, M.S.T.; Kariapper Ms Fau - Nair, B.M.; Nair Bm Fau - Schipper, M.; Schipper M Fau - Cook, A.C.; Cook Ac Fau - Lesniak, W.G.; Lesniak Wg Fau - Balogh, L.P.; Balogh, L.P. Fabrication of {198Au0} radioactive composite nanodevices and their use for nanobrachytherapy.
11. Laprise-Pelletier, M.; Simão, T.; Fortin, M.A.-O.X. Gold Nanoparticles in Radiotherapy and Recent Progress in Nanobrachytherapy.
12. Sioshansi, P.; Bricault, R.J. Low-energy 103pd gamma (X-ray) Source for vascular brachytherapy. *Cardiovascular Radiation Medicine* **1999**, *1*, 278-287, doi:https://doi.org/10.1016/S1522-1865(99)00015-3.
13. Keller, B.; Sankreacha, R.; Rakovitch, E.; O'Brien, P.; Pignol, J.-P. A permanent breast seed implant as partial breast radiation therapy for early-stage patients: A comparison of palladium-103 and iodine-125 isotopes based on radiation safety considerations.

*International Journal of Radiation Oncology*Biology*Physics* **2005**, *62*, 358-365, doi:https://doi.org/10.1016/j.ijrobp.2004.10.014.

14. Habash, R.W.; Bansal, R.; Krewski, D.; Alhafid, H.T. Thermal therapy, part 2: hyperthermia techniques. *Crit Rev Biomed Eng* **2006**, *34*, 491-542, doi:10.1615/critrevbiomedeng.v34.i6.30.
15. Kaur, P.; Aliru, M.L.; Chadha, A.S.; Asea, A.; Krishnan, S. Hyperthermia using nanoparticles--Promises and pitfalls. *Int J Hyperthermia* **2016**, *32*, 76-88, doi:10.3109/02656736.2015.1120889.
16. Gazeau, F.; Lévy M Fau - Wilhelm, C.; Wilhelm, C. Optimizing magnetic nanoparticle design for nanothermotherapy.
17. Kaur, P.; Hurwitz Md Fau - Krishnan, S.; Krishnan S Fau - Asea, A.; Asea, A. Combined hyperthermia and radiotherapy for the treatment of cancer.
18. Bakhmutov, V.I.; Berry, J.F.; Cotton, F.A.; Ibragimov, S.; Murillo, C.A. Non-trivial behavior of palladium(ii) acetate. *Dalton Transactions* **2005**, 10.1039/B502122G, 1989-1992, doi:10.1039/B502122G.
19. Lin, F.-h.; Chen, W.; Liao, Y.-H.; Doong, R.-a.; Li, Y. Effective approach for the synthesis of monodisperse magnetic nanocrystals and M-Fe3O4 (M = Ag, Au, Pt, Pd) heterostructures. *Nano Research* **2011**, *4*, 1223-1232, doi:10.1007/s12274-011-0173-2.
20. Mazumder, V.; Sun, S. Oleylamine-Mediated Synthesis of Pd Nanoparticles for Catalytic Formic Acid Oxidation. *J Am Chem Soc* **2009**, *131*, 4588-4589, doi:10.1021/ja9004915.
21. Liu, S.; Guo, S.; Sun, S.; You, X.-Z. Dumbbell-like Au-Fe3O4 nanoparticles: a new nanostructure for supercapacitors. *Nanoscale* **2015**, *7*, 4890-4893, doi:10.1039/C5NR00135H.
22. Jin, Y.; Jia, C.; Huang, S.-W.; O'Donnell, M.; Gao, X. Multifunctional nanoparticles as coupled contrast agents. *Nature Communications* **2010**, *1*, 41, doi:10.1038/ncomms1042.
23. van Rhoon, G.C.; Samaras, T.; Yarmolenko, P.S.; Dewhirst, M.W.; Neufeld, E.; Kuster, N. CEM43 degrees C thermal dose thresholds: a potential guide for magnetic resonance radiofrequency exposure levels? *Eur Radiol* **2013**, *23*, 2215-2227, doi:10.1007/s00330-013-2825-y.
24. Atkinson, W.J.; Brezovich, I.A.; Chakraborty, D.P. Usable frequencies in hyperthermia with thermal seeds. *IEEE Trans Biomed Eng* **1984**, *31*, 70-75, doi:10.1109/TBME.1984.325372.
25. Hergt, R.; Dutz, S. Magnetic particle hyperthermia—biophysical limitations of a visionary tumour therapy. *Journal of Magnetism and Magnetic Materials* **2007**, *311*, 187-192, doi:https://doi.org/10.1016/j.jmmm.2006.10.1156.
26. Stephenson, T.A.; Morehouse, S.M.; Powell, A.R.; Heffer, J.P.; Wilkinson, G. 667. Carboxylates of palladium, platinum, and rhodium, and their adducts. *Journal of the Chemical Society (Resumed)* **1965**, 10.1039/JR9650003632, 3632-3640, doi:10.1039/JR9650003632.
27. Carole, W.A.; Colacot, T.J. Understanding Palladium Acetate from a User Perspective. *Chemistry – A European Journal* **2016**, *22*, 7686-7695, doi:https://doi.org/10.1002/chem.201601450.

28. Stolyarov, I.P.; Demina, L.I.; Cherkashina, N.V. Preparative synthesis of palladium(II) acetate: Reactions, intermediates, and by-products. *Russian Journal of Inorganic Chemistry* **2011**, *56*, 1532-1537, doi:10.1134/S003602361110024X.
29. Qin, Y.; Ji, X.; Jing, J.; Liu, H.; Wu, H.; Yang, W. Size control over spherical silver nanoparticles by ascorbic acid reduction. *Colloids and Surfaces A: Physicochemical and Engineering Aspects* **2010**, *372*, 172-176, doi:https://doi.org/10.1016/j.colsurfa.2010.10.013.
30. Ji, X.; Song, X.; Li, J.; Bai, Y.; Yang, W.; Peng, X. Size Control of Gold Nanocrystals in Citrate Reduction: The Third Role of Citrate. *J Am Chem Soc* **2007**, *129*, 13939-13948, doi:10.1021/ja074447k.
31. Kielhorn, J.; Melber, C.; Keller, D.; Mangelsdorf, I. Palladium--a review of exposure and effects to human health. *Int J Hyg Environ Health* **2002**, *205*, 417-432, doi:10.1078/1438-4639-00180.
32. Mohammadi, Z.; Shalavi, S.; Jafarzadeh, H. Ethylenediaminetetraacetic acid in endodontics. *Eur J Dent* **2013**, *7*, S135-S142, doi:10.4103/1305-7456.119091.
33. Daunys, S.; Janoniene, A.; Januskeviciene, I.; Paskeviciute, M.; Petrikaite, V. 3D Tumor Spheroid Models for In Vitro Therapeutic Screening of Nanoparticles. *Adv Exp Med Biol* **2021**, *1295*, 243-270, doi:10.1007/978-3-030-58174-9_11.
34. Carvalho, M.P.; Costa, E.C.; Miguel, S.P.; Correia, I.J. Tumor spheroid assembly on hyaluronic acid-based structures: A review. *Carbohydr Polym* **2016**, *150*, 139-148, doi:10.1016/j.carbpol.2016.05.005.
35. Ku, A.; Facca, V.J.; Cai, Z.; Reilly, R.M. Auger electrons for cancer therapy – a review. *EJNMMI Radiopharmacy and Chemistry* **2019**, *4*, 27, doi:10.1186/s41181-019-0075-2.
36. Wang, R.; Liu, J.; Liu, Y.; Zhong, R.; Yu, X.; Liu, Q.; Zhang, L.; Lv, C.; Mao, K.; Tang, P. The cell uptake properties and hyperthermia performance of Zn(0.5)Fe(2.5)O(4)/SiO(2) nanoparticles as magnetic hyperthermia agents. *R Soc Open Sci* **2020**, *7*, 191139, doi:10.1098/rsos.191139.
37. Suk, J.S.; Xu, Q.; Kim, N.; Hanes, J.; Ensign, L.M. PEGylation as a strategy for improving nanoparticle-based drug and gene delivery. *Adv Drug Deliv Rev* **2016**, *99*, 28-51, doi:10.1016/j.addr.2015.09.012.

PhD portofolio

Publications

Maier A, van Oossanen R, van Rhoon GC, Pignol JP, Dugulan I, Denkova AG, Djanashvili K. From Structure to Function: Understanding Synthetic Conditions in Relation to Magnetic Properties of Hybrid Pd/Fe-Oxide Nanoparticles. Nanomaterials (Basel). **2022**.

van Oossanen, R.; Godart, J.; Brown, J.M.C.; **Maier, A**.; Pignol, J.P.; Denkova, A.G.; Djanashvili, K.; van Rhoon, G.C. Feasibility Study on the Radiation Dose by Radioactive Magnetic Core-Shell Nanoparticles for Open-Source Brachytherapy. *Cancers (Basel)* **2022.**

Van Oossanen, R.; **Maier, A**.; Godart, J.; Pignol, J.P.; Denkova, A.G.; van Rhoon, G.C.; Djanashvili, K.; Magnetic Hybrid Pd/Fe-oxide Nanoparticles Meet the Demands for Ablative Thermo-Brachytherapy, *International Journal of Hyperthermia* **2023. (**submitted**)**

Patents

EU-patent, *No. 2029314*, "Synthesis of Hybrid Palladium (103)/iron Oxide Nanoparticles for Thermo-brachy Therapy", **2021.**

Oral Presentations

A. Maier, R. van Oossanen, G. van Rhoon, A. G. Denkova and K. Djanashvili, Exploring the Synthesis Conditions for Magnetic Pd/Fe-oxide Nanoparticles. Nanotech France 2022, 16-17 June 2022, Paris, France.

A. Maier, R. van Oossanen, Robin A. Nadar, G. van Rhoon, A. G. Denkova and K. Djanashvili. Radiolabeled Magnetic Nanoparticles as Gamechangers in Cancer Therapy. XXXVth URSI General Assembly and Scientific Symposium, URSI GASS 2023, 19-26 August 2023, Sapporo, Japan.

Posters

Maier, A., R. van Oossanen, A. G. Denkova and K. Djanashvili. "Nanoparticles for image-guided thermo-brachytherapy" – RST/RID Science Day, 2 April 2019, Delft, The Netherlands.

Curriculum Vitae

Alexandra Maier was born on the 11th of January, 1992 in Bucharest, Romania. During high school she developed an interest for science, chemistry in particular, which motivated her to further pursue Chemical Engineering at Politehnica University of Bucharest, starting in 2011. During the four years of bachelor, she specialized in Polymer Science and Technology.

After successfully completing her bachelor's degree in 2015, she wanted to further pursue Chemical Engineering and got accepted for the Chemical Engineering Master in Science, Product Track, at TU Delft. During the MSc, she discovered her passion for research, with focus on the biomedical field. She started her master end project, named "Tubular Micro-origami: Self-folding hydrogel structures for vascular scaffolds", where she developed novel 2D hydrogel micro-patches with the ability to transform into 3D tubular architectures through a self-folding mechanism triggered via enzymatic degradation, and to accommodate cell adherence and proliferation, which made this micro-system an extremely useful strategy in the field of tissue engineering.

In 2018, after finishing her internship at TNO, she concluded her master and got offered to continue at TU Delft on a collaboration PhD project between TU Delft and Erasmus MC, under the supervision of Kristina Djanashvili and Antonia Denkova. During this time, as part of both Biocatalysis and Organic Chemistry (BOC) and Applied Radiation and Isotopes for Health (ARI) groups, she further continued her research in the biomedical field, focusing on cancer treatment, by researching and developing hybrid radioactive nanoparticles, as potential theranostic agents for image-assisted thermo-brachytherapy. This thesis is the result of all the research years during the PhD.

Acknowledgements

"*Nobody queues for a flat rollercoaster. A PhD has its ups and downs. You can only hope to enjoy more than to scream during the ride*!" I wrote this proposition thinking that my PhD has for sure been a crazy rollercoaster. Now, even though I did scream...a lot, mostly internally, and I felt like I was going down the rabbit hole, and climbing up mount Doom at the same time, I also enjoyed this crazy ride big time. This was mainly because of the many people who took the leap of faith with me and pushed me towards the end. To all of you, I want to thank, so here it goes.

First and biggest thanks go to my promotors, **Kristina** and **Antonia**, for your vote of confidence all those years ago in giving me the opportunity to be part of your team and trusted this project with me.

Kristina, one cannot ask for a better promotor. „Words are really too little" is what you e-mailed me in the emotionally hardest moment of my PhD, and that is how it feels when trying to thank you. Thank you for your infinite kindness, for *always* having my back, and for the patience you had with me and my perfectionism. This journey would have been undeniably tougher without you by my side. You were my supervisor, my friend, and my biggest cheerleader, always knowing when which was needed. I will always cherish your effort, the fun we had, and all the time we spent together, from research meetings and long workdays to evenings with great food and Codenames Undercover edition.

Antonia, one cannot get so lucky with a second promotor. I remember this story, now ironically funny, back then not so much, when the centrifuge broke *again* exactly before the too long-awaited radioactivity arrived. That was one of the lowest, most frustrating moments of my PhD and you welcomed me with so much positivity and encouragement. Your optimism gives hope, and that is a very big thing to offer. Thank you for all the help and knowledge, especially with the radioactivity, and for always being present.

You both bring light and humour at work every day, and that is what makes working with you so great.

The making of this thesis was strongly aided by the administrative and technical support and hard work of many people.

To **Anouk**, **Irma** and **Mieke**, thank you for always being helpful and caring and for making ARI and BOC groups so welcoming.

It's often said that nanoparticle synthesis is like cooking, but boiling radioactivity at 300 °C feels like cooking when the kitchen is on fire, an alarm is ringing, and three open tabs are playing music in the background. Therefore, I owe a huge thank you to all whom embraced my often too crazy experiments and offered a helping hand, making the process so much easier.

Astrid, **Baukje**, **Eline**, for always being my safety net in the ARI labs. **Eline**, you are sunshine during long lab days. **Laura**, **Marc**, for the hospitality in the BOC labs. **Lloyd**, for bearing with my centrifuge and I with so very much appreciated dark humour. You are a rock star. **Stephen**,

for all the synthesis and "relaxation" experiments you did with me, plus the guaranteed fun with dry ice and during Saturgays.
To everyone from **SBD**, thank you for the help and for always receiving my crazy permits with an open mind.

Anton, **Iulian**, **Swapna**, a huge thank you for your help and guidance with SQUID, Mössbauer and NMR measurements.

This thesis wouldn't be so far without the help I got from the students that trusted me with their projects: **Berend**, **Lex**, **Keshav**, **Olivier**. I learned a lot with and from all of you. Thanks!

My PhD project was a collaboration with **Erasmus MC** and **Elekta**. Special thanks to **Gerard** and **Jean-Philippe** for the help and advice offered during many user meetings.

I was lucky to be part of two research groups, and "adopted" by a third. This brought so much colour in my workdays. A PhD journey can feel lonely at times, but there was always comfort and joy in the people around to make up for it.

Starting with the **ARI group**, **Robin,** thanks for always bringing sugar, spice, and everything nice into work. I will really miss our fun talks either too early in the morning or too late in the evening. You are an inspiration, and your work ethic is unbeatable! Don't miss me too much!

A big shout-out to the girls' office: **HuanHuan**, your cheerful vibes were what kept our office alive at times. Thank you for your great energy. **Retni**, I cannot thank you enough for being a much-needed lifebuoy through my PhD. The greatest company in the lab and the best shoulder to cry on in the office, always kind, caring and able to bring a smile on my face. **Jackey**, thank you for trusting me with your first Halloween party, with advice and stories we shared. May the nanoparticles work in your favour, as you know the struggle best. **Svenja**, you showed me that a good day is a good day, but a bad day is a good story, so kudos to those a-bit-more-radioactive-than-expected and bottom low days. Also, a big thank you for all the breaks we took together and for keeping my mental health in check in the last stages of my PhD. By extension, **Albert**, thanks for bringing spice and joy to our office whenever you were around.
Gauri, **Bing**, welcome to the girls' office! I hope you'll have a great time with your PhDs and find as much comfort in this office as I did.

Rogier and **Robin N**, this thesis would not be what it is without all your help. **Rogier**, you were a great companion through this project, and without your knowledge and encouragements, some of the hard times would have been *much* harder. Thanks for being there, from failed experiments to the best beer recommendations in t'Koepeltje after a long week. **Robin N**, your enthusiasm in the lab was so motivating during the last stage of experiments. Thank you for all the spheroid work, the hours you spent looking at them, and the meetings we spent talking about them.
Runze, **Chao**, thanks for always being great colleagues, sharing advice and your lab equipment when needed.

Folkert, thank you for always being so helpful and caring. **Mehmet**, thank you for all the fun talks and the beers. **Delia**, ești atât de faină, de n-am cuvinte. Thank you for bringing the feeling of "home" into work and talks that brightened my days. **Henk, Koos**, thanks for always being so cheerful, you instantaneously make the day brighter and the bar on Fridays funnier.

I spent a lot of time moving in between buildings, so next to Applied Science, I would like to pay a visit to the **BOC group**. First, thanks to all of you for always being so kind and friendly whenever I would appear around like a wild Pokémon. **Allison**, **Aster**, **Albert**, **Andrada**, **Hannah**, **Luuk**, **Marine**, **Morten**, **Sam**, **Seb**, **Stefan**, **Thomas**, **Xiaoming**, **Yinqi**, thank you for the nice times during lunch, coffee breaks, beers, and group events.
Hugo, with the positivity and joy you always brought to my tables and parties, it was impossible not to have a great time. **Chiara**, to more *la dolce vita*, home-made pasta and ragù. You both are gems.
Caroline, thanks for the shared stories and passion for painting, I'm looking forward to another session. **Peter-Leon**, thank you for the last-minute help with EPR. It was a pleasure working with you. **Ulf**, thank you for being my promotor in the beginning of my PhD.

To my paranymphs, **David** and **Fabio**, the chosen ones. You are welcome! Our friendship stands as proof that love goes through the stomach. Thank you for opening your homes, your fridges and all your cupboards to me.

David, one of the best parts of my PhD is that I got to share it with you as my best friend. I *genuinely* can't imagine reaching the end without you. Thank you for being next to me in the rollercoaster, to the highest ups and to the lowest downs, you've been there for it all. You gave me strength, happiness and I always felt at "home" with you around. Without you, this crazy ride wouldn't have had so much flavour and laughter.
Patato, *alora due parole*…you are panna cotta in dark times. Thank you for letting me be your friend, your "little" sister when introducing me to Italy and your amazing family, your ghost writer, Tinder dating advisor, and the Lily to your Ted. You offered so much stability through this journey, and I always felt cared for. I cherish all the moments together. You are one of a kind.
Thank you **both** for taking the last leap of faith with me by accepting to be my paranymphs.

In **EBT** is where I always found fun, laughter and great company for lunches and many Friday evenings. To the "oldies" **Danny**, **Maria-Paula**, **Simon**, and to the goldies **Ali**, **Claudia**, **Kiko**, **Lemin**, **Maxim**, **Nina**, **Rodoula**, **Timmy**, **Stefan**, thank you for making **EBT** special, for opening your doors to me, for the humour and the relaxed vibes when highly needed.

Kiko, a very special thank you for all the crazy conversations you brought in my life and for the fun questions I would have probably never asked myself if it wasn't for you. You are precious to have around. Let's write & illustrate that book you have in mind. It'll be a blast.
Rodoula, **Angelos**, you guys are what Balkans have to offer best. The conversations, dinners, and drinks we shared are the closest I got here to what cosy Romanian evenings mean to me. You are the much-needed comfort when far away from home. Thank you.

EBT holds a special place in my heart also because it's the reason I found you, guys, **Ingrid**, **Flo**, **Mariana**, **Marta**, **Sergio**. You are my Delft family, and this story would have been grey without you in it. We spent so much time together, from best brunches, painting days, intense game sessions, dinners, parties, and holidays to "therapy sessions" and creating a safe space to be ourselves and let go of the struggles. I always felt understood and loved with you around.

Ingrid, you are warm baguette with the best butter on top. Thank you that the only pain I had in life when you were around was *pain au chocolat*, and for making adulthood seem so easy. **Flo**, you thought me kindness with every interaction we had. Thank you for allowing us to be kids around you. You are the best mom this group could have. **Mariana**, you should never worry about your RBF, because it's impossible not to love you. The organization and energy you put in this group are unmatchable. Thank you for always being my partner in crime with reality TV shows and books. **Marta**, you are living proof that strong essences are kept in small bottles. Thank you for the spice you bring and for always allowing me to be "Miserable, darling, as usual. Perfectly wretched". **Sergio**, we started this journey together and you brought so much sass, zazz and spark to it. Thanks for being so much fun, the sunshine to my grumpy self.

You all inspire me to be a better friend. Thank you from the bottom of my heart.

To the other great people I met in **BT**. **Aafke**, **Maxime**, **Marina**, thank you for all the fun we had organizing events during the BT PhD committee and for making the quarantine time so much better. **Marina**, you are the best example of force and endurance in this PhD. Thanks for the heart-to-heart conversations and for the smiles, despite the struggles. **Koen**, thank you for always being kind and warm.

For the friends I made during my MSc in TU Delft: **Katcha, Martin, Marie**, **Eva, Jaen, Jorrit**. Without your help and friendship through the master, this PhD might have not happened. It's always fun to be with you, so let's do it more often!

Ursula, **Hans**, **Cornelia**, **Katharina**, vielen Dank für die guten Gedanken und Fürsorge und dafür, dass ich mich in Deutschland immer wie zu Hause fühlen kann.

Georg, you were the Sam to my Frodo through this journey. "I can't carry it for you, but I can carry you"...and so you did. I cannot thank you enough for being my rock every single day, for bearing with my worst self with so much nurture and for bringing love, calm and freedom in our house. You were by my side through every research fail, writing struggle, mental breakdown, the loss of my mother, to always pick me up and bring me to the end. I cannot wait to start another journey with you, wherever your adventurous spirit takes us in this big world. I love you.

Ioana, **Miru**, **Sânzi**, stelele mele călătoare, nu pot să vă mulțumesc îndeajuns că sunteți o constantă în viața mea de atâția ani. Datorită vouă am învățat ce înseamnă *sisterhood* și *my happy place* încă e cu voi pe plajă în Vama Veche. Sper să rămânem mereu young and fresh ca la 16 ani. Big thanks also to your amazing partners who empower you every day to be such amazing friends. Și pentru cei mici, ai voștri, care aduc atât de multă bucurie.

Elena, cea mai bună prietenă pe care cineva o poate avea. Alexandra la 11 ani a făcut cea mai bună alegere, iar Alexandra la 31 incă e forever in your debt. Îți mulțumesc pentru că ai însemnat mereu *acasă* pentru mine.

Maria, **Dani**, **Mimi**, grijile au fost mai ușor de dus când ajungeam acasă și ne așezam la o masă împreună. Încurajările și gândurile bune din partea voastră au fost mereu fix ce aveam nevoie ca să îmi încarc bateriile. **Maria**, ești poezie în viața mea.
Sunteți fără de preț. Vă mulțumesc.

Tata, **mama**, de la voi am învățat ce înseamnă iubirea necondiționată. Toate sacrificiile voastre sunt motivul pentru care am ajuns aici. Mulțumesc că m-ați lasat mereu să fiu liberă în alegeri, că am avut parte de sprijinul și încurajările voastre în orice situație și că mereu m-am putut baza pe voi. Mulțumesc că m-ați invățat ce înseamnă perseverența și că în viață nimic nu se obține ușor, au fost cele mai importante lucruri de știut într-un doctorat.
Un ultim gând pentru mama, care știu că ar fi *atât* de mândră, aș vrea atât de mult să fii aici cu noi.
Sunt cine sunt mulțumită vouă. Vă iubesc.